UNIVERSITÉ DU QUÉBEC À MONTRÉAL

METHODOLOGIES DE RMN À L'ÉTAT SOLIDE POUR L'ÉTUDE *IN SITU* DES INTERACTIONS ENTRE PEPTIDES ANTIMICROBIENS ET MEMBRANES ÉRYTHROCYTAIRES

THÈSE
PRÉSENTÉE
COMME EXIGENCE PARTIELLE
DU DOCTORAT EN CHIMIE

PAR

KIRANA KIRANA

FÉVRIER 2024

UNIVERSITÉ DU QUÉBEC À MONTRÉAL

SOLID-STATE NMR METHODOLOGIES FOR THE *IN SITU* STUDY OF MOLECULAR INTERACTIONS BETWEEN ANTIMICROBIAL PEPTIDES AND ERYTHROCYTE MEMBRANES

THESIS
PRESENTED
AS A PARTIAL REQUIREMENT
OF THE DOCTORATE IN CHEMISTRY

BY

KIRANA KIRANA

FEBRUARY 2024

ACKNOWLEDGEMENTS

Firstly, I would like to express my sincere gratitude to my supervisors, Isabelle and Dror, for making this work possible. They have given me the opportunity to study at UQAM and embark on this fascinating research journey. Their guidance, motivation, and advice have helped me through all stages of my thesis writing. Isabelle, your friendly guidance, and encouragement have been invaluable to me over the past five years of my research journey. Your advice has refined my academic writing and sharpened my scientific thinking. Dror, thank you for your valuable suggestions and extended discussions which have greatly contributed to the improvement of this thesis. Thank you both for amazing support, mentorship, and inspiration.

I would like to specially thank Alex for his continuous support, understanding, and help with the figures and final preparation of the manuscript. Alex is also my supervisor and teacher, helping me to understand the core concepts of NMR. Alex, thank you for the enlightening discussions we've been having about NMR, your insights and expertise have been invaluable to me, and I am constantly learning every time.

Alex P and Mathew, thank you for your constant support and guidance. Your suggestions have enhanced my knowledge and improved my research and skills. I am also thankful to Vicky and Bryan for their assistance with my initial experiments on ghosts and bacteria. I would like to extend my sincere appreciation to JP, Pierre, Florent, Daman, Stéphane, and Arunima from Marcotte lab for their valuable help in various aspects and their kind support, and also thanks to Laila for her assistance with preparation of protocols and thanks to the J-F Paquin group for their contribution in the preparation of fluorinated lipids and FAs. I would also like to thank all members of Bourgault lab for their support in various ways.

Finally, I would like to express my heartfelt gratitude to my friends and family. I am grateful for your unwavering support, for being with me through the highs and lows of life, and for encouraging me when times were uncertain. Your unwavering belief in me and your constant encouragement have been a source of strength and motivation. Thank you for always being there for me.

TABLE OF CONTENTS

DEDICATION

To my parents

and

To all those who have taught me

LIST OF FIGURES

LIST OF TABLES

LIST OF ABBREVIATIONS, SYMBOLS, AND ACRONYMS

^{13}C	Isotope of mass 12 of carbon
^{15}N	Isotope of mass 15 of nitrogen
^{19}F	Isotope of mass 19 of fluorine
^{1}H	Proton
^{2}H	Deuterium/Deutérium
^{31}P	Isotope of mass 31 of phosphorus
AMPs	Antimicrobial peptides
AMR	Antimicrobial resistance
B. subtilis	*Bacillus subtilis*
B_0	Magnetic field
C14:0	Myristic acid
C15:0	Pentadecylic acid
C16:0	Palmitic acid
C16:0 ^{2}H	Deuterated palmitic acid
C16:1	Palmitoleic acid
C17:0	Methylhexadecanoic acid
C18:0	Stearic acid
C18:1	Oleic acid
C18:2	Linoleic acid
C20:0	Arachidic acid
Chol	Cholesterol
CL	Cardiolipin
CSA	Chemical shift anisotropy
cyC17:0	9,10-Methylenehexadecanoic acid
cyC19:0	11,12-Methyleneoctadecanoic
DARR	Dipolar assisted rotational resonance
DHSM	Dihydrosphingomyelin
DMPC	1,2-dimyristoyl-sn-glycero-3-phosphocholine
DOPC	1,2-dioleoyl-sn-glycero-3-phosphocholine
DOPE	1,2-dioleoyl-sn-glycero-3-phosphoethanolamine
DOPS	1,2-dioleoyl-sn-glycero-3-phospho-L-serine
DPC	Dodecylphosphocholine
DPPC	Dipalmitoylphosphatidylcholine
DPPC-d_{62}	Deuterated dipalmitoylphosphatidylcholine
E. coli	*Escherichia coli*
EDTA	Ethylenediaminetetraacetic acid
EFG	Electric field gradient
FAs	Fatty acids

FID	Free induction decay
FWHM	Full width at half maximum
GCMS	Gas chromatography coupled to mass spectrometry
GR	Globules rouges
GUVs	Giant Unilamellar Vesicles
HDPs	Host defence peptides
H_I or H_{II}	Hexagonal phases
HOESY	Heteronuclear Overhauser spectroscopy
$\vec{I}$	Spin angular momentum
L. lactis	*Lactococcus lactis*
L/P	Lipid-to-peptide
L_d	Liquid-disordered phase
L_o	Liquid-ordered phase
LPS	Lipopolysaccharides
LTAs	Lipoteichoic acids
LUVs	Unilamellar Vesicles
lysyl-PG	Lysyl-phosphatidylglycerol
L_α	Fluid disordered phase
L_β	Gel or ordered phase
M. tuberculosis	*Mycobacterium tuberculosis*
M_2	Second moment
MAS	Magic-angle spinning
MFFAs	Monofluorinated fatty acids
MFPAs	Monofluorinated palmitic acids
MHC	Minimum hemolytic concentration
MIC	Minimal inhibitory concentration
MLVs	Multilamellar Vesicles
n_0	Bilayer normal (director axis)
NOE	Nuclear Overhauser effect
NOESY	Nuclear Overhauser effect spectroscopy
P. aeruginosa	*Pseudomonas aeruginosa*
P. multocida	*Pasteurella multocida*
PA	Palmitic acid
PA-d_{31}	Deuterated palmitic acid
PA-F(4)	PA fluorinated at carbon 4
PA-F(8)	PA fluorinated at carbon 8
PA-F(14)	PA fluorinated at carbon 14
PDSD	Proton-driven spin diffusion
PGN	Peptidoglycan
PI	Phosphatidylinositol

PLs	Phospholipids
POPC	1-palmitoyl-2-oleoyl-glycero-3-phosphocholine
POPE	1-palmitoyl-2-oleoyl-sn-glycero-3-phosphoethanolamine
POPG	1-palmitoyl-2-oleoyl-sn-glycero-3-phospho-glycerol
RBCs	Red blood cells
REDOR	Rotational-echo double-resonance
RF	Radio-frequency
RFDR	Radio-frequency-driven recoupling
RMN-ÉS	Résonance magnétique nucléaire de l'état solide
RVS	Rosuvastatin
S. aureus	*Staphylococcus aureus*
S/N	Signal-to-noise
S_{CD}	Order parameter of the carbon deuterium bond
S_{CF}	Order parameter of the carbon fluorine bond
SM	Sphingomyelin
SPX	Sparfloxacin
SSBs	Spinning sidebands
SS-NMR	Solid-state nuclear magnetic resonance
T_1	Spin-lattice (longitudinal) relaxation
T_2	Spin-spin (transverse) relaxation
TAs	Teichoic acids
TI	Therapeutic index
T_m	Phase transition temperature
TOCSY	Total correlation spectroscopy
ν	Resonance frequency
$\vec{\mu}$	Nuclear magnetic moment
β	The average time-dependent angle between the bilayer normal and the C-^{2}H bond
δ_{iso}	Isotropic chemical shift
γ	Gyromagnetic ratio
$\Delta\nu_Q$	Quadrupole splitting
η	Asymmetry parameter
θ	The angle between B_0 and the bilayer normal
θ_m	Magic-angle spinning
σ	Chemical shift tensor
τ_c	Rotational correlation time
χ	Static quadrupolar coupling constant
ω_0	Larmor frequency

LIST OF UNITS

° C	Unit of temperature (degree Celsius)
Å	Unit of distance (angstrom)
g	Unit of acceleration (gravity)
Mol	Unit of concentration (mole)
h	Unit of time (hour)
Hz	Unit of frequency (hertz)
k	Kilo
mg	Unit of mass (milligram)
min	Unit of time (minute)
mL	Unit of volume (milliliter)
mM	Unit of concentration (millimolar)
ms	Unit of time (millisecond)
mV	Unit of electric potential (Millivolt)
nm	Unit of distance (nanometre)
ppm	Parts per million
rpm	Unit of frequency (revolutions per minute)
s	Unit of time (second)
µg	Unit of mass (microgram)
µL	Unit of volume (microliter)
µM	Unit of concentration (micromolar)

RÉSUMÉ

L'incidence des bactéries multirésistantes augmente dans le monde entier, et il est urgent de développer de nouveaux antibiotiques dotés de mécanismes d'action novateurs. Les peptides antimicrobiens (AMPs) sont considérés comme une avenue thérapeutique prometteuse et des antibiotiques à large spectre, car ils agissent en perturbant les membranes cellulaires bactériennes. Les AMP sont omniprésents dans la nature, produits par divers organismes et faisant partie intégrante de leur mécanisme de défense. Ces peptides présentent plusieurs modes d'action, notamment des interactions préférentielles avec les lipides des membranes cellulaires bactériennes. Leur action inclut la formation de pores dans les membranes ou leur micellisation via un mécanisme de type tapis.

De nombreuses études ont démontré les propriétés antibactériennes des AMPs. Cependant, l'interaction avec les cellules mammifères a été moins étudiée, et il est donc important de vérifier et de comprendre leur action potentielle sur les cellules eucaryotes telles que les érythrocytes (globules rouges ou GR) pour développer des médicaments sécuritaires et ciblés. Dans ce contexte, la résonance magnétique nucléaire de l'état solide (RMN-ÉS) peut fournir des informations au niveau atomique sur l'interaction des AMP avec les membranes. Cette approche est généralement réalisée avec des membranes lipidiques modèles, cependant, compte tenu de la complexité des membranes cellulaires, la RMN-ÉS *in cellulo* se distingue maintenant comme un outil extrêmement précieux pour obtenir une vision plus large de l'action des AMPs.

L'objectif de cette thèse était de comprendre l'effet des AMPs sur les membranes des érythrocytes au niveau atomique, et d'établir des approches de RMN-ÉS pour étudier les interactions entre les cellules entières et les peptides. Pour ce faire, l'auréine 1.2 et la caérin 1.1 ont été utilisées. Trois objectifs de recherche spécifiques ont été poursuivis: (1) Étudier l'interaction des AMPs *in situ* par RMN-ÉS du deutérium (^{2}H) ; (2) Développer une méthodologie pour étudier ces interactions par RMN-ÉS du fluor-19 (^{19}F) dans les cellules entières afin d'accélérer les mesures; (3) Établir une approche pour déterminer les distances internucléaires dans les cellules intactes basée sur la RMN-ÉS du ^{19}F.

Nous présentons d'abord l'incorporation d'acides gras déutérés et fluorés exogènes dans les membranes de fantômes d'érythrocytes. L'intégrité et la fluidité des membranes marquées est confirmée. L'étude de l'interaction de l'auréine et de la caérine avec les fantômes de globules rouges est révélée par la mesure de paramètres spectraux tels que les moments spectraux en ^{2}H et ^{19}F, l'anisotropie de déplacement chimique du ^{31}P et du ^{19}F, le déplacement chimique isotrope du ^{19}F et les temps de relaxation. Des analyses en microscopie et des tests de fuite sont également réalisés sur des érythrocytes intacts et des membranes modèles. Dans l'ensemble, les résultats confirment que l'auréine interagit via un mécanisme de type tapis et que la caérine forme un pore dans la membrane, similairement à leur action sur les membranes bactériennes.

Enfin, nous utilisons des membranes modèles incorporant des acides gras fluorés pour cartographier l'interaction du médicament fluoré rosuvastatine. La connectivité moléculaire est révélée entre la statine et le système lipide/acides gras, ainsi qu'entre les acides gras, en utilisant des expériences de RMN-ÉS bidimensionnelles homonucléaires et hétéronucléaires. Ce travail établit des bases solides pour des mesures futures en cellules entières.

Cette thèse montre que l'action membranaire de médicaments, tels que les AMPs, peut être étudiée in situ sur les érythrocytes au niveau moléculaire, par une combinaison de marquage

spécifique au ^{2}H ou au ^{19}F et d'expériences de RMN-ÉS. Elle met en évidence le rôle des interactions hydrophobes dans le mécanisme d'action des AMPs. D'une façon générale, elle ouvre la voie à la cartographie des médicaments dans une membrane lipidique intacte, et propose de nouvelles méthodologies robustes de RMN-ÉS susceptibles d'être utilisées pour l'étude de diverses cellules.

Mots clés : Peptides antimicrobiens, antibiotiques, globules rouges, fantômes érythrocytaires, bactéries, membrane lipidique, membrane cellulaire, marquage isotopique, profil lipidique, RMN de l'état solide, marquage isotopique, ^{2}deutérium, fluor-19, anisotropie de déplacement chimique, moment spectral, relaxation, RMN bidimensionnelle.

ABSTRACT

The incidence of multidrug-resistant bacteria is increasing worldwide, and there is an urgent need to develop new antibiotics with innovative mechanisms of action. Antimicrobial peptides (AMPs) are considered a promising therapeutic avenue and broad-spectrum antibiotics because many of them act by disrupting bacterial cell membranes. AMPs are ubiquitous in nature, produced by various organisms, and are an integral part of their defense mechanism. These peptides exhibit multiple modes of action, including preferential interactions with the lipids of bacterial cell membranes. Their action involves the formation of pores in membranes or micellization via a carpet-like mechanism.

Numerous studies have demonstrated the antibacterial properties of AMPs. However, the interaction with mammalian cells has been less studied, and it is important to verify and understand their potential action on eukaryotic cells such as erythrocytes (red blood cells or RBCs) to develop safe and targeted drugs. In this context, solid-state nuclear magnetic resonance (SS-NMR) can provide atomic-level information on the interaction of AMPs with membranes. This approach is usually carried out with model lipid membranes; however, given the complexity of cell membranes, in-cell SS-NMR now stands out as an extremely valuable tool to gain a broader insight into the action of AMPs.

The objective of this thesis was to understand the effect of AMPs on erythrocyte membranes at the atomic level and to establish SS-NMR approaches to study interactions between whole cells and peptides. To achieve this, aurein 1.2 and caerin 1.1 were used. Three specific research goals were pursued: (1) To investigate the *in situ* interaction of AMPs using ^{2}H SS-NMR; (2) To develop a methodology for studying these interactions using ^{19}F SS-NMR in whole cells to accelerate measurements; (3) To establish an approach to determine internuclear distances in intact cells based on ^{19}F SS-NMR.

Firstly, we present the incorporation of deuterated and fluorinated exogenous fatty acids (FAs) into erythrocyte ghost membranes. The integrity and fluidity of the labeled membranes are confirmed. The study of the interaction of aurein and caerin with RBC ghosts is revealed by measuring spectral parameters such as ^{2}H and ^{19}F spectral moments, the chemical shift anisotropy of ^{31}P and ^{19}F, the isotropic chemical shift of ^{19}F, and relaxation times. Microscopy analyses and leakage assays are also performed on intact erythrocytes and model membranes. Overall, the results confirm that aurein interacts via a carpet-like mechanism, and caerin forms a pore in the membrane, similar to their action on bacterial membranes.

Finally, we use model membranes incorporating fluorinated FAs to map the interaction of the fluorinated test drug rosuvastatin. Molecular connectivity is revealed between the statin and the lipid/FA system, as well as between FAs, using two-dimensional homonuclear and heteronuclear SS-NMR experiments. This work establishes solid foundations for future measurements in whole cells.

This thesis demonstrates that the membranous action of drugs, such as AMPs, can be studied *in situ* on erythrocytes at the molecular level through a combination of specific labeling with ^{2}H or ^{19}F and SS-NMR experiments. It highlights the role of hydrophobic interactions in the mechanism of action of AMPs. Overall, it paves the way for mapping drugs in intact lipid

membranes and proposes new robust SS-NMR methodologies suitable for the study of various cells.

Keywords: Antimicrobial peptides, antibiotics, red blood cells, erythrocyte ghosts, bacteria, lipid membrane, cell membrane, isotopic labeling, lipid profile, solid-state NMR, deuterium, fluorine-19, chemical shift anisotropy, spectral moment, relaxation, two-dimensional NMR.

CHAPTER I

Introduction

1.1 Antimicrobial resistance

Since their discovery at beginning of the twentieth century, antibiotics have become the most important class of drugs in modern medicine[1]. In 1928, Sir Alexander Fleming accidentally discovered penicillin in his culture plates. Near their edges, he found a colony of mold that could be distinguished from a bacterium colony, and which inhibited the growth of bacteria. This sparked the interest of Fleming and he started growing bacteria with mold in order to concentrate penicillin, and later used it as treatment for diseases caused by bacteria[2]. There after, penicillin gained its status as antibiotic and led to the rapid discovery of various antibiotics. This was the golden age of antibiotics, which peaked in the mid-1950s. Since then, antibiotics have contributed an important role in modern medicine which continues today[3]. Interestingly, in his 1945 Nobel Prize speech, Fleming warned that misuse of penicillin could lead to bacterial resistance[3]. The first reports of penicillin resistance had already appeared in the 1940s. Nevertheless, penicillin was commonly used in the 1950s and 60s and soon after, 80% of *Staphylococci* isolates were found to be resistant to this antibiotic[4,5]. Likewise, antibiotics resistance emerged rapidly in many infectious microorganisms (Table 1.1) and the effectiveness of antibiotic treatments kept decreasing[3].

Table 1.1: Examples of multidrug resistant bacteria (*Pseudomonas aeruginosa, Staphylococcus aureus*, *Escherichia coli*, *Mycobacterium tuberculosis, Enterococci)* involved in different types of infections[6-9].

Bacteria	Infections	Antibiotic resistance
P. aeruginosa	Blood, lungs (pneumonia)	Fluoroquinolones, polymyxins, aminoglycosides, β-lactams etc.,
Methicillin-resistant *S. aureus* (MRSA)	Blood, pneumonia, or surgical site infections	β-lactams, vancomycin, fluoroquinolones, macrolides etc.,
E. coli	Blood, urinary, lung	β-lactams, aminoglycosides, fluoroquinolones etc.,
M. tuberculosis	Lung	Isoniazid, rifampicin, fluoroquinolones etc.,
Vancomycin-resistant *Enterococci*	Blood, heart, intra-abdominal	Vancomycin

Drug resistance is a normal evolutionary process for microorganisms[10]. As shown in Fig. 1.1, when antibiotics are used in the treatment of disease-causing bacteria, at first most bacteria are highly susceptible to antibiotics, but some bacteria acquire resistance, and the new population will outcompete all others leading antibiotic resistance. Resistance is accelerated by the extensive and/or indiscriminate usage of antibiotics in animal for food production or relative sectors, generally as antibiotic growth promoters (AGPs), which are distinct from growth hormones. In fact, a large fraction of antibiotics were used in the past[11] as AGPs, and only in recent years some countries including Canada banned, either wholly or partially, the use of AGPs in livestock. In addition to antibiotics use as AGPs, social, ecological, and genetic factors also influence the antimicrobial resistance process[10], which is a "*forward process*"[12]. Strategies to improve or establish the appropriate use of available antibiotics are still needed.

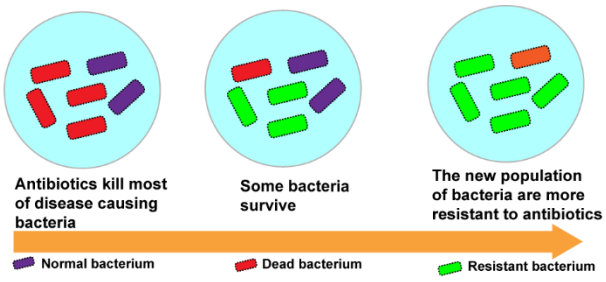

Figure 1.1: Antimicrobial resistance process.

In 2001, the World Health Organization (WHO) declared for the first time antimicrobial resistance (AMR) a global health concern[13], and the rise in bacterial infections that are resistant to known antibiotics alarming with a worldwide estimation of 4.95 million deaths associated with bacterial resistance in 2019, including 1.27 million deaths directly related bacterial infection[14] and predicted to increase up to 10 million AMR related deaths/year in 2050[14,15]. Unfortunately, over the past years, the discovery of new antibiotics to fight AMR has shown slow advances[16]. As of 2022 there are around 62 antibacterial candidates listed under clinical development[17], but approval of new drugs is very low. Also, most of these therapeutic candidates have to face challenges of bacterial resistance similar to all other first-line antibiotics. Therefore, the development of novel compounds with antibacterial properties and ability to bypass antibiotic resistance mechanisms is urgent an requirement, but such new candidates become difficult to find. In this regard, cationic antimicrobial peptides (AMPs) are one such category, that provides some optimism since they are distinctly different from other classes of antibiotics. However, like other antibiotics, the risk of

emergence of bacterial resistance depends not only on the nature of therapeutic molecules, but also on "*how much and how often*" they are used[18]. Nevertheless, the advancement of new findings such as AMPs is the first stepping stone.

1.2 Antimicrobial peptides

1.2.1 Origin, bioactivity and structure of antimicrobial peptides

AMPs are peptides usually isolated from organisms that have optimized them through thousands of years of evolution, in order to defend themselves from bacterial infections, which is why they are also called "host defence peptides" (HDPs). In this thesis for example, we will focus on two peptides that have been isolated from the skin of Australian tree frogs. It is also this evolutionary optimization which makes HDPs overcome bacterial resistance, and makes them promising candidates for human health and potential substitutes and source of inspiration for novel broad spectrum of antibiotics[19]. Among the multiple possible modes of action, several AMPs kill bacteria through damage of the cell membrane[20] (membranolytic AMPs), and some act on one or more intracellular sites[21] (nonmembrane-lytic AMPs), making the development of bacterial resistance more difficult[22].

AMPs are important biomolecules produced by a wide variety of organisms, including plants, insects, mammals and non-mammalian vertebrates[23]. As their name suggests, AMPs exhibit antimicrobial activity against various pathogens such as bacteria, fungi, and viruses, and thus play an important role in the host's innate immune response[23,24]. More than 24,000 AMP sequences have been identified so far, from both natural and synthetic origins[25]. AMPs typically contain 10 to 50 amino acid residues[26], and can be broadly classified into cationic and non-cationic peptides[27]. In most cases, AMPs are cationic peptides, with sequences including multiple Arginine, Lysine and Histidine residues. This thesis will focus on membranolytic cationic peptides. AMPs can also be classified into four different structural classes: α-helical, β-sheets, extended, and loop peptides (Fig. 1.2). The most common structures of AMPs found in nature are α-helical and β-sheets[28].

AMPs are amphipathic molecules with hydrophobic and hydrophilic regions. In cationic AMPs, electrostatic interactions play a crucial role in determining antibacterial activity with a certain selectivity for either Gram-negative or Gram-positive bacteria as well as eukaryotic cells. Hydrophobic interactions also play an important role in determining the activity of the peptide. By partitioning into the membrane interface, AMPs interaction will lead to an inevitable change in

bilayer energetics, which results in cell membrane destabilization of the targeted pathogens[29]. Indeed there is substantial evidence for interactions of AMPs with model membrane which shows membrane destabilization[30]. However, in the case of whole cells, some studies also indicate that AMPs exert their antibacterial activity by targeting one or more intracellular targets, thus inhibiting the growth of bacteria[21].

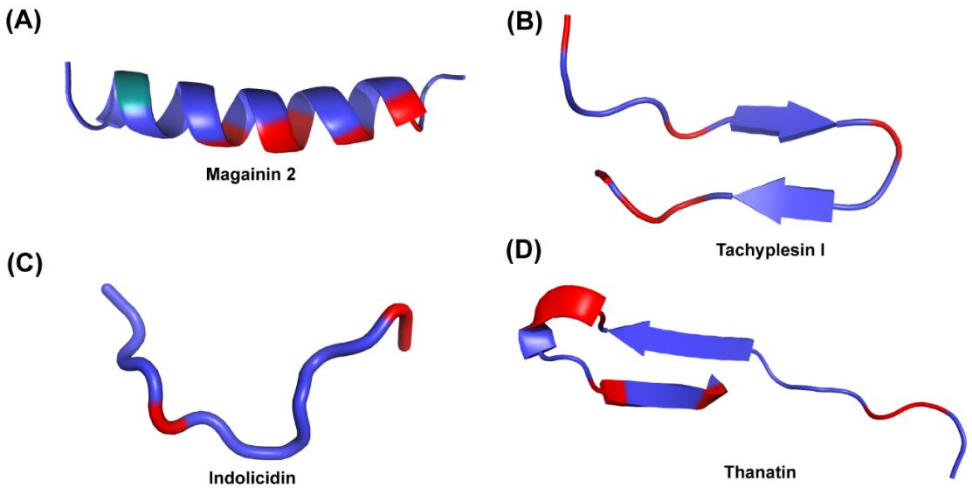

Figure 1.2: Structural classes of antimicrobial peptides with examples: (A) α-helical, magainin 2, (B) β-sheet, tachyplesin I, (C) extended, indolicidin and (D) loop, thanatin. Charged residues are indicated in red and green. (Adapted from Powers & Hancock[28] with permission).

1.2.2 Action mechanisms of AMPs

Various models have been proposed for the membranolytic interaction of AMPs[28,31,32]. Due to their amphipathic nature, the AMPs interact with the plasma membrane, first by accumulating at the membrane interface and then cell lysis can occur through various processes[32] including micellization (carpet-like model) or membrane penetration (pore model). Depending on the orientation of the peptides with respect to the lipids, the geometry and topology of the pore is described by the barrel-stave or toroidal models (Fig. 1.3).

In the barrel-stave model, peptides form channel like structures in the bacteria plasma membrane, which allow the passage of intracellular components through the pores, leading to cell lysis and leakage. In the toroidal model, AMPs form a pore by merging two lipid leaflets, and the edge of the pore is lined up by both peptides and lipids. This model also suggests that AMPs induce a distortion in the membrane curvature to stabilize the bilayer energetics. In general, many AMPs kill microbes via cell membrane perturbation through one or more of the above mechanisms[32,33].

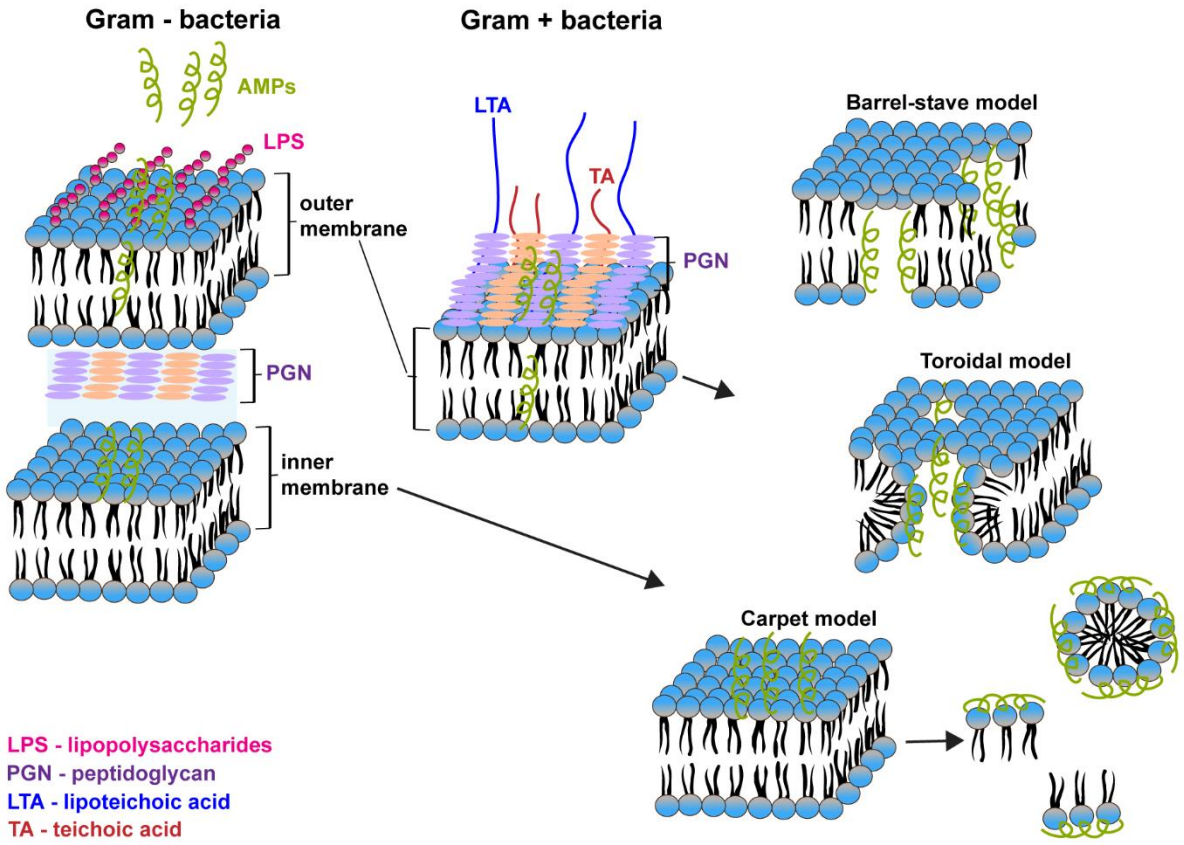

Figure 1.3: Action mechanisms of antimicrobial peptides (Adapted from Alkatheri et *al.*[33], with permission).

In bacteria, the cell envelope is an essential compartment providing a primary barrier to outside interactions. As shown in Fig. 1.3, Gram(+) bacteria are protected by a phospholipid (PL) membrane covered by a thick peptidoglycan (PGN). Gram(-) bacteria are made of an inner (IM) and an outer (OM) membrane separated by a thin PGN, and the OM is covered by lipopolysaccharides (LPS). The cell wall constituents act as a first line of defense, but cationic AMPs evolved in such a way that they act by bypassing cell wall barriers to destabilize membrane components. They are likely able to bind to the negatively-charged peptidoglycan or polysaccharide layer[34] at the bacterium surface at first, then interact with the membrane PLs (Fig. 1.3). However, mechanistic behavior of such process is yet to be elucidated.

As mentioned before, in some cases, the bactericidal effect can also be exerted through nonmembrane-lytic pathways[21], which involve the interaction of the peptides with intracellular targets such as nucleic acid biosynthesis or metabolic pathways. These specific mechanisms vary

from one peptide to another, and depend on the cell wall characteristics of the bacterium. In addition, different processes can occur at the same time to exert an effect. In general, the destabilization of the plasma membrane and/or interaction with intracellular targets are common features of the AMPs' mode of action[21,32,33].

The cell surface of bacteria comprises anionic constituents, such as LPS in Gram(-) bacteria, or teichoic acids (TAs) and lipoteichoic acids (LTAs) in the cell envelopes of Gram(+) bacteria (Fig 1.3). Both the LPS and LTA are anchored to the lipid membrane via different glycolipids, while TAs containing (glycerol-phosphate)-N-acetylmannosamine-β(1–4)-N-acetylglucosamine are covalently bound to other constituents such as 6′ hydroxyl of N-acetylmuramic acid residues in the PGN[35,36]. The PGN is one important component in cell envelope of bacteria, that determines the cell wall strength and its characteristics. It has an organized or layered structure with a relatively high porosity of 2-3 nm[37]. Cationic AMPs are believed to interact with these negatively-charged components through electrostatic interactions, which plays a key role in enhancing antimicrobial activity and add a certain selectivity towards bacterial over mammalian cells[38]. However, the selectivity for non-lipidic components in the cell envelope still needs to be examined experimentally since molecular-level comparisons of AMPs interaction with both bacteria and mammalian cells are scarce[38]. It has been reported that many AMPs preferentially interact with lipidic components of cell membranes, and that cell wall components in the cell surface indeed play a critical role in capturing AMPs towards the bacterial cell membrane[32] although, in some cases, they can hinder the activity of the AMPs[39].

The lipid constituents in the bilayer matrix play a significant role in cell selectivity. The phospholipid composition of bacterial cell membranes is considerably different from the one of mammalian cells[40]. In bacteria, it largely consists of the negatively-charged lipids phosphatidylglycerol (PG) and cardiolipin (CL), and contain zwitterionic phosphatidyl-ethanolamine (PE), as will be presented in Section 1.4. In the case of Gram(+) bacterial membranes, positively-charged lysyl-phosphatidylglycerol (lysyl-PG) is also found. The relative proportion of these lipids varies considerably in both Gram(-) and Gram(+) bacteria[32]. *A contrario*, mammalian cell membrane contain zwitterionic lipids in their outer leaflet such as phosphatidylcholine (PC), PE and sphingomyelin (SM)[40], while phosphatidylserine (PS) is found in the inner leaflet. This fundamental difference in lipid composition between bacterial and mammalian cells provides a certain selectivity to AMPs interactions. However, cholesterol in the

mammalian cell membrane triggers phase separation[41] with different domains of membrane order (low and high cholesterol regions), which play a significant role in the activity of AMPs. The real selectivity of AMPs thus needs to be monitored by comparing cell concentrations[42] (number of cells, as discussed below) or lipid concentrations[43] with quantitative biophysical methods.

1.2.3 Inhibitory concentrations *vs.* Hemolytic activity

An ideal therapeutic molecule should have a strong interaction with bacterial cells and no or very weak interaction with mammalian cells at the same concentration. As described above, AMPs can interact with both bacterial and mammalian cells, therefore understanding cell selectivity is critical. It is often measured in terms of therapeutic index (TI), which is defined as the ratio of the minimum hemolytic concentration (MHC) to the minimal inhibitory concentration (MIC) of a given bacterium[42,44]:

$$TI = \frac{MHC}{MIC} \tag{1.1}$$

where MHC is a measure of the minimal concentration inducing a 10% hemoglobin leakage in mammalian cells such as red blood cells (RBCs), and MIC is the minimal concentration at which the growth of bacteria is completely suppressed. The higher the TI value, the higher efficacy or high chance of AMPs to become an efficient therapeutic candidate.

As pointed out by others groups[38,42], cell selectivity is likely dependent on the cell concentration in a medium, as well as the cell type. In general, hemolysis assays are performed with a 5% hematocrite value, which corresponds to a cell concentration of 5-10×10^8 cells/mL, while typical antimicrobial assays are performed at ≈ 3-4 order of magnitude lower cell concentrations. In addition, cell surface area is also critical when examining the activity of AMPs; a certain number of peptides per cell are required to exert an effect, thus the relative peptide and cell/membrane lipid concentrations clearly play a role when determining the therapeutic value of AMPs[38,43,45]. Finally, not all the peptides in solution bind to available membrane surfaces: the actual binding depends on the peptide partition constant and it has been noted that the latter is quite high for many AMPs[45].

In practice, translating MICs values to therapeutic value is still challenging. It has been noted that MIC values vary exponentially with cell concentrations (or inoculum sizes)[46]. For example, the MIC of the AMP pexiganan was examined at different cell concentrations[46]. For 10^1-10^3 *E. coli* cells/mL, the MIC was ~1 μM and it steadily increased up to an MIC ≈ 100 μM for 10^8

cells/mL. Likewise, the AMP magainin 2 was tested at a low RBC density of 10^5 where a 10 μM peptide concentration was enough to lyse the cells[47], while at a RBC concentration of 10^5, the MIC values ranged from 2 to 16 μM for different bacteria[48]. Clearly, the cell selectivity or TI values are likely often overestimated and have even been criticized by others as an "experimental illusion"[38,42]. It is evidently difficult to predict the activity of AMPs *in vivo*, solely based on *in vitro* assays. However, it is a good starting point and clearly required to determine a TI rigorously. Carried out in the right conditions, it can help select potential therapeutic AMPs for clinical applications.

1.2.4 Therapeutic value of AMPs

Several AMPs have been tested for their therapeutic potency, and some of them successfully reached various stages of clinical trial (Table 1.2). All these peptides show similar traits of amphipathicity and antibacterial properties. For example, LL-37 human cathelicidin is able to kill a wide range of bacterial pathogens including a multidrug resistant bacterium[49] and was tested for diabetic foot ulcer as antibacterial or antibiofilm cream. Melittin is an AMP isolated from bee venom and shows inhibitory or bactericidal effect on different bacteria similar to LL-37[50]. Although it has higher hemolytic activity[51], it has been selected for clinical trial (Table 1.2). Similar to LL-37, Pexiganan (MSI-78) and other AMPs (Table 1.2) are also used in similar antibacterial applications, i.e. mainly topical use.

With an action mechanism different from traditional antibiotics, AMPs represent interesting therapeutic substitutes. As of today, an α-helical AMP like gramicidin and peptide-based molecules such as nisin, polymyxins, and daptomycin, have been approved for clinical use[52]. Clearly, naturally occurring AMPs are still limited to topical and/or intravenous applications, and this can be explained by different factors. For example, AMPs can be lysed by proteases[53] and their stability in the biological context are common concerns. AMPs can also act on eukaryotic cells, which limits their wider application. Their overall biocompatibility is dependent on various factors and the initial characterization of antibacterial and hemolytic assays is the first starting point. For this purpose, RBCs constitute excellent natural biomembrane systems to evaluate AMPs' therapeutic potential. It should be noted, however, that for applications where the concentration of RBCs is low or no RBCs are present, as in epidermal layers of the skin, the hemolytic activity may not play any critical role (as is the case for example for melittin).

In addition to the AMPs' biocompatibility, other issues such as cost effectiveness remain to be addressed. For example, these peptides are produced by solid phase synthesis at high costs. Production costs could be reduced by using other alternative biosynthetic approaches[54]. Finally, strategies, such as chemical engineering and the design of delivery systems, could improve the clinical potential of AMPs.

Table 1.2: Different antimicrobial peptides tested in clinical trials[52,55].

Name	Origin	Disease/target	Phase	Dosage	References
LL-37	Human cathelicidin	Diabetic foot ulcer (Antibacterial, Antibiofilm)	ii	0.5 mg/mL (topical)	NCT04098562
Melittin	Bee venom	Inflammation	i/ii	-	NCT02364349 NCT01526031
Pexiganan (MSI-78)	Magainin analogue (Frog skin peptide)	Diabetic foot ulcer (Antibacterial)	iii	0.8-2 % w/w (topical)	NCT00563394 NCT01590758
Omiganan (MBI-226)	Indolicidin analogue (Bovine leukocytes)	Catheter site infections (Antibacterial)	iii	1% gel (topical)	NCT00231153
Murepavadin (POL7080)	Protegrin analogue (Porcine leukocytes)	*Pseudomonas Aeruginosa* infection	ii	Intravenous	NCT02096328
PAC113	Histatin analogue (Human saliva)	Oral candidiasis (Antibacterial)	ii	0.15 % Mouth rinse	NCT00659971
hLF1-11	Lactoferrin protein derivative (Human)	Bacterial infections	i/ii	5 mg (Intravenous)	NCT00509938

1.3 Aurein 1.2 and caerin 1.1

1.3.1 Origin, structure and bioactivity

Amphibian skin secretions contain many complex antimicrobial molecules including AMPs. An integral part of the innate immune system, they are the first line of defense to combat various bacterial infections. A large number of AMPs have been isolated from different amphibians species[56] and the majority of these peptides exhibit similar traits. Aurein 1.2 and caerin 1.1 (Fig. 1.4) are ones of many such peptides, which show a wide range of antibacterial properties[56,57] and are both isolated from skin secretions of the *Litoria* genus of Australian tree frogs[56]. The sequences of aurein 1.2 with 13 residues and caerin 1.1 with 25 residues are both amphipathic with hydrophilic and hydrophobic residues. Both peptides are cationic and adopt an α-helix configuration in membrane environments where one face of the amphipathic pattern spontaneously interacts with the bilayer matrix[58]. This interaction induces membrane damage in the targeted pathogens. Amination of the C-terminal is believed to have an essential functional role in their

antibacterial action[59]. Aurein adopts a continuous α-helical structure upon membrane binding, while caerin forms a flexible hinge region, which affects its activity and induces differences in the action mechanism of this peptide as compared to aurein[58,59].

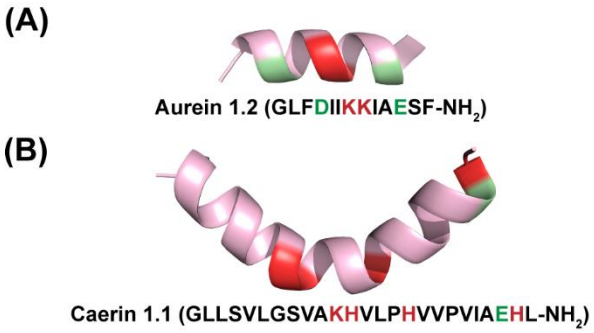

Figure 1.4: Tertiary structures of (A) aurein 1.2 (*pdb-1VM5*) and (B) caerin 1.1. Charged residues are indicated in red and green. (Wegener et al. [60], with permission).

Both aurein and caerin show an excellent antibacterial activity towards several Gram(+) and Gram(-) bacteria (Table 1.3), but have a higher activity towards Gram(+) strains, as revealed by lower MIC values. In all cases, the MIC value of caerin is lower compared to the one of aurein, which suggests higher antimicrobial activity of caerin. As will be detailed in the next section, Gram(+) bacteria, the *Lactococcus* and *Staphylococcus* genus of bacteria contain high proportions of anionic lipids, therefore aurein and caerin could be potential therapeutic candidates for targeting such bacteria. Numerous studies performed on model bacterial lipid membranes suggest that the membrane interaction of aurein is through a micellization process or carpet like mechanism, and that caerin interacts through a pore formation mechanism[58,61], although the occurrence of other nonmembrane-lytic interactions cannot be excluded[22], particularly in whole cells.

Table 1.3: Minimum inhibitory concentration (MIC in μM) of aurein 1.2 and caerin 1.1 towards Gram(+) *Bacillus subtilis*, *Lactococcus lactis*, *Staphyloccocus epidermidis* and *Staphylococcus aureus*, and Gram(-) *Escherichia coli* and *Pasteurella multocida*[56,57].

AMPs	*B. subtilis*	*E. coli*	*L. lactis*	*P. multocida*	*S. epidermidis*	*S. aureus*
Aurein 1.2	20	68	8	68	34	34
Caerin 1.1	12	39	0.6	10	5	1.2

1.4 Lipids, model membranes and erythrocyte ghosts

1.4.1 Lipids in biological membranes

The molecular interactions and biochemical activity of all living cells depend on functional compartmentalization, notably the plasma membrane[62]. It is described as "*spontaneously form*[ed of] *a simple, two-dimensional liquid controlling what enters and leaves the cell*"[62], which gives the very idea of a cell. The primary building blocks of the membranes are lipids, which have an amphiphilic character as they are composed of a hydrophilic head group and hydrophobic acyl chains. When in sufficient concentration in water, lipids spontaneously form a bilayer, creating an important interface between the intracellular and extracellular spaces. The conformation, organization and structural feature of a lipids play an important role in defining the properties of cell membranes, distinctly different from one organism to another and thus play a critical role in cell function[63].

The most common type of lipids found in eukaryotic and prokaryotic cell membranes are glycerophospholipids. The are composed of an interface region made by a glycerol backbone, to which two fatty acid chains are linked through ester bonds (in some cases ether bond[40]). The headgroup linked to the glycerol backbone is composed of a phosphate group bound to either choline, ethanolamine, serine, glycerol, or inositol (Fig. 1.5). In eukaryotic membranes such as erythrocytes, PC, sphingomyelin (SM) or dihydrosphingomyelin (DHSM) are found in the outer monolayer, while the inner layer contains PE, phosphatidylinositol (PI), and PS[40,62]. In addition to these phospholipids, eukaryotic cell membranes also contain glycolipids and cholesterol. Glycolipids are similar to phospholipids, but the phosphate group is replaced by carbohydrate molecules[64]. They are located mainly in the outer leaflet of eukaryotic cell membranes and make up only a small fraction of total lipids[62], except in plants where they are the main lipids. Cholesterol is an important constituent of mammalian cell membranes (approximately 30-40%)[65] and influences the membrane fluidity and viscoelastic properties of the membrane[66]. Cholesterol is absent in most prokaryotic cells such as bacteria.

The fatty acid chain profile varies significantly in mammalian cell membranes[64]. The most common acyl chains in erythrocyte membranes are the saturated palmitoyl with 16 carbons (C16:0), saturated and unsaturated oleoyl with 18 carbons (18:0, 18:1 and 18:2)[40], the relative proportions of which vary in different organisms[67].

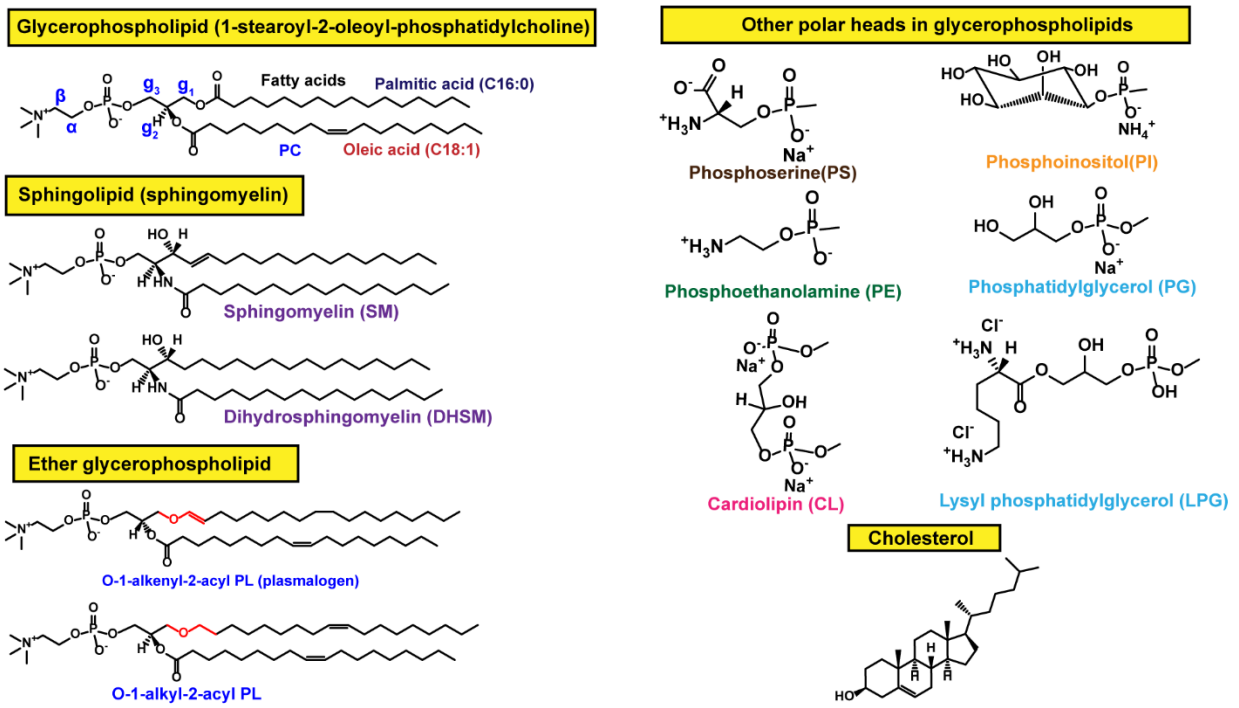

Figure 1.5: Structures of the major lipids found in biological membranes, with detail of the phospholipid headgroups (In case of CL, two glycerol backbone attached to two phosphate group).

The phospholipid composition of bacterial cell membranes plays a key role in the activity of AMPs. Gram(-) bacterial membranes typically contain 70-80 % zwitterionic PE and 20-30 % anionic lipids such as PG and CL, while Gram(+) bacterial membranes have a higher percentage of anionic lipids (Table 1.4). CL structurally resemble PG with four acyl chain attached to two glycerol backbone. Also, a fraction of PG is modified into Lysyl-PG, where a Lysine amino acid is linked to the lipid glycerol headgroup. Rehal et al.[68] measured an electrical potential of -55 to -68 mV in the vesicles formed with *S. aureus* lipid extracts, which contain PG and CL. The authors also noted that bacteria grown at a pH=5.5 (instead of a normal pH of 7.4) produced up to 55 % more lysyl-PG and that vesicles prepared from such lipid extract showed a positive electrical potential (+15 to +21 mV). The interaction of the AMP magainin 2 on both these lipid extracts showed that the peptide penetrated deeper into the lipid matrix with higher amounts of PG in the bilayer (bacteria cultured at pH 7.4) compared to the pH 5.5 extract. At the lower pH, the same peptide interacted only with the interfacial region of the membrane, inducing lesser impact. The anionic lipids PG and CL thus play a critical role in peptide-membrane electrostatic interactions. The diversity of fatty acids chain depending on the type of bacteria and its growth conditions[69].

Table 1.4: Major lipid classes in Gram(-) and Gram(+) bacteria.

Bacterium	Lipid composition					Major fatty acid chains	References
	PE	PG	lysyl -PG	CL	others		
Gram(-)							
E. coli	73	26	-	1-2	-	C16:0 (45 %), cyC17:0* (24 %), cyC19:0 (20 %), others (11 %)	Laydevant et al.[69]
P. multocida	80	18	-	-	2	C14:0 (16 %), C16:0 (39 %), C16:1 (40 %), others (5 %)	Hart et al.[70] and Fuller et al.[71]
Gram(+)							
B. subtilis	25	49	11	12	3	*i/a** C15:0 (40 %), *i/a* C17:0 (53 %), others (7 %)	Appendix A
L. lactis	-	65	23	-	12	C16:0 (24 %), C16:1 (9 %), C18:1 (43 %), cyC19:0 (15 %), others (9 %)	Exterkate et al.[72] and Veerkamp et al.[73]
S. aureus	-	60	30	5	5	*i/a** C15:0 (35 %), *i/a* C17:0 (10 %), C18:0 (20 %), C20:0 (22 %) others (13 %)	Rehal et al.[68] and Durham & Kloos [74]

*i/a** = *iso/anteiso* forms in acyl chains ; cy = one cyclopropane configuration is present in acyl chain.

1.4.2 Physico-chemical behavior of lipids in membranes

Phospholipids in an aqueous environment can form various structures or phases, including monolayers or bilayer lamellar phases, as well as nonlamellar phases such as micelles, hexagonal or cubic phases (Fig. 1.6). The formation of these phases depends on different physicochemical characteristics of lipids such as chemical nature, composition, and its phase transition temperature as will be detailed below. In the last decades, the physical chemistry of lipid phases has been extensively studied using various techniques including, calorimetry, crystallography, spectroscopy and microscopy[75,76]. The bilayer structure is the most basic framework of all living cell membranes

and various morphological requirements as well as the physiological function of cells are determined by the individual lipid species.

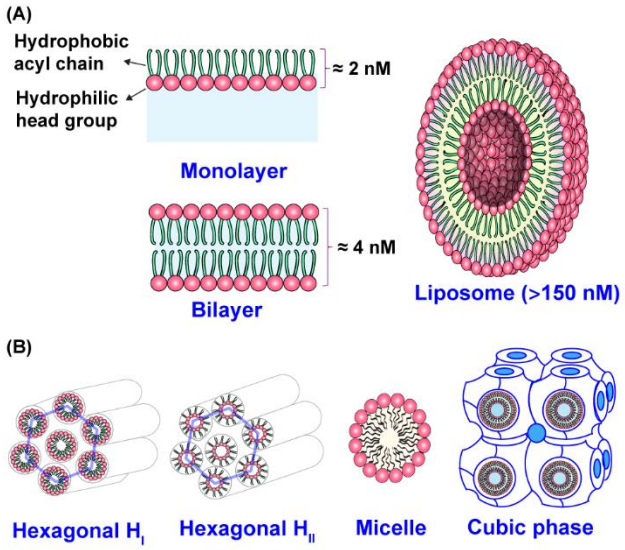

Figure 1.6: Schematic representation of molecular self-association of lipids in water. (A) Lamellar phases and (B) non-lamellar phases.

The cell membrane in its entirety shows a high degree of dynamical behavior with a diverse lipid profile and other membrane components such as proteins, and carbohydrates. The nature of these individual lipid molecules present in the membrane matrix primarily contribute to balancing the dynamics and stability of the cell membrane[77]. At the cross section of the lipid bilayer, the interface region, which divides the hydrophilic and hydrophobic moieties of the lipids, is the most important part of the monolayer responsible for structural stability of the membrane. Small changes in this specific area lead to exposure of the hydrophobic tails, which is energetically unfavorable[77]. Thus, changes in such area affect the membrane morphology, and this behavior is generally expressed by the concept of *lateral pressure*[78] (Fig. 1.7A). The balance of these attractive and repulsive forces shapes the organization of lipids and its polymorphism[79]. As noted by Brown[79], the lateral pressure profile is an invisible quantity (not an experimentally accessible) and only theoretical models such as molecular dynamics (MD) simulations allow us to relate the lateral pressure to the stability of membrane components[80]. In this context Shahane *et al.*[81] used MD simulations to determine the lateral pressure profile of model membranes representative of bacterial and mammalian cell membranes. These authors showed that membranes made of palmitoyloleoyl PE (POPE) and POPG in a 2:1 molar ratio are mostly shaped by the POPE contribution in the centre of bilayer, while POPG's contribution is predominant in the water and

headgroup region. Likewise, the authors show that cholesterol is the predominant contributor to lateral pressure in model mammalian bilayers composed of POPC:Chol:SM. This fundamental difference of individual lipid species governs the various interactions in membrane environments.

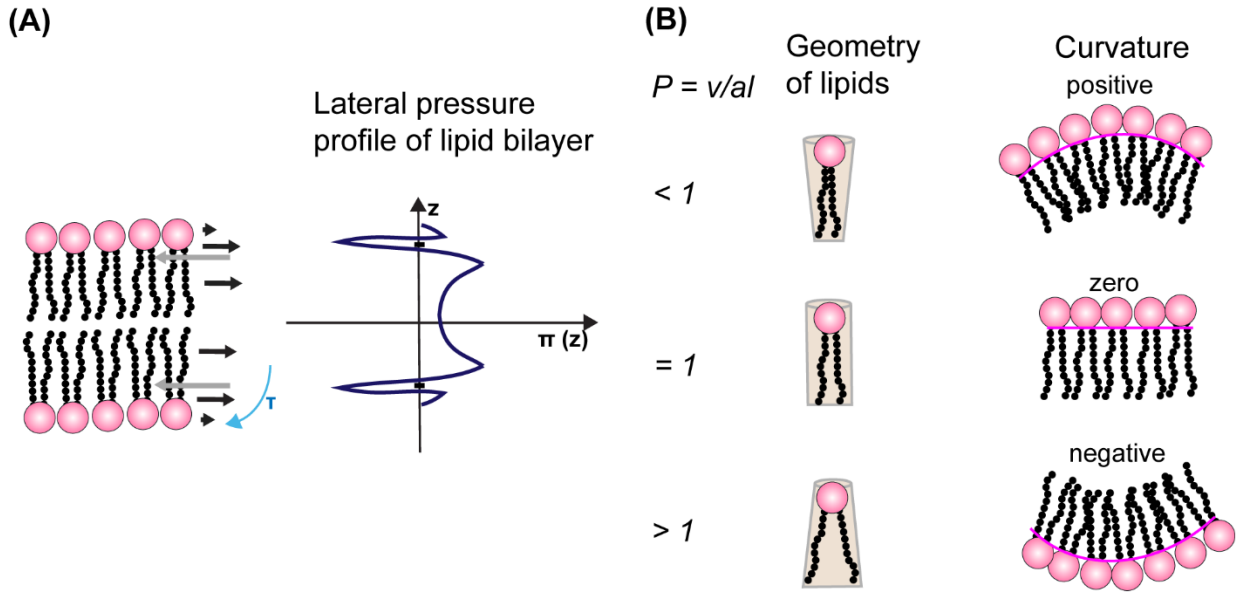

Figure 1.7: (A) Representation of the lateral pressure profile across the lipid bilayer and, **(B)** the different molecular geometry of lipids and their packing parameter P with respective curvature models, *v* refers to molecular volume, *a* is the cross-sectional area of the head group, and *l* is the length of the molecule. (Adapted from Frolov et al.[77] and Brown[79], with permission).

Lateral forces balance at equilibrium and the pressure integral becomes zero[77], although the resulting torque might remain unbalanced in lipid monolayers. As a result, elastic stress is in-built for bilayer, and this induces a propensity to form curved structures as represented in Fig. 1.7B. This behavior depends on the geometry or shape of the individual lipids and is generally described by the packing parameter (P), first conceptualized by Israelachvili–Mitchell–Ninham[82] and defined as:

$$P = \frac{v}{al} \qquad (1.2)$$

where *v* is the molecular volume, *a* is the cross-sectional area of the head group, and *l* is the length of the molecule. As noted by Bagatolli & Mouritsen[78], *v, a* and *l* are average molecular properties of lipids and cannot be assigned one value as such since lipids are in a dynamic state. The average P value is, however, still useful in predicting the structure of the lipid assembly. For example, a P value different from unity experiences a built-in curvature stress and results in a propensity to form curved structures or, in some instances, non-lamellar structures. The transition of bilayer (or

lamellar phase) to non-lamellar phase depends on stored stress and can be accelerated by not only thermodynamic parameters, such as pressure or temperature[83], but also peptides (for example AMPs) or proteins, which interact with the lipid matrix[84].

As discussed in previous sections, the interaction mechanism of AMPs with the lipid bilayer varies with the peptide structure and lipid compositions. The relationship of curvature stress and action mechanism of AMPs has been discussed by Haney et al.[85]. They proposed that a toroidal pore induced by AMPs can be thought of as hexagonal phases (H_I or H_{II}) with a positive membrane curvature. The micellization of lipid bilayers by AMPs can also be viewed as a positive curvature stress. Both these models are not entirely different from one another, and the micellization process (or carpet-like model) can be understood as an extreme stage of the pore model. Negative membrane curvatures can also occur in some peptide-membrane interactions at intermediate stages[85]. In general, membrane-interacting AMPs accelerate the formation of curvature stress or induce a deformation in lipid bilayers.

The phospholipids in bilayer environments are also controlled by thermodynamic variables, and undergo a phase transition at a temperature that is phospholipid-specific[86]. This transition between a gel or ordered phase (L_β) to a fluid disordered phase (L_α) with increasing the temperature, can be experimentally quantified using various techniques including nuclear magnetic resonance (NMR) experiments. This is done by monitoring a parameter (such as a peak intensity, area or spectral moment) as a function of temperature (Fig. 1.8). The inflection point in the resulting continuous transition curve allows determining the main gel-to fluid phase transition temperature (T_m). However, in this continuous transition process, two or three lipid phases can co-exist and induce a broadening of the phase transition. The phase transition in pure lipids is usually steep, while the association of lipids with additional components such as cholesterol leads to a more complex phase diagram[87]. Many other factors also influence the T_m, including phospholipid acyl chain length, the presence of unsaturations and nature of the lipid headgroups. In the context of peptide-membrane interactions, previous studies have demonstrated that AMPs can affect the T_m in lipid bilayer, by inducing lipid ordering or disordering[88]. As mentioned above, T_m of lipids can be obtained using NMR, for example if the lipids are enriched with deuterium, one can access the acyl chain order using ^2H SS-NMR. Deuterated lipids have identical molecular properties as non-deuterated lipids, except for small perturbations where specific hydrogen bonding is involved[89]. The quadrupolar coupling constants of CD_2 or CD_3 group of acyl chains or spectral

properties such as second moment M_2 (Fig. 1.8) can be obtained, and provide the order parameter S_{CD}, which is sensitive to temperature. This measurement provides information on characteristics of the gel phase with higher S_{CD} or M_2 values or the fluid phase with lower S_{CD} or M_2 values, and its variation with temperature allows T_m to be determined. Theoretical part of deuterium NMR will be more detailed in chapter 2.

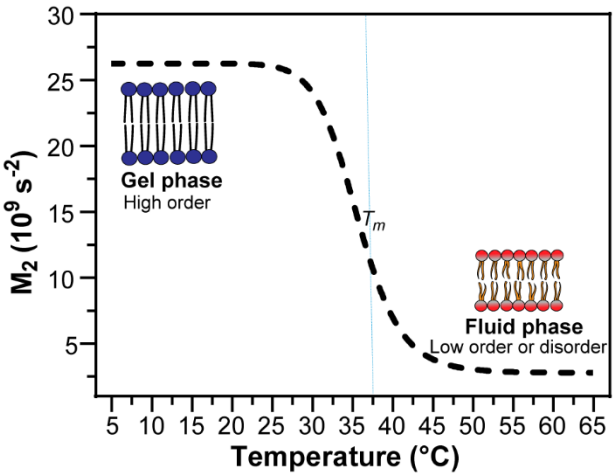

Figure 1.8: Representative deuterium second moment *vs.* temperature plot.

Lipids in biological membranes, including in eukaryotic cells, exhibit complex phase behaviors with heterogeneous lipid compositions and domains, often named "rafts" with liquid-ordered (L_o) and liquid-disordered (L_d) phases. Phospholipids and cholesterol mixtures are exemplary models for mimicking such membrane systems, and their phase diagrams have been extensively characterized in the past[90,91]. The dynamics of membrane components are described by the notions of mobility, *"which includes translational and rotational motions of proteins and the translational diffusion of lipids in the plane of the membrane",* and fluidity *"the segmental motions of lipid acyl chains and the reorientational motions of lipid polar head groups*"[92]. Both mobility and fluidity are intertwined. In the case of pure homogeneous systems, the disordered state of lipid bilayers can be considered as fluid, while, in an heterogeneous system with both ordered and disordered state, cholesterol acts as a "*fluidity buffer*"[93] since it has been shown to promote a state of intermediate fluidity by rigidifying fluid lipids and making rigid lipids more fluid[93]. Even without cholesterol, small patches of ordered domains (or microdomains) of lipids are present in prokaryotic membrane systems with specific polar headgroup and the support of

membrane proteins[94]. The concepts of mobility, fluidity and heterogeneity are all included in the foundational idea of the 'fluid' and 'mosaic' state of biomembranes[95].

Certainly, *"fluidity is the way to life"*[96] and both eukaryotic and prokaryotic cells evolved towards maintaining membrane fluidity. From a thermodynamic point of view, biomembranes, with their complex structures, should be described as *quasi-equilibrium* structures[97], meaning systems with some distance from equilibrium[98]. Cells taken in their entirety are open dissipative structures (far-from-equilibrium), which maintain their local level of order or organization at the cost of creating entropy (disorderliness) in the environment[97,98]. Non-equilibrium treatments of such complex systems are interesting and particularly relevant for biomembranes with heterogeneities (rafts or domains)[99,100]. More specifically, in the case of AMP-membrane interactions, it is predicted that AMPs line up at boundaries between ordered and disordered domains - a scenario that is energetically favorable[101] which could result in pore formation.

In addition to fluidity, composition heterogeneity of biomembranes results in morphological and functional asymmetries[102], and these phenomena happen over various timescales (Fig. 1.9). This asymmetry and dynamics of membrane constituents are key factors that rule the organization and stability of biomembranes. The dynamical behavior varies for the different individual molecular constituents. For example, the rotation of lipid molecules along their axes perpendicular to the plane of the membrane within the monolayer occurs at frequencies of 10^7-10^8 s^{-1}, while transmembrane proteins exhibit rotational frequencies of 10^4-10^6 s^{-1}. Similarly, transbilayer movements of individual lipids occur at frequencies of 10^3-10^{-4} s^{-1}, while this movement is nonexistent for proteins. As mentioned above, deuterium NMR is useful for probeing phase behavior and it is sensitive to molecular motions. In the fluid state of membranes, distinct dynamics of CD_2 or CD_3 segments can be obtained through deuterium order parameter measurement. Indeed, there is a different hierarchy of motions present in biological membranes as summarised in figure 1.9B, particularly for lipids. Molugu et al.[103] characterise them into three main broad categories : i) segmental motions of acyl chains, ii) slower rotations of the highly entangled lipids (molecular diffusion), and iii) collective deformations spanning a broad range of timescales which influence the entire assembly. Here in this thesis, the orientation and dynamical dependency of lipid membrane is studied using various SS-NMR experiments involving dipolar, quadrupolar and chemical shift anisotropy (CSA) measurement. In addition, dynamical behavior of lipids was

probed by relaxation measurement using ^{19}F probe, after ^{19}F labeling different location of the membrane, as will be detailed in chapter 2-4.

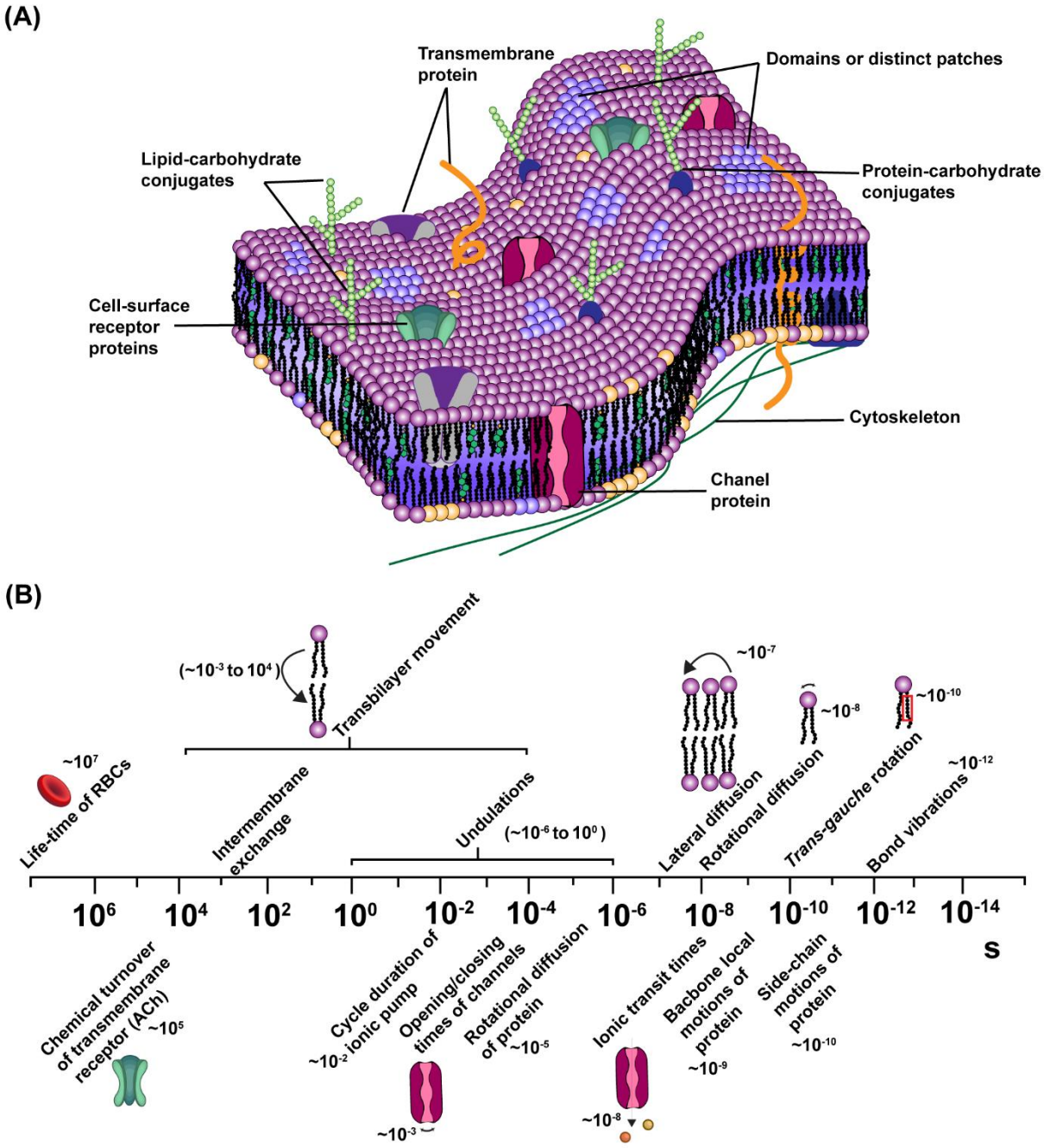

Figure 1.9: (A) Typical structural framework and lateral heterogeneity of eukaryotic cell membranes. **(B)** Time characteristics of different events in cell membranes (Values are obtained from Jain[102], Luckey[104] and Margineanu[97]).

All motional characteristics of lipids, proteins and their carbohydrate conjugates primarily arise from size or structural differences. However, molecules of the same type do not necessarily

exhibit the same motional characteristics. Altogether, both low frequency and high frequency motions of lipids are particularly sensitive to local perturbations of the membrane. Such time-dependent events can be altered by the interaction of molecules, such as AMPs, with the membrane. In summary, all membrane constituents, particularly lipids and their physical and chemical properties, significantly influence the interactions of AMPs with biomembranes or whole cell systems.

1.4.3 Model membranes

Over the past decades, significant efforts have been put to study synthetic lipid bilayers, often referred to as *model membranes* or *membrane mimetics*[105]. In general, the physicochemical characteristics of model membranes attempt to closely represent the state of natural biomembranes, although they lack their complexity, they are elegantly simple.

Model membranes are more similar to liquid crystals in comparison to solid or liquid states[106] and SS-NMR is indeed useful for characterising such sample at the atomic level. Generally, Multilamellar Vesicles (MLVs) are widely used in SS-NMR studies with one or more types of pure lipids. Preparation of MLVs is rather simple, just by freezing and thawing (above T_m) lipids and creating homogeneous onion-like layered structures. Other forms of vesicles such as Large Unilamellar Vesicles (LUVs) and Giant Unilamellar Vesicles (GUVs) are also used in other techniques, for example, fluorescence-based assays or microscopy experiments[107]. The simplification of natural membrane as model MLVs is necessary for SS-NMR experiments, before diving into whole cell system.

As mentioned in the earlier sections, plasma membrane lipid profile varies from one organism to another. Prokaryotic systems such as bacterial plasma membrane, generally, contain high amount of lipids with either PG or PE as head group. Eukaryotic plasma membranes such as RBC ghosts contain high amount of PC and cholesterol. Fatty acid profiles in both bacteria and RBCs also vary depending on the organism[32,40] and can be found as saturated, unsaturated, or branched, favouring fluid state membranes with highly dynamic features. Therefore, membrane mimetics are generally prepared to replicate both natural membrane head group and fatty acid profiles at best, depending on experimental requirements. For example, bacterial model membranes are usually prepared using negatively charged PG, which is mixed with zwitterionic PE at different ratios depending on the required model (Gram(+) or Gram(-) bacteria). Sometimes PE is replaced by

zwitterionic PC, as its perdeuterated analogous is available commercially and affordable in comparison to deuterated PE or PG[32], particularly, in the context of SS-NMR studies of AMPs and membrane interaction[32,108,109]. For example, aurein 1.2 and caerin 1.1 AMPs interaction studies employed PC/PG combinations[58,61,110]. In general, lipids with a fatty acid combination of palmitic acids and oleic acids (POPC, POPG or POPE etc.,) are preferred as they closely represent natural membrane lipids[40,111,112]. However, various version of PC such as DMPC, DOPC or DPPC, are also used as a models for SS-NMR experiments[58,61,113]. Also, model eukaryotic membranes are often made of one component, either DMPC or POPC lipids[58,61,112] and only few studies have used more realistic models which include cholesterol and/or sphingolipids (SM)[40,109,113], as will be discussed in this thesis. Although, the behaviour of cholesterol in the presence of lipids has been well characterised in the past, particularly by SS-NMR[66,114-116], interaction of AMPs with a combination of complex mixtures of lipids for example, PC/SM/cholesterol brings new challenges, as more than one phase in such sample is expected from its phase diagram, as will be detailed below.

Indeed, gel-to-fluid phase transition in pure lipids can be assigned to a single value (T_m), but its association with additional components such as other lipids or cholesterol makes the phase transition curve broader depending on the concentration of both the components. As seen in Fig. 1.10, an idealised phase diagram of a binary mixture of phospholipids in aqueous dispersions has primarily three regions: i) below the lower curve with an ideally mixed gel state, ii) above the convex curve with an ideally mixed fluid state, and iii) for a given mole fraction (between a and b) both gel and fluid phases coexist in equilibrium[102]. In such a scenario with mixed bilayers, the phase transition depends not only on temperature but also on relative mole ratios of phospholipids (Lever rule). In general, the Gibbs phase rule can be applied to determine the number of experimental variables (also called degrees of freedom *F* or variance) with *C* chemical components and *P* phases existing in equilibrium. At constant pressure, Gibbs phase rule reduces to:

$$F=C-P+1 \qquad (1.3)$$

Where, "1" indicate the varying temperature and for binary mixture of lipids with $C=2$ in the presence of excess water, which is not counted as a component, the phase rule then reduces to $F=3-P$, i.e., a maximum of three phases can coexist at the eutectic point for a given temperature and composition. An ideal mixing of lipids depends on the chemical nature of lipids, for example, DMPC/DPPC binary mixture shows an ideal mixing behavior[117,118]. However, due to their

difference in T_m (DPPC at 41 °C and DMPC at 24 °C), a gel and fluid coexisting region is expected. Complication of this type of phase diagrams increases with the mismatch in acyl chain lengths, and with differences in their structures.

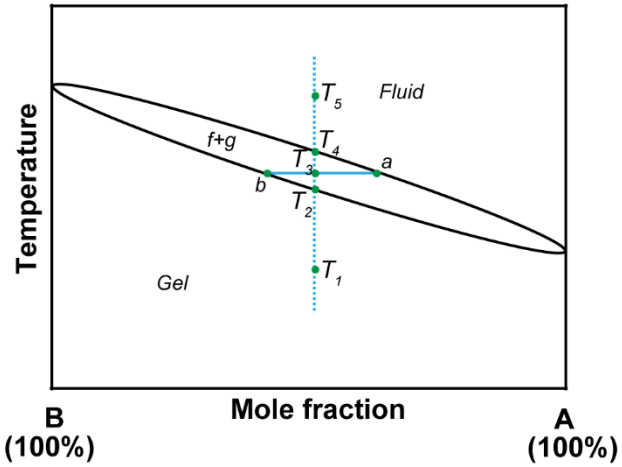

Figure 1.10: Typical phase diagram of ideally mixed phospholipids in aqueous dispersions.

As mentioned above, model membranes with cholesterol can also show a complex phase behavior, and such a phase diagram of ternary mixtures of PC/SM/cholesterol are well described in the literature[119,120]. As seen in Fig. 1.11, a coexisting phase is found, similar to the binary mixture of lipids, and at certain biologically relevant compositions and temperatures, phospholipids and cholesterol phase separate into liquid ordered (L_o) and liquid disordered (L_d) phases, as indicated by two liquids region in Fig 1.11. Also, several studies indicated that the presence of cholesterol in the bilayer alter the lateral organisation of phospholipids[121,122] and promote lateral segregation with coexisting L_o and L_d phases also referred as *''lipid rafts''*[119] where cholesterol would have higher affinity towards SM over PC. This is relevant in the context of AMPs and membrane interactions, since boundaries of L_o domains are where AMPs binding and formation of local curvature is predicted[123,124]. Overall, a more realistic model membrane in experimental studies is necessary to obtain insight into different behavior of intact cell membranes.

Following the Gibbs phase rule, a very complex phase behavior is expected in lipid mixtures as found in biological membrane, and not many techniques are available for the characterisation of such system. SS-NMR provides a certain opportunity in this direction, for example using ^{2}H, ^{31}P or ^{19}F SS-NMR, even in intact cell membrane, as will be discussed in this thesis. Experiments on intact cell membranes are therefore an important goal, and they are necessary, since model membranes lack many different constituents found in native membranes, for example extracellular

matrix and proteins. Moreover, lipid profiles of native biological membranes is complex and *"it is an article of faith amongst membranologists that this complexity serves a purpose"*[86].

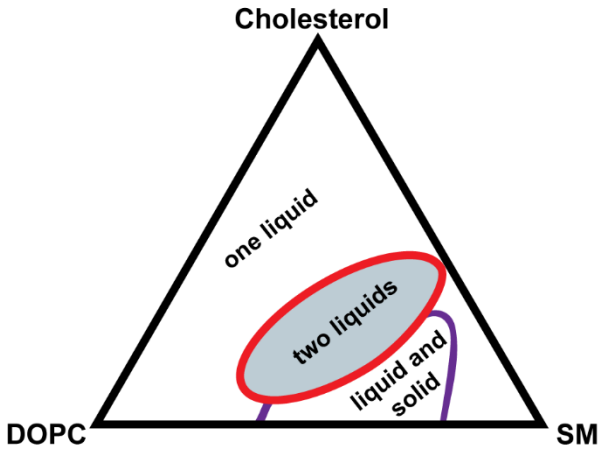

Figure 1.11: Typical phase diagram of ternary mixtures of DOPC/SM/cholesterol (Adapted from Semrau et al[119], with permission).

1.4.4 Erythrocyte ghosts

Erythrocytes or red blood cells (RBCs) are the most abundant cells in our body where they play an important role in oxygen delivery[125]. Their flexible, biconcave shape enables them to squeeze through narrow capillaries of the veins. Their average life span in the circulation is approximately 120 days. Due to their relative biological simplicity, i.e. an absence of nucleus and other intracellular organelles, RBCs they are excellent model biological cells systems, considering that they contain proteins, lipids, and their glycoconjugate in plasma membrane, also contains an intricate network of extracellular matrix and intracellular cytoskeleton, which provide strength and structural stability for membrane bilayers. Because of their biocompatibility, biodegradability and relative stability, erythrocytes are particularly studied in drug delivery applications as carrier of drugs into other cells[126]. RBCs are also a reference when it comes to test the toxicity of therapeutic molecules towards mammalian cells through quantification of the hemoglobin leakage that they caused. This allows evaluating the membrane damage caused by molecules, such as AMPs and, as mentioned in section 1.2.5, a therapeutic index can be obtained by measuring the minimum lytic concentration. In the context of peptide-membrane interactions, whole erythrocytes can provide a measurement of the concentration of peptide required to lyse the cells and its dependency on total cell concentration[42].

Erythrocyte ghosts are hemoglobin-free post-hemolytic residues of erythrocytes[127] and primarily contain the plasma membrane with a composition almost identical to the original intact cells. There are many ways to prepare ghosts depending on the application. A common method of preparation involves osmotic lysis using a hypotonic solution for hemoglobin removal, followed by resealing in physiological conditions. These methods have been extensively investigated in the past, notably by Hoffman, Steck, Dodge and several others[127-130]. Also, one main advantage of removing hemoglobin from the erythrocytes is to remove the paramagnetic effect from iron which cause perturbation on SS-NMR signals. But this is just a first principle argument, paramagnetic perturbation of erythrocytes in SS-NMR is yet to be validated and perhaps performing SS-NMR experiments in the context of peptide-whole cells interactions is even possible with intact erythrocytes by specific isotope labeling such as ^{2}H or ^{19}F, similar to ghosts as will be detailed in this thesis. Also, other reason to use ghosts is to remove ^{31}P background signal from metabolites trapped in RBCs such as adenosine triphosphate (ATP). More generally, erythrocyte ghosts (or erythrocytes) are whole cell models for biophysical studies to understand mechanistic and dynamical behavior of membrane interactions, particularly, with membrane active AMPs and one might also consider other eukaryotic cells with additional components such as the nucleus, for studying nonmembrane-lytic AMPs.

1.4.5 Labeling of ghost membranes for biophysical studies

In cell biology, it is important to understand how cellular processes occur in native conditions. However, a challenge of whole cells is the absence or low availability of traceable natural probes. With the advancement of fluorescence imaging techniques, microscopic methods have been primary tools for cell biologists to determine and understand the organization and physical state of a cell or membrane - specific information accessible through appropriate fluorescence labeling. However, fluorescence microscopy methods have their limits and understanding certain molecular and/or dynamic details of cells or cellular constituents remains difficult. For example, studies have reported the possible perturbing effect of fluorescence probes[131]. Moreover, light microscopy do not provide information at the atomic level. Therefore, it is limited in terms of the information it can provides on molecular interactions[132].

In this regard, over the last 10 to 15 year, in-cell solid-state NMR (SS-NMR) has proved a valuable technique to study molecular details of intact cells[133,134]. In-cell NMR includes the study

of whole cells that can be lyophilized or inactive (intact) cells, as well as living (*in vivo*). In this thesis, some challenges of in-cell NMR are discussed. As summarized by Sani & Separovic[135], 4 points need to be considered: (i) natural membranes are extremely heterogeneous, which precludes the control of specific interactions with lipid species or domains, (ii) the limited lifetime of cells undergoing MAS conditions prevents long multidimensional experiments, (iii) background signal is often significant and must be filtered; and (iv) a multitude of conformational states may exist, giving rise to broad signals.

Indeed, since biological membranes are extremely heterogeneous, it is merely impossible to control specific interactions will all lipid species. However, it is possible to monitor certain lipid groups or formation of other polymorphs, for example, micelles or curvature regions. As shown by Sebastiao et al[136], two distinct ^{31}P peaks separated by ≈0.66 ppm were observed for erythrocyte ghosts under MAS SS-NMR and 1D static ^{31}P SS-NMR spectra report the specific changes in overall morphology of cell membranes as will be detailed in the thesis. Also, as discussed in Yan et al[137], in model membranes consisting of more than one lipid, it also possible to monitor specific interactions with specific lipid head groups using 2D PROCSA, which has yet to be employed for in-cell NMR experiments[83]. In addition, integrity of cells under MAS can be preserved by performing fast data acquisition, using specific isotopic labeling such as ^{2}H or ^{19}F, while reducing the background signal at the same time. Among various cell types, erythrocyte ghosts are robust for MAS experiments. Different conformational states can be identified by using dynamic filters in SS-NMR experiments, as detailed by Poulhazan et al[138], for microalgae cells with specific isotopic labeling of cell compartments.

In case of prokaryotic cells like bacteria, membranes can be labeled by exploiting their natural lipid biosynthesis pathway[51, 59]. Bacteria are grown in a medium containing exogenous FAs which are used in the membrane lipids synthesis. Previous reports have demonstrated the usefulness of such strategy to study the interaction of AMPs and intact bacteria[57,69,139,140]. However, the occurrence of passive labeling (direct incorporation as FAs) can not be excluded from such protocols (briefly described in Chapter 6). Overall, either by active lipid biosynthesis or passive labeling, interactions of AMPs with a bacterial membrane can be monitored as a function of peptide concentration, to help understanding mechanistic behoviors of AMPs.

For erythrocyte membrane, there are some earlier NMR reports on erythrocyte ghosts that have employed phosphorus-31 (^{31}P) - a natural probe present in the phospholipids headgroup - to

study the membrane phase behavior[141,142]. Later, isotope labeling of ghost membranes followed. More specifically, deuterium (^{2}H) probes on either fatty acids or lipid acyl chains were used to improve the signal-to-noise (S/N) ratio of the SS-NMR spectra, and to study phase behavior and dynamic aspects of the membrane[143,144]. ^{2}H probes provide information on the acyl chain order, phase, and dynamics. Replacing hydrogen atoms with deuterium in acyl chains of lipids does not affect the lipid organization in the membrane, although the T_m can be slightly reduced. For example, the T_m of DMPC-d54 is 2 °C lower than DMPC[89].

Labeling using either fatty acids or lipids have both their own merits and demerits, but in both cases, their incorporation in an intact cell is challenging. In previous reports, lipid labeling[144] was achieved with the help of PC-transfer protein, and it has been noted that the fluid phase of erythrocyte membranes was stable even at -5 °C. On the other hand, fatty acids[143] were incorporated with lyophilization and exhibited similar traits of membrane phase behavior. However, the efficiency of labeling was poor and fast data acquisition was difficult. In this thesis, intact erythrocyte ghosts were labeled through the incorporation of fatty acids using micelles, as will be presented in Chapter 3. It is worth noting that incorporation of fatty acids is less difficult than labeling using lipids.

1.5 Motivation and thesis objectives

Despite the fact and relevance that AMPs interact preferentially with bacterial membranes, it is equally important to understand their action mechanism on mammalian cell membranes such as erythrocytes. To reach the market, AMPs should not target mammalian cells, therefore if we know the molecular details of AMPs interactions, this will contribute to design safer therapeutic drug candidates, since AMPs are considered a promising therapeutic avenue. Also, in-cell SS-NMR is an emerging field and techniques developed during this project can also open up the possibility of screening potential antibiotics to assess their interaction with erythrocyte membranes.

In this context, the objective of this thesis is to study the interaction mechanism of AMPs with whole erythrocyte ghosts by SS-NMR. The specific objectives were to establish specific isotopic labeling of the erythrocyte ghost membrane using fatty acids, and to develop a SS-NMR methodology to examine the interaction of AMPs with the membrane. **Chapter 3** focuses on **optimizing the ^{2}H labeling of ghosts** by the incorporation of exogenous deuterated PA (palmitic acid) into the **ghost membrane** environment and the characterization of ghost membrane lipids.

Also, to compare ordering effects of PAs in ghosts membrane bilayers *vs.* different model membranes. Then, to study the interactions of two AMPs aurein 1.2 and caerin 1.1 with erythrocyte or erythrocyte ghost membranes using microscopy, leakage assays and ^{31}P, ^{2}H SS-NMR experiments. For leakage assays, different model membrane were also used for comparison.

Chapter 4 focused on the fluorine-19 (**^{19}F) labeling of ghosts.** In this case, ^{19}F labeled PA was used, with ^{19}F atoms strategically placed at **carbon positions 4, 8, or 14** along the acyl chain. Using ^{19}F SS-NMR experiments in this section, the S/N ratio was improved. Initially, ^{19}F probes were evaluated for their usefulness to study peptide-membrane interactions using model membranes. Then, ^{19}F experiments were employed to study ghost membranes, and the ^{19}F probes shown to be sensitive to the effects of caerin. Both chapter 3 and chapter 4 highlights the usefulness of ^{2}H and ^{19}F SS-NMR experiments to study AMP interactions with whole cell systems.

Chapter 5 focused on ^{19}F SS-NMR study of lipid/PAs bilayer, two ^{19}F labeled PAs (at **position 4 and 8** in acyl chain) were simultaneously incorporated to a model membrane in order to measure internuclear distances from specific location of membranes to a **fluorinated drug molecule** or a molecule of interest. First objective is to establish the **^{19}F-^{19}F** internuclear distances from **PA-F(4)** to **PA-F(8)** and then to measure contact from these ^{19}F-PAs to a drug molecule. In the broader context, goal is to establish different SS-NMR experiments to probe membrane phase behavior and distance mapping for whole cell interactions, while performing faster acquisition and reducing background signal at same time. Specific goals are to finding the adequate experiments in both gel and fluid state of membranes. In addition to **^{19}F-^{19}F** measurement, other experiments such as **^{1}H-^{19}F and ^{1}H-^{1}H** based methods are employed for comparison.

Chapter 6 summarizes the main conclusion of this thesis and gives brief information or ideas for future perspectives, which are emanated from these thesis chapters, including some preliminary data already obtained.

CHAPTER II

Introduction to solid-state NMR experiments

2.1 Introduction

Nuclear magnetic resonance (NMR) spectroscopy is the primary technique utilized in this thesis. The goal of this chapter is to briefly describe the concepts necessary for the understanding of the various NMR experiments used. These exploited the chemical shift anisotropy (CSA), dipolar and quadrupolar interactions, magic-angle spinning (MAS) of the sample, spectral moment calculation and relaxation time measurement. The descriptions are based on different books[145-147] and reviews on magnetic resonance and biomembranes[103,148]. Emphasis is particularly given to ^{31}P, ^{2}H and ^{19}F SS-NMR experiments for the study of lipid membranes.

2.2 Brief introduction to NMR

The NMR phenomenon[149] involves atoms of non-zero spin which interact with the magnetic field (B_0), causing them to occupy different energy states (Zeeman splittings). The energy absorption from an external radio-frequency (RF) field causes the spins to make a transition to another energy state, thus creating a change in population of the various spin states. When the RF field is turned off, the precessing spins return back (relax) to equilibrium with a specific frequency and the transient magnetization (M_z) of these spins can be detected as a free induction decay (FID), then Fourier transformed to obtain a frequency (or NMR) spectrum.

The nuclear magnetic moment $\vec{\mu}$ is defined as the product of the spin angular momentum $\vec{I}$ and a proportionality constant γ (or gyromagnetic ratio).

$$\vec{\mu} = \gamma \vec{I} \tag{2.1}$$

The distinct energy of each state (E_m *or* E_n) is directly proportional to the strength of the applied magnetic field B_0 and specific to each atomic nucleus and characterized by γ. In the presence of a strong magnetic field (applied along the z-axis direction) the energy of the magnetic moment $\vec{\mu}$ is given by eq. (2.3):

$$E = -\mu_Z \, . B_O \tag{2.2}$$

$$E = -\gamma I_Z . B_O = \omega_0 I_Z \tag{2.3}$$

where ω_0 is known as the Larmor frequency ($\omega_0 = \gamma B_0$).

All nuclei in a sample may not necessarily experience the same B_0. The electron cloud surrounding a nucleus creates a small opposing field B_i. Thus, the field experienced by a nucleus can be expressed as eq. (2.4):

$$B_{local} = B_O\,(1 - \sigma) \tag{2.4}$$

where σ is constant of proportionality called "shielding constant". As a result of the shielding, the resonance condition eq. (2.3) becomes

$$\nu = \frac{\omega_0}{2\pi} = \frac{\gamma.B_O\,(1-\sigma)}{2\pi} \tag{2.5}$$

The difference in resonance frequencies between the nucleus of interest (ν) and a reference nucleus (ν_{ref}) is expressed as a "chemical shift" (δ) expressed in parts per million or ppm:

$$\delta = \frac{(\nu - \nu_{ref})}{\nu_{ref}}\,10^6 \tag{2.6}$$

Chemical shift values are independent of the magnetic field used. The NMR spectrum provides structural information since the resonance frequency of the different nuclei in a molecule depend on their chemical environment.

2.3 Solid-state NMR study of lipids

2.3.1 Introduction

Solid-state NMR has been employed to address structural and dynamical questions in lipid membrane samples. The various approaches can be broadly separated in two categories. First, in static samples, spectra have a characteristic lineshape called "powder spectrum" from which structural and dynamic information can sometimes be extracted. In the case of lipids, the most frequent static experiments analyse the ^{31}P and ^{2}H powder patterns, which respectively originate from the lipid head group and deuterated acyl chains. The second category of experiments relies on Magic-Angle Spinning (MAS) of the lipid membrane samples. This technique results in line narrowing and enables the measurement of molecular connectivity and distance relationships by exploiting spin−spin interactions.

As mentioned in a previous section, the ^{31}P nucleus is naturally present in phospholipids. Broadband ^{31}P NMR spectrum originates from the phospholipid head group, but it indicates an orientational dependency of the whole lipid membrane. The study of the, ^{2}H nucleus is enabled by isotopic enrichment, usually in the acyl chain regions, and ^{2}H SS-NMR allow the measurement of the acyl chains dynamics, often using order parameters. As will be seen in Chapter 4, the incorporation of a ^{19}F probes at different locations along the lipid acyl chain also provides order

and dynamical information on membranes. In this section, basic theoretical information that will be necessary to interpret spectra obtained from NMR of these three nuclei will be discussed.

2.3.2 Chemical shift anisotropy (CSA)

As mentioned above, chemical shifts result from differences in the electronic cloud that surrounds the nucleus. If the electron density is uniform in all directions there is a unique shielding constant (σ), and the spectrum is said to be isotropic. If the local field (eq. 2.4) depends on the molecular orientation with respect to the applied magnetic field B_o then the shielding is anisotropic. This orientation dependency of the chemical shift is referred to as "chemical shift anisotropy" (CSA). Depending on the local symmetry around the nucleus, the CSA varies as a function of molecular orientation or fluctuations in molecular motion. The anisotropic contribution to the chemical shift can be expressed in terms of a tensor. The powder pattern or line shape of the spectrum arise from the principal components of the shielding tensor (σ_{xx}, σ_{yy}, σ_{zz}). In such a case the CSA (or spectrum width) can be directly measured and described with an isotropic σ_{iso}, anisotropic δ_{aniso} and asymmetry parameter η, which are defined as follows:

$$\delta_{aniso} = \sigma_{zz} - \sigma_{iso} \tag{2.7}$$

$$\eta = \frac{\sigma_{yy} - \sigma_{xx}}{\delta_{aniso}} \tag{2.8}$$

$$\sigma_{iso} = \frac{\sigma_{xx} + \sigma_{yy} + \sigma_{zz}}{3} \tag{2.9}$$

As seen in Fig. 2.1, an effect of η on spectra is simulated for a single ^{13}C nucleus with an isotropic chemical shift of 0 ppm and a CSA of 10 ppm, a type of CSA pattern that is generally seen in solids and depends on the orientation of molecules with respect to the applied magnetic field B_o. Such analysis is usually performed using specific nuclei such as ^{31}P, ^{13}C, ^{15}N or ^{19}F, under ^{1}H decoupling.

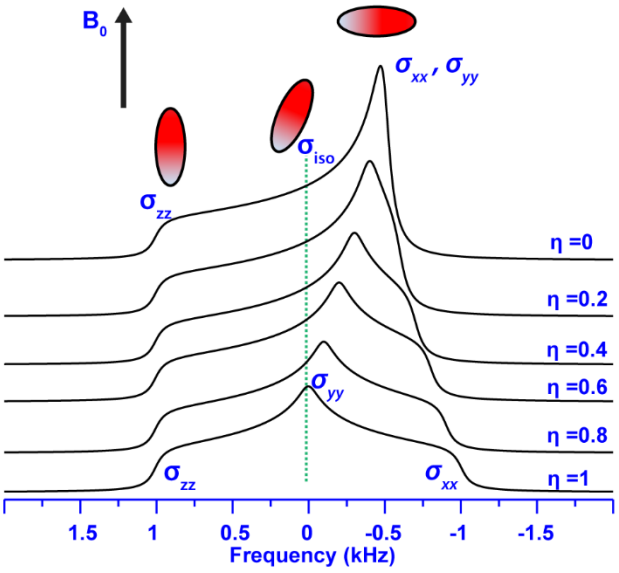

Figure 2.1: The effect of asymmetry parameter (η) on powder spectra, simulated by Simpson program[150].

In membrane systems in the fluid phase, fast axial diffusion of lipids ($\tau \approx 10^{-7}$-10^{-8} s)[104,151] in the membrane plane make the anisotropy axially symmetric (η=0 in Fig. 2.1 and Fig. 2.2), and gives rise to a typical powder spectrum averaged by two tensor component, σ_{zz} ($\sigma_{/\!/}$) oriented parallel and σ_{xx} or σ_{yy} ($\sigma_{\perp}$) oriented perpendicular to the magnetic field B_o. Such a CSA spectrum is sensitive to phase behavior or local motions of lipids in a membrane environment. As seen in Fig. 2.2, a typical ^{31}P SS-NMR spectrum of lipids in a lamellar bilayer, the line shape of this spectrum is distinctly different in comparison to nonlamellar hexagonal or micellar structures. In case of lamellar fluid membranes, a ^{31}P CSA of ≈ 25 ppm is usually observed in various phospholipids[83]. In the gel phase, ^{31}P line shapes display small asymmetry parameters but noticeable higher values (> 30 ppm) are typically observed[83]. A nonlamellar hexagonal phases is generally seen with a specific lipid headgroup with certain temperature or composition, in such cases, a pronounced effect on the $\sigma_{/\!/}$ tensor component will describe the spectrum with more reduction in the width of spectrum, for example, POPE at 75 °C[83] (Fig. 2.2). Other cases such as micelles or lipids in a solution, only the trace of the tensor will describe the spectrum (eq. 2.9 and Fig. 2.2), due to the molecular reorientation and rapid tumbling of the lipids. This line shape can also be representative of lipids in high curvature regions in the membranes, due to the specific molecular reorientation of lipids, but it will be characterised by a broad isotropic peak, the line-width of such a spectrum

being higher in comparison to micellar phase spectra, due to certain motional restriction, as will be detailed in chapter 3 and 4.

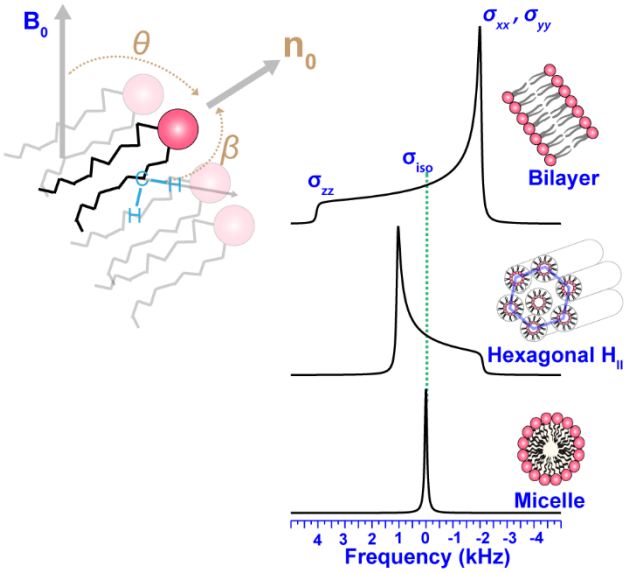

Figure 2.2: A typical example of static ^{31}P SS-NMR spectra of lipids in different phases and their dependency on molecular orientation or fluctuations of molecular motions (spectra are simulated using experimental CSA value from Warschawski et *al.*[83]). θ is the angle between B_o and the bilayer normal (director axis, n_0), which gives the orientation dependent ^{31}P chemical shift frequency and β is the average time-dependent angle between the bilayer normal and C-H bond (also, C-^{2}H or C-F) in a methylene or methyl group of acyl chains.

Similar spectral characteristics are expected in ^{19}F SS-NMR spectra in membranes depending on the ^{19}F position in membranes. For example, Gagnon et *al.*[152] observed a ^{19}F CSA values in DMPC, fluorinated at different location of membranes, and a noticeable decrease in CSA value is observed towards the chain ends. This is an averaging effect due to the additional fast motions of lipids, such as *trans-gauche* isomerisations ($\tau \approx 10^{-10}$ s)[104] and will reduce the width of the spectrum as will be detailed in chapter 4. In the context of peptide-membrane interactions, fluctuations of certain molecular motion in lipids can be monitored using a ^{31}P or ^{19}F powder spectrum. ^{19}F being isostere of ^{1}H, it can be readily incorporated into AMPs, for example, Drouin et *al.*[153] fluorinated the PGLa (α-helical) and $(KIGAKI)_3$ (β-stranded) membrane-active peptides and shown the usefulness of ^{19}F SS-NMR for membrane-peptide interactions. Authors have noticed some conformation changes with fluorinated peptides with certain ^{19}F-labels and discussed the adequate labeling strategies and potential of ^{19}F SS-NMR. In this thesis, ^{19}F labeling is pursued from a membrane perspective, and the potential of ^{19}F NMR will be detailed in chapter 4.

2.3.3 Magic-Angle Spinning (MAS)

MAS is the most effective way to remove the effects of anisotropic, dipole-dipole, and weak first-order quadrupolar interactions (will be detailed in next section). This technique mimics the rapid tumbling of molecules in liquids (or micelles) to average the interactions in a solid. This can be carried out by rotating the sample at an angle commonly known as "Magic", i.e., θ_m=54.7 ° with respect to the external magnetic field direction (Fig. 2.3). MAS will cancel all interaction terms with a $(3cos^2 \theta_m - 1)$ dependency[146] if the spinning frequency is sufficiently high (factor of 3 to 4 times higher), for example, ^{1}H-^{1}H dipolar interactions broaden the ^{1}H line width in the order of 40 kHz[154] and spinning the sample above 40 kHz would drastically make the ^{1}H line width narrower. At present, the achievable spinning frequencies are up to 124 kHz with specialized diamond rotors[155]. A sample with an intrinsic molecular motion would reduce ^{1}H-^{1}H dipolar interactions, hence providing sufficiently narrow ^{1}H line, and in that case, a slower MAS frequency will be sufficient to remove residual interactions. In the case of a spin system with a lower gyromagnetic ratio, a slower MAS frequency is also sufficient to remove anisotropic or dipolar interactions. For example, in the case of ^{13}C-^{13}C, the dipolar interactions are on the order of up to ~2 kHz.

Slower spinning often results in *"spinning sidebands"*, which appear on each sides of the isotropic central peak, and are separated by the MAS frequency. As with static spectra, this distribution of time-dependent sidebands provides quantitative information on local changes in molecular motions, which in the case of lipids often results from the phase behavior and molecular perturbation of lipid molecules in a membrane environment[156].

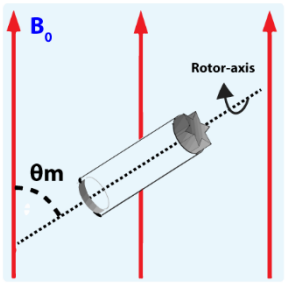

Figure 2.3: Magic angle spinning (θ_m= 54.7 °) used in solid-state NMR experiments.

2.3.4 Dipolar and quadrupolar interactions

Spin-spin interactions occur between a pair of nuclear spins, either through-bond (known as J-coupling or scalar coupling) or through space (direct or dipolar coupling). These interactions can be homonuclear (between same nuclei, such as ^{1}H-^{1}H) or heteronuclear (between different nuclei,

^{1}H-^{13}C). J-couplings give rise to a small line splitting (order of Hz) in the NMR spectrum, which depends on the magnitude of the interactions. It is generally hardly distinguishable on a SS-NMR spectra considering the intrinsic line broadening due to relaxation, dipolar couplings or CSA. The dipolar interaction is inversely proportional to the cube of the distance, *r,* between the interacting nucleus and can be described by:

$$D = \frac{\mu_0 \hbar \gamma_I \gamma_S}{8\pi^2 r^3} \qquad (2.10)$$

where μ_0 is the permeability of vacuum, γ_S and γ_I are the gyromagnetic ratios of the coupled spins, $\hbar$ is Planck's constant divided by 2π. As seen in Fig. 2.4, a spin system with a higher gyromagnetic ratio, such as ^{19}F and ^{1}H has higher dipolar coupling value (order of kHz for a given distance).

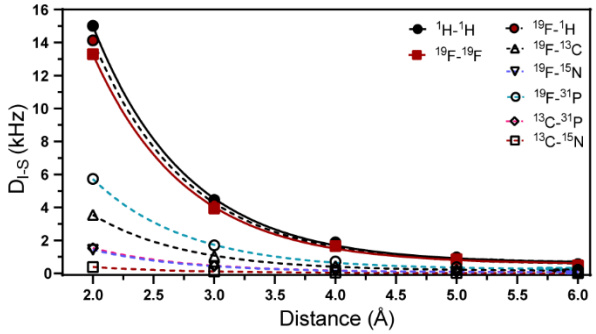

Figure 2.4: Dipolar coupling *vs.* distance plot for various spin systems.

Magic-angle spinning of the sample allows measuring connectivity and distance between nuclei, either from peak intensities in 2D correlation experiments or from quantitative measurements using dipolar recoupling experiments[157].

Atomic nuclei with a spin number greater than ½, such as ^{2}H with S=1, are called quadrupolar since their nuclear charge distribution is non-spherical and they thus possess a nuclear electric quadrupole moment Q. The interaction of the ^{2}H quadrupole moment with the electric field gradient (EFG) in a C-^{2}H bond gives rise to quadrupolar interactions[103]. In general, quadrupolar coupling in membrane samples is on the order of ten to hundreds of kilohertz (kHz). Due to the occurrence of two allowed transitions for the ^{2}H nucleus, C-^{2}H bonds in deuterated lipid membrane samples give rise to two resonances separated by a quadrupole splitting ($\Delta\nu_Q$), which is affected by the orientation relatively to the B_0 direction, as well as with lipid motions with respect to the bilayer normal, and therefore an average $\Delta\nu_Q$ is given[158,159] by:

$$\Delta\nu_Q = \frac{3}{2}\,\chi\left(\frac{(3cos^2\,\theta-1)}{2}\right)\left\langle\frac{(3cos^2\,\beta-1)}{2}\right\rangle \quad (2.11)$$

where $\chi = e^2qQ/h$ is the static quadrupolar coupling constant (≈168 kHz for C-^{2}H bond), as summarised in Fig. 2.2, θ is the angle between B_0 and the bilayer normal (director axis), β is the average time-dependent angle between the bilayer normal and the C-^{2}H bond in a methylene or methyl group. The splitting magnitude in ^{2}H SS-NMR powder spectra is directly proportional to the C-^{2}H bond segmental order parameter S_{CD}:

$$S_{CD} = \left\langle\frac{(3cos^2\,\beta-1)}{2}\right\rangle \quad (2.12)$$

In general, lipids in membrane systems exhibit various motions and the quadrupole splitting depends on the time scale of these motions. Typically, molecular motions that are fast on the ^{2}H NMR timescale (<10^{-5} s is slow) implies that only the average orientation of the C-^{2}H bond can be observed. The powder spectrum for a membrane sample with deuterated acyl chains gives a characteristic quadrupolar splitting specific to each methylene or methyl groups along the chain. Due to superposition, it is difficult to assign each methylene splitting. However, it they can be distinguished using a well-known deconvolution technique named *dePaking*[160], thus providing order profile of acyl chains.

As shown by equations 2.11 and 2.12, there is a direct relationship between the ^{2}H powder spectrum and the segmental order parameter of one C-^{2}H bond. With perdeuterated membrane samples, we expect a superimposition of powder spectra, one for each C-^{2}H bond. In the case of high resolution ^{2}H SS-NMR spectra, often obtained with model membranes, one can separate the various powder spectra, and hence the various segmental order parameters. But in the case of cellular samples, the resolution is such that individual spectra overlap and only an average order parameter can be determined. Using the ^{2}H either static or MAS spectra, one can measure spectral moments, which provide information on the average orientational ordering of the acyl chains. The moments of a MAS spectrum with a lineshapes of $f(\omega)$ is defined by eq. 2.13:

$$M_n = \frac{\int_0^\infty \omega^n f(\omega)\,d\omega}{\int_0^\infty f(\omega)\,d\omega} \quad (2.13)$$

M_2 is related to the mean square order parameter S^2_{CD}[148] such as:

$$M_2 = \frac{9\Pi^2}{20}\chi^2\,\langle S_{CD}^2\rangle \quad (2.14)$$

where, χ is the static quadrupolar coupling constant with value ≈168 kHz. M_2 can thus be extracted from a ^{2}H SS-MAS spectrum using eq. 2.13 or another method described by Warnet *et al*[156] as:

$$M_2 = \omega_r^2 \frac{\Sigma_{n=0}^{\infty} n^2 A_n}{\Sigma_{n=0}^{\infty} A_n} \qquad (2.15)$$

where, ω_r being the spinning rate ($\omega_r = 2\pi\upsilon r_r$, where υ_r is expressed in Hz) and A_n being the area of the nth sideband. The measurement of M_2 is a useful approach to study the phase behavior of membrane lipids or molecular perturbations in a membrane environment, and its usefulness is demonstrated in Chapters 3 and 4. Even in the case of dipolar couplings, such as those dominating ^{19}F SS-MAS spectra, where the quadrupolar splittings are absent, the analysis of M_2 enables the quantification of residual dipolar linewidths and provides a quantitative description of the membrane lipid order.

2.3.5 Relaxation times

As mentioned before, to obtain an NMR spectrum, the magnetization (created by the nuclear spins) is first perturbed away from the Z-direction (equilibrium conditions) to the XY-plane by a suitable RF pulse scheme. Nuclei *relax* back to equilibrium by two processes, one called spin-lattice (longitudinal) relaxation (T_1), and another spin-spin (transverse) relaxation (T_2) (Fig. 2.5). Those relaxation times are sensitive to molecular motions, in particular to their rotational correlation times (τ_c) as can be seen in Fig. 2.5. Due to the presence of various motions in lipid bilayers, measurement of relaxation times is particularly interesting to assess the dynamics in a lipid membrane. In Chapter 4, the usefulness of ^{19}F relaxation will be demonstrated.

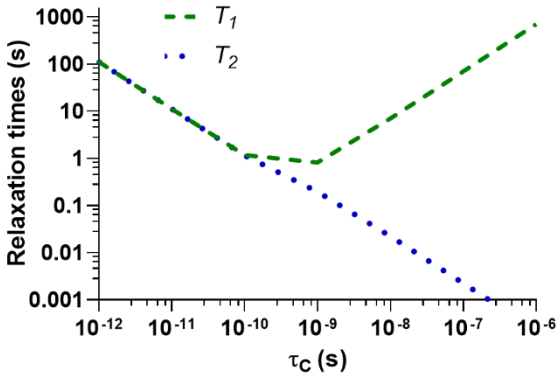

Figure 2.5: Dependency of relaxation times and rotational correlation times (τ_c) in a 400 MHz spectrometer.

2.3.6 2D experiments in SS-NMR

As mentioned in earlier sections, internuclear connectivity in a biomolecule can be mapped using two-dimensional (2D) SS-NMR experiments, depending on the resolution and the type of 2D experiment. They are generally categorised into homonuclear and heteronuclear experiments and employed in structure determination of various biomolecules, such as carbohydrates, lipids, and proteins. Such experiments involve a transfer of magnetisation from one spin to another causing the "cross-peaks" in 2D spectrum. The connectivity or distance information is encoded as cross-peak intensities and the "mixing period" in 2D pulse sequences (Fig. 2.6) determine the nature of the developing spectral information[161]. The mixing period usually lasts for up to several ms, depending on the type of experiment used and the cross-peak buildup rate for a given distance, which should be compared to a known distance. However, one might have to consider different possible mechanisms of magnetisation transfer to elucidate the structural characteristics, for example, cross-peaks due to nuclear "Overhauser effect (NOE)" is distinctly different from coherent dipolar coupling exchange process.

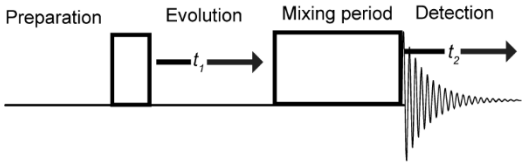

Figure 2.6: Four main periods in 2D NMR experiments (Adapted from Hwang et *al.*[161] with permission).

In fluid phase membrane samples, ^{1}H line width is narrowed down under MAS condition, and 2D ^{1}H-^{1}H NOESY (Nuclear Overhauser effect spectroscopy) experiments provide useful informations on molecular connectivity. For example, Huster et *al.*[162] determined the interaction between cholesterol and lipids using ^{1}H NOESY. Comparing spin diffusion and NOE in lipid membranes, Huster and Gawrisch[163] conclude that ^{1}H magnetisation transfer between different resonances of lipids in fluid membrane sample are due to NOE, while Chen and Stark[164] suggest the possibility of simultaneous NOE and spin diffusion. In short, NOE is a relaxation driven process, cross-correlations result from a number of interacting spins[149] and they are typically observed for up to 5 Å distances. Nuclear spin diffusion is driven by dipolar interactions, generally observed in solids, and that can be relayed up to 20 Å away[165]. In the context of peptide-membrane interaction, these experiments are useful for determining the spatial location of peptides in the

membrane, particularly, using NOESY or HOESY (heteronuclear Overhauser spectroscopy) experiments, and they can be done at higher temperature, which is indeed relevant for whole cells, where the biological conditions involve cell membranes in the fluid state. In Chapter 5 such ^{1}H-^{1}H correlation experiment will be detailed. In addition, ^{1}H-^{19}F HOESY, ^{19}F-^{19}F PDSD (proton-driven spin diffusion), and ^{19}F-^{19}F DARR (dipolar assisted rotational resonance) will be detailed with an example of fluorinated drug and fluorinated membrane. Other heteronuclear such as RFDR (radio-frequency-driven recoupling) or REDOR (rotational-echo double-resonance) experiments also discussed in Chapter 5 and 6, which can be performed in gel phase of membrane.

NOESY or HOESY involve transfer of magnetisation through NOE, and give cross-peaks in 2D spectra, there-by containing structural information. PDSD and DARR correlate spins indirectly, the magnetization going through ^{1}H-^{1}H magnetization transfer. DARR relies on ^{1}H-^{1}H coherent dipolar couplings, while PDSD relies on ^{1}H incoherent spin diffusion. Cross-peaks intensities depend on the spatial proximities, and are therefore used for various biomaterial characterisation. For example, Arnold et *al.*[166] employed such ^{13}C-^{13}C PDSD and DARR experiments for the characterisation of whole cell *Chlamydomonas reinhardtii* microalgae.

The RFDR experiment on the other hand uses homonuclear dipolar couplings such as ^{1}H-^{1}H or ^{19}F-^{19}F though selective recoupling for transferring magnetization. For example, Guo et *al.*[167] employed such experiments for the characterisation of fluorine-containing pharmaceutical compounds. The REDOR experiment uses selective heteronuclear dipolar recoupling for transferring magnetization. For example, Toke et *al.*[168] used such ^{13}C-^{19}F REDOR method to determine the orientation of a membrane-active peptide in lipid bilayer. Shcherbakov et *al*.[157] summarise that any dipolar coupling that is smaller than 30 Hz is difficult to measure by RFDR/REDOR experiments, and that by using ^{19}F and ^{1}H, one can measure distances of up to 15 Å. In this thesis, the potential for such distance measurement experiments for AMPs and membrane interactions will be discussed, in the context of ^{19}F labeling in membranes.

CHAPTER III

In situ solid-state NMR study of antimicrobial peptide interactions with erythrocyte membranes

Kiran Kumar[1,2], Mathew Sebastiao[1,2], Alexandre A. Arnold[1,2], Steve Bourgault[1,2], Dror E. Warschawski[1,3] & Isabelle Marcotte[1,2]

[1] Department of Chemistry, Université du Québec à Montréal, P.O. Box 8888, Downtown Station, Montreal, Canada H3C 3P8

[2] Quebec Network for Research on Protein Function, Engineering and Applications (PROTEO), Québec, Canada

[3] Laboratoire des Biomolécules, LBM, CNRS UMR 7203, Sorbonne Université, École normale supérieure, PSL University, 75005 Paris, France

Published in *Biophysical Journal* (2022) DOI: 10.1016/j.bpj.2022.03.009
Also, selected for new and notable in *Biophysical Journal* (2022) DOI:10.1016/j.bpj.2022.03.008

N.B. References cited in this chapter are presented at the end of the thesis

3.1 Abstract

Antimicrobial peptides stand as promising therapeutics to mitigate the global rise of antibiotic resistance. They generally act by perturbing the bacterial cell membrane, and are thus less likely to induce resistance. Since they are membrane-active molecules, it is critical to verify and understand their potential action towards eukaryotic cells to help design effective and safe drugs. In this work, we studied the interaction of two antimicrobial peptides, aurein 1.2 and caerin 1.1, with red blood cell (RBC) membranes using *in situ* ^{31}P and ^{2}H solid-state nuclear magnetic resonance (SS-NMR). To do so, we established a protocol to integrate up to 25% of deuterated fatty acids (FAs) in the membranes of ghosts, which are obtained when hemoglobin is removed from RBCs. The FA incorporation and the integrity of the lipid bilayer were confirmed by SS-NMR and fluorescence confocal microscopy. Leakage assays were performed to assess the lytic power of the AMPs. The *in situ* perturbation of the ghost membranes by aurein 1.2 and caerin 1.1 revealed by ^{31}P and ^{2}H SS-NMR is consistent with a membrane perturbation through a carpet mechanism for aurein 1.2, while caerin 1.1 would act on RBCs via pore formation. These results are compatible with fluorescence microscopy images of the ghosts. The peptides interact with eukaryotic membranes following similar mechanisms that take place in bacteria, thus highlighting the importance of hydrophobicity in determining such interactions. Our work bridges model membranes and *in vitro* studies and provides an analytical toolbox to assess drug toxicity towards eukaryotic cells.

3.2 Introduction

Antimicrobial resistance affects the lives of many people around the world, and for this reason, the World Health Organization has recently published its first list of antibiotic-resistant bacteria that should be prioritized in the development of new treatments[169]. New drug candidates with novel action mechanisms must be urgently proposed[170], and in this regard, antimicrobial peptides (AMPs) are a promising therapeutic alternative that could be submitted to advanced chemical engineering to become new antimicrobial drugs[31]. The antimicrobial activity of AMPs involves different possible action mechanisms that cause bacterial cell death, including perturbation of the plasma membrane[32,171]. Because these mechanisms are entirely distinct from those of current clinically-used antibiotics, there is great interest in their development as therapeutics against antibiotic-resistant bacterial infections[172]. Besides their direct cytotoxicity towards bacteria and fungi, several AMPs exhibit antiviral[173], antiparasitic[174] and anticancer properties[175]. Those biologically-active candidates are not only able to kill bacteria but also to modulate host immunity[176] since AMPs have evolved as integral components of strategic and carefully regulated mechanisms of immunity against infection[171].

In general, the outer surface of Gram(+) and Gram(-) bacteria contain peptidoglycan, and either teichoic acids or lipopolysaccharides[177,178], each conferring a net negative charge. In addition, the outer leaflet of the lipid bilayer in bacterial membranes often contains zwitterionic phosphatidylethanolamine (PE) as well as negatively-charged lipids such as phosphatidylglycerol (PG) and cardiolipin (CL)[179,180], thus promoting electrostatic interactions with cationic AMPs[181]. In contrast, the outer leaflet of most mammalian cell membranes, including the erythrocyte membrane, mainly consists of zwitterionic phospholipids such as phosphatidylcholine (PC) and sphingomyelin (SM), as well as cholesterol[182]. These fundamental differences between bacterial and eukaryotic membrane compositions should offer some specificity. Although many factors can influence this selectivity, including molecular shapes of both lipids and peptides[183], it has been proposed that charged peptides would preferentially interact and affect the microbial membrane integrity with higher potency than they do eukaryotic membranes[184,185]. One major challenge is to identify AMPs for their potential therapeutic use and selectivity towards bacteria, without affecting eukaryotic cells such as erythrocytes. Many studies have shown the potential of AMPs through their interaction with model membranes[58,186-188]. However, model membranes have limited complexity and therefore overlook potentially important features of the cellular envelope. In this

regard, *in vivo* studies are becoming more widespread, including *in-cell* solid-state nuclear magnetic resonance (SS-NMR) spectroscopy[57,166,189]. In our previous study, aurein 1.2 (GLFDIIKKIAESF-NH_2) and caerin 1.1 (GLLSVLGSVAKHVLPHVVPVIAEHL-NH_2) - natural AMPs isolated from the skin secretions of Australian tree frogs - were investigated[56,190-192]. Their interaction with intact Gram(+) and Gram(-) bacteria was studied by *in vivo* ^{2}H SS-NMR following specific deuteration of their membrane phospholipid acyl chains[57].

In this report, we have investigated the action of these two cationic peptides on erythrocyte ghost membranes. The term "ghost" is used to describe the discoid bodies obtained after the removal of hemoglobin from erythrocytes[127]. As post-hemolytic remains of RBCs, their cell surface and membrane composition, including lipids, proteins, and other plasma membrane components, has been shown to be similar or even identical to that of intact RBCs[127,130]. Hence ghosts can be used to study the lipid phase, dynamics and interactions in RBC membranes[144]. Devoid of signal-perturbing hemoglobin or cytoplasmic phosphorus-containing molecules, ghosts are better-suited systems for SS-NMR studies.

We have first optimized and characterized the deuteration of erythrocyte ghosts with efficient incorporation of perdeuterated exogenous palmitic acid (PA-d_{31}) in their membranes. Palmitic acid was chosen since saturated acyl chains with 16 carbons are the most abundant type of fatty acid (FA) chains in erythrocyte lipids (see Fig. 3.5 in results section) and it is commercially available in its deuterated form. Similar labeling had been attempted in the past by Davis *et al.*[143] who intercalated PA-d_{31} molecules into lyophilized human erythrocytes and rehydrated them prior to NMR experiments. They obtained a 5 % deuteration of the membranes and monitored the second moment of ^{2}H SS-NMR spectra as a function of temperature, showing no detectable phase transition down to 2°C, suggesting that PA-d_{31} molecules are present in all lipid regions of the membrane. In this work, we have improved the FA incorporation in the ghost membranes, reaching a level of 25% deuteration. We have assessed changes in the lipid headgroup profile by ^{31}P solution NMR, and in the FA chain composition by gas chromatography coupled to mass spectrometry (GCMS). We have also validated the PA-d_{31} insertion by ^{2}H SS-NMR and GCMS, and the membrane integrity by ^{31}P SS-NMR, and confocal fluorescence microscopy.

Following the characterization of deuterated ghosts, we have studied the effect of caerin 1.1 and aurein 1.2. Hemolytic and leakage assays were used to determine the lytic action of AMPs on erythrocyte and model membranes. Then ^{31}P and ^{2}H SS-NMR and confocal microscopy were

employed to investigate the interactions of the peptides with erythrocyte ghost membranes. By performing these experiments at various lipid-peptide molar ratios, an overall picture of peptide interactions with erythrocyte membranes is proposed. Moreover, by determining the conditions in which these peptides perturb the membrane, their relative selectivity towards bacterial membranes is established.

3.3 Materials and methods

3.3.1 Materials

Caerin 1.1 and aurein 1.2 were synthesized by GenScript Corporation (Piscataway, NJ, USA) with >98.3% purity. Sphingomyelin (SM) (egg, chicken), 1,2-dioleoyl-sn-glycero-3-phosphocholine(DOPC), 1,2-dioleoyl-sn-glycero-3-phosphoethanolamine (DOPE), 1,2-dioleoyl-sn-glycero-3-phospho-L-serine (DOPS), 1-palmitoyl-2-oleoyl-glycero-3-phosphocholine (POPC), 1-palmitoyl-2-oleoyl-sn-glycero-3-phosphoethanolamine (POPE) and 1-palmitoyl-2-oleoyl-sn-glycero-3-phospho-glycerol (POPG) were obtained from Avanti Polar Lipids (Alabaster, AL, USA). Ethylenediaminetetraacetic free acid (EDTA) was purchased from Fisher Scientific (Fair Lawn, NJ, USA), while deuterated palmitic acid (PA-d_{31}), cholesterol, deuterium-depleted water, Triton X-100, fatty acid methyl ester mix C4-C24 (FAME mix), [16-[(7-nitro-2-1,3-benzoxadiazol-4-yl)amino] palmitic acid (NBD-PA), 1,1'-dilinoleyl-3,3,3',3'-tetramethylindo-carbocyanine 4-chlorobenzenesulfonate (Fast DiI) and all other solvents and chemicals were purchased from Sigma Aldrich (Oakville, ON, Canada). Fresh horse RBCs packed 100% were purchased from Cedarlane Laboratories (Burlington, ON, Canada). Deionized 18.2 MΩ.cm Milli-Q water was used in all experiments (Millipore).

3.3.2 Ghost sample preparation and labeling

Ghosts were prepared as previously described[130] with some modifications. Concentrated horse RBCs were suspended in a 40 mL round bottom centrifugation tube with isotonic HEPES buffer (20 mM HEPES, 150 mM NaCl, pH 7.4), and centrifuged at 500 g for 5 min at 4°C. Supplementary washes (2 to 3) in the same buffer were carried out until the supernatant became clear. After the final wash, the pellet was resuspended in 20 mL hypotonic HEPES buffer (20 mM HEPES, pH 7.4) and centrifuged at 25,000 g for 40 min at 4°C (rotor JA-20, Beckman). The supernatant was then removed, and the pellet transferred into new centrifuge tubes, leaving behind the “red button”

that contains proteases. Additional washes (3 to 4) with the same buffer were carried out until the pellet became white.

A 0.5 mM Triton X-100 / 0.25 mM PA-d_{31} mixed micelle[193] solution in isotonic buffer was prepared in a sealed glass vial with 3 freeze (-20ºC) / thaw (95 ºC) cycles. The white ghost pellet was then resuspended in 320 mL isotonic buffer to which 80 mL of the mixed micelle solution were transferred and incubated for 15 min at 37°C. The mixture of ghosts and micellized PA-d_{31} was then centrifuged at 25,000 g for 20 min at 4ºC in different 20 mL aliquots. The excess detergent was washed away by centrifugation in isotonic buffer twice more at 25,000 g for 20 min at 4ºC. The ghost pellets were pooled together in a 1.5 mL Eppendorf tube and centrifuged at 20,000 g for 20 min at 4ºC. The pellet was then washed in an isotonic buffer prepared with deuterium-depleted water (DD water), first at 20,000 g for 20 min at 4ºC, and then at 100,000 g and 4ºC for 20 min. This concentrated pellet was collected and stored at 4ºC prior to the experiments. To calculate the lipid-to-peptide ratios, the lipid concentration after ghost preparation was determined by high-resolution ^{31}P solution NMR after lipid extraction, as described in the supplementary information (Fig. S3.1).

3.3.3 Preparation and labeling of liposomes

Multilamellar liposomes (MLV) were prepared, using the film method as described by Warschawski *et al.*[83]. Lipid powders (including cholesterol and labeled PA-d_{31}) were dissolved in 1:2 Methanol/$CHCl_3$ solution and dried under a nitrogen stream. Residual organic solvent in lipid film was removed by high vacuum for at least 2 h. The film then hydrated with a physiologically relevant buffer (20 mM HEPES, 150 mM NaCl (pH 7.4)) in DD water. Lipid dispersion was vortexed and freeze-thawed 5-8 times (10 min at −20°C followed by 10 min at 55°C) and transferred directly into a 4 mm rotor.

3.3.4 Microscopy sample preparation

Ghosts 1 % (v/v) were labeled with Fast-DiI (1/1000) using 10 rpm longitudinal rotation for 1 h at 37 ºC, then pelleted at 16,000 g for 15 min. The pellet was resuspended in 500 µL HEPES buffer then transferred to Sarstedt 8-well microscopy slides (300 µL) and left to stand for 30 min to allow ghosts immobilization. NBD-PAs were incorporated to ghosts along with PA or PA-d_{31}as described above in section 3.2.2. After addition of an appropriate amount of AMPs, calcein influx

experiments were performed by adding 0.5 mM calcein directly into 1 % (v/v) ghosts. Images were acquired using a Nikon confocal microscope with a 60x oil-immersion lens and processed using ImageJ software.

3.3.5 Lipid and fatty acid profile

The lipid profile was determined following the procedure of Laydevant *et al.*[194]. Lipid extraction was performed in triplicate using the Folch protocol[195], and freeze-dried sample weights were measured using XP205 Mettler Toledo Analytical Balance (up to 0.01 mg readability). Then samples were dissolved in a biphasic solution composed of 200 µL CD_3OD, 500 µL $CDCl_3$ (organic phase) and 50 µL of a 200 mM EDTA (acid form) at pH 6.00 ± 0.04 (aqueous phase). Solution NMR spectra were acquired using a 600 MHz Bruker Avance III HD (Milton, Canada) spectrometer equipped with a 5-mm broad band probe, operating at 243 and 600 MHz for ^{31}P and ^{1}H, respectively. 1D ^{31}P NMR spectra were obtained with ^{1}H decoupling and employed 384 scans at 25 °C with a 10 s relaxation delay to obtain quantitative data. To identify the lipid profile, commercially available pure synthetic lipids (DOPC, DOPE, DOPS and SM) solutions were spiked in the sample. Remaining ambiguities were resolved by 2D ^{31}P-^{1}H TOCSY NMR experiments as described by Balsgart et al.[196], at 25 °C with 12k data points in the direct dimension and 200 data points in the indirect dimension, a repetition delay of 2 s, a TOCSY mixing time of 70 ms. The acquisition time in the direct dimension was 2.8 s, for a total acquisition time of 22 h per 2D spectrum.

Samples used for solution NMR analyses were then recovered and prepared for FA analysis by GCMS. Briefly, samples were filtered then transesterification was carried out in 2 mL of H_2SO_4 (2% in methanol) and 0.8 mL of toluene for 10 min at 100°C.The GC-MS analyses were carried out as described by Laydevant *et al.*[194] using a polar HP-5MS column (30 m length × 250 µm diameter × 0.25 µm film thickness). The injection volume was 1 µL and the oven temperature was programmed to heat at 140 °C for 5 min followed by a 4°C/min ramp up to 300°C, prior to electron ionization and detection with a quadrupole MS. Data acquisition and processing were performed with the Chemstation software.

3.3.6 Hemolysis assay

The hemolytic activity of the AMPs was determined by measuring the hemoglobin released from horse RBCs as described previously[185]. A volume of 500 µL of packed RBCs was centrifuged at 500 g and 4°C for 5 min to recover the erythrocytes, and the supernatant was removed. The pellet was subsequently washed 3 times with 10 mL of PBS isotonic buffer to obtain a clear supernatant. The 30-µL erythrocyte pellet was resuspended in 270 µL of a solution containing the AMPs at the desired concentration (diluted in PBS buffer) to obtain a final concentration of 5 % RBCs (v/v) containing about 5 to 10 × 10^8 cells/mL. The sample was incubated at 37°C for 1 h. The PBS buffer and 1% Triton X-100 solution were respectively used as negative (A_0) and positive controls (A_{100}). After a 500 g centrifugation for 5 min, the hemoglobin concentration in the supernatant (diluted to 2% RBCs in PBS buffer) was determined using a UV-visible spectrophotometer by monitoring the optical density at 576 nm. The percentage of hemolysis was calculated with the following equation:

$$\%hemolysis = \frac{A - A_0}{A_{100} - A_0} \times 100 \quad (3.1)$$

3.3.7 Carboxyfluorescein leakage assays

Large unilamellar vesicles (LUVs) that mimic erythrocyte and bacterial membranes were prepared for the carboxyfluorescein (CF) leakage experiments by encapsulating CF into LUVs. About 20 mM lipids were rehydrated in a buffer (20 mM HEPES at pH 7.4) containing 46 mM CF and multilamellar vesicles (MLV) were prepared using 5 freeze–thaw cycles and a 5-min vortex step each time. LUVs were obtained by extruding the MLV suspension through a polycarbonate filter with 100 nm pores (Avanti Polar Lipids, Alabaster, AL, USA). The CF-containing vesicles were separated from non-entrapped CF using a Sephadex G25 Fine (20×80 mm) size-exclusion chromatographic column eluted with buffer. The lipid concentration of separated LUVs was determined by a phosphorus assay in triplicates. The 12.5 µL of the liposome suspension of each lipid system were resuspended in 87.5 µL of solution containing the AMPs at the desired concentration (diluted in HEPES buffer) and the sample was incubated at 37°C for 1 h. The buffer and 1% Triton X-100 were respectively used as negative (F_0) and positive controls (F_{100}). The percentage of CF released was measured using a microplate reader set at $\lambda_{emission}$ = 517 nm and $\lambda_{excitation}$ = 495 nm. The percentage of leakage (%L) was calculated with the following equation:

$$\%L = \frac{F - F_0}{F_{100} - F_0} \times 100 \quad (3.2)$$

3.3.8 Solid-state NMR and spectral moment analysis

^{31}P and ^{2}H SS-NMR spectra were acquired using a Bruker Avance III-HD wide bore 400 MHz spectrometer (Milton, Canada), with respective resonance frequencies of 162 and 61.5 MHz. Static ^{31}P SS-NMR spectra were obtained using a phase-cycled Hahn echo pulse sequence[197], with high-power (50 kHz) ^{1}H decoupling during acquisition. Using a 90° pulse length of 3 µs, an inter pulse delay of 35 µs, data were collected using 1024 points with a recycle delay of 3 s and a total of 14 k scans per spectra, amounting to 12 hours of acquisition. Magic-angle spinning (MAS) ^{2}H SS-NMR experiments were carried out using a 10 kHz spinning frequency and a phase-cycled quadrupolar echo sequence[156], with 100 k data points, acquired with a 90° pulse length of 4 µs, a rotor-synchronized interpulse delay of 96 µs and a recycle time of 500 ms. A total of 44 k scans per spectra were acquired for 8 hours. A line broadening of 100 Hz was applied to all spectra, and the ^{31}P chemical shift anisotropy (CSA) was determined by line fitting using Bruker Topspin 4.0.6 and Sola (Solid Lineshape Analysis) softwares.

^{2}H spectral moment analysis was performed using MestRenova software V6.0 (Mestrelab Research, Santiago de Compostela, Spain). Second spectral moments, M_2, were calculated using equation (3.3)[156].

$$M_2 = \omega_r^2 \frac{\Sigma_{N=0}^{\infty} N^2 A_N}{\Sigma_{N=0}^{\infty} A_N} = \frac{9\Pi^2 \chi_Q^2}{20} \langle S_{CD}^2 \rangle \qquad (3.3)$$

where ω_r is the angular spinning frequency, N is the side band number, and A_N is the area of each sideband obtained by spectral integration, S^2_{CD} is the mean square order parameter, and χ_Q is the static quadrupolar coupling constant equal to 168 kHz for a C-D bond in acyl chains. The M_2 value provides a quantitative description of the membrane lipid ordering and is particularly sensitive to the gel-to-fluid phase transition. Despite using deuterium-depleted water, a residual HDO peak remains, which accounts for 10 to 15% of the total ^{2}H NMR spectral intensity. This residual peak is excluded from the spectral moment calculation.

3.4 Results

3.4.1 Incorporation of fatty acids into erythrocyte ghost membranes

Plasma membranes of RBCs are significantly different from those of bacteria. Notably, they contain 30-40% cholesterol, and their phospholipid acyl chains show a higher degree of ordered phase than those of fluid bacterial membranes. While erythrocyte ghost membranes have

previously been labeled with deuterated FAs[144], here we show that the labeling can be improved to facilitate the study of peptide-membrane interactions. A first set of experiments was performed to optimize the incorporation conditions of PA-d_{31} into ghost membranes. Optimal insertion was achieved by incubating ghosts in the presence of Triton X-100/PA-d_{31} mixed micelles. In the presence of ghost membranes, these micelles are in a dynamic association-dissociation equilibrium, the kinetics of which depend on temperature, pressure and concentration[198]. They were diluted such that the concentration of Triton X-100 was decreased to 0.1 mM during the incorporation step, i.e., well below the critical micelle concentration of Triton X-100 (0.23 mM)[193]. Nonionic surfactants such as Triton X-100 tend to undergo a slow dissociation during which the exchange of FAs between the mixed micelles and phospholipid bilayers occurs. Since the FA incorporation in the bilayer is thermodynamically favorable, the exchange equilibrium is shifted towards the bilayer, and the ghost membrane can thus be efficiently ^{2}H-labeled[199,200]. Although a full quantitative understanding of this process is beyond the scope of this work, the relative partitioning of PA versus Triton X-100 in the membrane is likely to be a key factor for the successful labeling. Indeed, the partition coefficient of PA is two orders of magnitude higher than the one of Triton X-100 in PC membranes (103×10^{3} M^{-1} for PA versus 3×10^{3} M^{-1} for Triton X-100)[201,202]. Palmitic acid is thus favorably inserted into the membrane, and the residual detergent, which favorably remains in the buffer, can be removed by a series of washing steps.

At a concentration of 0.1 mM, the surfactant proved to be harmless to the cell membranes, as demonstrated elsewhere[193,203]. This is supported by the ^{31}P SS-NMR spectrum (Fig. 3.1B) which is characteristic of an intact lamellar lipid phase, and comparable to PC/SM/cholesterol/PA-d_{31} (5:3:7:5 molar ratio) model RBC membranes (Fig. 3.1C), as well as to unlabeled ghosts (Fig. 3.1A). The ^{31}P CSA value of deuterated ghosts is in good agreement with those of unlabeled ghosts and model membranes, as well as past studies in lipid bilayers[137] (Fig. 3.1). As shown in Fig. 3.2A, 3.2B and 3.2C, the integrity of the RBC ghost morphology is further confirmed by confocal fluorescence microscopy. Z-stack of multiple optical sections also reveals that ghosts retain the biconcave disc shape of RBCs (Fig. 3.2D).

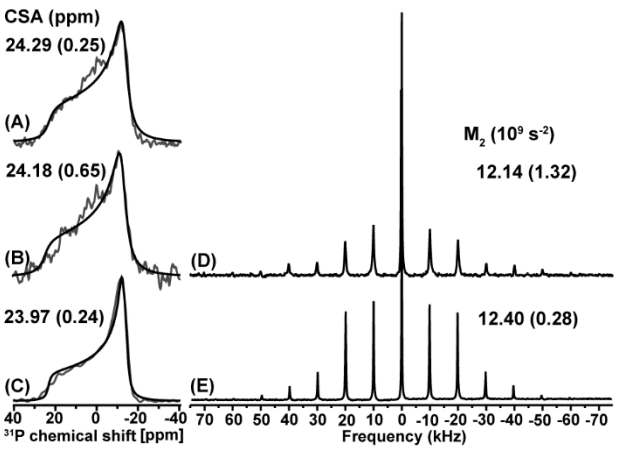

Figure 3.1: Static ^{31}P SS-NMR spectra with spectral fitting and average CSA of **(A)** unlabeled, **(B)** deuterated ghosts and **(C)** DOPC/SM/Chol/PA-d_{31} (5:3:7:5) model membranes. ^{2}H SS-NMR spectra with MAS (10 kHz) of **(D)** deuterated ghosts and **(E)** DOPC/SM/Chol/PA-d_{31} (5:3:7:5) model membranes with M_2 values. All spectra were recorded at 293 K. The residual HDO peak in deuterium-labeled ghosts accounts for 10 to 15 % of the total ^{2}H intensity and is not integrated in the M_2 calculation.

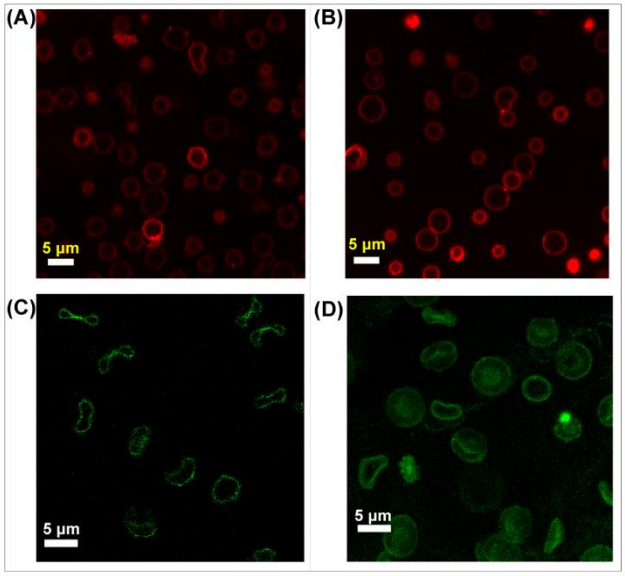

Figure 3.2: Characteristic confocal fluorescence microscopy images of prepared erythrocyte ghosts indicating that the membranes are intact, the incorporation of PA-d_{31} does not appreciably alter the overall morphology, and PA molecules are evenly dispersed throughout the plasma membrane. (A) Non-deuterated ghosts labeled with the lipophilic tracer FAST-DiI (red). (B) Ghosts with PA-d_{31} incorporated into the plasma membrane, labeled with the lipophilic tracer FAST-DiI (red). (C) Deuterated ghosts prepared in the presence of fluorescent NBD palmitic acid (green). (D) Z projection of multiple planes of the deuterated ghosts prepared with fluorescent NBD palmitic acid (green).

To ensure that the ghost membranes were effectively labeled, ^{2}H SS-NMR spectra were recorded (Fig. 3.1D) using MAS, thus providing a high signal-to-noise (S/N) ratio in a few hours, similarly to bacteria[32]. The presence of spinning sidebands proves that a significant amount of deuterated FAs are no longer incorporated in fast tumbling objects such as micelles, but are rather found in an environment with restricted motions such as a membrane bilayer. Moreover, the ^{2}H spectrum is very similar to the one obtained for a model membrane with the same lipid composition (Fig. 3.1E), confirming that PA-d_{31} is indeed in a membrane environment. The incorporation of PA is further supported by fluorescence microscopy images, which locate NBD-PAs, a fluorophore structurally similar to PA-d_{31}, in the ghost membranes (Fig. 3.2C, D).

The incorporation of PA-d_{31} in ghost membranes was further ascertained by comparing the FA ordering in labeled ghosts and in model membranes with increasing composition complexity. To do so, the second spectral moment, M_2, from ^{2}H SS-NMR spectra was determined at several temperatures. Indeed, if PA-d_{31} is incorporated in the ghost membranes, the evolution of its ^{2}H second spectral moment – which reflects the fluidity of the membrane - with temperature is expected to be similar to the one in a model membrane which closely matches the lipid composition of ghosts Fig. 3.1 D-E. As shown in Fig. 3.3, the ordering of PA-d_{31} in DOPC/Chol/PA-d_{31} and, to a lesser extent, in DOPC/PA-d_{31}, shows a reduction with increasing temperature. The addition of sphingomyelin appears to cancel this temperature dependence. Interestingly, PA-d_{31} ordering in labeled ghosts as a function of temperature closely follows the one of the model membranes which composition is the closest to erythrocyte membranes (DOPC/SM/Chol/PA-d_{31}) (Fig. 3.3). The temperature dependence of ^{2}H M_2 values thus appears to confirm the incorporation of FAs into the ghost membrane. Moreover, as shown by ^{31}P SS-NMR and confocal fluorescence microscopy, the membrane integrity of these labeled ghosts is preserved.

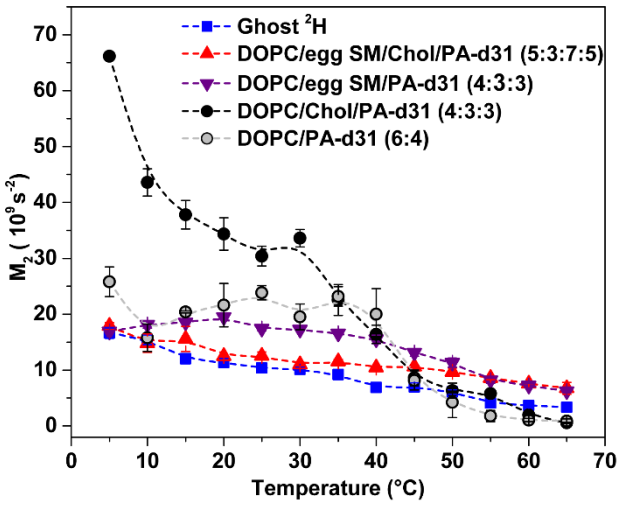

Figure 3.3: Membrane fluidity of model membranes and ghosts incorporating PA-d_{31}, as a function of temperature, as reported by the second spectral moment, M_2, calculated from ^{2}H SS-NMR spectra. The similarity between the M_2 values obtained for labeled ghosts and model membranes with the closest lipid composition are a strong indication that PA-d_{31} is incorporated in the ghost membrane.

3.4.2 Lipid composition of erythrocyte and ghost membranes

To characterize possible alterations to the lipid profile upon ^{2}H-labeling of RBC ghost membranes, phospholipids were identified and quantified using 1D ^{31}P solution NMR after lipid extraction (see Fig. S3.2 in the Supplementary information). ^{31}P resonances of the main phospholipids (PE, PC, SM and PS) were identified by comparison with the chemical shifts of standards and the literature[194]. Lipid proportions were determined by integrating those resonances and are reported in Table S3.1.

To identify other lipids, in particular ether-linked phospholipids, we used a 2D ^{1}H–^{31}P TOCSY experiment in solution NMR[196], as shown in Fig. 3.4. All ^{1}H and ^{31}P chemical shifts have been reported in Table S3.1, and two ^{31}P lipid columns, at -0.75 and 0.18 ppm, showed a marked shift of their g2 glycerol proton, from 5.05 ppm to 4.97 ppm. We assign this shift to originate from a change in linkage from an ester to an ether group, in ether PC (PCe) and ether PE (PEe) - the additional oxygen in ester linked lipids further deshielding the glycerol protons[204]. One last ^{31}P lipid column, at 0.22 ppm, was not assigned from the 1D ^{31}P solution NMR spectra. Its proton NMR pattern is similar to that of SM, and we assigned it to dihydrosphingomyelin (DHSM), which is compatible with previous assignment in a different context[205]. While PCe is only *ca.* 20% of the

total PC lipids, we note that around 60% of SM lipids are DHSM, and that almost all of PE lipids are actually PEe.

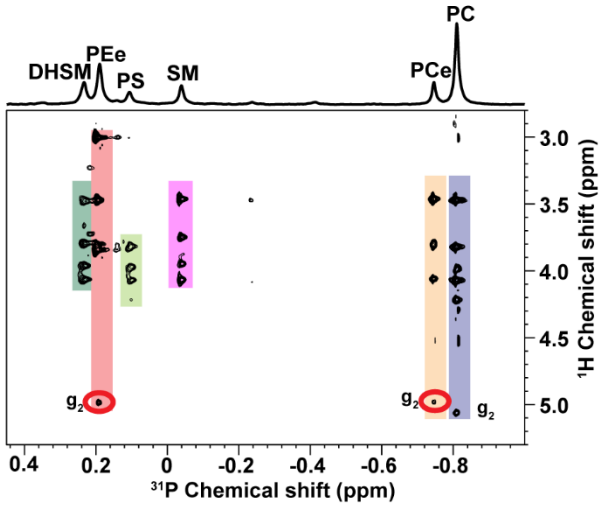

Figure 3.4: 2D ^{1}H–^{31}P TOCSY spectrum of RBC membrane phospholipids extracted by the Folch method and solubilized in CD_3OD:$CDCl_3$ solution to which and small amount of EDTA aqueous solution is added. This eliminates ionic species from the organic phase and improves lipid solubility (see Materials and Methods section for more details).

After the determination of lipid proportions by ^{31}P solution NMR, the FA proportions were determined by GCMS after lipid hydrolysis. The complete and unambiguous quantification of the phospholipid profile of native horse RBCs, ghosts and ^{2}H-labeled ghosts is summarized in Fig. 3.5 and shows that the membrane phospholipidic profile is in good agreement with the literature[206], and that it was unaltered during the preparation of ghosts and the incorporation of deuterated FAs. As determined by GCMS and shown in Fig. 3.5, the incorporation of PA-d_{31} was highly successful since it represents about 25% of the total FA chains in the ghost membrane. Consequently, a change in membrane fluidity is expected since the labeled ghosts contain about 65% of saturated FAs, as compared to 50% in native RBCs. The incorporation of PA-d_{31} together with protonated unsaturated FAs such as oleic acid (C18:1) could help reestablish a more natural saturated/unsaturated FA ratio, as done with bacteria[57,207]. However, considering the low ^{2}H NMR S/N ratio obtained with ^{2}H-labeled ghosts, the addition of protonated FAs would reduce the sensitivity of the ^{2}H SS-NMR experiments, thus prohibiting this approach. The lower S/N ratio obtained with ^{2}H-labeled ghosts, as compared to ^{2}H-labeled bacteria[57,139], can be explained by the impossibility to prepare ghost samples with sufficient concentration through centrifugation even

at 100,000 g. Moreover, exogenous PA-d_{31} is used by bacteria for the phospholipid synthesis, thus increasing the membrane labeling. Nevertheless, the NMR and GC-MS results show that ghosts can be labeled and enable membrane-peptide interaction studies by SS-NMR.

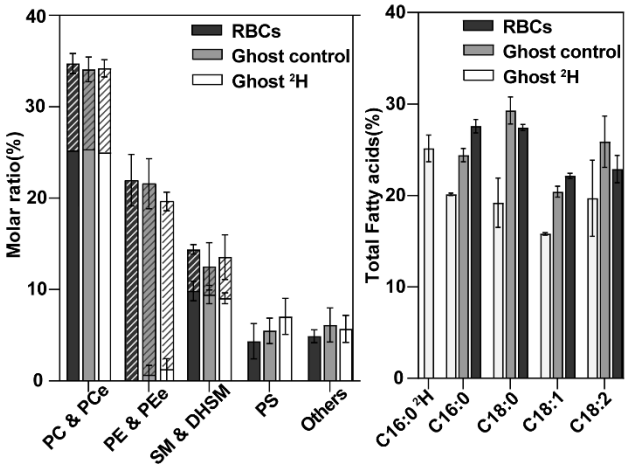

Figure 3.5: Phospholipid headgroup (left panel) and fatty acyl chain profile (right panel) of horse red blood cells, ghosts and deuterated ghosts obtained from ^{31}P NMR and GCMS analyses, respectively. Crosshatched areas correspond to ether linked or DHSM lipids. Complete data are reported in Tables S3.1 and S3.2.

3.4.3 Effect of antimicrobial peptides on erythrocyte membranes

3.4.3.1 Leakage experiments

The perturbation of phospholipid bilayers by AMPs can occur through various processes[184], most notably *via* a carpet-like mechanism or pore formation[22]. At different stages of these processes, membrane disruption is such that, in the case of RBCs, it can lead to hemoglobin leakage, which can readily be monitored. The lytic activity of caerin 1.1 and aurein 1.2 on actual RBCs and model membranes has previously been determined[61,112,208-210]. Nevertheless, we measured the lytic activity of these peptides on RBCs reporting both peptide and lipid concentrations, thus enabling the calculation of L/P molar ratios at which lysis occurs. This additional information allows direct comparison with our leakage assays on RBC ghosts and erythrocyte models with a membrane composition (POPC/SM/Chol) closer to RBCs than previously reported.

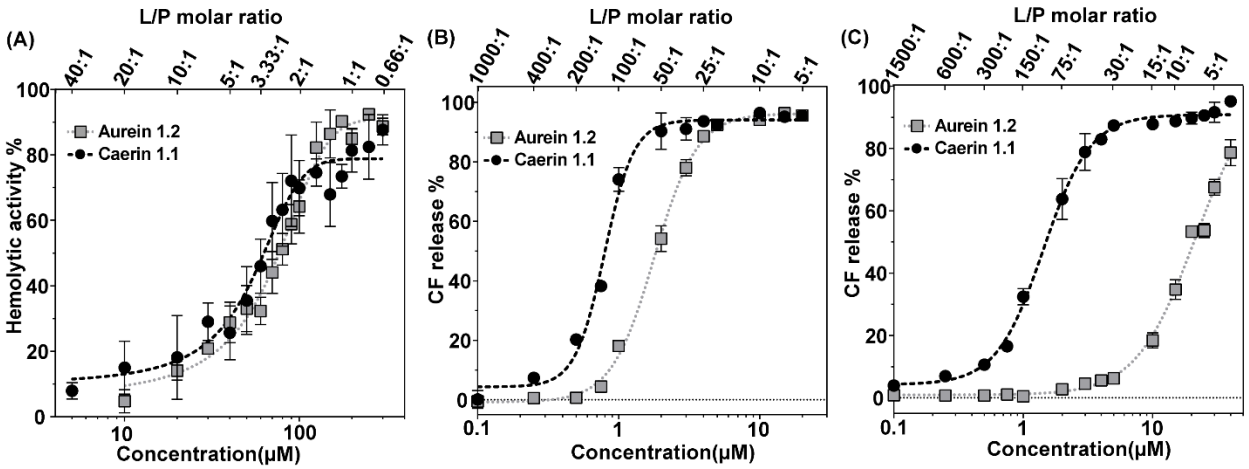

Figure 3.6: Lytic activity of antimicrobial peptides on erythrocytes and model membranes as determined by **(A)** hemoglobin leakage of RBCs with a phospholipid concentration of 200 μM, **(B)** carboxyfluorescein leakage of POPC/SM/Chol LUVs with a lipid concentration of 100 μM and **(C)** carboxyfluorescein leakage of POPE/POPG with a lipid concentration of 150 μM. Results are presented as the mean of triplicate assays. Dashed and dotted lines correspond to the best fit to a sigmoidal curve. Note that in order to compare the relative effects of the AMPs on whole cells and lipid model membranes, molar L/P ratios are indicated. Details of the experimental estimation of RBC lipid concentration are presented in the supplementary information. For comparison with other works, data presented as a function of L/P weight ratios are also reported in the supplementary information (Fig. S3.3).

As shown in Fig. 3.6A, although caerin 1.1 seems to have a higher lytic potency on RBCs than aurein 1.2 (with a higher hemolytic activity and a plateau at a higher L/P molar ratio), differences are much smaller than in model membranes (Fig. 3.6B and 3.6C) and fall within the experimental uncertainty. The threshold concentrations and L/P molar ratios at which membrane perturbation occurs are reported in Table 3.1. Characteristic literature values are also indicated in order to compare our results with those of previously published antimicrobial assays. By examining the results in Table 3.1, it appears that caerin systematically shows a higher permeabilization potency than aurein in all membrane systems. Indeed, our results show that caerin has lower minimum inhibitory concentrations (MIC) on both *E. coli* and *B. subtilis*, and higher LR50s on model membranes and, to a lesser extent, RBCs. It is noteworthy that lysis of 50% of the RBCs occurs at L/P molar ratios that are one to two orders of magnitude lower than in the model eukaryotic (POPC/SM/Chol) or bacterial (POPE/POPG) membranes. This result indicates that RBCs are significantly more resistant than model membranes to AMP-induced lysis, and highlights the importance of assessing AMP activities on intact cells.

Table 3.1: Comparison of effect of the antimicrobial peptides on red blood cells (RBCs), model RBCs and bacteria membranes, as well as different bacteria. The leakage assays were performed on intact RBCs. The minimum hemolytic concentrations causing 10% leakage of RBCs (MHC) and the lipid-to-peptide molar ratio at which 50 % leakage occurs (LR50) are obtained by fitting of the leakage assays shown in Fig. 3.6A.

AMPs	RBCs	POPC/SM/ Chol	POPE/POPG	RBCs	*E. coli*		*B. subtilis*	
	LR50[a]	LR50[a]	LR50[a]	MHC[b] (μM)	MIC[c] (μM)	TI[d]	MIC[c] (μM)	TI[d]
Aurein 1.2	2.6:1 (0.2)	54.3:1 (2.4)	7.2:1 (0.1)	15.8 (2.7)	68	0.23 (0.04)	20	0.79 (0.13)
Caerin 1.1	3.2:1 (0.2)	124.7:1 (2.0)	100.3:1 (10.2)	12.1 (3.6)	39	0.31 (0.09)	12	1.00 (0.30)

[a]*LR50: L/P molar ratio at which 50% of RBCs or membranes are lysed.*
[b]*MHC: minimum hemolytic concentration causing 10% hemolysis of RBCs.*
[c]*MIC: minimum inhibitory concentration*[57]
[d]*TI: therapeutic index, i.e., MHC/MIC.*

Working with actual RBCs enables us to elucidate the action mechanism of AMPs on these eukaryotic membranes, but also to address the question of their selectivity towards bacterial membranes. Indeed, a striking difference is observed for aurein, for which 8 times more peptide is required to achieve a 50% lysis of the bacterial model membranes as compared to model RBC membranes, despite the negative charge of the former. On the other hand, caerin shows a strikingly lower selectivity with 50% lysis of both model membranes at roughly the same L/P ratios (126:1 and 105:1). One might thus expect aurein to show a higher toxicity than caerin for RBCs. However, the LR50s of both peptides on RBCs are very similar (2.6:1 (0.2) and 3.2:1 (0.2) for aurein and caerin, respectively) and no significant differences in the concentrations at which the peptides lyse 10% of RBCs are observed.

To quantify the selectivity of both AMPs towards bacteria, and therefore their potential toxicity, the therapeutic index (TI) was calculated. This index is defined as the ratio between the MHC and the MIC, which we obtained in our previous work on bacteria[57]. A large TI value indicates a higher selectivity towards a given bacterium. Table 3.1 shows that the calculated TI values for aurein 1.2 and caerin 1.1 are low, thus revealing a poor selectivity of both peptides towards bacteria, a tendency already observed previously[110,208]. Both peptides seem to be more selective to the

Gram(+) *B. subtilis* with TI values three times the ones obtained for *E. coli*, although differences between the two peptides might be obscured by the poor accuracy on MHC values. Further chemical modifications would be required to enhance the selectivity of these AMPs towards bacteria to reduce their cytotoxicity. It should be noted, however, that it is for the moment difficult to compare TI values between different studies since they are determined with various assays and different blood-resident cells[185].

3.4.3.2 Solid-state NMR experiments

To investigate the interaction of AMPs with erythrocyte membranes, the perturbation of the phospholipid headgroups and deuterated hydrophobic core of RBC ghosts were respectively studied by static ^{31}P and magic-angle spinning ^{2}H SS-NMR (Fig. 3.7). Note that the ^{31}P SS-NMR experiments shown in Fig. 3.7 were carried out on non-deuterated ghosts to approach native conditions and keep the samples as fresh as possible; however, experiments performed with deuterated ghosts did not reveal significant differences (Table S3.3 and Fig. S3.4).

As seen in Fig. 3.7, a narrow peak appears on the ^{31}P NMR spectrum at *ca.* 0 ppm when the proportion of aurein 1.2 is increased. This type of central peak has been discussed by Yang *et al.*[211] and can either result from phospholipids in rapidly-reorienting small objects such as micelles, or from phospholipids in high-curvature membrane regions such as buds, cubic phases or toroidal pores. Those cases differ by their relaxation times and linewidths, the narrowest lines being assigned to micelles, and the broader ones to high-curvature regions.

In the case of aurein, the breadth of this central peak (*ca.* 1000 Hz) gradually decreases to a value of 200 Hz, consistent with the formation of micelles that end up being released from the membrane, leading to the sharp peak at a 1.7:1 L/P molar ratio. Interestingly, the CSA value of the remaining lamellar phase is unchanged up to an L/P ratio of 3:1 (Table S3.4). Simultaneously, the PA dynamics in the hydrophobic core increases, as revealed by the decrease in the spinning sideband (SSB) intensities on the ^{2}H SS-NMR spectra, and the concomitant decrease in M_2 values (see Fig. 3.7A and Fig. 3.8B). We note that we had reported an increase in M_2 in the early stages of the interaction of aurein with *B. subtilis* membranes[57]. Thus differences between the first stages of aurein association with Gram(+) bacteria and ghosts cannot be excluded.

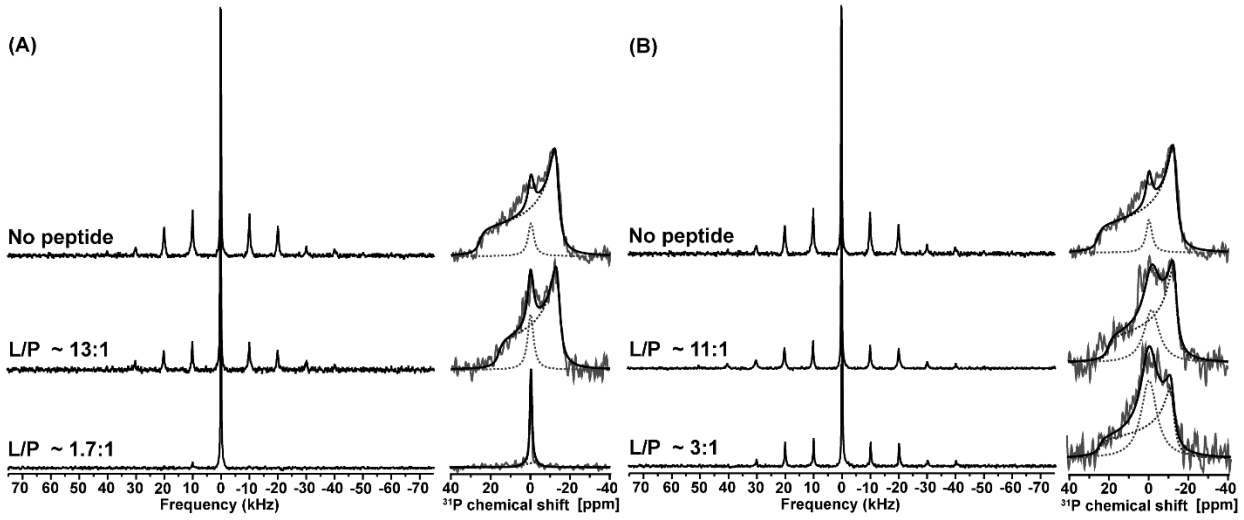

Figure 3.7: ^{2}H MAS (10 kHz) SS-NMR spectra (left) and ^{31}P static SS-NMR spectra (right) of ghosts, acquired at 293 K, with different concentrations of **(A)** aurein 1.2 and **(B)** caerin 1.1. The corresponding lipid-to-peptide molar ratios (L/P) are indicated. ^{31}P static and ^{2}H MAS SS-NMR spectra were respectively obtained with unlabeled and deuterated ghosts. For ^{31}P SS-NMR spectra, dotted lines represent spectral fitting of both the broad anisotropic component and the central peak (numerical values are in Tables S3.3 and S3.4).

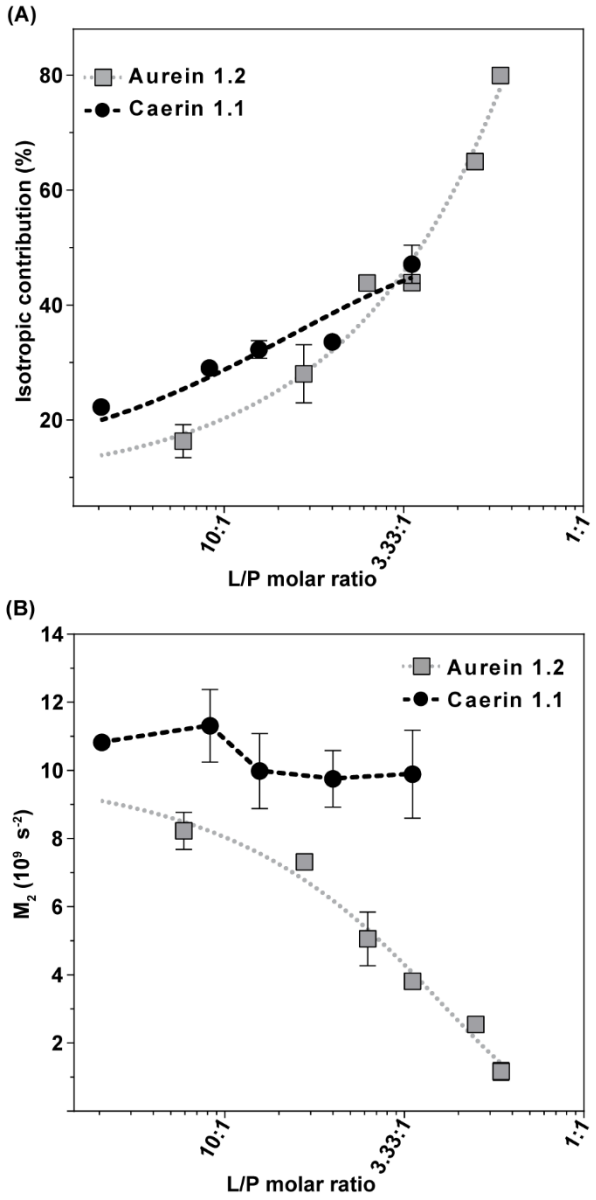

Figure 3.8: Effect of aurein 1.2 and caerin 1.1 on erythrocyte ghosts as a function of the lipid-to-peptide (L/P) molar ratio, at 293 K. **(A)** Isotropic contribution to the ^{31}P SS-NMR spectra of unlabeled ghosts. **(B)** Second spectral moment (M_2) of deuterated ghosts determined from ^{2}H MAS SS-NMR spectra. Phospholipid concentrations range from 4 mM to 9 mM. Dashed and dotted lines correspond to the best fit to a sigmoidal curve or a simple guide to the eye when fitting was not possible (caerin 1.1 panel B).

The behavior of caerin is significantly different compared to aurein. As the peptide concentration increases, an isotropic peak intensifies on the ^{31}P spectra, and remains broad (full width at half height of 1000-1500 Hz) at all concentrations (Fig. 3.7B and 3.8B), compatible with phospholipids in high-curvature membrane regions. Interestingly, and in contrast with the effect

of aurein, the PA dynamics with caerin concentration evolves in two stages, as revealed by ^{2}H SS-NMR (Fig. 3.8, Table S3.4). In a first stage, the dynamics slightly diminishes, as seen by the increase in M_2 from 9.9 with no caerin (not shown on logarithmic scale) to 11.3×10^9 s^{-2} when caerin concentration is increased up to an L/P molar ratio of 6:1. When the peptide concentration is further raised, lipid dynamics increase to return to the initial M_2 value, and remain constant up to the maximum L/P ratio studied (3:1). We should point out that this behavior is different from the one we observed in *B. subtilis* bacterial membranes[57] and could indicate subtle differences in the pore formation molecular mechanism between the two cell types.

3.4.3.3 Microscopy experiments

Confocal microscopy results further support our SS-NMR findings. With both Fast-DiI and NBD-PA labeling, both the labeled and unlabeled ghosts appear to be destroyed by aurein 1.2 at a L/P molar ratio of 1.7:1 (Fig. 3.9 center column and Fig. S3.5). Aurein 1.2, with its relatively short 13 amino-acid sequence, has been shown to perturb both bacterial and mammalian model membranes through a carpet-like mechanism[61]. Both our SS-NMR and fluorescence microscopy results support a similar action towards RBC ghosts.

A contrario, caerin 1.1, with its 25 amino-acid sequence that can span the membrane, triggers hemolysis at lower concentrations than aurein (Fig. 3.6). The fluorescence confocal microscopy images in Fig. 3.9 recorded using FAST DiI entrapped in ghosts show intact membranes in the presence of caerin at concentrations where hemoglobin was shown to leak from the cells (Fig. 3.6). Interestingly, the NBD-PA labeled ghosts (Fig. 3.9 and Fig. S3.6) show intense spots on the membrane where the dye appears to concentrate. Since the hemolysis assays were carried out with RBCs while SS-NMR measurements were performed with labeled ghosts, we thus imaged the calcein influx on ghosts by fluorescence microscopy. The results (shown in Fig. S3.7) not only prove that the influx in the ghosts membrane is possible but also that the membrane can be crossed by molecules as large as calcein.

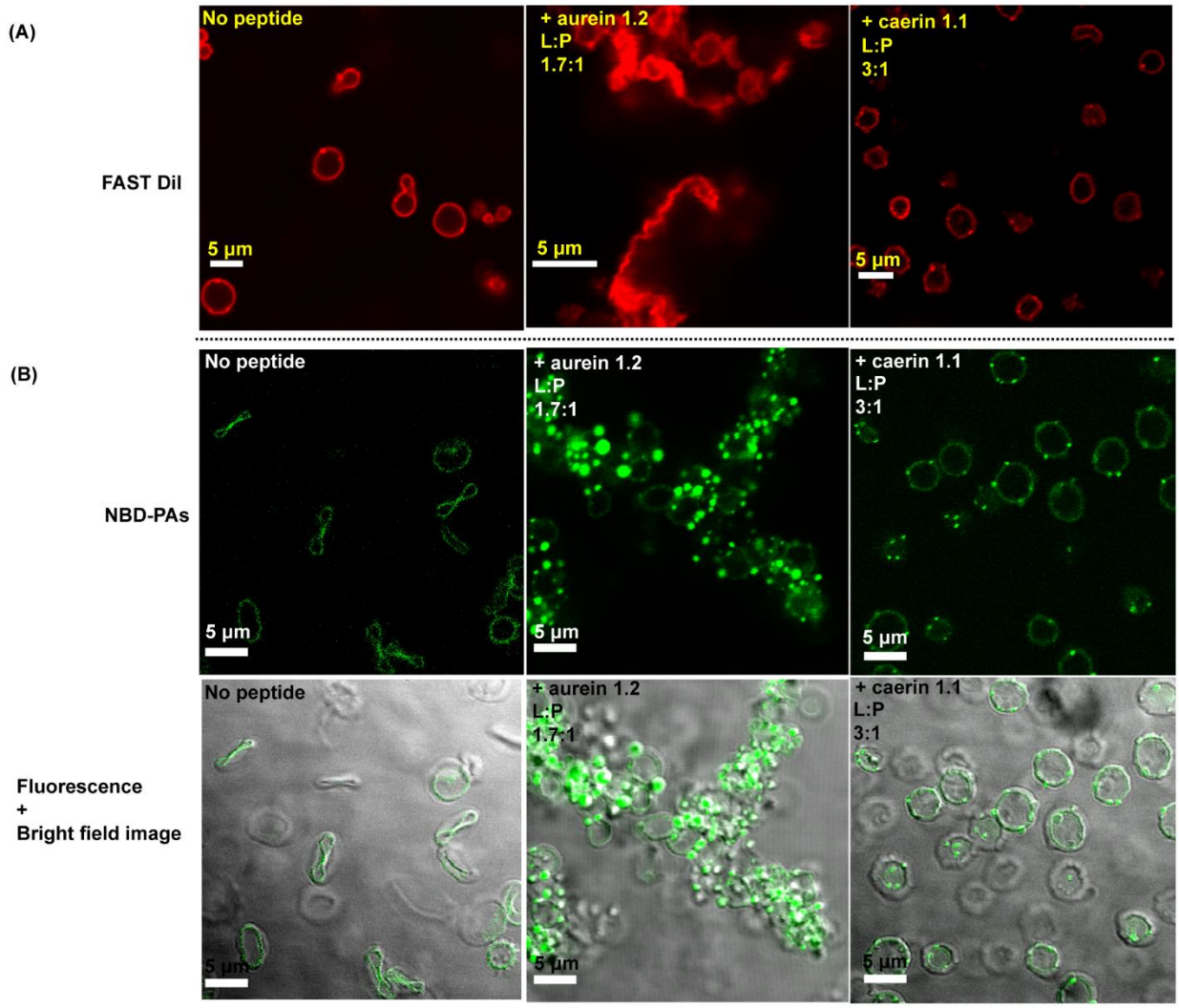

Figure 3.9: Confocal fluorescence microscopy images of **(A)** FAST DiI entrapped in the unlabeled ghosts with addition of AMPs and **(B)** NBD-PAs entrapped in the deuterated ghosts with addition of AMPs. The corresponding lipid-to-peptide molar ratios (L/P) are indicated.

3.5 Discussion

These results, analyzed together with those of the hemolysis assay, can be interpreted in terms of membrane perturbation mechanisms. The fact that aurein 1.2 exerts its hemolytic action at later stages than caerin 1.1, that the lipid dynamics in the hydrophobic region increases when the peptide concentration increases, and that small rapidly-reorienting objects are formed, all indicate a carpet-like mechanism, as schematized in Fig. 3.10A. This mechanism is also supported by the more diffuse appearance of fluorescence labeled ghosts as seen by confocal fluorescence microscopy (Fig. 3.9).

In the case of caerin 1.1, the leakage results, ^{31}P SS-NMR spectra and confocal microscopy images are compatible with a pore-forming mechanism (represented in Fig. 3.10B), where the broad isotropic contribution would result from high-curvature regions in the membrane such as those expected in a toroidal pore[212]. It is also tempting to assign the bright NBD-PA fluorescence spots to pore locations although an unambiguous explanation for the concentration of the fluorescent tag in the pores remains elusive. Nonetheless, other mechanisms have been described that cannot be ruled out[183,184]. In particular, dynamic models in which the membrane only transiently becomes permeable could be considered. A full proof of pore formation can only be obtained by more detailed spectroscopical measurements which are currently under way.

It should be noted that ^{2}H SS-NMR spectra monitor the acyl chain order profile of the PA-d_{31} molecules inserted into the ghost membrane, and not of the endogenous phospholipids' chains, although this "reporter" molecule is very likely to reflect the overall state of the membrane. As a result of the presence of PC, SM and cholesterol in ghost membranes, liquid-ordered (L_o) and liquid disordered (L_d) domains can coexist, a delicate phase equilibrium that can potentially be perturbed by the addition of PA-d_{31}[213]. The preferential interaction of an AMP with membrane domains of lower thickness or at domain boundaries has recently been predicted and reported[124,214]. A preferential interaction of caerin with the L_d domain could expel the PA into the L_o phase or at the interface, resulting in a stiffening of the rest of the membrane. This would explain the different dynamical behavior of PA-d_{31} upon caerin addition as compared to aurein. It is noteworthy that the effects of AMPs observed by SS-NMR on labeled ghost membranes occur at L/P molar ratios similar to those observed in the hemolytic assays on intact RBCs. We thus consider that despite the changes in the FA chain profile due to labeling (an unavoidable drawback required to perform experiments on whole cells rather than model membranes), the mechanisms of action that we have elucidated are closely related to those taking place in intact RBCs.

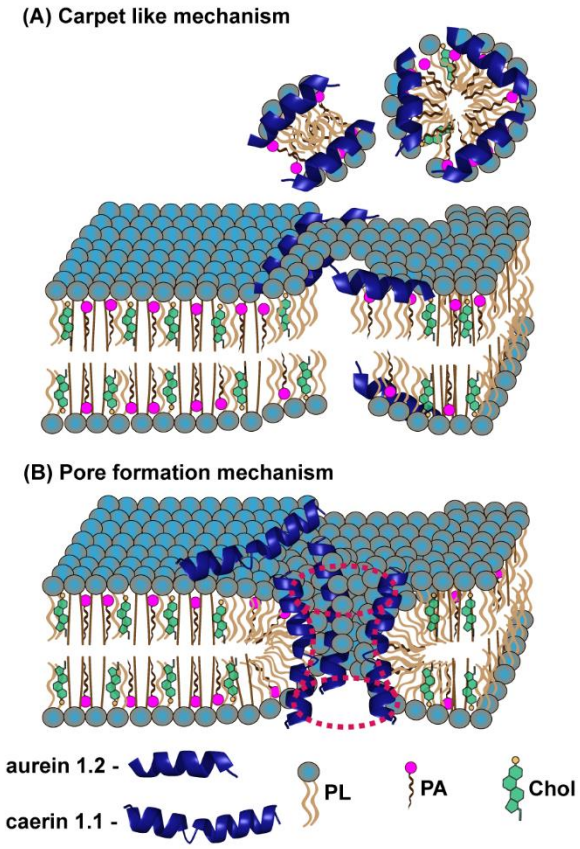

Figure 3.10: Cartoon representation of AMPs' potential action mechanisms on ghost membranes incorporating deuterated palmitic acid. (**A)** Carpet mechanism with aurein binding on the surface and then disrupting the membrane by micellization. (**B)** Pore formation by caerin after binding on the surface.

Altogether, our results indicate that aurein 1.2 and caerin 1.1 would interact with erythrocyte membranes via similar mechanisms that take place with bacterial membranes, and that their relative potency is maintained[110]. Both peptides have been shown to at least partially adopt an α-helical structure when interacting with membranes[112]. These α-helices are amphipathic with all charged and polar residues found along one side of the helix, and amino acids with non-polar side chains on the opposite side (Fig. S3.8)[215]. The interaction with the membrane results from electrostatic and hydrophobic interactions, as well as from the respective shapes of lipids and peptides[184,185]. The fact that the AMPs maintain similar action mechanisms on RBC and bacteria membranes despite differences in surface charge seems to indicate that hydrophobic interactions play an important role in dictating this mechanism. Electrostatic interactions are likely to play a greater role in the "capture" of the AMPs, thus explaining their higher potency towards bacteria.

3.6 Conclusions and perspectives

In this study, we have taken a new approach in understanding the action mechanism of AMPs on erythrocyte membranes. Preparing ghosts by removing the contents of erythrocytes preserves the cell surface and membrane composition whilst ensuring minimal interference with ^{31}P and ^{2}H SS-NMR analysis. The successful non-biochemical labeling of erythrocyte ghost membranes with deuterated FAs opens the possibility for other types of lipid labeling, such as with ^{13}C-labeled FAs for example.

Using hemolysis assays, ^{31}P static and ^{2}H MAS SS-NMR, we have confirmed the poor therapeutic quality of both aurein 1.2 and caerin 1.1 in their current version[110,208]. While both antimicrobial peptides lyse bacteria at low concentrations, they present poor selectivity between Gram(+) and Gram(-) bacteria, and we showed that their hemolytic potency is too high for a safe use in the clinics. We have also shown that higher concentrations of these peptides are required to perturb intact RBCs as compared to model membranes. This may be explained by the fact that RBC membranes have not only lipids but also glycocalyx on their surface, which is rich in carbohydrates, and many transmembrane proteins embedded. Although our experimental protocols are established in order to compare similar L/P ratios in erythrocytes, ghosts and model membranes, we want to stress that in some medical cases, the ratio of bacteria to red blood cells, or other mammalian cells, may be such that a small concentration of AMPs may be enough to kill all bacteria while leaving most mammalian cells alive.

Despite these concentration considerations, AMPs' mechanisms of interaction on RBCs are shown to be similar to those adopted in bacteria. Such a similarity may be specific to the peptides studied here, as many factors need to be taken into account when comparing peptide-membrane interactions with different cell membrane types. Comparison between erythrocytes and bacteria highlights the importance of hydrophobic effects in determining the mode of peptide interaction with membranes. A detailed understanding of the interaction of AMPs with mammalian cells constitutes an essential step for their use as therapeutics in the clinics, and for their improvement before reaching the market. It should be noted that the methodology described here does not rely on cell metabolism and can, at least in principle, be transposed to other eukaryotic cells, or those of other organisms.

3.7 Author contributions

Conceptualization, A.A.A., D.E.W., and I.M.; methodology, data collection, and initial analysis, K.K. and M.S.; additional analysis, A.A.A.,D.E.W., and I.M.; original draft preparation, K.K. and A.A.A.; review and editing, S.B., A.A.A., M.S., D.E.W., and I.M.; supervision and fundingacquisition, D.E.W., S.B., and I.M. All authors have read and agreed to the published version of the manuscript.

3.8 Acknowledgments

This research was funded by the Natural Sciences and Engineering Research Council (NSERC) of Canada (grant RGPIN-2018–06200 to I.M.) and the Centre National de la Recherche Scientifique (UMR 7203 to D.E.W.). K.K. would like to thank the Quebec Network for Research on Protein Function, Engineering, and Applications (PROTEO) - strategic cluster of the Fonds de recherche du Québec – Nature et technologies (FRQNT) - for the award of a scholarship. M.S. is grateful to the NSERC for the award of a scholarship.

3.9 Supplementary information

Lipid concentration

To determine the final lipid concentration in the NMR or leakage assay samples, and therefore determine lipid-to-peptide (L/P) ratios, the amount of lipids as a function of starting RBCs or ghosts volume needs to be determined. This was carried out using ^{31}P NMR and the well-resolved PC peak at -0.81 ppm present in all samples.

In brief, the integral of the PC ^{31}P NMR peak as a function of RBC (or ghost) sample volume was plotted, as seen in Fig. S3.1A. Since RBCs (or ghosts) are composed of 33 % PC, the final total lipid concentration in the sample is obtained by multiplying the determined concentration by three.

The corresponding integrals were related to PC concentrations using a calibration curve determined with solutions of DOPC at various known concentrations (Fig. S3.1B). The obtained lipid concentration can be converted into lipid weight, by using an average molecular weight:

$$w_n = \sum_i^n w_i x_i$$

Where w_i is the molecular weight of each lipid molecule and x_i is the molar fraction of each lipid (headgroups determined by ^{31}P NMR and acyl chain lengths determined by GCMS). In the case of ghosts, the average molecular weight is 735 g/mol. The conversion of Fig. S3.1A from concentration to weight is shown in Fig. S3.1C.

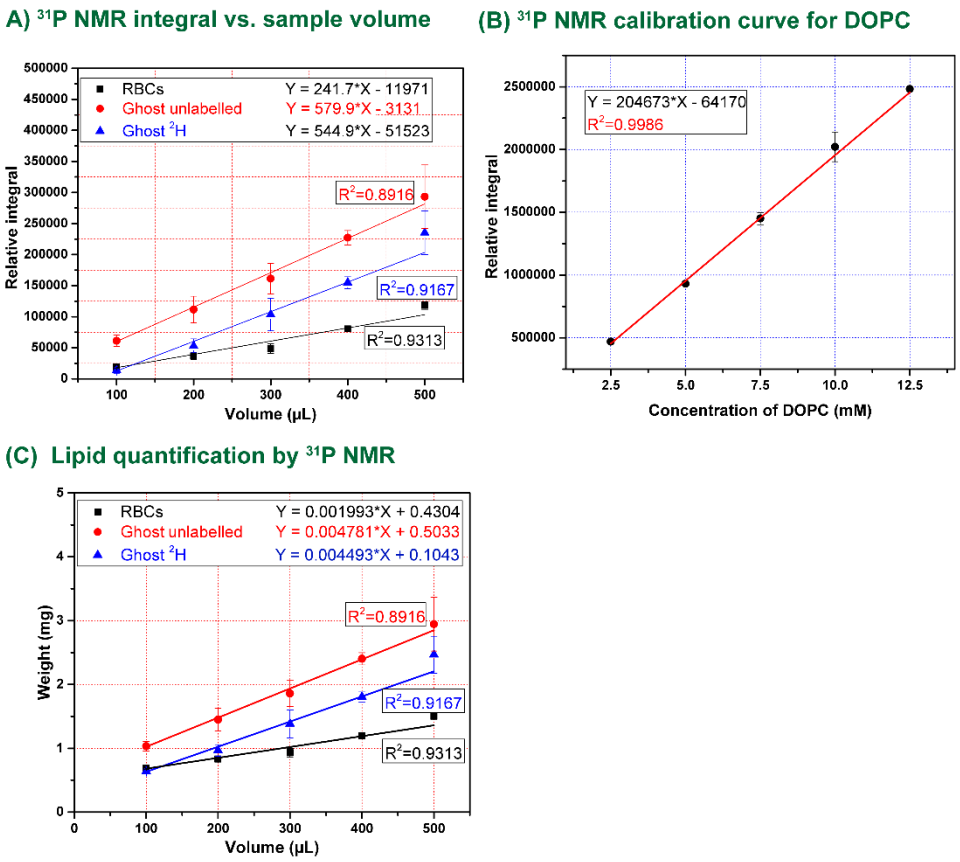

Figure S3.1: (A) Integral of the PC ^{31}P NMR peak as a function of RBC (or ghost) sample volume. **(B)** Integral of the PC ^{31}P NMR peak as a function of DOPC concentration. **(C)** RBC (or ghost) lipid weight as a function of sample volume.

Lipid profile and chemical shifts

We have identified and quantified the phospholipids (PLs) in RBCs, unlabeled ghosts and deuterated ghosts samples after performing lipid extraction, ^{31}P 1D, ^{1}H 1D and ^{31}P-^{1}H 2D solution NMR experiments, as well as GCMS on hydrolyzed fatty acids (FAs). Figure S3.2 contains the overlay of ^{1}H and ^{31}P NMR spectra.

All chemical shifts have been determined from the 2D spectra, except for the γ protons of PC and SM, determined from ^{1}H 1D spectra, and the γ protons of PCe and DHSM, which have been interpolated.

Numerical results, including ^{1}H and ^{31}P chemical shifts, lipid classes and FA abundances, are presented in Tables S3.1 and S3.2, as the mean of triplicate measurements.

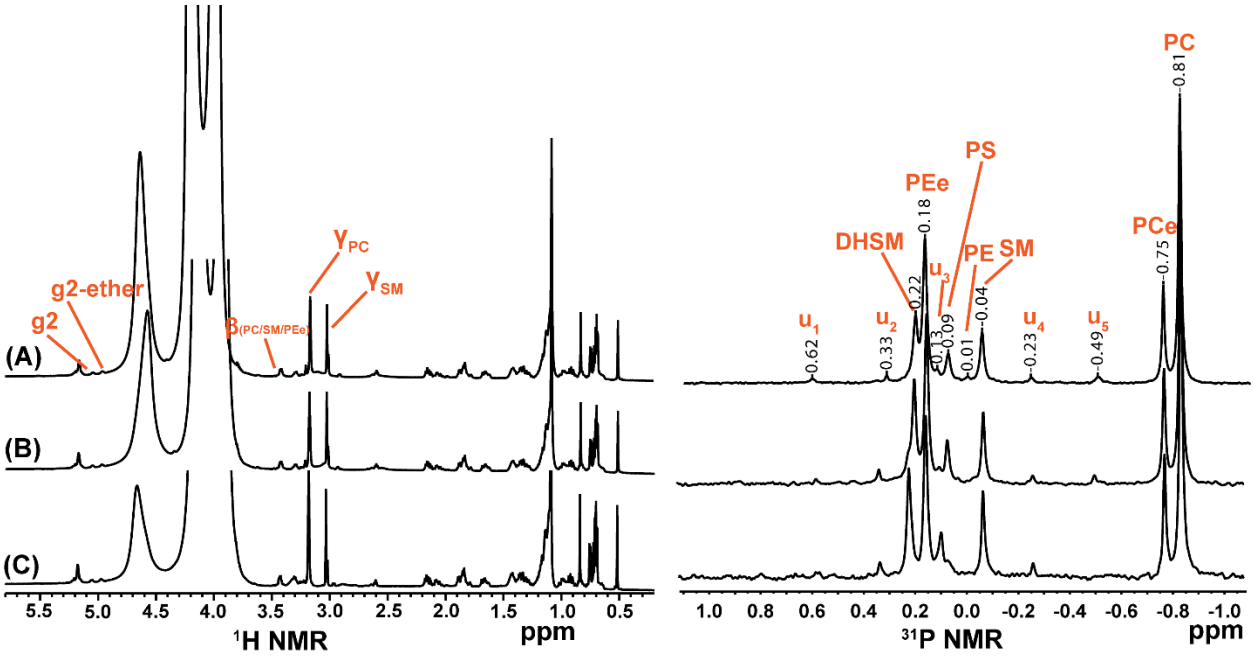

Figure S3.2: ^{1}H- and ^{31}P-NMR spectra of (A) unlabeled ghost PLs, (B) deuterated ghosts PLs and (C) RBCs membrane PLs. All spectra were acquired at 298 K, and "u" indicates unassigned peaks.

Table S3.1: Distribution (%) of phospholipids in horse RBC membranes as determined by ^{1}H- and ^{31}P solution NMR, with ^{31}P and ^{1}H chemical shifts. Standard deviations are indicated.

PLs	Chemical shift (ppm)		Abundance (%)		
	^{31}P	^{1}H	RBCs	Unlabeled ghosts	^{2}H ghosts
PC	-0.81	α: 4.08 β: 3.43 γ: 3.18 g1: 3.98, 4.23 g2: 5.05 g3: 3.80	34.8 (1.1)	34.1 (1.3)	34.2 (0.9)
PCe	-0.75	α: 4.07 β: 3.42 γ: ~3.2 g1, g3: 3.79 g2: 4.97	9.6 (2.1)	8.8 (0.7)	9.3 (0.9)
PE	0.01	-	-	1.9 (0.6)	1.3 (1.2)
PEe	0.18	α: 2.93 β: 3.43 g1: 3.83 g2: 4.97 g3: 3.78	22.0 (2.8)	21.6 (2.7)	19.7 (1.0)
PS	0.09	α: 4.08 β: 3.80 g1: 4.23 g2: 5.04 g3: 3.97	4.4 (1.9)	5.5 (1.4)	7.1 (2.0)
SM	-0.04	α: 4.08 β: 3.42 γ: 3.03 -CHNH-: 3.95 -$POCH_2$-: 3.73	9.9 (1.1)	9.5 (1.0)	9.1 (0.6)
DHSM	0.22	α: 4.07 β: 3.44 γ: ~3.0 -CHNH-: 3.96 -$POCH_2$-: 3.78	14.4 (0.5)	12.6 (2.6)	13.6 (2.4)
Others	-		4.9 (0.7)	6.1 (1.9)	5.7 (1.5)

Table S3.2: Distribution (%) of total fatty acids in horse RBCs membranes as determined by GCMS. Standard deviations are indicated.

FAs	Abundance (%)		
	RBCs	Unlabeled ghosts	^{2}H ghosts
C16:0 ^{2}H	-	-	25.2 (1.5)
C16:0	27.6 (0.7)	24.4 (0.7)	20.1 (0.1)
C18:0	27.4 (0.5)	29.3 (1.5)	19.2 (2.7)
C18:1	22.1 (0.3)	20.4 (0.6)	15.8 (0.1)
C18:2	22.9 (1.5)	25.9 (2.8)	19.7 (4.2)

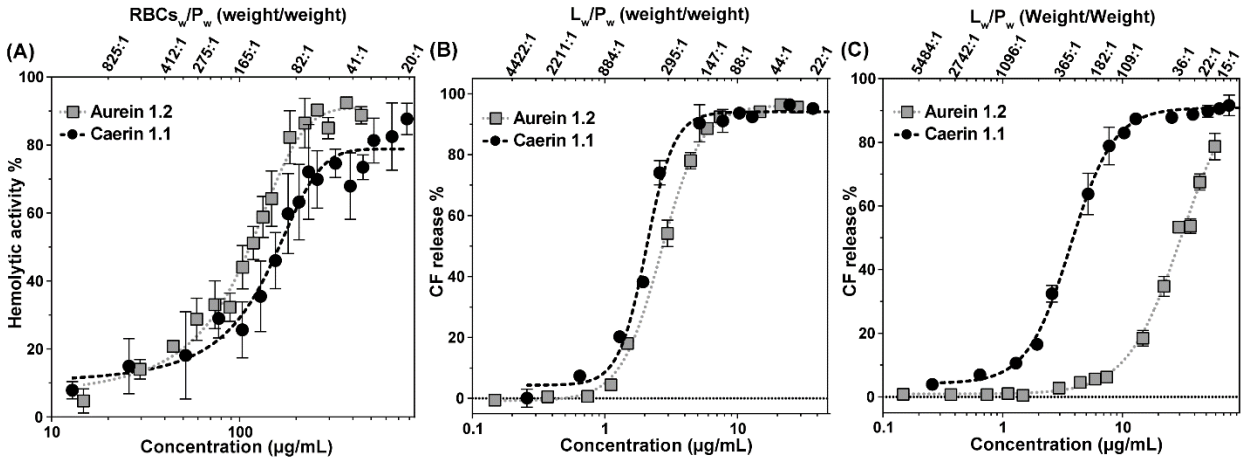

Figure S3.3: Lytic activity of antimicrobial peptides on erythrocytes and model membranes as determined by **(A)** hemoglobin leakage of RBCs with a phospholipid concentration of 200 µM, **(B)** carboxyfluorescein leakage of POPC/SM/Chol LUVs with a lipid concentration of 100 µM and **(C)** carboxyfluorescein leakage of POPE/POPG with a lipid concentration of 150 µM. Results are presented as the mean of triplicate assays. Dashed and dotted lines correspond to the best fit to a sigmoidal curve. All data are reported as a function of RBC or lipid-to-peptide weights. Data as a function of lipid-to-peptide molar ratios are shown in Figure 3.6 of the article.

Additional ^{31}P NMR spectra:

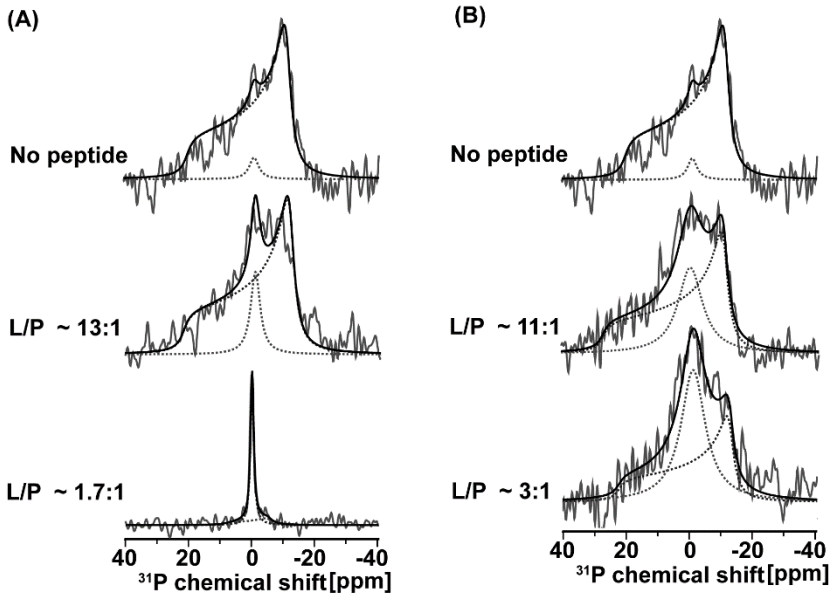

Figure S3.4: ^{31}P static SS-NMR spectra of deuterated ghosts, acquired at 293 K with the addition of different concentrations of **(A)** aurein 1.2 and **(B)** caerin 1.1. The corresponding lipid-to-peptide molar ratios (L/P) are indicated. Dotted lines represent spectral fitting of the anisotropic components and the isotropic peak.

Table S3.3: ^{31}P NMR isotropic contribution (%) for unlabeled and deuterated ghosts with different concentrations of peptides. Standard deviations are indicated.

Aurein 1.2				Caerin 1.1			
Unlabeled ghosts		Deuterated ghosts		Unlabeled ghosts		Deuterated ghosts	
L/P	Isotropic contribution (%)	L/P	Isotropic contribution (%)	L/P	Isotropic contribution (%)	L/P	Isotropic contribution (%)
-	8.3 (2.1)	-	4.1 (0.3)	-	8.3 (2.1)	-	4.1 (0.3)
13:1	16.3 (2.9)	13:1	18.9 (7.8)	22:1	22.3 (0.1)	-	-
6:1	28.0 (5.0)	6:1	28.8 (2.5)	11:1	29.0 (1.0)	11:1	34.2 (1.5)
4:1	43.8 (0.1)	-	-	8:1	32.3 (1.5)	-	-
3:1	43.9 (1.2)	-	-	5:1	33.6 (0.2)	-	-
2:1	65.0 (0.3)	-	-	3:1	47.1 (3.3)	3:1	58.4 (7.8)
1.7:1	79.9 (0.1)	1.7:1	78.2 (3.5)				

Table S3.4: Effect of the antimicrobial peptides on the second spectral moment, M_2, from the ^2H SS-NMR MAS spectra, as well as ^{31}P CSA with standard deviation, as a function of the lipid-to-peptide molar ratio (L/P). ^{31}P and ^2H SS-NMR data were obtained with unlabeled and deuterated ghosts, respectively.

Aurein 1.2			Caerin 1.1		
L/P	M_2 (10^9 s^{-2})	CSA (ppm)	L/P	M_2 (10^9 s^{-2})	CSA (ppm)
-	9.9 (0.5)	26.1 (0.2)	-	9.9 (0.5)	26.1 (0.2)
13:1	8.2 (0.5)	23.2 (4.7)	22:1	10.8 (0.2)	25.2 (0.9)
6:1	7.3 (0.1)	26.2 (2.2)	11:1	11.3 (1.1)	23.9 (2.5)
4:1	5.1 (0.8)	25.9 (2.4)	8:1	10.0 (1.1)	24.5 (0.5)
3:1	3.8 (0.0)	25.9 (1.6)	5:1	9.8 (0.8)	23.7 (0.1)
2:1	2.5 (0.1)	24.5 (0.7)	3:1	9.9 (1.3)	22.1 (2.1)
1.7:1	1.2 (0.3)	7.4 (3.6)			

Additional confocal fluorescence microscopy images:

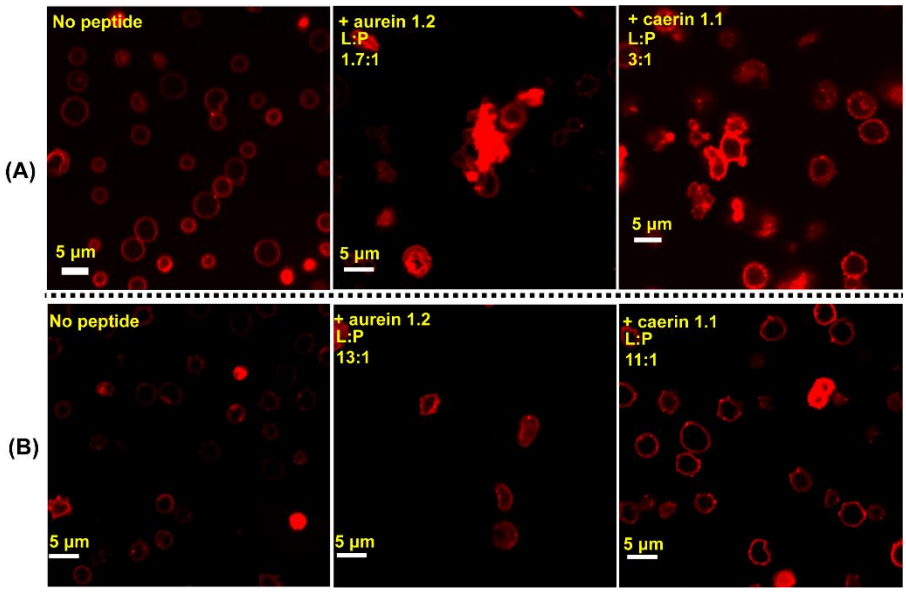

Figure S3.5: Confocal image of the fluorescence of Fast DiI entrapped in **(A)** deuterated ghosts and **(B)** unlabeled ghosts with different concentrations of aurein 1.2 and caerin 1.1.

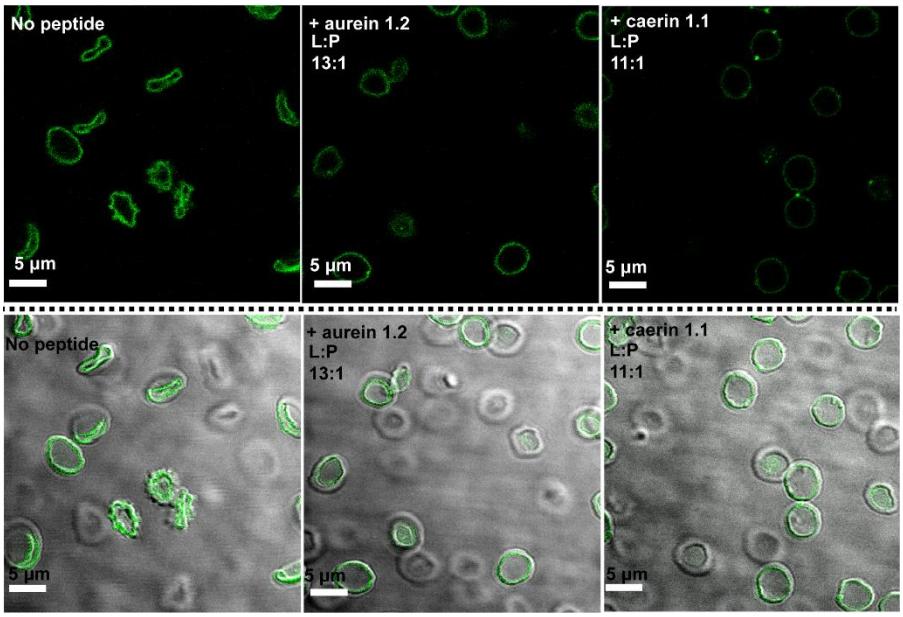

Figure S3.6: Confocal image of the fluorescence of NBD-PAs entrapped in deuterated ghosts with different concentrations of aurein 1.2 and caerin 1.1.

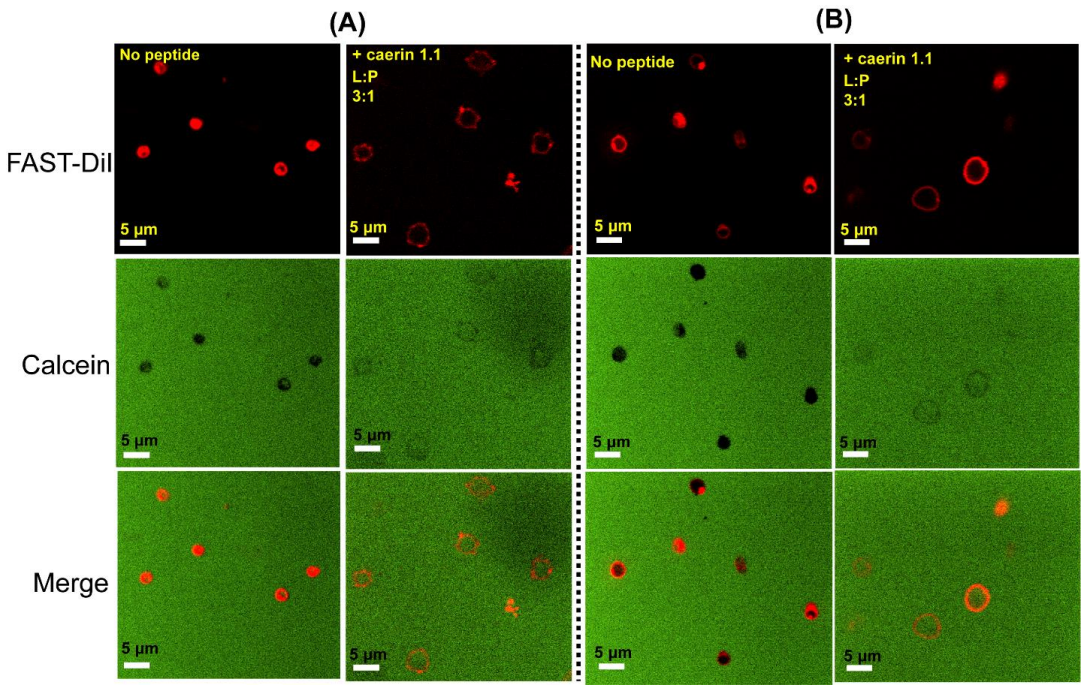

Figure S3.7: Confocal fluorescence microscopy image of FAST DiI entrapped in the ghost membrane pool and calcein leakage experiments of **(A)** unlabeled ghosts and **(B)** deuterated ghosts with addition of AMPs

Helical wheel representations of AMPs

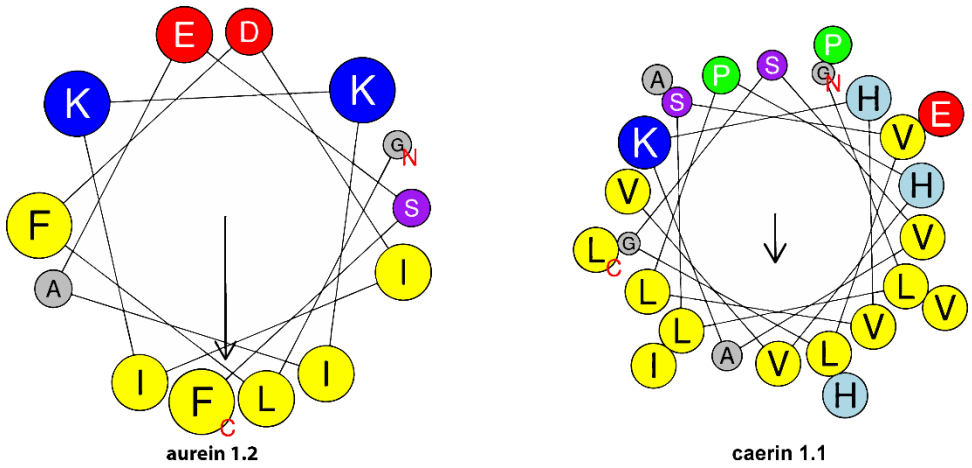

Figure S3.8: Helical wheel representations of aurein 1.2 (left) and caerin 1.1 (right), showing their amphiphilicity (https://heliquest.ipmc.cnrs.fr).

CHAPTER IV

^{19}F solid-state NMR approaches to probe antimicrobial peptide interactions with membranes in whole cells

Kiran Kumar[1], Alexandre A. Arnold[1], Raphaël Gauthier[2], Marius Mamone[2], Jean-François Paquin[2], Dror E. Warschawski[1,3] & Isabelle Marcotte[1]

[1]Departement of Chemistry, Université du Québec à Montréal, P.O. Box 8888, Downtown Station, Montreal, Canada H3C 3P8

[2]PROTEO, CCVC, Département de chimie, Université Laval, 1045 Avenue de la Médecine, Québec, Québec, G1V 0A6, Canada

[3]Laboratoire des Biomolécules, LBM, CNRS UMR 7203, Sorbonne Université, École normale supérieure, PSL University, 75005 Paris, France

Published in *Biochimica et Biophysica Acta (BBA)-Biomembranes (2024): 184269*
DOI: 10.1016/j.bbamem.2023.184269

N.B. References cited in this chapter are presented at the end of the thesis

4.1 Abstract

Cationic antimicrobial peptides (AMPs) are considered potential therapeutic candidates due to their broad-spectrum and membrane-lytic activity. Since preferential interactions with bacteria are important, it is also crucial to investigate and understand their effects on eukaryotic cells. In this study, we utilized ^{19}F solid-state nuclear magnetic resonance (SS-NMR) as a new approach to examine the interaction of AMPs with erythrocyte membranes. To do so, we employed red blood cell ghosts devoid of hemoglobin and developed a protocol to label their lipid membranes with monofluorinated palmitic acid (PA) at carbon positions 4, 8, or 14 along the acyl chain. This strategy allowed us to probe different locations in the bilayer. The incorporation of fluorinated PAs into the membranes and the preservation of ghost integrity were confirmed through SS-NMR and fluorescence confocal microscopy. After an initial evaluation on a model membrane, we demonstrated, using caerin 1.1, that both static and magic-angle spinning ^{19}F SS-NMR experiments enable the investigation of AMPs' interactions with whole cell membranes. Notably, changes in chemical shift anisotropy, second spectral moments, and relaxation times proved highly sensitive to the effects of AMPs. Our findings suggest the formation of high-curvature regions, indicative of pore formation by caerin 1.1, akin to its antimicrobial mechanisms. In summary, the straightforward incorporation of monofluorinated FAs and rapid NMR signal acquisition offer promising avenues for the study of whole cells using ^{19}F SS-NMR.

4.2 Introduction

Antimicrobial resistance by disease-causing bacteria has become a global health threat with ensuing socioeconomic issues[1,10]. In recent decades, bacterial resistance has increased at an alarming rate, sustained by an extensive usage of antibiotics. There is thus an urgent need for alternative solutions to combat bacterial resistance and in this context, antimicrobial peptides (AMPs) and their mimics stand as promising antibiotic molecules. Indeed, their action mechanisms involving bacterial membrane disruption, damage to intracellular biomolecules and other oxidative damages[22], are nonspecific and thus hard to evolve against. More than 24,000 AMP sequences have been identified so far, both from natural and synthetic origins[25] and only a small number AMPs or their mimics have reached clinical trials[55] or are already commercialized as antimicrobial agents (e.g. bacitracin, gramicidin D, polymyxin B)[55]. *In vivo* stability and low toxicity towards human cells are key factors to access the pharmaceutical market.

Since many AMPs target the bacterial lipid membrane, considerable efforts have been put into characterizing their interaction with cell membranes[184,216]. Solid-state NMR (SS-NMR) has proved to be a unique tool to study such interactions at a nanoscopic level. Different NMR-active nuclei such as ^{1}H, ^{2}H, ^{13}C, and ^{31}P are used to study the biophysical properties of lipid membranes in the presence of AMPs[66,113,217]. Deuterium is mostly used to characterize lipid chain order and molecular events happening in the core of the bilayer environment, while phosphorus allows probing the lipid headgroups or assessing the overall topology of the lipid organization[218,219]. After some initial work on whole cells in the late 70s and early 80s, the field has heavily relied on model membranes until the early 2010s when our group and others reintroduced the use of whole-cell ^{2}H labeling[133,139,220]. Our laboratory has also developed the use of magic-angle spinning (MAS) combined to ^{2}H SS-NMR to reduce the experimental time and ensure that cells remain intact[156].

^{19}F is an NMR-active nucleus with interesting properties, notably high sensitivity with low background in biological systems, strong dipolar couplings and a large chemical shift range. This sparked interest in its use to study native membranes already in the late seventies and early eighties, with papers showing that the incorporation of fluorinated fatty acid (FA) probes in native membranes was feasible[221,222]. Wild-type and auxotroph *Escherichia coli* strains were successfully labeled[223,224] as well as *Acholeplasma laidlawii* membranes[221], with FAs fluorinated at different positions, and with only weak perturbations to the membrane[221,223]. McDonough *et al.*[222] also showed that monofluorinated palmitic acids (H-C-F) had a less perturbing effect than difluorinated

analogues (F-C-F), and also reported that a single fluorine atom in the bilayer was likely to have a less perturbing effect compared to bulkier electron spin or fluorescent probes. In all these studies, it was shown that an order profile along the acyl chains - similar to the one obtained by ^{2}H SS-NMR - could be determined using ^{19}F SS-NMR. However, except for one application from the group of Auger[152,225], the use of ^{19}F SS-NMR has not been extensively developed to study AMP interactions *from a membrane point of view*. Indeed, the high sensitivity and almost complete absence of this nucleus in nature has stemmed a significant body of work on fluorinated peptides[153,226-228], but not on fluorinated membranes.

Early work on ^{19}F-labeled membranes either by a fluorinated fatty acid or phospholipid focused on static (no magic-angle spinning, MAS) samples and without ^{1}H decoupling[221-224,229]. The order profile in the acyl chains was, however, shown to be accessible and described by order parameters obtained through spectral fitting and normalizing by a rigid linewidth. More recently, ^{19}F-labeled phospholipids synthesis was achieved and labeled lipids were incorporated into model membranes[152,230-233]. ^{19}F positions spanning the whole acyl chain length and showed by ^{19}F SS-NMR that the ^{19}F chemical shift anisotropy (CSA) decreased monotonically from the headgroup to the end of the acyl chain, thus informing on motion throughout the membrane. They also reported the strong ^{19}F isotropic chemical shift variation along the acyl chain. Protons were decoupled, but MAS was not used in this study.

^{19}F NMR thus appears as an excellent candidate to investigate membrane-AMP interactions in intact cells. In this work, we reintroduce the use of monofluorinated FAs (MFFAs) to label intact red blood cell (RBC) membranes and establish a ^{19}F SS-NMR approach to study AMP-membrane interactions. More specifically, we incorporated into erythrocyte ghosts MFFAs labeled at positions 4, 8 and 14 on the acyl chains (**Fig. 4.1A**). Ghosts are erythrocytes from which hemoglobin has been removed, thus reducing potential interference of the paramagnetic heme group with NMR signals. After an initial assessment on a model membrane, we show how both in-cell static and MAS ^{19}F SS-NMR can be exploited to study the pore formation mechanism of AMPs using caerin 1.1 - a natural AMPs isolated from the skin secretions of Australian tree frogs as a model.

4.3 Materials and methods

4.3.1 Materials

Caerin 1.1 was purchased from GenScript Corporation (Piscataway, NJ, USA) with >98 % purity. Protonated and deuterated dipalmitoylphosphatidylcholine (DPPC and DPPC-d_{62}) were obtained from Avanti Polar Lipids (Alabaster, AL, USA). Ethylenediaminetetraacetic free acid (EDTA) was bought from Fisher Scientific (Fair Lawn, NJ, USA), while unlabeled palmitic acid, deuterium-depleted water, Triton X-100, fatty acid methyl ester mix C4-C24 (FAME mix), [16-[(7-nitro-2-1,3-benzoxadiazol-4-yl)amino] palmitic acid (NBD-PA), 1,1'-dilinoleyl-3,3,3',3'-tetramethylindocarbocyanine 4-chlorobenzenesulfonate (Fast DiI) and all other solvents and chemicals were purchased from Sigma Aldrich (Oakville, ON, Canada). Fresh horse RBCs packed 100% were purchased from Cedarlane Laboratories (Burlington, ON, Canada). Deionized 18.2 MΩ.cm Milli-Q water was used in all experiments (Millipore-Sigma, Oakville, ON, Canada). Fluorine-labeled fatty acids were synthesized following a protocol detailed in the Appendix B.

4.3.2 Multilamellar vesicles (MLVs) preparation

MLVs were prepared using dry film method as described by Warschawski *et al.*[83]. The lipid mixture (including ^{19}F-labeled PAs) was dissolved in 1:2 methanol/$CHCl_3$ solution and dried under nitrogen stream. Remaining traces of organic solvent in the lipid film were removed by high vacuum for at least 2 h. The lipid film was then hydrated with a physiologically-relevant solution of 150 mM NaCl (pH 7.0) prepared with ^{2}H-depleted water. The lipid dispersion was vortexed and freeze-thawed 3 to 5 times (10 min at −20 °C, followed by 10 min above 40-55 °C) and transferred directly into a 4-mm rotor.

4.3.3 Preparation of ^{19}F-labeled erythrocyte ghosts

Erythrocyte ghosts were prepared as described by Kumar *et al.*[40]. Briefly, 3-4 mL of concentrated horse RBCs were suspended in a 40 mL round bottom centrifugation tube with 25 mL isotonic HEPES buffer (20 mM HEPES, 150 mM NaCl, pH 7.4), and centrifuged at 500 g for 5 min at 4 °C. Then three supplementary washes were done with the same buffer until the supernatant became clear. After the final wash, the pellet was resuspended in 20 mL hypotonic HEPES buffer (20 mM HEPES, pH 7.4) and centrifuged at 25,000 g for 40 min at 4 °C (rotor JA-20, Beckman). The supernatant was then removed, and the pellet transferred into new centrifuge

tubes, leaving behind the “red button” that contains proteases. Additional washes (3 to 4) with the same buffer were carried out to obtain a hemoglobin-free white ghosts pellet.

A mixed micelles solution of 0.5 mM Triton X-100 / 0.25 mM of ^{19}F-labeled PA in isotonic buffer was prepared in a sealed glass vial with three freeze (-20 °C)/thaw (95 °C)/vortex shaking cycles. The white ghost pellet was then resuspended in 320 mL isotonic buffer to which 80 mL of the mixed micelles solution were transferred, and incubated for 15 min at 37°C. The mixture of ghosts and micellized ^{19}F-labeled PA was then centrifuged at 25,000 g for 20 min at 4 °C in different 20 mL aliquots. The excess detergent was washed away twice by centrifugation in isotonic buffer at 25,000 g for 20 min at 4 °C. The ghost pellets were pooled together in a 1.5 mL Eppendorf tube and centrifuged at 20,000 g for 20 min at 4 °C. The pellet was then washed with an isotonic buffer and centrifuged at 100,000 g and 4 °C for 20 min. This concentrated pellet was collected and stored at 4°C prior to the experiments and used within 3-4 days.

4.3.4 Sample preparation for confocal microscopy

A total of 1 % (v/v) of ^{19}F-labeled ghosts were labeled with the fluorophore Fast-DiI (1/1000) using a 1 h incubation at 37 °C, followed by pelleting at 16,000 g for 15 min, or with NBD-PA directly incorporated into ghosts along with ^{19}F-labeled PA as described above in section (2.3). The pellet was resuspended in 500 µL of HEPES buffer then transferred to Sarstedt 8-well microscopy slides (300 µL) and left to stand for 30 min to allow ghosts immobilization. Samples were incubated for 1 h at 37 °C after addition of an appropriate amount of caerin 1.1 into 1 % (v/v) ghosts, and single frame per second images were generated using a Nikon confocal microscope with a 60x oil-immersion lens. Images were processed using ImageJ software.

4.3.5 Fatty acid profile and labeling efficiency

FA analyses were carried out using gas chromatography coupled to mass spectrometry (GCMS) as described by Laydevant et al.[69] following lipid extraction and transesterification. Briefly, lipids were extracted (triplicates) using the Folch protocol[139], then transesterified using 2 mL of H_2SO_4 (2% in methanol) and 0.8 mL of toluene for 10 min at 100 °C. A polar HP-5MS column (30 m length × 250 µm diameter × 0.25 µm film thickness) was used with an injection volume of 1 µL, and the oven temperature was programmed to heat at 140 °C for 5 min followed by a 4 °C /min ramp up to 300 °C, prior to electron ionization and detection with a Agilent quadrupole MS. Data acquisition and processing were done with the Chemstation software.

4.3.6 Solid-state NMR and spectral analysis

All SS-NMR spectra were recorded using a Bruker Avance III-HD wide-bore 400 MHz spectrometer (Milton, ON, Canada) equipped with a double tuned 4mm-HFX probe and a ^{1}H-^{19}F filter. Static ^{19}F and ^{31}P SS-NMR spectra were obtained using a phase-cycled Hahn echo pulse sequence, with an inter pulse delay of 35 μs and high-power (50 kHz) ^{1}H decoupling during acquisition. The 90° pulse length was 4 μs for ^{19}F SS-NMR and 3 μs for ^{31}P SS-NMR. Data were collected using 2048 points for ^{19}F SS-NMR and 1024 points for ^{31}P SS-NMR. The recycle delay was 2 s for ^{19}F SS-NMR and 3 s for ^{31}P SS-NMR. A total of 12 k scans per ^{19}F spectra for ghosts and 1 k scans for MLVs were collected, amounting to 7 hours of acquisition for ghosts and 35 mins for MLVs. And a total of 14 k scans per ^{31}P spectra for ghosts and 1 k scans for MLVs were collected, amounting to 12 hours of acquisition for ghosts and 50 mins for MLVs. The ^{31}P chemical shifts were referenced to the phosphoric acid (H_3PO_4) signal at 0 ppm, while the ^{19}F chemical shifts were referenced to the trifluoroacetic acid (TFA) signal at -76.5 ppm.

^{2}H and ^{19}F SS-NMR experiments were also carried out at 10 kHz MAS frequency. A phase-cycled Hahn echo sequence was used for both MAS ^{2}H SS-NMR experiments with MLVs samples and MAS ^{19}F SS-NMR analysis of ghosts. ^{2}H SS-NMR spectra were recorded with 100 k data points, a 4 μs 90° pulse length, rotor-synchronized interpulse delay of 96 μs and recycle time of 500 ms. A total of 1024 scans per spectra were collected, amounting to 8 min acquisition time. ^{19}F ssMAS spectra were collected with 3 k data points, a 4 μs 90° pulse length, rotor-synchronized interpulse delay of 94 μs and recycle time of 2 s. In model membrane sample a total of 512 scans per spectra were collected, amounting to 18 minutes of acquisition time with a recycle time of 2 s and in ghost sample a total of 6k scans per spectra were collected, amounting to 3.5 hours of acquisition time with a recycle time of 2 s.

^{31}P and ^{19}F CSA values were determined by line fitting using the Bruker Topspin 4.0.6 software with Sola (Solid Lineshape Analysis) program and values from minimum two replicates are reported. Since the CSA is proportional to the order parameter, a bond order parameter S_{CF} was calculated using equation (1)[223]. The ^{19}F CSA measured on pure and dry fluorinated PAs at -30 °C was taken as the rigid CSA (≈ 18 ppm):

$$S_{CF}=\frac{Observed\ ^{19}F\ CSA}{Rigid\ ^{19}F\ CSA} \qquad (4.1)$$

^{2}H spectral moment analysis was performed using MestRenova software V6.0 (Mestrelab Research, Santiago de Compostela, Spain). Second spectral moments, M_2, were calculated using equation (4.2)[32,103] and values from minimum two replicates are reported.

$$M_2 = \omega_r^2 \frac{\Sigma_{N=0}^{\infty} N^2 A_N}{\sum_{N=0}^{\infty} A_N} = \frac{9\Pi^2 \chi_Q^2}{20} \langle S_{CD}^2 \rangle \quad (4.2)$$

where ω_r is the angular spinning frequency, N is the side band number, and A_N is the area of each sideband obtained by spectral integration, S^2_{CD} is the mean square order parameter, and χ_Q is the static quadrupolar coupling constant equal to 168 kHz for a C-D bond in acyl chains. The M_2 value provides a quantitative description of the membrane lipid ordering and is particularly sensitive to the gel-to-fluid phase transition.

4.4 Results

4.4.1 Fluorinated FAs as reporters of membrane structure and order

FAs are molecular probes that can be readily incorporated into biological membranes to study their biophysical properties in native cellular conditions[40]. The incorporation of exogenous FAs into living cells is often easier than other labeling strategies exploiting the cell's biochemistry[144,234]. Moreover, free FAs are natural constituents of cell membranes where they are involved in various cellular processes and play a role in regulating cellular functions and membrane fluidity[235]. However, incorporating high concentrations of FAs can change the bilayer phase behavior - an effect that has been addressed in previous works[236-239]. For example, the gel (L_β)-to-fluid (L_α) phase transition temperature (T_m) of a lipid membrane is increased by the presence of FAs, and a coexistence of gel and fluid phases can occur at certain phospholipid/FA ratios[238]. Nevertheless, FAs remain accurate reporters of variations in the lipid order in a membrane system[238]. Therefore, before incorporating MFFAs in whole cells' membranes, we characterized their effect on the membrane fluidity and as a function of the fluorine atom position on the acyl chain.

We used model dipalmitoylphosphatidylcholine (DPPC) membranes to assess the effect of palmitic acid (PA) fluorinated at positions 4, 8 or 14, referred to as PA-F(4), PA-F(8) and PA-F(14) (**Fig. 4.1A**). The addition of perdeuterated DPPC (DPPC-d_{62}) allowed monitoring the membrane order profile by measuring the variation of the second spectral moment (M_2) calculated

from ^{2}H SS-NMR spectra as a function of temperature, as described elsewhere[148,156]. Examples of such spectra, can be found in **Fig. S4.1**.

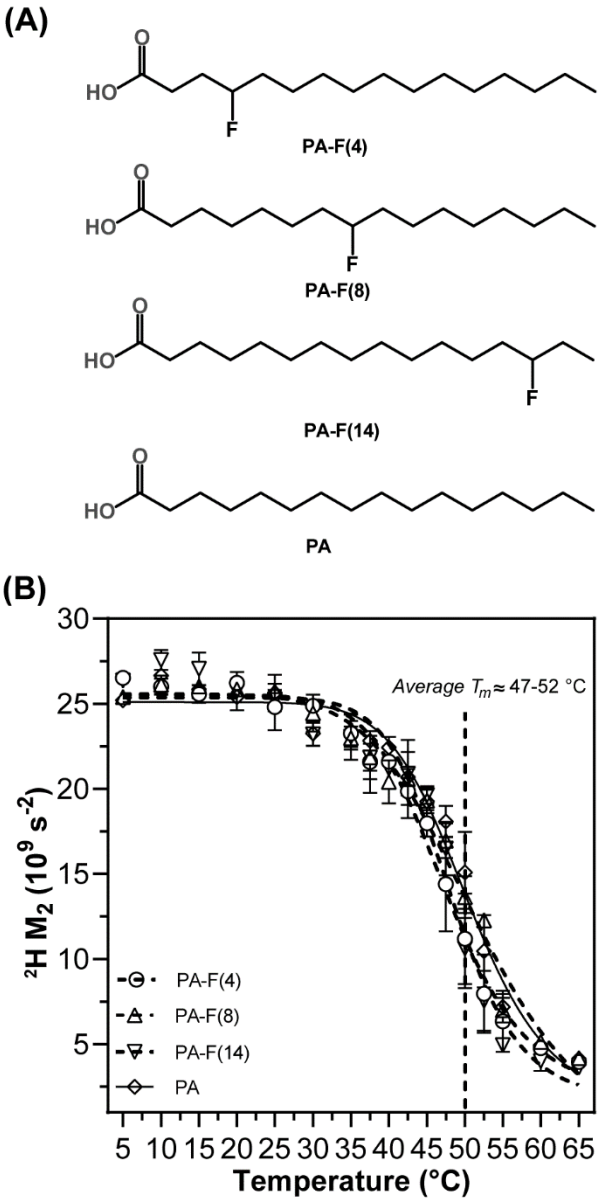

Figure 4.1: Effect of fluorination on DPPC-d_{62}/PA model membranes. **(A)** PAs were fluorinated at different positions along the acyl chain. **(B)** Second spectral moment (M_2) as a function of temperature. M_2 values were obtained from the ^{2}H SS-NMR MAS spectra (Fig. S4.1) of DPPC/DPPC-d_{62}/PA and fluorinated PA analogues at a molar ratio of 1:1:1. M_2 reports on acyl chain order and values are indicated with standard deviations.

As shown in **Fig. 4.1B**, the order profile as well as T_m of DPPC varies very little when comparing fluorinated and non-fluorinated samples. The average T_m determined by ^{2}H SS-NMR is centered at ≈ 47-52 °C. Our results are consistent with previous studies of the phase behavior of

PA-containing DPPC bilayers[236,239]. In their investigation of the pseudo-binary phase diagram of DPPC/PA mixtures, Inoue *et al.*[239] reported a T_m ~53-54 °C at 2:1 DPPC/PA molar ratio. The melting of the acyl chain can also be monitored using the ^{1}H SS-NMR intensity of the main-chain CH_2 peak, as well as other lipid resonances (**Fig. S4.2**). In this case, T_m is centered at ~53-54 °C (**Fig. S4.3**) - a difference expected between protonated and deuterated phospholipid analogues[240]. Overall, our results show that the insertion of one fluorine atom in the bilayer (positions 4, 8 and 14 on PA acyl chain), has a very weak perturbing effect.

The pioneering work on ^{19}F-labeled biological membranes from the late 70's and early 80's was technically limited to non-spinning samples and ^{19}F detection without ^{1}H decoupling. The single recent work on membranes labeled with monofluorinated phospholipids carried out by Gagnon et al.[152] showed that, with ^{1}H decoupling, the ^{19}F lineshape could be used to assess the local order at a given acyl chain position. They also reported a strong ^{19}F isotropic chemical shift difference along the phospholipid acyl chains - a property that could be exploited to determine the acyl chain order in multiply labeled FAs or lipids using MAS. In their study, similarities are observable between ^{31}P and ^{19}F lineshapes, indicating that ^{19}F could be exploited in a similar fashion to ^{31}P to study the formation of fast tumbling structures that can be induced by membrane-active AMPs[58]. This is notably the case of AMPs that act through a carpet mechanism[40,58].

We verified whether ^{19}F SS-NMR spectra of model membranes labeled with MFFAs could reflect changes in membrane structure and acyl-chain local order. **Fig. 4.2** compares the static ^{31}P and ^{19}F SS-NMR spectra of DPPC membranes incorporating PA-F(4), PA-F(8) or PA-F(14). ^{31}P spectra indicate changes in the phospholipids headgroup dynamics while ^{19}F spectra probe the hydrophobic region of the bilayer. The ^{31}P spectra lineshapes in **Fig. 4.2** are characteristic of lipids in a lamellar phase with axial symmetry, and clearly reveal a gel (L_β)-to-fluid (L_α) phase transition. For such systems, this transition can be quantified by measuring the chemical shift anisotropy (CSA), which value is related to the spectrum width and decreases with increasing molecular dynamics. As seen in **Fig. 4.3A**, characteristic gel phases were detected up to 30 °C with a ^{31}P CSA value of 36 ppm that gradually dropped to 25 ppm at 45 °C, as the first components of the bilayer reach their phase transition temperature. In comparison, we determined CSA of 36-40 ppm in pure DPPC/DPPC-d_{62} membranes (**Fig. S4.4**) at a gel phase (up to 25 °C), which gradually dropped to 29 ppm at the fluid phase (42 °C). The addition of protonated PA shifted T_m to ~45-50 °C, as expected from the DPPC-PA phase diagram[239].

^{19}F SS-NMR lineshapes of the MFFAs show strong similarities with ^{31}P SS-NMR spectra, in particular in the gel phase with powder patterns characteristic of multilamellar vesicles (**Fig. 4.2**). As shown in **Fig. 4.3A**, the change in CSA values through the gel-to-fluid phase transition is analogous to the one observed with ^{31}P SS-NMR. The gel phase is maintained up to 25 °C with ^{19}F CSA values of 14-16.5 ppm, and a noticeable larger CSA of 16.5 ppm when the ^{19}F-label is on the 8th carbon position, indicating a higher degree of order at the center of the lipid monolayer. Although ^{19}F CSA values are smaller than those of ^{31}P, they are very sensitive to changes in membrane fluidity. Indeed, when transitioning from the gel to the fluid phase, ^{19}F CSA values are reduced by 87% on average. Above 25 °C up to about 42 °C, a coexistence of gel and fluid phases is observed in the ^{19}F spectra (**Fig. 4.2 and 4.3**), consistent with the DPPC-PA phase diagram[239]. In the fluid phase, the ^{19}F CSA values range from ~1 (PA-F(14)) to 4 (PA-F(4)) ppm, depending on the fluorine atom position. This result is in agreement with the conformation and order profile along the acyl chains, with position 4 close to the headgroup undergoing less *trans-gauche* isomerisations than the 14th position, closer to the terminal methyl group.

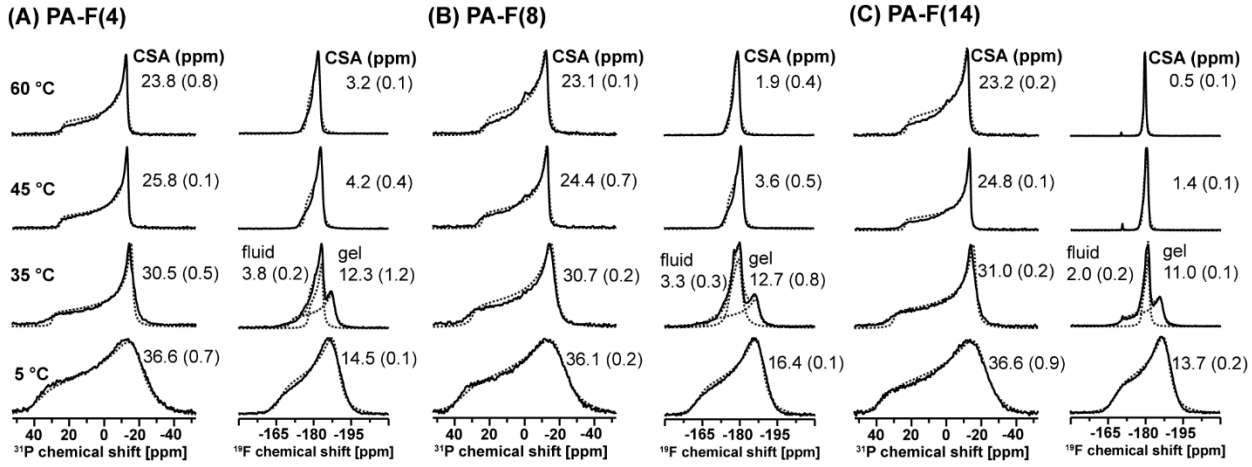

Figure 4.2: Static ^{31}P and ^{19}F SS-NMR spectra of DPPC model membranes incorporating monofluorinated PAs, at a DPPC/DPPC-d_{62}/PA molar ratio of 1:1:1. (A) with PA-F(4), (B) PA-F(8) and (C) PA-F(14). Experiments were performed at different temperatures with ^{1}H decoupling. Fitted spectra are shown as dashed lines. Average CSA values are indicated, with standard deviation.

Positioning ^{19}F atoms at different places along the FA acyl chain enables assessing the local order of the bilayer's hydrophobic region, from the interface to the core[152,223,229]. Providing that FAs undergo fast rotational motion along their long axis, this order can be quantified by introducing an order parameter, which describes the dynamic reorientation of a bond with respect to the main axis. This parameter is obtained by normalizing a given NMR-measured quantity in a mobile segment by its value in the static case. In the case of ^{2}H SS-NMR for example, this is the quadrupolar coupling for a static C-D bond[148].

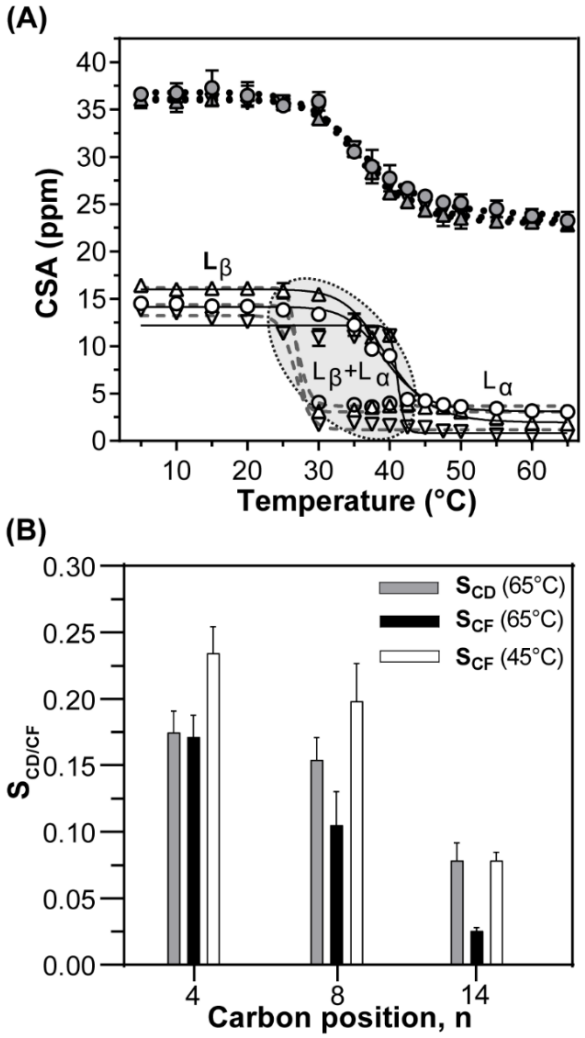

Figure 4.3: (A) Temperature dependence of the static ^{31}P (dotted lines) and ^{19}F (solid & dashed lines) CSA values for DPPC membranes with MFPA at a molar ratio of 1:1, calculated from Fig. 4.2. Symbols are (○): PA-F(4), (△): PA-F(8) and (▽): PA-F(14) with filled symbols corresponding to ^{31}P NMR and empty ones to ^{19}F NMR. Note the presence of two components detected by ^{19}F NMR in the coexistence region. **(B)** ^{2}H (S_{CD}) and ^{19}F (S_{CF}) order parameter profile of the acyl

chain in ^{19}F-labeled DPPC membranes as a function of the fluorine atom position, at 45 and 65 °C, with standard deviation.

In early ^{19}F SS-NMR studies, spectra were recorded without ^{1}H decoupling; the CSA and dipolar couplings interactions could therefore not be isolated, and were estimated by computer-assisted line fitting[223,229]. Here, we introduced a C-F bond order parameter, S_{CF}, defined as the ratio between the experimentally-measured CSA and its value for an immobile C-F bond (Equation 1). By definition a rigid molecule with an all-*trans* conformation has an order parameter of $S_{CF} = 1$ while this value is 0 in the case of fast isotropic motions. **Fig. 4.3b** shows the S_{CF} bond order parameters for PA-F(4), -F(8) and -F(14) in model membranes. As a means of comparison, the S_{CD} order parameter of DPPC-d_{62} measured in the same sample is also presented (**Fig. S4.5)**. The evolution of the two order parameters adequately reflect dynamic changes with carbon position and temperature, confirming that the S_{CF} of MFFAs can be efficiently employed to measure the order profile along the acyl chains.

In the case of intact cells, measuring the acyl chain order at each carbon position is usually impossible. When perdeuterated lipids are used, the distribution of quadrupolar couplings, which reflects the overall dynamics in the membrane, can be assessed by measuring the second spectral moment, M_2, of the ^{2}H SS-NMR spectra[148]. As we showed in a previous work, M_2 can also be determined under MAS conditions, which enhances the signal-to-noise (S/N) ratio and decreases the acquisition time[156]. **Fig. 4.4** shows ^{19}F SS-NMR spectra obtained in the gel and fluid states under 10 kHz MAS. The resulting increase in S/N ratio with respect to the static spectra is *ca.* ≈ 5-6-fold, corresponding to a reduction in acquisition time by a factor 25-36 for the same S/N ratio. This important gain in sensitivity enables recording spectra without ^{1}H decoupling (**Fig. S4.6**) - an important alternative since not all laboratories are equipped with probes that can detect ^{19}F while decoupling ^{1}H. At an MAS frequency of 10 kHz, the ^{19}F CSA (ranging between 0.3 kHz in the fluid phase and 6.5 kHz in the gel phase) should be entirely averaged out. While spectra are dominated by an isotropic peak (δ_{iso}), 1-2 spinning sidebands (SSBs) are observed even in the ^{1}H-decoupled spectra albeit with lower intensity as compared to non-decoupled spectra. In principle, ^{1}H-^{19}F dipolar couplings should be eliminated by the strong ^{1}H decoupling, and the intermolecular ^{19}F-^{19}F dipole-dipole interactions significantly reduced by MAS. However, it is possible that residual dipolar couplings (^{1}H-^{19}F and/or ^{19}F-^{19}F) remain, or that internal acyl chain motions result in incomplete MAS averaging. In any case, a variation in the SSB intensities is observed with

temperature – a feature that can be exploited to assess the overall membrane dynamics, as will be shown below. Interestingly, the isotropic chemical shift (**Table S4.1**) is sensitive to the ^{19}F position on the FA chain, and also to the membrane lipid phase for positions 8 and 14 (**Fig. 4.4 and Fig. S4.6**). Indeed, two peaks are observed in the gel-fluid coexistence region (between 25 °C and 52 °C) separated by up to 0.8 ppm for these positions. The isotropic resonances are separated by up to 1.1 ppm between the gel (5 °C) and fluid (60 °C) phases (**Fig. 4.4A).** These peaks are easier to distinguish in the ^{1}H-decoupled spectra where they are almost baseline-resolved.

As mentioned, the presence of SSBs allows measuring the ^{19}F spectral moment value (M_2), which reports on the membrane fluidity. **Fig. 4.4B** shows the evolution of M_2 as a function of temperature for both ^{1}H-coupled and decoupled spectra. Spinning sidebands were more intense when no decoupling was applied and the M_2 values varied between 38×10^6 s^{-2} in the gel phase down to 2-3 $\times 10^6$ s^{-2} at 60 °C (fluid phase) for ^{19}F at positions 4 and 8. When the 14^{th} carbon was ^{19}F-labeled (closer to the terminal methyl group) the M_2 value was smaller in the gel phase (25-32 $\times 10^6$ s^{-2}) as compared to PA-F(4) and PA-(F8), but their M_2 values in the fluid phase were all very similar (2-3 $\times 10^6$ s^{-2}). When ^{1}H decoupling was applied, the SSBs' intensity was significantly reduced, as previously mentioned. The M_2 values dropped to 6.8 and 11.7 $\times 10^6$ s^{-2} in the gel phase for positions 8 and 14, respectively. In the fluid phase, the SSBs almost disappeared and the M_2 values were further reduced to 1×10^6 s^{-2}. Overall, our results show that M_2 values vary sufficiently between the gel and fluid phases for both ^{1}H-coupled and decoupled spectra to be used to assess membrane fluidity and detect phase transition temperatures. When feasible, we recommend recording the spectra with and without ^{1}H decoupling. In favorable cases, ^{1}H decoupling might allow determining the gel phase proportion by a simple integration of the isotropic lines since the ^{19}F isotropic chemical shift varies with membrane melting. On the other hand, the second spectral moment variation is larger on spectra without ^{1}H decoupling and membrane fluidity can thus be assessed from the M_2 with a higher precision.

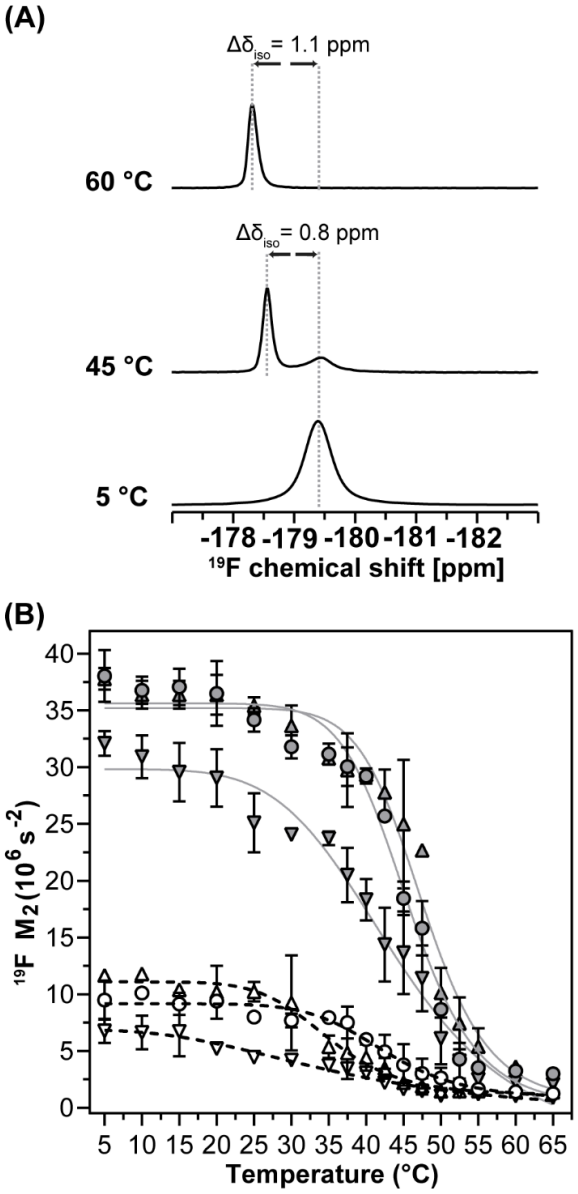

Figure 4.4: (A) MAS (10 kHz) ^{19}F SS-NMR spectra of DPPC/PA-F(8) model membranes, with change in isotropic chemical shift ($\Delta\delta_{iso}$) values as function of temperature. **(B)** Second spectral moment with standard deviation, calculated from the ^{19}F SS-NMR MAS spectra (Fig. S4.6) of DPPC/DPPC-d_{62} with fluorinated PAs analogues in a 1:1:1 molar ratio. Experiments were carried out at different temperatures with (black, dashed line) and without (grey, solid line) ^{1}H decoupling and symbols are (○): PA-F(4), (△): PA-F(8) and (▽): PA-F(14).

Since MAS considerably enhances the signal intensity, we further evaluated the membrane dynamics in a site-resolved fashion by measuring the spin-lattice (T_1) and spin-spin relaxation (T_2) times at each position by ^{19}F SS-NMR (**Table S4.1**). Both T_1 and T_2 values increased as the ^{19}F atom position moved from the headgroup region to the center of the bilayer. The same trend was

observed with increasing temperature (data not shown), confirming that T_1 and T_2 values indeed report changes in dynamics. The concomitant increase in T_1 with dynamics indicate that the correlation times of the motions contributing to longitudinal relaxation are in the nanosecond timescale, i.e. faster than the inverse of the Larmor frequency ($\tau_C < 1/\omega_0 \approx 3$ ns). Motions with this type of correlation times are most likely trans-gauche isomerisations. If such motions are affected by the interaction with AMPs, a corresponding change in T_1 should thus be observed.

4.4.2 Monofluorinated fatty acids to study whole cell membranes

Once the ^{19}F SS-NMR methods were established in model membranes, we assessed their application to study membranes in intact cells. Early work on bacterial membranes established the possibility of labeling intact bacteria with fluorinated FAs[223,229]. Here, we focused on erythrocyte ghosts, which we had successfully labeled with deuterated PA (PA-d_{31}) in a previous study[40]. Using a similar protocol, we achieved the incorporation of MFFAs into ghosts with labeling levels up to 30%, as determined by GC-MS (**Fig. S4.7**). Moreover, fluorescence microscopy images of the ^{19}F-labeled ghosts obtained with lipophilic tracer FAST-DiI and the NBD-PA fluorophore which is structurally similar to PA, show that they retain their original RBC morphology (**Fig. 4.5A**).

Fig. 4.5B shows static ^{19}F SS-NMR spectra of RBC ghosts incorporating MFPAs at 20 ^{o}C, which are all characteristic of lipids in a lamellar phase. ^{31}P SS-NMR spectra are also shown for comparison. As was the case in model membranes, ^{19}F spectra are characteristic of the acyl chain order at each carbon position. Indeed, the ^{19}F CSA value at the 4th position close to PA's headgroup is 7.7 ppm, which is smaller than at the 8th position (10.1 ppm). The small CSA value of 4.5 ppm at position 14 reflects the high mobility in the middle of the bilayer. As established in section 3.1, we used the CSA values to determine the order parameter as a function of the fluorine atom position, and found S_{CF} values of 0.43, 0.56 and 0.27 for positions 4, 8 and 14, respectively. the higher order determined for PA-F(8) is in line with the characteristics expected in a membrane with a high cholesterol content, where the central portion of the acyl chains is known to be more rigid compared to the chain's beginning or end[241].

^{19}F SS-NMR MAS spectra (**Fig. 4.5B)** show that the trend of the isotropic linewidth as a function of the fluorine atom position is similar to that of the CSA values. The more rigid 8th position has the broadest full width at half maximum (FWHM=180 Hz), followed by the 4th

position (158 Hz) then the more mobile 14th position (103 Hz). We further explored the membrane dynamics by monitoring the ^{19}F relaxation times of the MFFAs' isotropic resonance in ghosts (which we will refer to as P_1 peak). As reported in Table 4.1, T_1 values vary with the ^{19}F atom position, similarly to model DPPC membranes. Values of 328, 414 and 607 ms were respectively determined for positions 4, 8 and 14, i.e., shorter than in DPPC bilayers. This suggests that fluorinated PA probes experience an increase in motions on the nanosecond timescale when incorporated in the ghost membranes, revealing the higher fluidity of ghost membranes as compared to those formed by DPPC. T_2 values in ghosts, which range from 1.5 ms for F(4) to 2.4 ms for F(14), do not differ significantly from those determined in model membranes, implying that millisecond timescale motions are similar in these two types of bilayers. The T_2 value for PA-F(8) is the lowest (1.3 ms), consistent with the lowest FWHM value.

Isotropic peaks observed on ^{19}F MAS spectra are sufficiently well separated to be resolved in a mixture of the three FAs, or if a triply labeled FA was prepared. The acyl chain order could then be studied in a single experiment while benefiting from the high sensitivity offered by MAS, providing that a triple labeling would not affect the membrane assembly. Altogether, our results show that both membrane structure and dynamics are measurable by labeling whole cells such as RBC ghosts with MFPAs. Their physicochemical properties can thus be investigated, enabling the study of their interaction with membrane-active molecules.

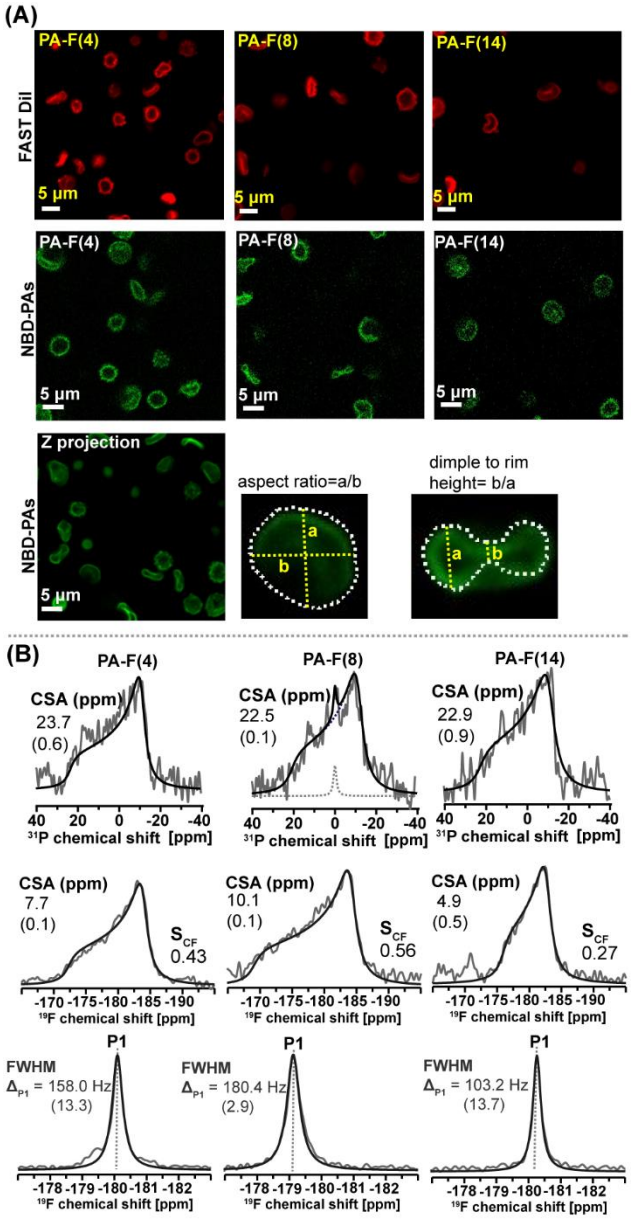

Figure 4.5: (A) Confocal fluorescence microscopy images of erythrocyte ghosts labeled with fluorinated PAs. Secondary fluorophore labeling was achieved using lipophilic tracer FAST DiI (red) after fluorination, NBD-PA (green) labeling was achieved along with the fluorination protocol. Scale bars are 5 µm and Z projection image of labeled ghosts with an average aspect ratio is indicated **(B)** Static ^{31}P (top), static ^{19}F (middle) and ^{19}F MAS (10 kHz) SS-NMR spectra of erythrocyte ghosts labeled with fluorinated PAs, recorded at 293 K with ^{1}H decoupling. CSA and FWHM values are indicated, with standard deviation. Note the significant improvement in S/N ratio between ^{31}P and ^{19}F NMR.

4.4.3 Interaction of caerin 1.1 with ^{19}F-labeled erythrocyte ghosts

We verified the applicability of our ^{19}F SS-NMR approach to study the interaction mechanism of an AMP with intact cells. To do so, we used caerin 1.1 – a 25 amino-acid cationic peptide with the following primary sequence: GLLSVLGSVAKHVLPHVVPVIAEHL-NH_2. This AMP was shown to create pores in RBC ghosts labeled with deuterated PA (PA-d_{31}) by ^{31}P and ^{2}H SS-NMR in our previous work[40]. **Fig. 4.6A-C** present the static ^{19}FSS-NMR spectra of the ghosts labeled at positions 4, 8 and 14, for different lipid-to-peptide (L/P) molar ratios. The ^{31}P SS-NMR spectra are available in the SI (**Fig. S4.8**) for comparison. The ^{19}F spectra show the presence of a central resonance at approximately 180 ppm with a linewidth ranging from 300 to 400 Hz in the presence of caerin 1.1. Rather than resulting from small fast tumbling objects, the breadth of this line could for example indicate the presence of high-curvature regions in the ghost membranes (see below). ^{19}F CSA values decrease as a function of peptide concentration for ghosts containing PA-F(8) and PA-F(14), indicating an increased mobility at these positions. An opposite trend is observed for ghosts labeled with PA-F(4), suggesting a proximity of the AMP to the headgroup region of the membrane with local motion hindrance.

The membrane perturbing effect revealed by ^{19}F static NMR (and ^{31}P) correlates well with caerin-induced RBC leakage assays[40]. Indeed, the appearance of the isotropic peak in the ghosts and the RBC leakage occur at roughly the same L/P ratios. These observations are in good agreement with our previous work[40] as well as fluorescence microscopy images in **Fig. S4.9**, which suggest the formation of pores in the ^{19}F-labeled ghosts membrane. It should be noted that the L/P ratio refers the total number of molecules present *in the whole sample*; the local ratio at the actual membrane is most certainly smaller due to AMP partitioning between the membrane and buffer.

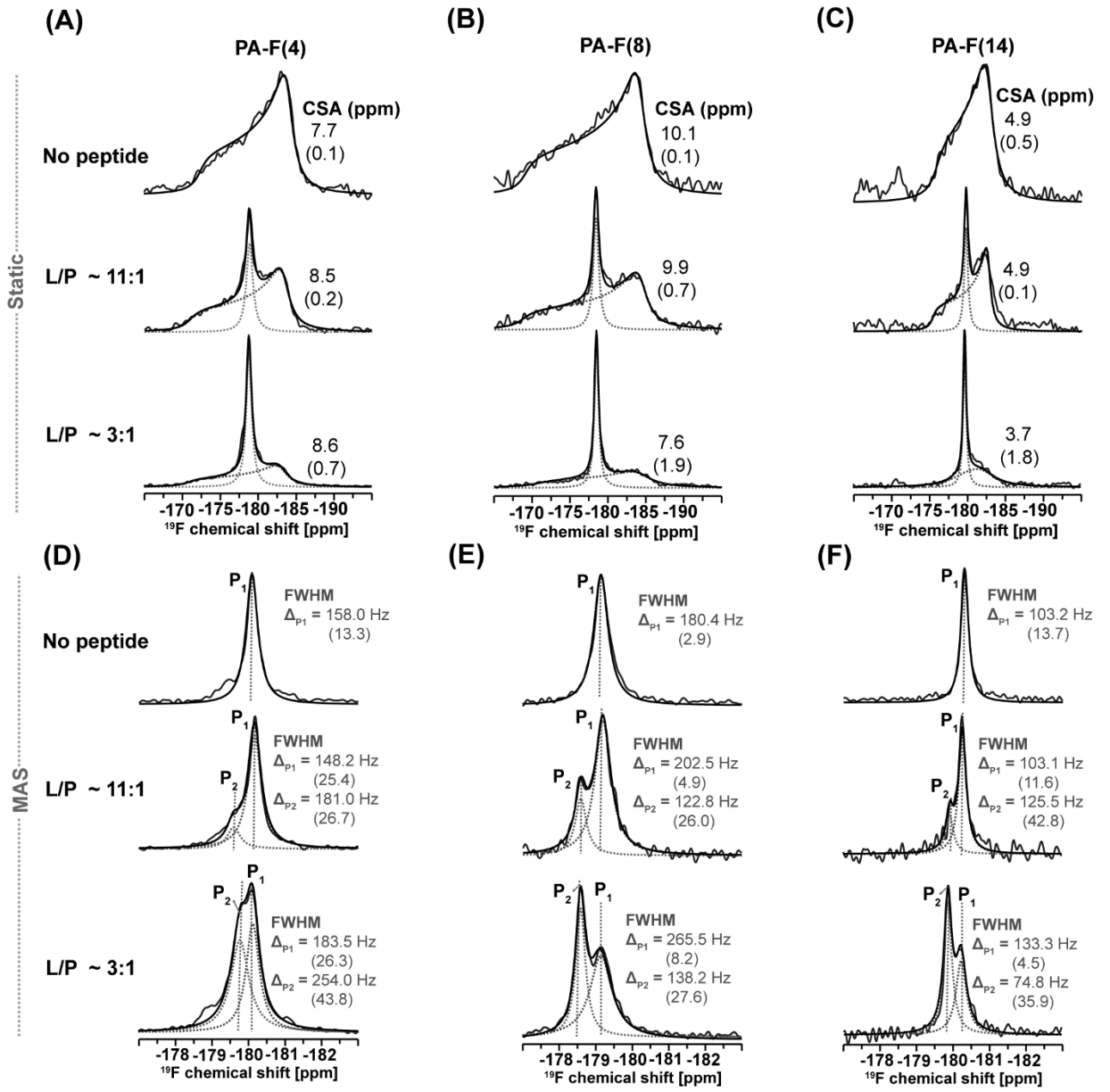

Figure 4.6: Static **(A-C)** and MAS **(D-F)** ^{19}F SS-NMR spectra of erythrocyte ghosts labeled with PA-F(4) **(A and D)**, PA-F(8) **(B and E)** and PA-F(14) **(C and F)**, exposed to different concentrations of caerin 1.1. Spectra were recorded at 293 K with ^{1}H decoupling. CSA and FWHM values are indicated, with standard deviation.

Fig. 4.6D-F show the ^{19}F MAS SS-NMR spectra of fluorinated ghosts with different concentrations of caerin 1.1. As was the case in model membranes, the anisotropic interactions are conveniently averaged by MAS even at a moderate frequency of 10 kHz. Without peptide, the area of each broad spectrum is concentrated into a single narrow line (noted P_1) with an associated increase in the S/N ratio. Interestingly, when caerin is added, an additional resonance (P_2) emerges

and its intensity increases with peptide concentration. This peak is observed with all MFFA analogues. Both P_1 and P_2 resonances are best resolved when the ^{19}F atom is located at positions 8 and 14. The appearance of two isotropic peaks upon caerin addition suggests that the MFFAs are in two different environments, which we quantified by integrating P_1 and P_2 lines. As shown in **Fig. 4.7 (Table S4.2)**, the P_2 contribution to the MAS ^{19}F SS-NMR spectra is in excellent agreement with the isotropic contribution to the static ^{19}F and ^{31}P SS-NMR spectra.

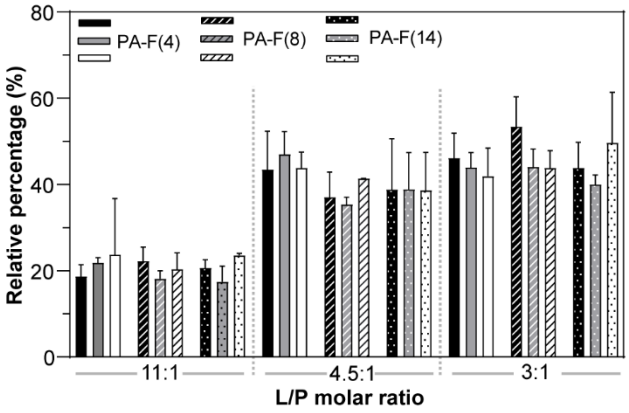

Figure 4.7: Isotropic contribution in the static ^{31}P (black) and ^{19}F (grey) SS-NMR spectra compared to the P_2 contribution (white) in the MAS (10 kHz) ^{19}F SS-NMR spectra as a function of caerin 1.1 concentration in erythrocyte ghosts containing monofluorinated palmitic acids.

We then explored dynamics changes in the membrane in the presence of AMPs by measuring T_1 and T_2 relaxation times under MAS. At all fluorine atom positions, the T_1 relaxation time of the P_2 resonance is consistently shorter than that of P_1 by approximately 100 ms, suggesting that the presence of interacting caerin increases the motions on the nanosecond timescale that contribute to T_1 relaxation. On the other hand, the T_2 values are similar for P_1 and P_2. When comparing the T_1 and T_2 values of the ghosts/AMP systems with those of MFFAs incorporated in fast reorienting isotropic dodecylphosphocholine (DPC) micelles, Table 4.1 shows that P_2's T_1 values are slightly smaller, and T_2 values are an order of magnitude smaller in the AMP-perturbed ghosts.

The presence of an isotropic peak in the static spectra, a small change in T_1 and strong reduction in T_2 have been shown, in the case of ^{31}P SS-NMR, to be characteristic of high-curvature regions such as cubic or hexagonal phases[211,242]. In full analogy, we thus assign the isotropic peak in our static ^{19}F spectra and P_2 peak in the MAS spectra to high-curvature regions induced by the AMP. Our NMR and microscopy results rule out a carpet mechanism, which results in the formation of micelles. *A contrario*, the presence of high curvature regions could be due to the formation of

toroidal pores for example, a result consistent with our leakage assay and fluorescence microscopy results[40]. Control experiments (not shown) rule out the possibility of hexagonal phase formation.

Table 4.1: Average ^{19}F chemical shifts and ^{19}F T_1 values in different systems incorporating monofluorinated PA probes, with standard deviation. Values calculated from MAS ^{19}F SS-NMR spectra recorded at 293 K with ^{1}H decoupling.

^{19}F analogue	DPC Micelles			DPPC/DPPC-d_{62}/PA			Ghosts* (P_1)			Ghosts + Caerin 1.1 (P_2)		
	δ_{iso} (ppm)	T_1 (ms)	T_2 (ms)	δ_{iso} (ppm)	T_1 (ms)	T_2 (ms)	δ_{iso} (ppm)	T_1 (ms)	T_2 (ms)	δ_{iso} (ppm)	T_1 (ms)	T_2 (ms)
PA-F(4)	-180.4	382 (53)	23.8 (14.6)	-180.9	611 (47)	1.7 (0.2)	-180.1	328 (27)	1.5 (0.3)	-179.7	226 (24)	1.1 (0.1)
PA-F(8)	-178.2	487 (18)	18.4 (8.1)	-179.7	760 (163)	2.2 (0.1)	-179.2	414 (4.2)	1.3 (0.4)	-178.6	310 (77)	0.9 (0.1)
PA-F(14)	-179.9	731 (10)	24.9 (5.8)	-181.3	883 (54)	2.2 (0.1)	-180.3	607 (19.1)	2.4 (0.1)	-179.9	472 (69)	1.8 (0.2)

*P_1 has the same isotropic chemical shift and T_1 values, without and with caerin 1.1.

4.5 Discussion

The objective of this study was to leverage the labeling of whole cells with MFFAs to investigate specific interactions using ^{19}F SS-NMR. Fluorine offers several key advantages, including its high sensitivity, which reduces acquisition time (a critical factor for whole-cell and *in vivo* studies), its low occurrence in biological samples, which minimizes background signals, and its broad chemical shift range, allowing for sensitivity to even minor structural changes. Fluorine is an isostere of hydrogen that alters the hydrogen bonding properties and dipole moment of the molecule in which it is incorporated[243,244]. As a consequence, fluorination can change the polarity and hydrophobicity of a molecule to an extent that will depend on the location and level of fluorination[243]. Here, we showed, as have others in similar systems, that the incorporation of MFFAs has only minor effects on the membrane structure[152,223,229], and that it can report changes in the bilayer's dynamics that are of great relevance to the study of membrane-protein interactions[57,69,223,229]

Using model DPPC membranes incorporating PA fluorinated at three different positions along the acyl chains, we established that changes in the ^{19}F CSA, isotropic chemical shift and linewidth, as well as T_1 and T_2 relaxation times, can inform on changes in the lipid bilayer dynamics. To further characterize these changes, we introduced the order parameter S_{CF} as well as M_2 measurements, similar to the widely used ^{2}H SS-NMR study of perdeuterated lipids. We then

showed that ^{19}F SS-NMR is a valuable tool to describe the membrane state in whole erythrocyte ghosts and to monitor AMP-membrane interactions. The results obtained here using our ^{19}F SS-NMR methodology are consistent with previous work reporting a pore formation mechanism for caerin, thus validating our approach.

^{19}F static spectra enabled the distinction between lamellar and non-lamellar phases with a higher sensitivity than ^{31}P SS-NMR. Preliminary data also show that hexagonal phases can be identified by ^{19}F NMR (data not shown). In addition, ^{19}F NMR with appropriate labeling could replace ^{31}P NMR in membranes deprived of phospholipids, such as plant membranes for example. The spectra can be interpreted in terms of an order parameter reflecting the acyl chain order in a similar way to static ^{2}H SS-NMR. The use of MAS, combined to the large chemical shift range of ^{19}F NMR enables distinguishing lamellar and high-curvature regions in a spectrum where anisotropic interactions are fully averaged and all the intensity is concentrated into sharp peaks. This greatly reduces the experimental time and also opens the possibility of measuring relaxation times, allowing to probe dynamical properties of the molecules.

In summary, by adequately selecting the ^{19}F position on the acyl chain, ^{19}F SS-NMR can provide the same information as ^{2}H and ^{31}P SS-NMR in lipid systems. Typically, knowledge of acyl chain order necessitates the measurement of anisotropic interactions such as CSA, quadrupolar couplings, or dipolar couplings[83,103]. While the simplest approach may involve studying static samples, it is conceivable to reintroduce these anisotropic interactions, thereby harnessing the advantages offered by both MAS and static spectra [83]. In this regard, the broader range of ^{19}F chemical shifts, compared to ^{31}P and even more so to ^{2}H, becomes advantageous. Additionally, information obtained from anisotropic interactions can be readily complemented by relaxation time measurements, as demonstrated in this study.

4.6 Conclusions

In this work, we showed how ^{19}F SS-NMR is a useful tool to understand the interaction of AMPs with model membranes and more importantly whole cells. The incorporation of fluorinated FA probes placed at different depths in the membrane enables mapping changes in dynamics at various locations in the membrane hydrophobic core, thus complementing other biophysical methods such as ^{31}P SS-NMR to describe membrane-peptide interactions. Considering its location in the middle of the acyl chain, PA-F(8) would be the preferred MFFA if a single position needs

to be chosen. ^{19}F SS-NMR experiments can be carried out with static samples or under MAS, with and without ^{1}H decoupling, each of these approaches having its advantages. The results presented in this work should guide the choice of a ^{19}F SS-NMR experiment to investigate lipid membranes in both model and cell systems, whether it concerns membrane structure, dynamics, or a peptide mode of action. We exemplified our methodology with the study of the cationic AMP caerin 1.1 as it interacts with erythrocyte membranes. The labeling strategy presented in this work should be widely applicable to other cells such as bacteria.

4.7 Author contributions

Kiran Kumar: Formal analysis, Investigation, Methodology, Validation, Visualization, Writing – original draft. Alexandre A. Arnold: Conceptualization, Formal analysis, Investigation, Methodology, Supervision, Validation, Writing – review & editing. Raphael ¨ Gauthier: Investigation, Methodology. Marius Mamone: Investigation, Methodology. Jean-François Paquin: Investigation, Supervision, Methodology, Resources, Writing – review & editing. Dror E. Warschawski: Conceptualization, Formal analysis, Methodology, Supervision, Writing – review & editing. Isabelle Marcotte: Conceptualization, Funding acquisition, Project administration, Resources, Supervision, Writing – review & editing, Methodology.

4.8 Acknowledgements

This research was funded by the Natural Sciences and Engineering Research Council (NSERC) of Canada (grant RGPIN-2018–06200 to I.M.) and the Centre National de la Recherche Scientifique (UMR 7203 to D.E.W.). K.K. would like to thank the Quebec Network for Research on Protein Function, Engineering, and Applications (PROTEO) - strategic cluster of the Fonds de recherche du Québec – Nature et technologies (FRQNT) - for the award of a scholarship. The authors thank Mathew Sebastiao (Université du Québec à Montréal) for technical assistance and Pierre Audet (Université Laval) for the loan of the HFX probe.

4.8 Supplementary information

Examples of ^{2}H SS-NMR spectra :

Second spectral moments, M_2 were extracted from following MAS ^{2}H SS-NMR spectra using equation 2 mentioned in section 2.6. and a typical gel phase spectrum at 5 °C have an M_2 of 25-26 $\times 10^6$ s^{-2} and at fluid phase 60 °C, the samples have an M_2 of 2.9-4.8 $\times 10^6$ s^{-2}.

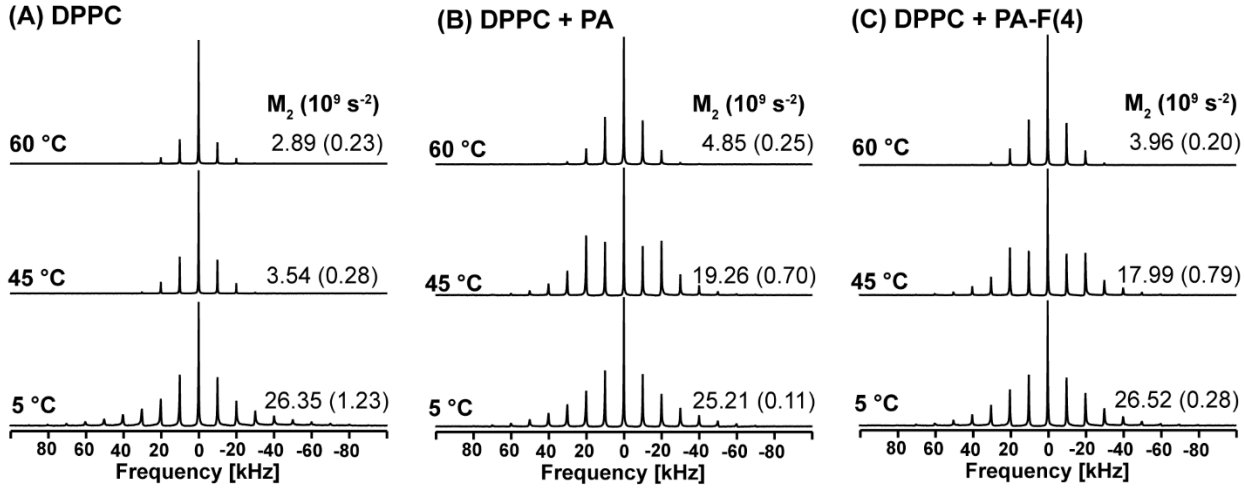

Figure S4.1: Representative MAS ^{2}H SS-NMR spectra of **(A)** DPPC/DPPC-d_{62} (1:1), **(B)** DPPC/DPPC-d_{62}/PA (1:1:1) and **(C)** DPPC/DPPC-d_{62}/PA-F(4) as a function of temperature, recorded with 10 kHz MAS. M_2 values are indicated, with standard deviation.

Examples of ^{1}H SS-NMR spectra:

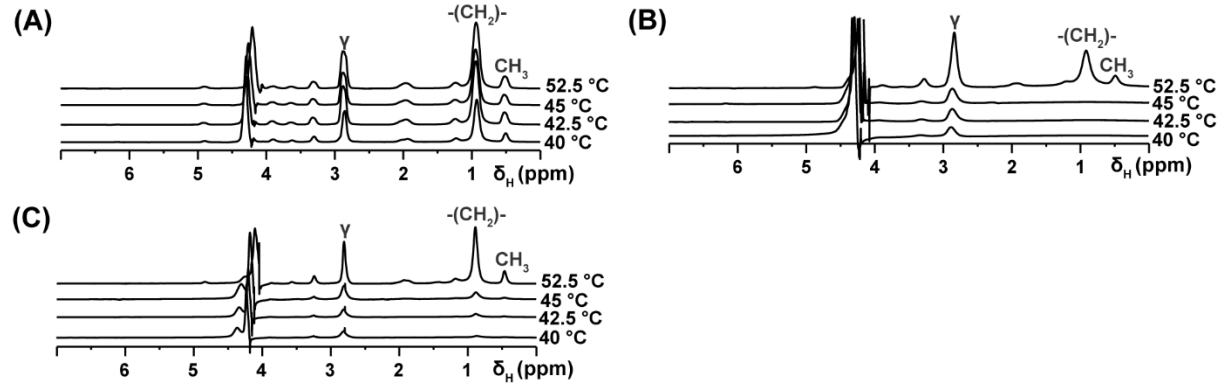

Figure S4.2: Representative ^{1}H SS-NMR spectra of **(A)** DPPC/DPPC-d_{62} (1:1), **(B)** DPPC/DPPC-d_{62}/PA (1:1:1) and **(C)** DPPC/DPPC-d_{62}/PA-F(4) as a function of temperature, recorded with 10 kHz MAS.

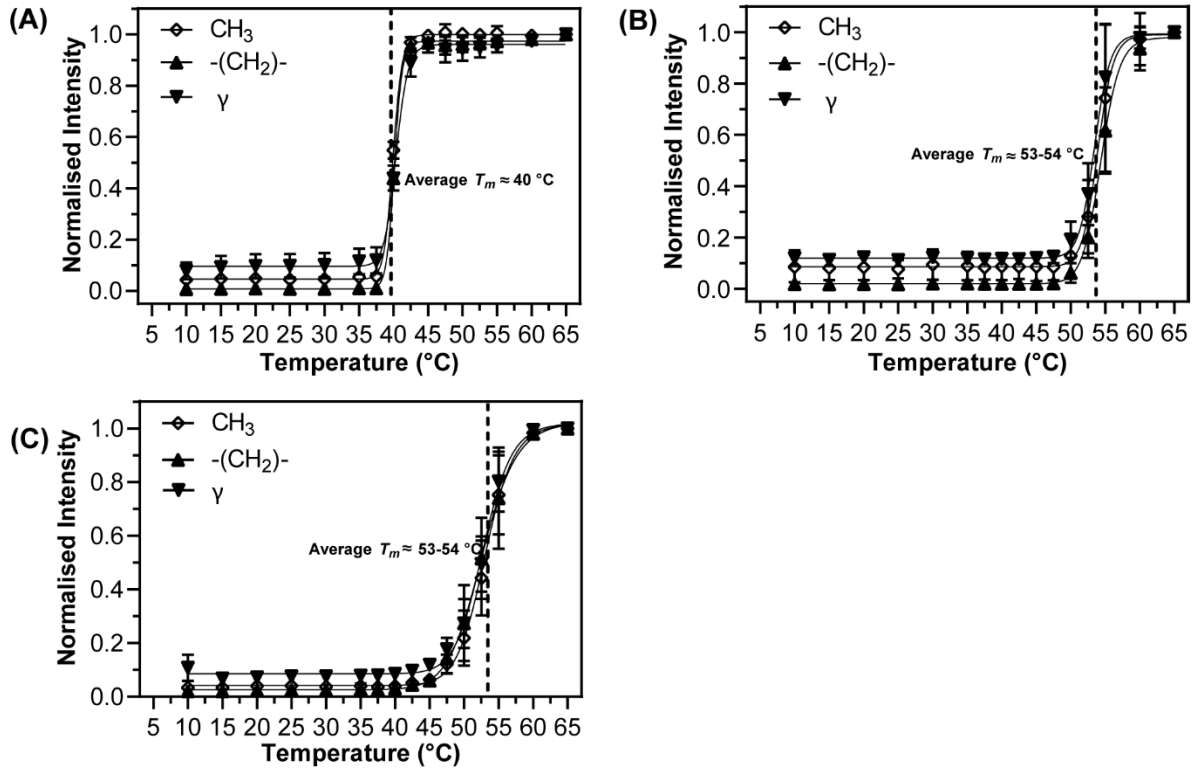

Figure S4.3: Determination of the gel-to-fluid phase transition temperature (T_m) of **(A)** DPPC/DPPC-d_{62} (1:1), **(B)** DPPC/DPPC-d_{62}/PA (1:1:1) and **(C)** DPPC/DPPC-d_{62}/PA-F(4) (1:1:1) through monitoring of the intensity of the methyl, methylene and γ protons from ^{1}H SS-NMR spectra, recorded with 10 kHz MAS (Fig. S4.2). Standard deviations are indicated.

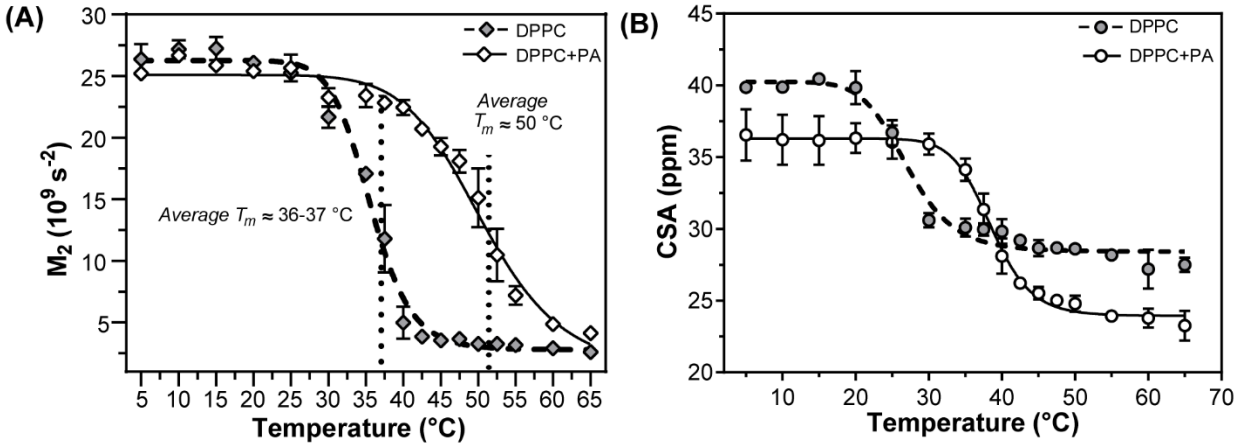

Figure S4.4: Temperature dependence of the M_2 and CSA values for DPPC/DPPC-d_{62} (1:1) without (dashed line) and with (solid line) protonated PA, respectively calculated from the ^{2}H (10 kHz MAS) and ^{31}P SS-NMR spectra. CSA and M_2 values are indicated, with standard deviation.

Example of ^{2}H static SS-NMR spectra: Using static ^{2}H SS-NMR spectrum below (left), a dePaked spectrum is obtained (right) and using separated resonance line segmental bond order parameter is determined.

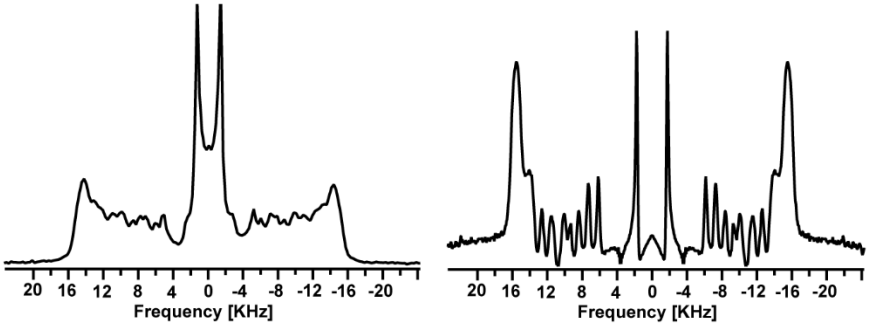

Figure S4.5: Representative ^{2}H static powder-type spectrum of DPPC/DPPC-d_{62}/PA-F(4) (left) and the spectrum is dePaked (right) with separated resonance lines. Spectrum is obtained at fluid phase (65 °C) with 10 kHz MAS.

Additional ^{19}F MAS SS-NMR spectra:

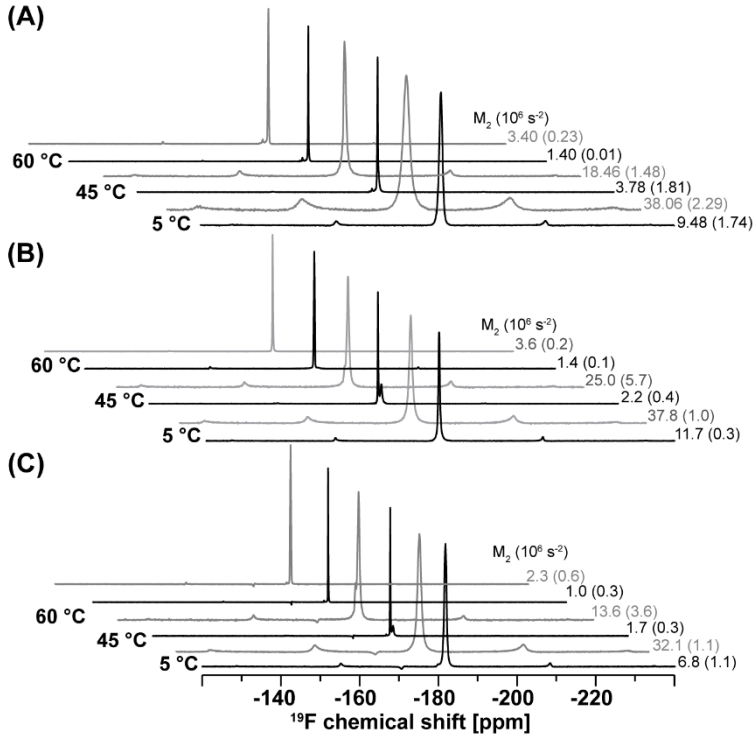

Figure S4.6: Representative MAS ^{19}F SS-NMR spectra of DPPC/PA model membrane with fluorinated PA analogue of **(A)** PA-F(4) , **(B)** PA-F(8) and **(C)** PA-F(14), acquired at different temperatures with (black) and without (grey) ^{1}H decoupling and M_2, calculated from corresponding spectra are noted with standard deviation.

Table S4.1: Summary of the isotropic chemical shift (δ_{iso}) values as well as T_1 and T_2 relaxation times of monofluorinated PA analogues incorporated in DPPC model membranes of molar ratio of 1:1:1. Values are obtained from ^1H decoupled spectra and standard deviations are presented.

^{19}F analogue	DPPC/DPPC-d_{62}/PA					
	278 K			293 K		
	δ_{iso} (ppm)	T_1 (ms)	T_2 (ms)	δ_{iso} (ppm)	T_1 (ms)	T_2 (ms)
PA-F(4)	-180.9	546 (5)	1.6 (0.1)	-180.9	611 (47)	1.7 (0.2)
PA-F(8)	-179.4	652 (49)	2.2 (0.1)	-179.7	760 (163)	2.2 (0.1)
PA-F(14)	-181.7	712 (50)	2.2 (0.2)	-181.3	883 (54)	2.2 (0.1)

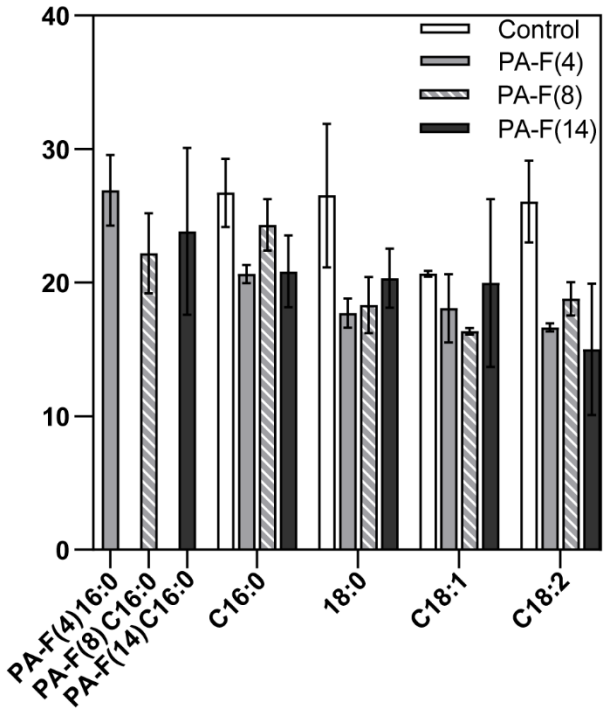

Figure S4.7: Fatty acyl chain profile of fluorinated erythrocyte ghosts labeled with fluorinated PA analogues obtained by GCMS. Standard deviations are presented.

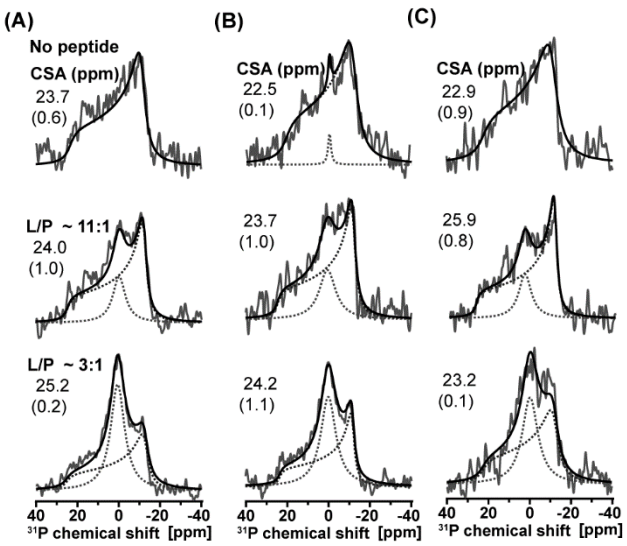

Figure S4.8: Static ^{31}P SS-NMR spectra of erythrocyte ghosts labeled with **(A)** PA-F(4), **(B)** PA-F(8) and **(C)** PA-F(14), exposed to different concentrations of caerin 1.1. Spectra were recorded at 293 K with ^{1}H decoupling. CSA values are indicated, with standard deviation.

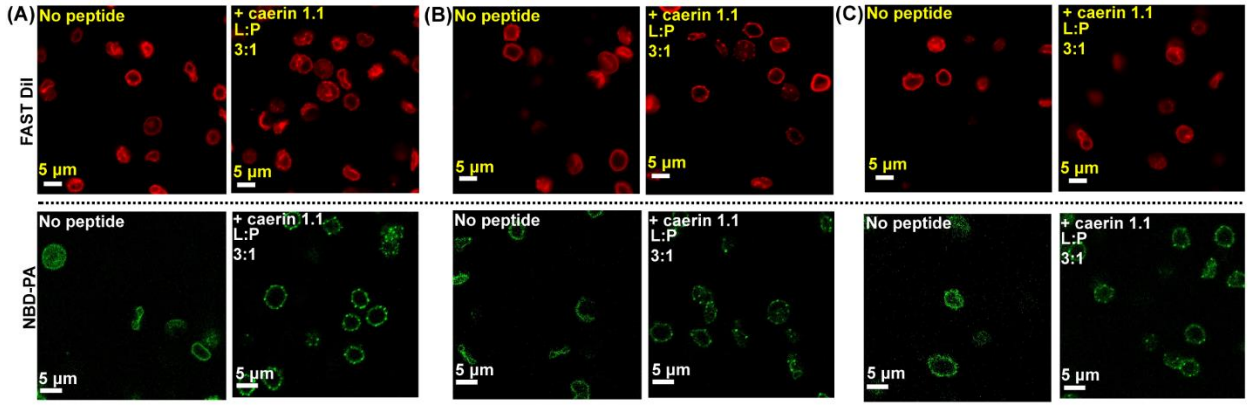

Figure S4.9: Confocal fluorescence microscopy images of fluorinated PAs labeled erythrocyte ghosts with addition of caerin 1.1, **(A)** PA-F(4), **(B)** PA-F(8) and **(C)** PA-F(14). Secondary fluorophore labeling was achieved using lipophilic tracer FAST DiI (red) after fluorination, NBD-PA (green) labeling was achieved along with the fluorination protocol. The corresponding L/P molar ratios are indicated, and the scale bars are 5 µm.

Table S4.2: Isotropic contribution from static ^{31}P and ^{19}F SS-NMR spectra and P_2 contribution from MAS (10 kHz) ^{19}F SS-NMR spectra as a function of caerin 1.1 concentration. Corresponding lipid-to-peptide (L/P) molar ratio is denoted. Values are indicated, with standard deviation.

	Static ^{31}P NMR			Static ^{19}F NMR			MAS ^{19}F NMR		
	PA-F(4)	PA-F(8)	PA-F(14)	PA-F(4)	PA-F(8)	PA-F(14)	PA-F(4)	PA-F(8)	PA-F(14)
L/P	Isotropic contribution (%)						P_2 contribution (%)		
11:1	18.7 (2.7)	22.3 (3.2)	20.6 (2.0)	21.8 (1.2)	18.1 (1.9)	17.4 (3.7)	23.7 (13.0)	20.4 (3.8)	23.6 (0.5)
4.5:1	43.5 (8.9)	37.0 (5.8)	38.8 (11.8)	47.0 (5.3)	35.4 (1.7)	38.9 (8.5)	43.8 (3.7)	41.4 (0.1)	38.7 (8.8)
3:1	46.1 (5.8)	53.4 (6.9)	43.8 (5.9)	43.9 (3.4)	44.0 (4.2)	40.0 (2.2)	41.9 (6.6)	43.8 (4.0)	49.7 (11.7)

CHAPTER V

Fluorinated palmitic acid to investigate molecular interactions in lipid membranes by ^{19}F solid-state nuclear magnetic resonance

Kiran Kumar[1], Alexandre A. Arnold[1], Raphaël Gauthier[2], Marius Mamone[2], Jean-François Paquin[2], Dror E. Warschawski[1,3] & Isabelle Marcotte[1]

[1]Departement of Chemistry, Université du Québec à Montréal, P.O. Box 8888, Downtown Station, Montreal, Canada H3C 3P8

[2]PROTEO, CCVC, Département de chimie, Université Laval, 1045 Avenue de la Médecine, Québec, Québec, G1V 0A6, Canada

[3]Laboratoire des Biomolécules, LBM, CNRS UMR 7203, Sorbonne Université, École normale supérieure, PSL University, 75005 Paris, France

Article in preparation

N.B. References cited in this chapter are presented at the end of the thesis

5.1 Abstract

Due to its absence in nature and favorable magnetic properties, fluorine-19 is an ideal nucleus to study biological systems by nuclear magnetic resonance (NMR) spectroscopy. In this work, we used a mixture of monofluorinated palmitic acids (PAs) as tracers to investigate the molecular interaction of the drug rosuvastatin in model lipid membranes. More specifically, PAs labeled at the 4^{th} and 8^{th} carbon positions of their acyl chains were co-incorporated in phospholipid bilayers to probe different depths of the hydrophobic core. First, the ^{19}F chemical shift anisotropy indicative of membrane fluidity, was simultaneously determined in the FAs and the fluorinated drug using slow magic-angle spinning (MAS) ^{19}F solid-state NMR. Membrane heterogeneity and selective partitioning of rosuvastatin into fluid regions could thus be evidenced. We then examined the possibility of mapping intermolecular distance in bilayers, both in the fluid and gel phases, using ^{19}F-^{19}F and ^{1}H-^{19}F correlation experiments by SS-NMR using MAS. Spatial correlations were evidenced between the two PAs in the gel phase, while contacts between the statin and the lipids were detected in the fluid phase. This work paves the way to mapping membrane-active molecules in intact membranes, and stresses the need for new labeling strategies for this purpose.

5.2 Introduction

Solid-state nuclear magnetic resonance (SS-NMR) experiments can provide information on both structural and dynamical aspects of molecular interactions with biological membranes[103,245-248]. In the case of complex cellular systems with many different constituents, determining the location of a guest molecule in the membrane is challenging. Notably, establishing the structural connectivity or distance relationships to the molecules found in the membranes, such as lipids, proteins and carbohydrates, is particularly daring.

Depending on the experimental needs, different membrane mimetic systems can be employed[105]. Rapidly reorienting model membranes such as a micelles, are readily accessible and amenable to ^{1}H-based solution NMR experiments, which allow a fast signal acquisition and spectral resolution[133,249]. These experiments can be complemented by isotopic labeling strategies to constrain the structure of molecules or elucidate their spatial organization[249]. However, monolayered model systems reproduce the membrane poorly. Moreover, the NMR strategies that they enable cannot be applied to slow-tumbling lipid bilayers, such as multilamellar vesicles (MLVs), and to whole cells membranes. Dynamical constraints and accurate distance measurement are challenging in such systems, particularly in the natural fluid state of the membrane where often both solution and SS-NMR experiments breakdown. From an NMR point of view, the challenges faced arise not only from low sensitivity and spectral overlap but also from motional and spatial heterogeneity.

In this regard, fluorine-19 (^{19}F) labeling of membrane lipids provides several benefits, notably its high sensitivity and absence in biological systems, thus limiting the possibility of signal overlap[223,250]. The usefulness of fluorinated PAs was demonstrated in our previous studies (Kumar *et al* 2024)[251], in which different locations across red blood cell ghosts membranes were probed using single monofluorinated PAs on either the carbons 4, 8 or 14 of the acyl chains. This allowed probing the interaction of an antimicrobial peptide at different locations of the membrane's hydrophobic core.

In this work, we extend our previous study by showing that the information offered by the different ^{19}F-PAs can be simultaneously obtained in a multiply labeled model membrane. We first examine different ^{19}F-^{19}F magnetization transfer mechanisms in model lipid membranes using the bifluorinated antibiotic sparfloxacin and applied to another monofluorinated drug molecule Rosuvastatin (RVS). This drug was selected because statins are well known for their "pleiotropic"

action[252], which involves interaction with the lipid bilayer where they are known to modulate the structure and dynamics of membranes by exerting their effect on lipids or cholesterol[253,254] and even induce phase separation or the formation of lipid rafts in the membrane[252,253].

We then examine to what extent ^{19}F-^{19}F distances can be measured in a membrane environment in both the solid-like gel phase and the more native fluid phase. We exemplify these distance measurements by examining the proximity between ^{19}F-PAs and the monofluorinated rosuvastatin, which has been shown to insert in POPC (1-palmitoyl-2-oleoyl-glycero-3-phosphocholine) bilayers[253]. All experiments are carried out under slow magic-angle spinning (MAS) conditions, which enable the measurement of anisotropic interactions with site-specific resolution of the various ^{19}F-PAs and statins. At faster although moderate spinning frequencies, only the central isotropic peak remains and two-dimensional correlation experiments are used to elucidate the molecular proximity.

Overall, we show that ^{19}F MAS SS-NMR of multiply labeled membranes can provide valuable information on molecular structure and proximity in an anisotropic lipid system, even in the fluid state. Accurate distance measurements are indeed possible in membranes by employing ^{19}F. However, additional hurdles such as unfavorable dynamics or phase separation need to be taken into account, especially in the case of whole cell systems.

5.3 Materials and methods

5.3.1 Materials

All lipids and detergent molecules used in this study were obtained from Avanti Polar Lipids (Alabaster, AL, USA), which include 1-palmitoyl-2-oleoyl-glycero-3-phosphocholine (POPC), dodecylphosphocholine (DPC). Rosuvastatin, sparfloxacin, deuterium-depleted water, as well as all other solvents and chemicals were purchased from Sigma Aldrich (Oakville, ON, Canada). Deionized 18.2 MΩ.cm milli-Q water was used in all experiments (Millipore-Sigma, Oakville, ON, Canada). Monofluorinated fatty acids were synthesized following a protocol detailed in (Kumar *et al* 2023)[40].

5.3.2 Multilamellar vesicles preparation

MLVs were prepared using the dry film method described by Warschawski *et al.*[83]. Briefly, the lipid mixture (including ^{19}F-labeled PAs) was dissolved in a 1:2 methanol/$CHCl_3$ solution and dried under nitrogen stream. Remaining traces of organic solvent in the lipid film were removed

by high vacuum for at least 2 h. Rosuvastatin or sparfloxacin dissolved in 1:2 methanol/$CHCl_3$ were directly added to the dry lipid film, followed by a 1-2 h solvent evaporation step. The mixed lipid film containing the statin was then hydrated with a physiologically relevant solution of 150 mM NaCl (pH 7.0) prepared with ^{2}H-depleted water if necessary. The lipid dispersion was submitted to a series of 3 to 5 cycles of freeze (10 min at −20 °C), thaw (10 min above 40-55 °C) and vortex shaking, and finally transferred into a 4-mm or 1.9-mm SS-NMR rotor.

5.3.3 Solid-state NMR experiments

All SS-NMR spectra were recorded using a Bruker Avance III-HD wide-bore 400 MHz spectrometer (Milton, ON, Canada) equipped with either a double tuned 4 mm-HFX probe and a ^{1}H-^{19}F filter, allowing to observe ^{19}F with ^{1}H decoupling, or alternatively a 1.9 mm-HXY probe converted into FXY probe, with no ^{1}H decoupling. Static ^{19}F SS-NMR spectra were obtained using a phase-cycled Hahn echo pulse sequence, with an interpulse delay of 35 µs and high-power (50 kHz) ^{1}H decoupling during acquisition. The 90° pulse length was 4 µs and data were collected using 2048 points for ^{19}F SS-NMR with a recycle delay of 3 s. The ^{19}F chemical shifts were referenced to the trifluoroacetic acid (TFA) signal at -76.5 ppm.

^{19}F SS-NMR experiments were carried out at different MAS frequency with a phase-cycled Hahn echo sequence. 1D static or 1 kHz ^{19}F spectra were collected with the 4mm-HFX probe using 1024 scans per spectra, for a total acquisition time of 50 min with a recycle delay of 3 s. The same probe was used to record 10 kHz MAS spectra, obtained with 128 scans and a total acquisition time of 6 min with a recycle delay of 3 s. For all ^{19}F MAS spectra, a minimum of 3 k data points were collected, with a 4-µs 90° pulse length, and interpulse delays were rotor-synchronized. When necessary, ^{1}H-^{19}F cross polarization (CP) was performed for 1 ms. Fast MAS at 33 kHz was carried out with a 1.9mm-HXY probe, and 1D ^{19}F spectra were collected using 32 scans and a total acquisition time of 2 min, without ^{1}H decoupling.

2D ^{1}H-^{1}H NOESY experiments were done at different mixing times, with a total of 1k data points × 512 increments, each with 16 scans, for a maximum acquisition time of 6.5 h. 2D ^{1}H-^{19}F HOESY experiments were carried out with different mixing times and ^{1}H decoupling, with a total of 2k data points × 512 increments, each with 32 scans, for a maximum acquisition time of ~ 35 h. For both experiments, a recycle delay of 2 to 3 s was used. 2D ^{19}F-^{19}F PDSD (proton-driven spin diffusion) with no recoupling, or DARR (dipolar-assisted rotational resonance) with ^{1}H

recoupling, were carried out at various mixing times, with a total of 2k data points × 384 increments of 8 scans each, leading to a maximum of 2.5 hour acquisition time, with a recycle delay of 2 s. When necessary, ^{1}H-^{19}F CP was performed for 1 ms . 2D ^{19}F-^{19}F RFDR experiments were done with 1k data points × 512 increments of 16 scans each, amounting to a maximum of 4.5 hours of acquisition time, with 1 ms ^{1}H-^{19}F CP and a recycle delay of 3 s. For all experiments, the 50 kHz ^{1}H and 62.5 kHz ^{19}F RF field strengths were used and calibrated independently.

^{19}F CSA values were determined by line fitting using the Bruker Sola (Solid Lineshape Analysis) software. ^{1}H-^{1}H NOESY and ^{19}F-^{19}F PDSD or DARR buildup curves were generated using respective cross peak volumes and normalised with respect to diagonal peaks, and to the number of protons. Since there is no diagonal in the HOESY spectra, peak volumes were normalized to the highest signal, from n and o peaks, and with respect to the number of protons.

5.3.4 Density functional theory (DFT)

Geometry optimization of rosuvastatin or sparfloxacin were carried out by DFT computations using B3LYP exchange correlation functional, together with 6-311G basis set and default methanol or water as the solvation medium. All computations were performed with the Gaussian 09 software suite. By using these optimized minimum energy structures, magnetic shielding tensors were calculated by the GIAO B3LYP/CC-PVDZ method. Distances and isotropic shielding tensors obtained from DFT structural coordinates for both the investigated molecules were compared with the NMR results.

5.4 Results and Discussion

5.4.1 Molecular dynamics through ^{19}F CSA measurement

Information at different depths of the lipid bilayer were simultaneously obtained by incorporating PAs fluorinated at different positions. **Fig. 5.1A** shows the static spectra recorded as a function of temperature, of a POPC model membrane in which two types PAs, fluorinated at position 4 or 8, are co-incorporated (**Fig. S5.1)**. Similarly to the values reported by Kumar *et al.* 2024[251], a higher CSA value of ≈16-17 ppm was measured in the gel phase at -15°C and up to -3 °C. The CSA value dropped to 6-7 ppm in the fluid phase. The two overlapping powder patterns could not be resolved under these conditions; however, two resonances were resolved using MAS (**Fig. 5.1B and C**) assigned to the two PAs fluorinated on positions 4 (δ_{iso}, -180.6 ppm) and 8 (δ_{iso},

-178.9 ppm), respectively. The site-specific CSA values can be determined by fitting the spinning sideband manifolds obtained at a low spinning frequency. As seen **Fig. 5.1B,** with 1 kHz MAS, the spectra in the gel phase (-15 °C and -3 °C) reveal a CSA value of ≈17 ppm and ≈16 ppm for PA-F(8) and PA-F(4), respectively. This small difference is invisible on the static spectra. In the fluid phase, the CSA values are divided by two and a slight increase of 0.5-0.8 ppm is noticeable in the slow-MAS spectra with both PAs, but they closely agree with the values obtained from the static spectra. Since the CSA is almost completely averaged-out at a spinning frequency of 10 kHz, the best MAS frequency to be used for a CSA analysis is a compromise between sensitivity (intensity of the spinning sidebands) and precision in the CSA measurement (number of sidebands). In a model membrane with a high ^{19}F-PA proportion (33 mol %), spinning frequencies on the order of 1-2 kHz are adequate, but faster frequencies are likely to be necessary in whole cells. Alternatively, 2D experiments that can recouple the CSAs under fast MAS and separate them according to their isotropic chemical shift have been developed for ^{13}C- and ^{31}P SS-NMR[83,255] and could be adapted to ^{19}F SS-NMR. This site-specific information should also be accessible using other membrane mimetics.

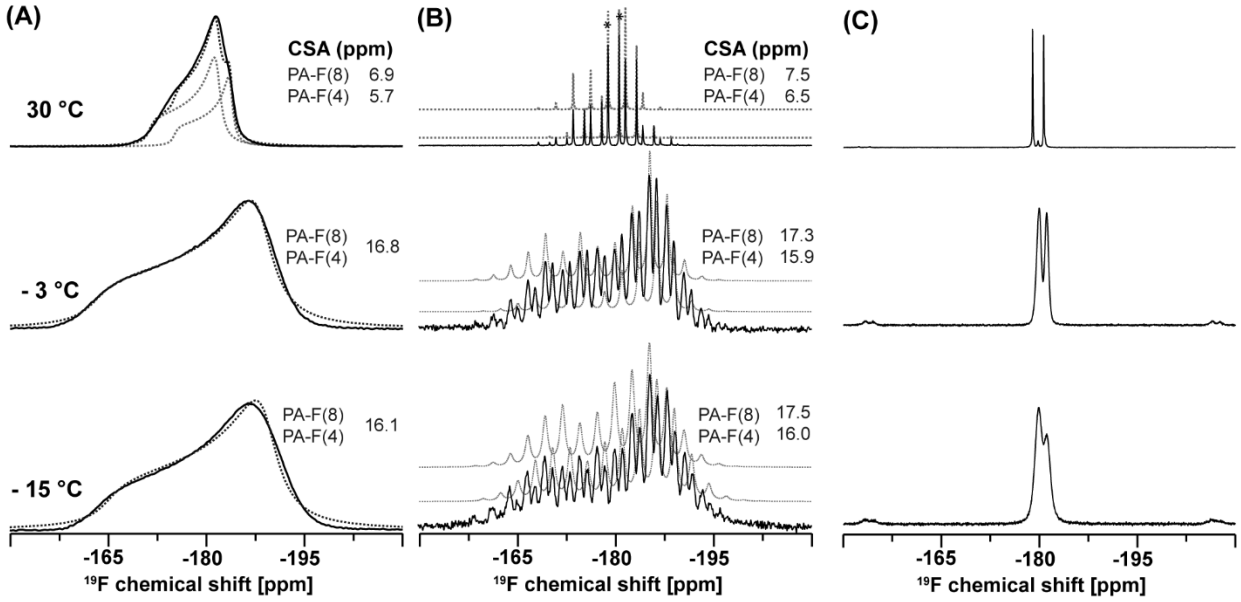

Figure 5.1: (A) Static, (B) 1 kHz and (C) 10 kHz MAS ^{19}F SS-NMR spectra of POPC model membranes incorporating monofluorinated PAs, at a POPC/PA-F(4)/PA-F(8) molar ratio of 4:1:1. Experiments were performed at different temperatures with ^{1}H decoupling. CSA values extracted from simulations are indicated on the spectra.

The ^{19}F nucleus on phospholipid or FA acyl chains are particularly sensitive to the bilayer ordering. However, it is also interesting to monitor the response of a fluorinated molecule to the phase transition of the membrane in which it is incorporated. Indeed, a great number of membrane-active drugs are fluorinated[83,255] and their ^{19}F spectra have been shown to help assess their membrane interaction[256,257]. Due to the strong structure dependence of the ^{19}F isotropic chemical shift values for drugs are likely to differ from those of ^{19}F-labeled acyl chains in lipids or FAs. It should therefore be possible to monitor the structure and dynamical properties of both a membrane-active drug and the hydrophobic core of the membrane – as revealed by the ^{19}F labeled acyl chains - on the same spectrum.

We thus examined the monofluorinated rosuvastatin (RVS), incorporated in POPC/^{19}F-PA model membranes. As shown in **Fig. 5.2,** the ^{19}F spectra of RVS as well as PA-F(4) and PA-F(8) are well separated and, using MAS, the CSA values of all fluorinated species could be measured. Our results indicate that the ^{19}F CSA values of the FAs below and above the main melting temperature of the membrane are only slightly reduced in the presence of the statin. Interestingly, the CSA of the statin, which is axially symmetric and of similar in width to the one of the FAs above the T_m, is only slightly modified when the temperature goes down to -3 $^{\circ}$C. The asymmetry is still very small, and the CSA value increases only 1 ppm. RVS, thus, appears to remain mostly in a fluid environment, most likely segregated from the PA-rich gel phase regions of the membrane. At a lower temperature (-15 $^{\circ}$C), the CSA increases and becomes asymmetric **(Fig. 5.2A)**, and no resonance is detected with slow MAS **(Fig. 5.2B)**. Suggesting that the statin is ejected from the bilayer.

Using a model membrane with multiple ^{19}F-labels, a simple slow MAS ^{19}F spectrum can thus be used to assess the local dynamics of the bilayer's hydrophobic core and evaluate membrane heterogeneity and drug location. Further insights might be obtained by determining ^{19}F-^{19}F internuclear distances.

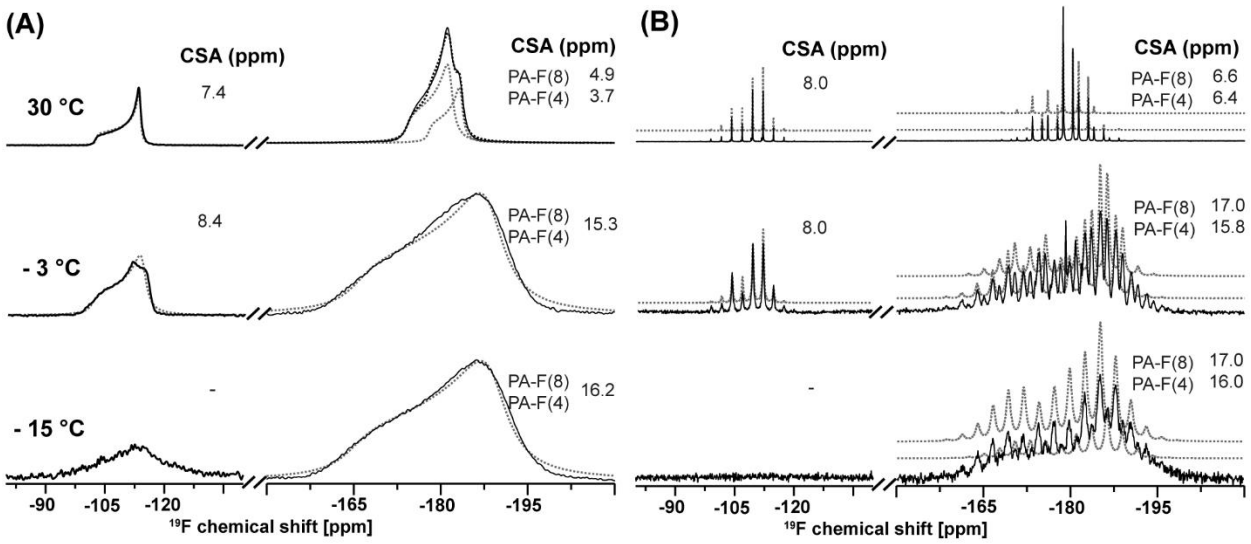

Figure 5.2: (A) Static and (B) 1 kHz MAS ^{19}F SS-NMR spectra of POPC model membranes incorporating monofluorinated PAs, at a POPC/PA-F(4)/PA-F(8) molar ratio of 4:1:1, with RVS at a lipid/PAs/RVS molar ratio of 40:20:3. Experiments were performed at different temperatures with ^{1}H decoupling. CSA values extracted from simulations are indicated on the spectra. PA resonances are on the right (circa -180 ppm), while statin resonances are on the left (circa -105 ppm). Full spectra are available on **Figure S5.2**.

5.4.2 Molecular structure through ^{19}F-^{19}F distance measurements

A more accurate description of the membrane composition might be obtained by assessing ^{19}F-^{19}F internuclear distances (or, semi-quantitatively, proximities) between FAs and between the FAs and a membrane-active drug. The accurate measurement of such distances in membrane samples is, however, notoriously difficult, in particular due to the dynamics in hydrated fluid biomembranes. The ideal type of experiment to use needs to be determined and, most importantly, a single-set of experiments might not be valid in both the gel and the fluid phases.

In SS-NMR, distances are usually obtained through magnetization transfer, which mechanism depends on the physical state of sample. In rigid molecules, distances can be deduced from the measurement of coherent dipolar couplings between isolated spins, through dipolar recoupling sequences such as R2 (rotational resonance), REDOR (rotational-echo double resonance) or RFDR (radio-frequency-driven recoupling). In the presence of molecular motion, coherent dipolar couplings are averaged out, and an indirect way to access distances is to measure incoherent dipolar couplings through relaxation, spin diffusion or Nuclear Overhauser Enhancement (NOE) effects. Some two-dimensional (2D) SS-NMR sequences also allow detecting correlations between spins

that are not directly coupled. For example, in ^{13}C-^{13}C DARR and PDSD, the magnetization goes from a ^{13}C to a neighbouring ^{1}H, then to another neighbouring ^{1}H, and then back to a ^{13}C, usually nearby in space. Those sequences differ by their ^{1}H-^{1}H magnetization transfer mechanism, DARR relying on ^{1}H-^{1}H coherent dipolar couplings, while PDSD counts on ^{1}H incoherent spin diffusion. Similarly to the cases discussed above, DARR is more efficient in rigid molecules, while PDSD can be used with rigid molecules as well as in the presence of motion.

Membranes in the gel phase belong to the first category, where R2, REDOR, RFDR, DARR or PDSD have been used to measure distances in lipids[258-260] and in peptides[258,261-268]. In the fluid phase, ^{1}H-^{1}H NOESY under MAS has been employed to study lipid structure and dynamics, and the relative effects of NOE and spin diffusion[163,164,269]. Ramamoorthy and Jiadi also used this approach for the structural assessment of a membrane-bound antimicrobial peptide[270].

The magnetization transfer mechanisms between fluorine spins needs to be identified in order to extract distances, for example from ^{19}F-^{19}F cross peak buildup rates. We thus first used a standard molecule with similar NMR characteristics (isotropic chemical shift differences and CSAs) to the spin pair (RVS-monofluorinated PA) for which an unknown distance is to be determined. Hence we measured this buildup rate in a standard molecule with a well-known ^{19}F-^{19}F distance, namely sparfloxacin (SPX). This fluoroquinolone has two fluorine atoms (**Fig. 5.3A**) separated by a distance of ~ 4.73 Å. Moreover, previous theoretical studies have shown that similar types of molecules interact with lipid membranes, fluoroquinolones being found either on the surface or in the core of the bilayer, depending on the pH[271]. By adding a small amount of dipalmitoylphosphatidylcholine (DPPC), the two SPX polymorphs present in the pure compound are reduced to a single component and the system is in a dynamical regime similar to the one of the POPC/PA membranes. As seen in **Fig. 5.3B**, the two fluorine spins of SPX have isotropic chemical shifts of -85.1 ppm and -76.8 ppm, respectively, and noticeable differences in CSA values. This difference could result from a ring current effect due to circulating π electrons around the carbon and fluorine atoms, as commonly seen in ^{1}H NMR.

Interestingly, direct intramolecular ^{19}F-^{19}F dipolar coupling measurement in SPX incorporated into DPPC model membranes (DPPC/SPX molar ratio of 2:1) is possible using RFDR (**Fig. S5.3**) and, with a value of 5 Å, is in good agreement with the DFT-derived distance. **Fig. 5.4A** shows the 2D ^{19}F-^{19}F PDSD spectrum, and **Fig. 5.4B** the 2D ^{19}F-^{19}F DARR spectrum with additional ^{1}H-

^{1}H dipolar recoupling. The peaks are well resolved, even at a moderate spinning of 10 kHz, and correlation cross peaks are clearly noticeable.

Roos et al.[272] have shown that two scenarios need to be considered when measuring of ^{19}F-^{19}F internuclear distances: one in which the isotropic chemical shifts are identical but CSAs differ, and one where the isotropic chemical shifts significantly differ. In the first case, moderate spinning frequencies (10-25 kHz) and no ^{1}H-^{1}H recoupling (PDSD) are optimal for magnetization transfer while, in the second case, ^{1}H-^{1}H recoupling (DARR) accelerates this transfer[272]. The effect of ^{1}H-^{1}H recoupling and MAS frequency are thus good criteria to determine the regime in which a given ^{19}F pair is. **Fig. 5.4C** shows that at 10 kHz MAS, the cross peak intensity reaches its maximum after a short mixing time of 50 ms, with or without recoupling, while PDSD carried out at the much faster spinning frequency of 33 kHz slows down this transfer (**Fig. 5.4D**). With an isotropic chemical shift difference of 8 ppm and relatively large CSAs, the DPPC/SPX system appears to be in an intermediate situation.

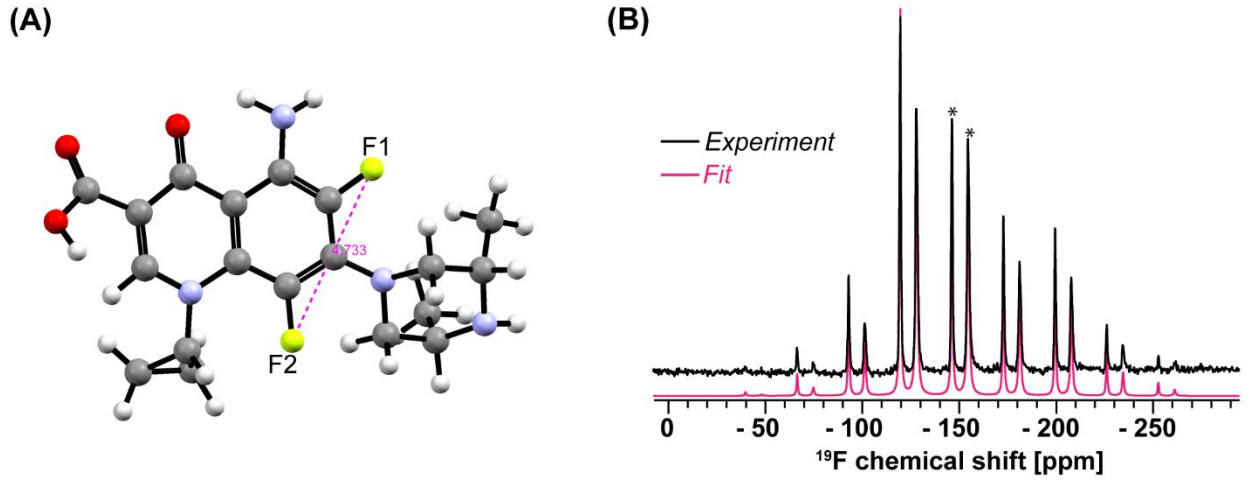

Figure 5.3: (A) DFT optimised structure of sparfloxacin and (B) ^{1}H-^{19}F CP MAS SS-NMR spectrum of the drug in DPPC at a DPPC/SPX molar ratio of 2:1. Experiments were performed at 5 $^{\circ}$C with ^{1}H decoupling, and MAS at 10 kHz. Asterisks (*) refer to isotropic peaks.

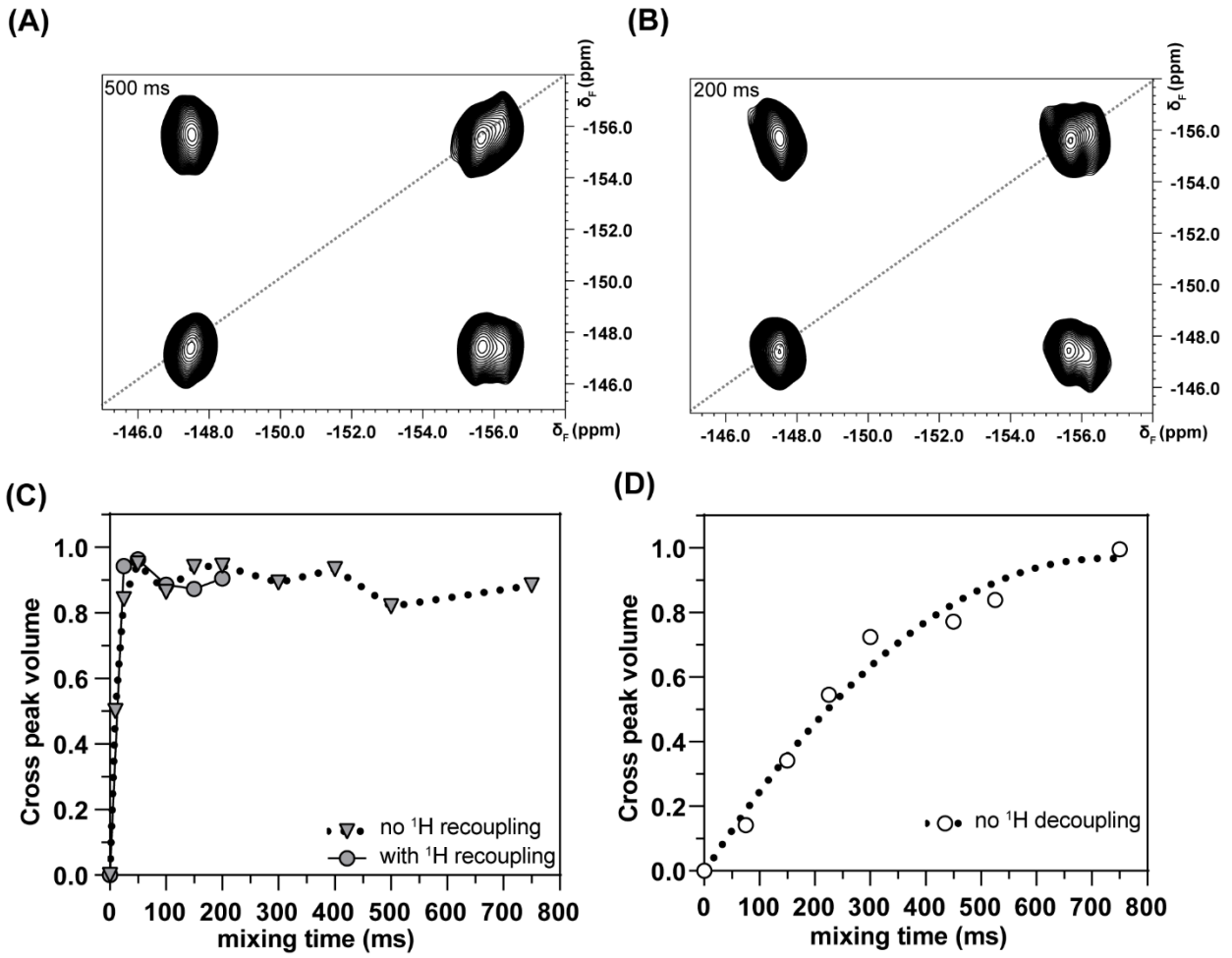

Figure 5.4: MAS-assisted 2D ^{19}F-^{19}F SS-NMR correlation spectra of sparfloxacin at a DPPC/SPX molar ratio of 2:1. (A) PDSD without ^{1}H recoupling and (B) DARR with ^{1}H recoupling. (C) Buildup curve obtained from 2D ^{19}F-^{19}F correlation spectra at 10 kHz MAS with ^{1}H decoupling (recoupled during mixing time) and (D) at 33 kHz MAS without recoupling or decoupling. Experiments were performed at 5 °C.

We then examined the possibility of measuring intermolecular distances between monofluorinated FAs or between a fluorinated drug and a FA, in order to determine the membrane structure or drug location. All our attempts to detect ^{19}F-^{19}F correlations between FAs in the model POPC/FA membranes in the fluid state have failed using RFDR, PDSD or DARR (data not shown). We therefore considered membranes in the gel state, at -3°C. It was not possible to establish spatial correlations between FAs through direct ^{19}F-^{19}F dipolar couplings via RFDR (data not shown). However, the 2D ^{19}F-^{19}F correlation spectra of fluorinated PAs incorporated in POPC membranes could be obtained using a standard ^{19}F-^{19}F PDSD **(A)** or a ^{19}F-^{19}F DARR **(B)** sequence

(**Fig. 5.5**). In the gel state, the peaks are well resolved, and correlation peaks between position 4 and 8 are clearly visible. DARR cross peaks, when ^{1}H recoupling is performed, are weaker than those observed on the PDSD spectrum (**Fig. 5.5B)**. This raises the question of the magnetization transfer mechanism between the fluorine spins. Lipid membranes form 2D liquid crystals with various types of motions depending on the phase. As shown before at -3 °C, the POPC/PA membrane exhibits motional restriction characteristic of the gel phase (**Fig. 5.2)**, at least in the PA-rich regions. Interestingly, ^{19}F PA(4)-PA(8) cross peaks could only be detected the gel phase. The fact that only this solid-like state provides the appropriate dynamical regime for magnetization transfer to occur is a good indication that ^{19}F-^{19}F NOE or ^{1}H spin diffusion are not the most efficient transfer mechanisms. Moreover, the intermolecular distance in this case is likely beyond the longest distance detectable by ^{19}F-^{19}F NOE, which can be estimated to 4-5 Å.

Without ^{1}H recoupling, the build-up of the off-diagonal ^{19}F-^{19}F cross peak intensities reaches a plateau at a mixing time of 200 to 300 ms, with a maximum transfer of 50 % at 10 or 13.3 kHz MAS frequencies, and of 80 % at a slower 3.3 kHz MAS (Fig. 5.5C). The reintroduction of ^{1}H–^{1}H dipolar couplings in DARR clearly reduces the magnetization transfer, as the maximum transfer at 200 ms reaches 20% at 10 or 13.3 kHz, and 60% at slower 3.3 kHz MAS (Fig. 5.5D). While in the case of ^{13}C SS-NMR, DARR has been shown to accelerate spin exchange[166], the behavior observed here is reminiscent of that observed for ^{19}F spins with the same isotropic chemical shift and different anisotropic chemical shifts, where the absence of ^{1}H-^{1}H irradiation accelerates the build up rate by up to a factor of 5[272]. The small difference in isotropic chemical shifts (1.7 ppm) between the PAs labeled on position 4 and 8, thus appears to be sufficiently small to favor this type of CSA-mediated spin diffusion. No cross peak intensity between FAs and the statin could be detected with mixing times up to 750 ms (data not shown). The strong discrepancy in isotropic chemical shifts (ca. 80 ppm) most likely prevents the same type of phenomenon to take place[272].

The magnetization transfer here is thus likely induced by a combination of CSA and dipolar mediated spin diffusion process, through a network of dipolar-coupled nuclei. Although NOE between dipolar-coupled fluorines cannot be entirely excluded, the abundance of ^{1}H nuclei with a high γ leads to a more tightly bound network through which diffusion is likely much more efficient. In the motionally-restricted gel phase, both dipolar couplings and large CSAs can contribute to magnetization transfer. The interplay of these NMR interactions will result in variations of cross

peak intensity buildup with and without ^{1}H recoupling and at different spinning frequencies[272]. As shown in **Fig. 5.5C and Fig. 5.5D**, with slower MAS frequency, the buildup rate is relatively faster, thus also confirming that the PA-F(4)/PA-F(8) pair is indeed in the case where isotropic chemical shifts are identical but CSAs differ. For this situation, the CODEX experiment should enable the detection of longer distances by ^{19}F SS-NMR[272].

The ^{19}F-^{19}F build ups in SPX and the POPC/PA membrane in the gel phase must be compared with caution, but we can assume that the slower magnetization transfer between PA-F(4) and PA-F(8) is indicative of a longer average intermolecular distance between them than the intramolecular 4.73 Å between the two fluorines of SPX. In no case under these conditions was a correlation between the drug and any of the FAs observed. Overall, the fact that a PA-F(4)/PA-F(8) distance can be measured, while no proximity between either PAs and the statin is observed, likely results from a phase separation between a PA partitioning into the gel phase, and statin partitioning into the fluid phase. While this information could already be guessed from the lineshape analysis of the 1D spectra, these results are a clear indication that a ^{19}F-^{19}F distance with a labeled PA can be measured within the bilayer. Admittedly, this type of information will become valuable if a distance can be measured between a FA and a guest molecule in the membrane.

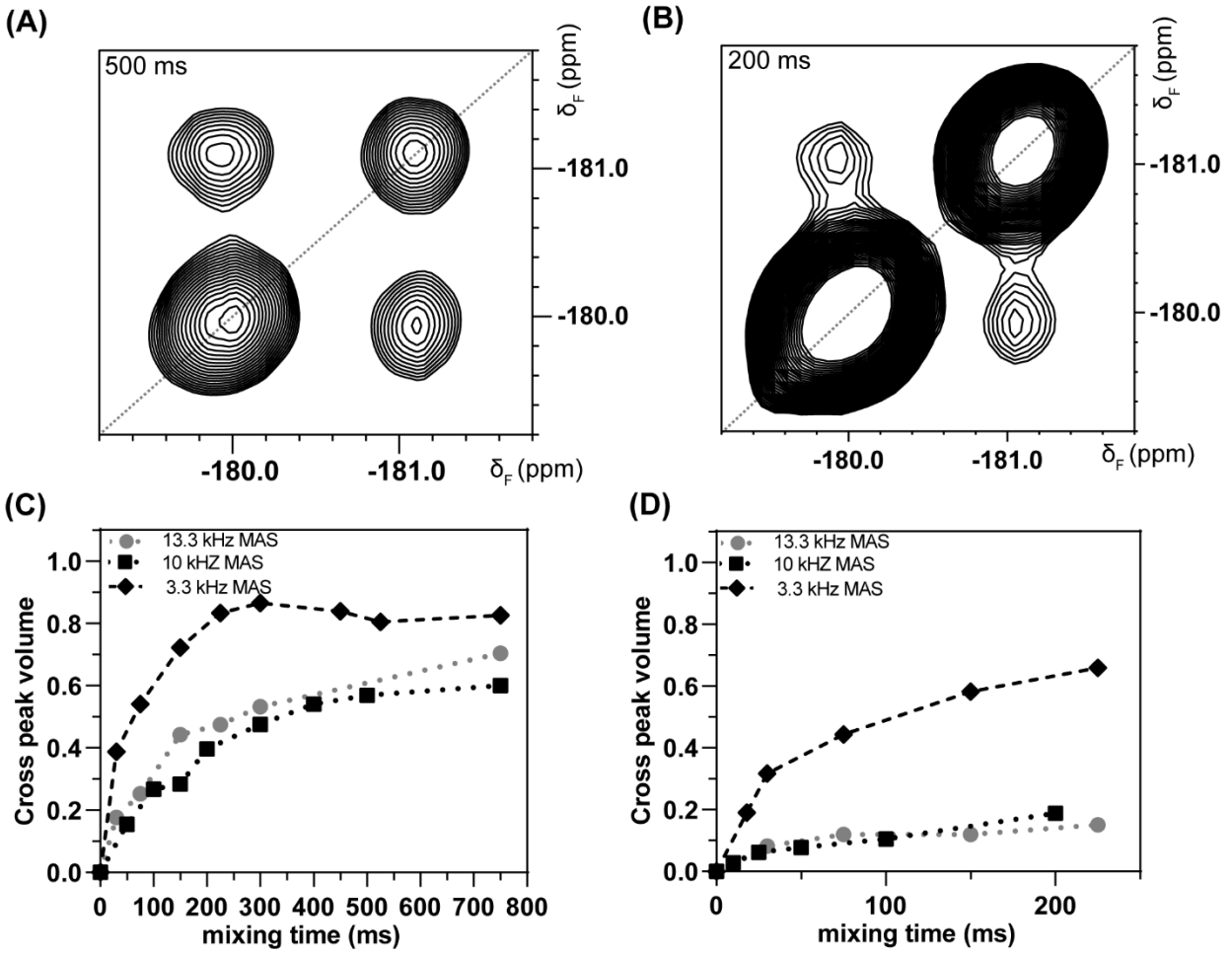

Figure 5.5: MAS-assisted 2D ^{19}F-^{19}F SS-NMR spectra of monofluorinated PAs incorporated in POPC membranes. (A) PDSD spectrum without ^{1}H-^{1}H recoupling and (B) DARR spectrum with ^{1}H-^{1}H recoupling. The POPC/PA-F(4)/PA-F(8) molar ratio is 4:1:1. (C) Buildup curve for 2D ^{19}F-^{19}F correlation spectra at different MAS frequencies obtained without ^{1}H-^{1}H recoupling and (D) with ^{1}H-^{1}H recoupling at different mixing times. Experiments were performed at -3 ˚C with ^{1}H decoupling during acquisition.

5.4.3 Localization of fluorinated molecules in a lipid bilayer

As mentioned earlier, our primary goal for ^{19}F labeling was to map the insertion of a guest molecule (drug or peptide) within the membrane by determining its distance relatively to ^{19}F atoms located at various positions on the FA acyl chain. As demonstrated in the previous section, it should indeed be possible using a POPC/^{19}F-PAs system. We thus attempted to locate RVS in the bilayer, using ^{19}F SS-NMR. The phase separation into PA-rich gel phase regions and POPC-rich fluid ones - in which the statin preferably partitions - prevents the measurement of RVS-PA distances. By

increasing the temperature, the bilayer can be made homogeneous but, unfortunately, in the fluid state, local motions drastically reduce coherent dipolar couplings and CSA, to the extent that standard SS-NMR techniques break down. Overhauser-effect cross-relaxation, on the other hand, has been shown to be efficient in fluid membranes, and ^{1}H-^{1}H homonuclear NOESY has indeed been used to locate statin molecules in lipid bilayers[253].

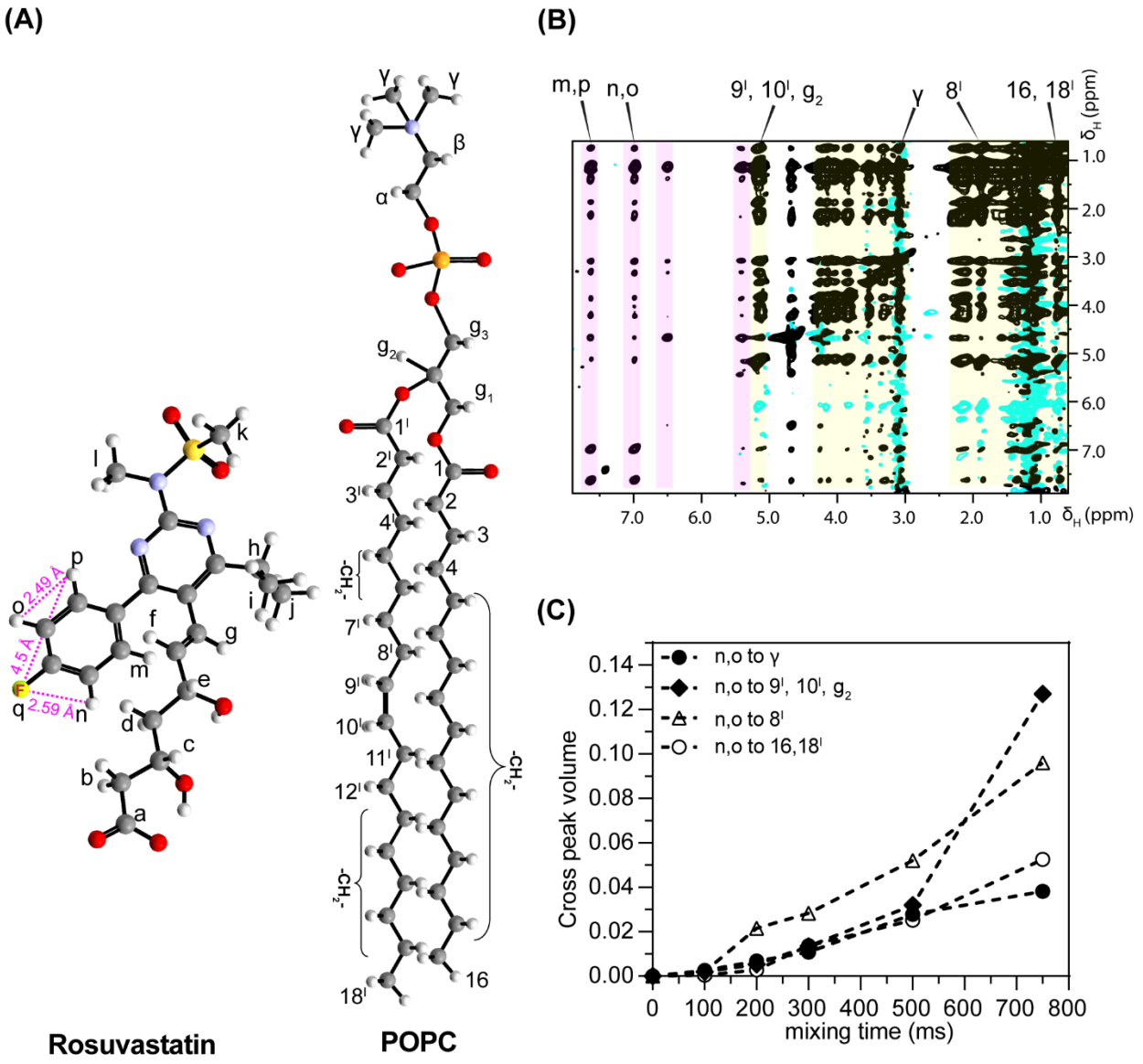

Figure 5.6: (A) DFT optimised structure of RVS and manually modeled structure of POPC. (B) 10 kHz MAS ^{1}H-^{1}H 2D NOESY spectrum with a 500 ms mixing time, of RVS incorporated into POPC/PA-F(4)/PA-F(8) of 4:1:1, with a lipid/PAs/RVS molar ratio of 40:20:3. (C) NOESY buildup curve for the cross peaks between the aromatic statin protons and the lipid protons. Experiments were performed at 35 °C. Black peaks are positive cross peaks. Blue peaks are negative signals that can be considered as artifacts.

Fig. 5.6 shows that ^{1}H-^{1}H NOEs could effectively be detected within the aromatic ring of rosuvastatin, as well as between RVS's aromatic protons and the lipids' protons, including the acyl chains. Whether these acyl chains belong to POPC or to the FAs could not be determined at this stage due to spectral overlap. Likewise, it was not possible through ^{1}H-^{1}H NMR to establish spatial proximities between FAs. As might be expected, the intramolecular cross peak buildup is fast within the aromatic ring of RVS, which reaches a plateau at a mixing time of *ca.* 500 ms, corresponding to a distance of ~2.49 Å. A much slower buildup was observed between these aromatic ^{1}H and those of the choline headgroup, the glycerol and the terminal acyl methyl group, with a slightly faster buildup for the statin to glycerol (g_2) NOE. An intermolecular distance between 2.5 and 5 Å is thus expected. The precise location of RVS with respect to the bilayer core cannot be determined, since contacts are evidenced with both the headgroup, middle section and acyl chains. One might also consider the presence of spin diffusion, which would prevent any such precise conclusions. Moreover, faster buildups of the cross peaks between the statin-protons and 8^{l} acyl chain protons, and with the g_2 protons were noticeable and thus, statins are likely positioned closer to these two protons, in the upper part of the membrane.

The use of ^{19}F-labeled FAs should enable the measurement of ^{1}H-^{19}F distances using *heteronuclear* Overhauser experiments (HOESY) in the fluid phase - the natural state of biological membranes. The maximum distance that ^{1}H-^{19}F Overhauser effect allows to probe probably lies slightly below the 5 Å standard upper distance stated for the ^{1}H-^{1}H case. The main advantage of using ^{19}F NMR is the reduction in spectral overlap, easily enabling the identification of fluorinated molecules including FAs - a key feature if the measurements are performed in a complex environment such as a native whole cell membranes. **Fig. 5.7** shows a ^{1}H-^{19}F 2D HOESY spectrum with a mixing time of 500 ms, of RVS incorporated into POPC/PA-F(4)/PA-F(8) membranes, at 35°C and MAS at 10 kHz. Intermolecular contacts between the statin's ^{19}F atom at around -110 ppm and the ^{1}H of acyl chains are readily detectable and easy to identify. The build up of characteristic statin intramolecular cross peaks, as well as intermolecular statin cross peaks with choline, glycerol and acyl chain terminal groups are shown in **Fig. 5.8A & C**. The fastest buildups are, of course, the intramolecular ones, between the statin ^{19}F and aromatic protons, followed by the intermolecular cross peak between the statin ^{19}F and the 8^{l} proton on the lipid acyl chain, again asserting statin location in bilayer.

These ^{1}H-^{19}F results enable a more precise characterization of the statin insertion than by using the traditional ^{1}H-^{1}H approach. Indeed, the intermolecular buildup provides an estimate on the distance, which falls below the longest intramolecular distance of ~4.5 Å and also sets an upper limit as to the distances that can be probed. Cross peaks with a slow build up are observed between methyl groups (k, l) of RVS and both PAs, indicating that RVS are located close the 4th and 8th carbon of the acyl chains in the membrane. In addition, both ^{19}F atoms of PAs give strong correlations to 8^{I} protons of lipids, confirming their close proximity to lipids. A cross peaks with fast buildup is noticeable between the PA-F(4) to RVS's methylene (h), while no cross peak is observed between (h) and PA-F(8), indicating the proximity of h and PA-F(4) (**Fig. 5.7** and **5.8D**). Although, direct ^{19}F-^{19}F experiments did not provide useful information in the fluid state, the location of statin in the bilayer is thus confirmed by ^{1}H-^{19}F experiments.

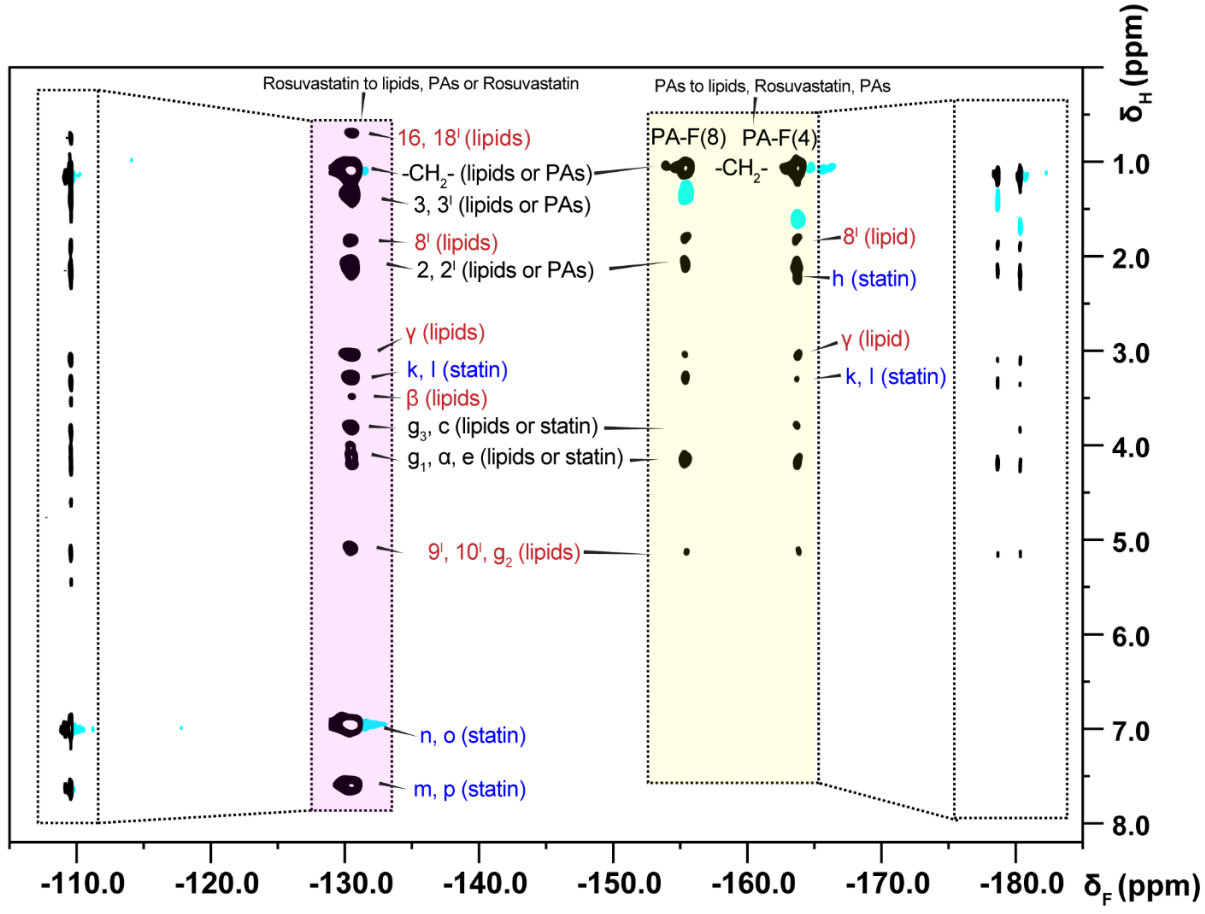

Figure 5.7: 10 kHz MAS ^{1}H-^{19}F 2D HOESY spectrum, with 500 ms mixing time, of RVS incorporated into POPC/PA-F(4)/PA-F(8) of 4:1:1, with a lipid/PAs/RVS molar ratio of 40:20:3. Experiments were performed at 35 °C. Black peaks are positive cross peaks. Blue peaks are negative signals that can be considered as artifacts.

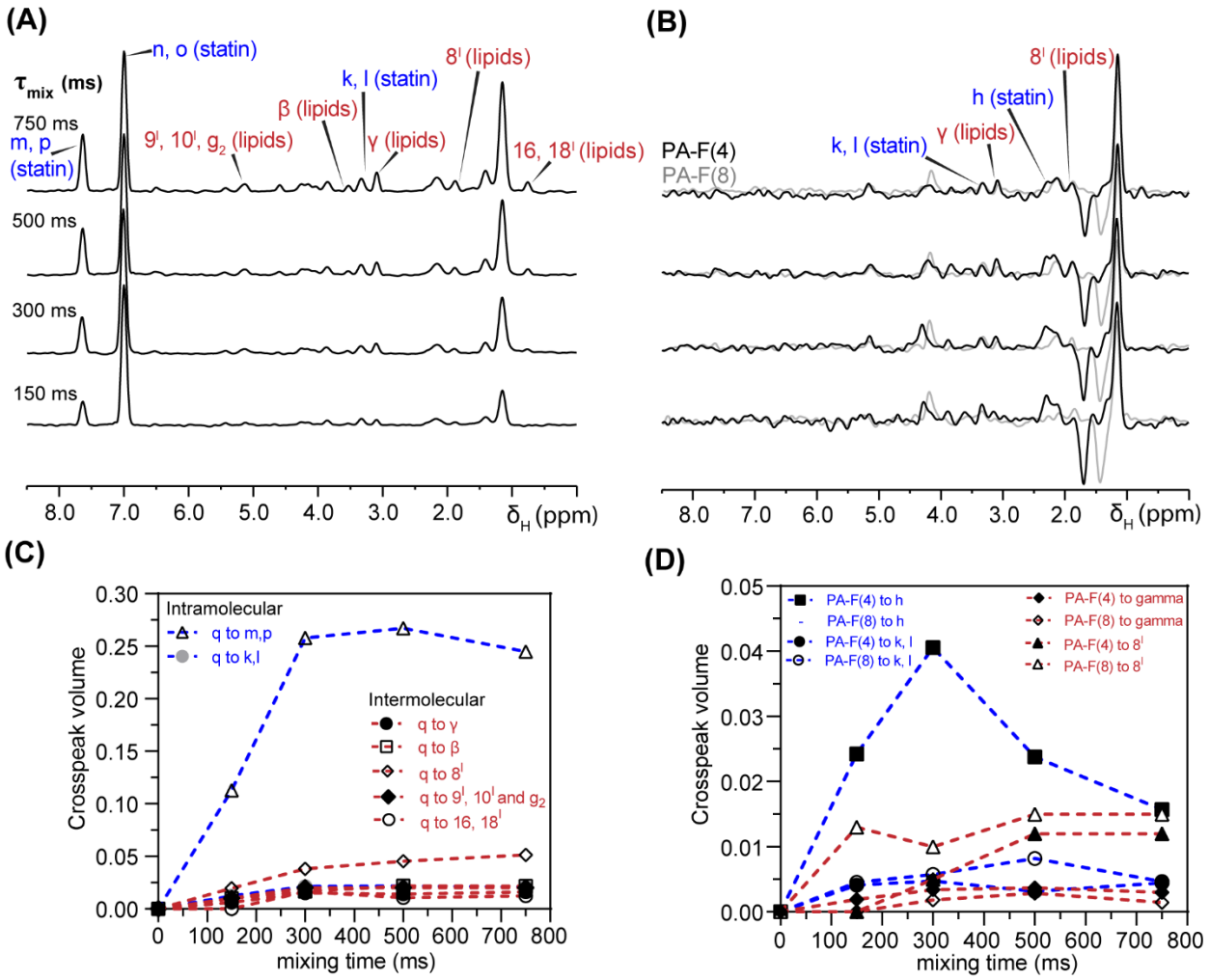

Figure 5.8: 1D ^{1}H slices from the 10 kHz 2D ^{1}H-^{19}F HOESY at different mixing times, of RVS incorporated into POPC/PA-F(4)/PA-F(8) of 4:1:1, with a lipid/PAs/RVS molar ratio of 40:20:3. (A) at the ^{19}F chemical shift of statin, and (B) at the ^{19}F chemical shift of PAs, and (C) 10 kHz 2D ^{1}H-^{19}F HOESY build up curves between the fluorine of statin to aromatics protons of statins and lipid protons. Peak integral is normalised to n, o peaks (~2.59 Å). All experiments were performed at 35 °C with ^{1}H decoupling.

5.5 Conclusion

This work showed that the incorporation in model membranes of FAs with ^{19}F labels at different positions on the acyl chain allows studying the interaction of host molecules. Structural questions could be addressed by measuring ^{19}F-^{19}F distances, or at least enable establishing spatial proximities. Below the phase transition temperature, phase separation could be evidenced by detecting spatial contacts between PAs, but no contact between PAs and rosuvastatin. Magnetization transfer mechanisms were carefully analysed and in the fluid phase, we showed that

one could only rely on NOEs, and demonstrated the advantages of using ^{1}H-^{19}F NOEs, easing spectral assignment and greatly reducing spectral overlap.

Within a broader context of whole cell SS-NMR, and the long-term goal of in cell NMR, two strategies need to be developed. The first one attempts to measure internuclear distances in conditions as native as possible, therefore in the fluid phase, using heteronuclear ^{1}H-^{19}F NOEs. This implies the development of more strategically fluorinated molecules, to make distance measurements amenable. A second strategy would be to use SS-NMR approaches, by first freezing down membrane motions, while maintaining membrane structure and preventing phase separation or conformational change.

5.6 Author contributions

Kiran Kumar: Formal analysis, Investigation, Methodology, Validation, Visualization, Writing – original draft. Alexandre A. Arnold: Conceptualization, Formal analysis, Investigation, Methodology, Supervision, Validation, Writing – review & editing. Raphael ¨ Gauthier: Investigation, Methodology. Marius Mamone: Investigation, Methodology. Jean-François Paquin: Investigation, Supervision, Methodology, Resources, Writing – review & editing. Dror E. Warschawski: Conceptualization, Formal analysis, Methodology, Supervision, Writing – review & editing. Isabelle Marcotte: Conceptualization, Funding acquisition, Project administration, Resources, Supervision, Writing – review & editing, Methodology.

5.7 Acknowledgements

This research was funded by the Natural Sciences and Engineering Research Council (NSERC) of Canada (grant RGPIN-2018–06200 to I.M.) and the Centre National de la Recherche Scientifique (UMR 7203 to D.E.W.). K.K. would like to thank the Quebec Network for Research on Protein Function, Engineering, and Applications (PROTEO) - strategic cluster of the Fonds de recherche du Québec – Nature et technologies (FRQNT) - for the award of a scholarship. The authors thank Pierre Audet (Université Laval) for the loan of the HFX probe.

5.7 Supplementary information

Additional spectra and assignments of RVS:

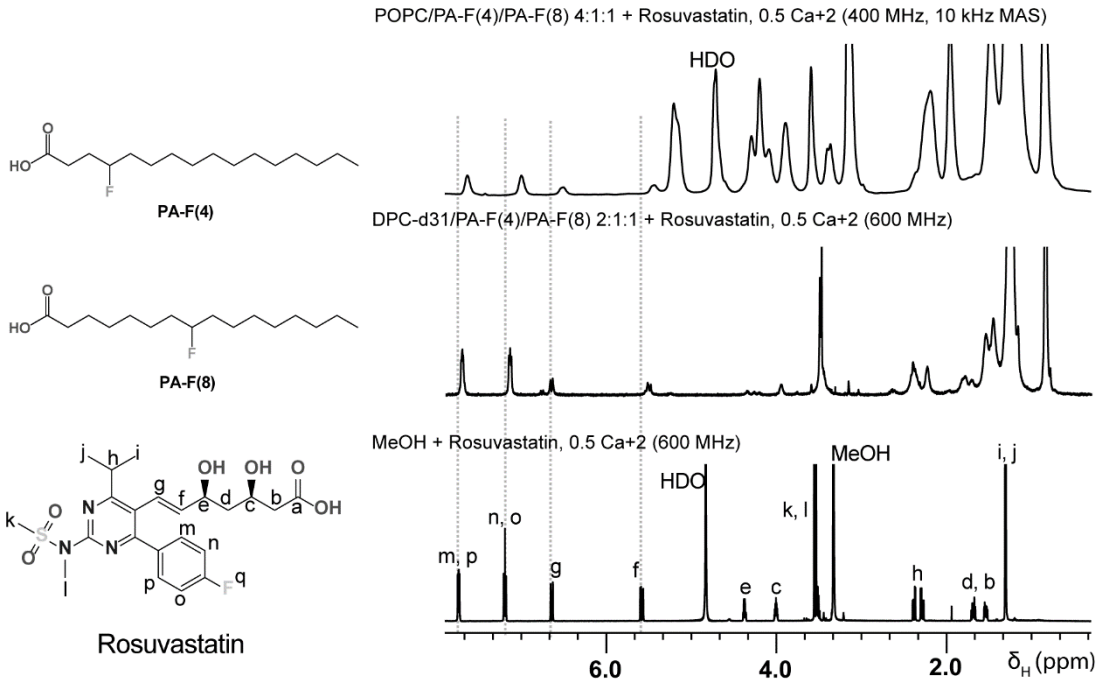

Figure S5.1: ^{1}H NMR spectrum and assignments of RVS molecule in different systems. All experiments were performed at 30 °C.

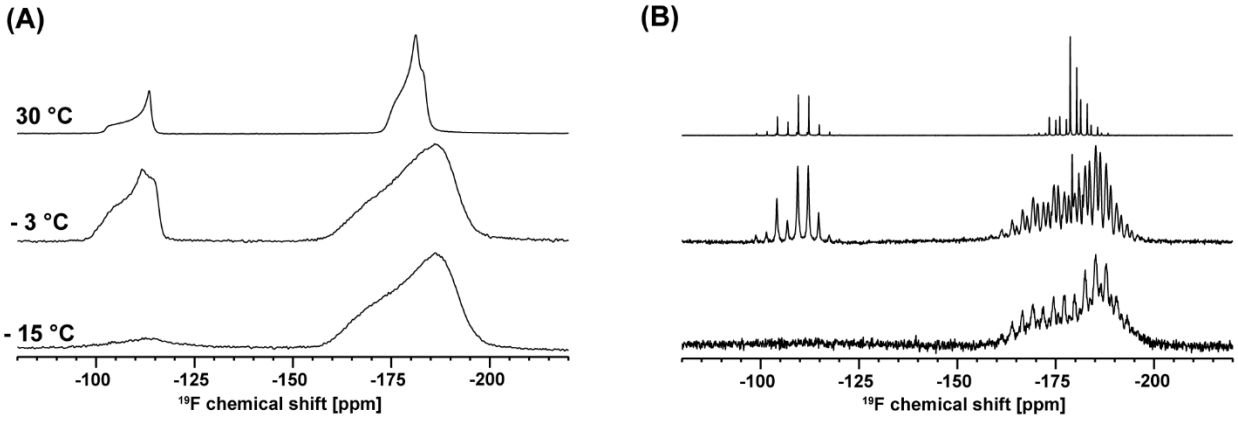

Figure S5.2: (A) Static and (B) 1 kHz MAS ^{19}F SS-NMR spectra of POPC model membranes incorporating monofluorinated PAs, at a POPC/PA-F(4)/PA-F(8) of 4:1:1, with RVS at a lipid/PAs/RVS molar ratio of 40:20:3. Experiments were performed at different temperatures with ^{1}H decoupling. PA resonances are on the right (circa -180 ppm), while statin resonances are on the left (circa -105 ppm).

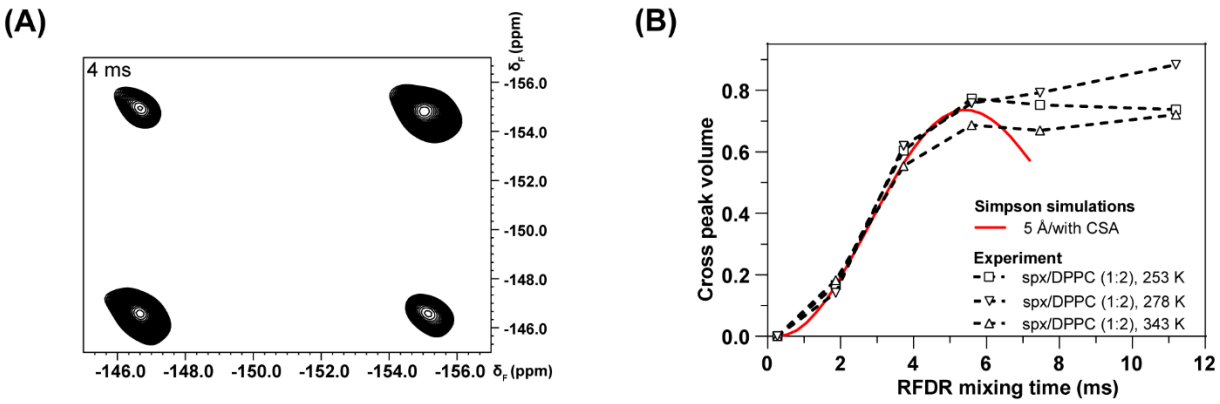

Figure S5.3: (A) 2D ^{19}F-^{19}F RFDR spectrum, with 4 ms mixing time, and (B) ^{19}F-^{19}F RFDR buildup curve in DPPC/spx (2:1) samples, obtained at 10 kHz MAS frequency with ^{1}H decoupling.

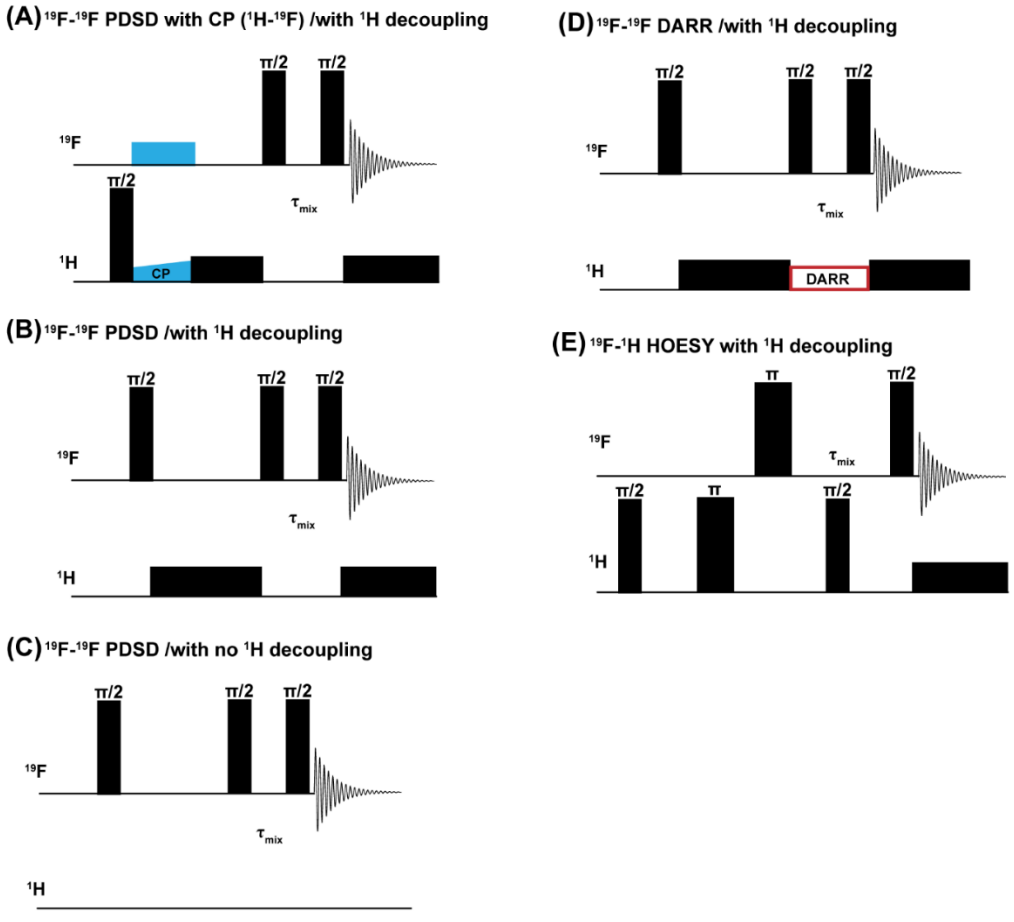

Figure S5.4: Typical pulse sequence used in 2D PDSD, DARR and HOESY experiments

CHAPTER VI

Conclusion and Perspectives

Cell membranes are complex dynamic assemblies of various biomolecules including diverse lipids which makes the exploration of plasma membranes a frontier. The physical and chemical properties of lipid membranes have been well characterized in the past decades using model membranes or membrane mimetics. As summarised by Edidin[273], three main components which are missing in model systems are: (1) dynamics, (2) membrane traffic, and (3) association of the cytoskeleton with the bilayer. Although dynamics in model membranes resemble that of plasma membranes, it is not complete, considering the diversity of molecules, specific ordered domains, cytoskeleton and various other plasma membrane constituents. In this regard, the main focus of this thesis was to study the molecular interaction of peptides with intact erythrocyte ghosts, using specific ^{2}H and ^{19}F membrane labels and to characterize major plasma membrane lipids from erythrocytes.

In summary, this thesis shows that erythrocyte ghosts can be labeled efficiently with ^{2}H- and ^{19}F-PAs for the study of AMPs interaction with their membranes. The labeling strategy should be amenable to other isotopic and FAs labels. At first, a detailed lipid profile characterization of the erythrocytes ghosts was presented and their dynamics in erythrocyte membrane studied, and compared with their representative model membranes. The use of ^{31}P and ^{2}H SS-NMR to study erythrocyte membrane perturbation by AMPs aurein 1.2 and caerin 1.1 was discussed, and lipid-to-peptide molar ratios where membrane perturbation occurred were identified. Leakage assays performed on intact erythrocytes, ghosts, and model membranes of bacteria/erythrocytes allowed to identify a minimum value for lytic activity in such systems, which was then compared with a reported MIC. This comparison showed that both these AMPs have a higher activity towards erythrocyte membranes and a poor therapeutic potency in their current versions. However, one might have to consider MICs cautiously, as mentioned in the section 1.2.5, comparing activity with a same cell concentration of bacteria and erythrocytes might provide a better insight on their therapeutic value. SS-NMR experiments performed on ghost membranes revealed that AMPs perturb erythrocytes by a similar mechanism of action as the one that takes place in bacteria, also confirmed by microscopy experiments. Aurein 1.2 interacts via a carpet like mechanism, and caerin 1.1 forms a pore in the membrane, creating high-curvature regions in the membrane.

In a second step, the use of ^{19}F SS-NMR for studying peptide-membrane interactions was assessed, probing ^{19}F labels at different depths of the membrane. This was done by using monofluorinated PA on position 4, 8 or 14. First, conditions were established on model membranes. By monitoring of the ^{19}F CSA, the isotropic chemical shift, and relaxation times, our work ascertained that caerin 1.1 acts via a pore formation mechanism in erythrocyte membranes. Lastly, the use of ^{19}F SS-NMR to determine intermolecular distances in membrane bilayers was evaluated. Model PC membranes integrating both PA-F(4) and PA-F(8) were used to map the insertion depth of a test drug – the fluorinated rosuvastatin – and develop the SS-NMR methodology. Various 2D correlation experiments were assessed on membranes in the gel and fluid phases. They allowed the detection of inter-PA contacts in the gel phase, and drug-lipid contacts in the fluid phase. These experimental strategies aim to set the adequate conditions for future whole cell experiments and other AMPs studies.

Overall, this thesis aimed to better understand the action of AMPs on cell membranes, and the methodological approach established open the possibility of developing new biophysical and SS-NMR tools for whole cell and *in vivo* studies. It should be noted that the methodology can be transposed to study other microorganisms, prokaryotes or eukaryotes. Furthermore, the techniques developed in this thesis can also enable the screening of antibiotics to assess their interactions with erythrocyte membranes.

6.1 ^{31}P, ^{2}H and ^{19}F SS-NMR of erythrocyte ghosts

The dynamics of phospholipids in biological membranes provides an essential meaning, and are characteristic of the structure and function of cell membranes. The study of phospholipid models was performed using various experimental techniques, and the challenge was to keep membranes in the fluid phase, as in native membranes. SS-NMR provides certain opportunities in this direction, as it is feasible with intact cells, for example, as seen in Chapters 3 and 4 using erythrocyte ghosts. The membrane phase of ghosts can be studied using ^{31}P SS-NMR, but fast data acquisition can be facilitated by using ^{2}H and ^{19}F labels. Specific labeling also enables to study the dynamics at different depths of the bilayer, and to study molecular interactions with erythrocyte membranes. Although deuterated and fluorinated PAs have been employed in this thesis as a labeling strategy, one might consider using labeled lipids such as DPPC-d62 for labeling, as shown by Maraviglia et *al.*[144]. However, no morphological alteration of erythrocyte membranes was seen

using PAs and labeling using PAs is superior in terms of simplicity. Notably, they are amenable to an aqueous environment by incorporating them as mixed micelles, as seen in Chapter 3, and stable micelles can facilitate the PAs incorporation into biological membranes at a relatively lower temperature and in a few steps. Also, deuterated PAs are commercially available and cheaper than deuterated lipids, and different isotopic analogues are available such as ^{13}C labeled PAs.

6.2 ^{19}F labeling of model membrane and other cells

This thesis showed that, ^{19}F PAs are an excellent probes to study the membrane phase behavior and dynamics. Likewise, ^{19}F labels can also be incorporated on phospholipids to prepare simple model membranes. For example, Gagnon et *al.*[232] have shown the use of fluorinated DMPC in the study of membrane-active peptides as well as the possibility of fluorinating DMPC at different positions along the acyl chains. This labeling method can be extended to various other biologically relevant lipids such as POPC and SM. Fluorinated cholesterol is already commercially available and can also be used in specific membrane-peptide interactions studies. However, one might study ^{19}F labels in membrane cautiously, since a high content of ^{19}F labels might affect the membrane organisation. Indeed, Gagnon et *al.*[232] showed that incorporation of a fluorine label into extreme segments of the phospholipid acyl chain, such as position 2 or 14 (in DMPC), induced significant perturbations.

One main advantage of using PAs in prokaryotic systems such as bacteria is that it will contribute to the conversion of PAs into desired lipids, through biosynthesis. ^{2}H and ^{19}F labels have already been employed in past works for whole cell labeling, mainly for prokaryotic cells such as bacteria. For example, Tardy-Laporte et *al.*[139] have used the deuteration of *E. coli* cells and proposed a methodology for studying molecular interactions with intact cells. Likewise, others[57,69,140,156,207] have extensively followed the deuteration in *E. coli* and *B. subtilis* to investigate interactions of different antimicrobials including AMPs by in-cell ^{2}H SS-NMR. ^{19}F labels for whole cell SS-NMR had not been pursued thoroughly, besides some early attempts. Gent et *al.*[223] have ^{19}F-labeled *E. coli* cells, and conducted ^{19}F SS-NMR experiments to study membrane fluidity, mainly relying on static spectra for analysis, without ^{1}H decoupling. Macdonald et *al.*[221] have followed ^{19}F labeling in *Acholeplasma laidlawii B* membranes and described the order profile, but again the analysis was done mainly using static spectra without ^{1}H decoupling. Static

experiments, particularly without ^{1}H decoupling, limit the possibility of fast NMR signal acquisition. Our preliminary experiments demonstrate the possibility of ^{19}F labeling for the fast acquisition of bacteria with a specific interest in the Gram (+) *B. subtilis*, which has a single plasma membrane (Fig. 6.1).

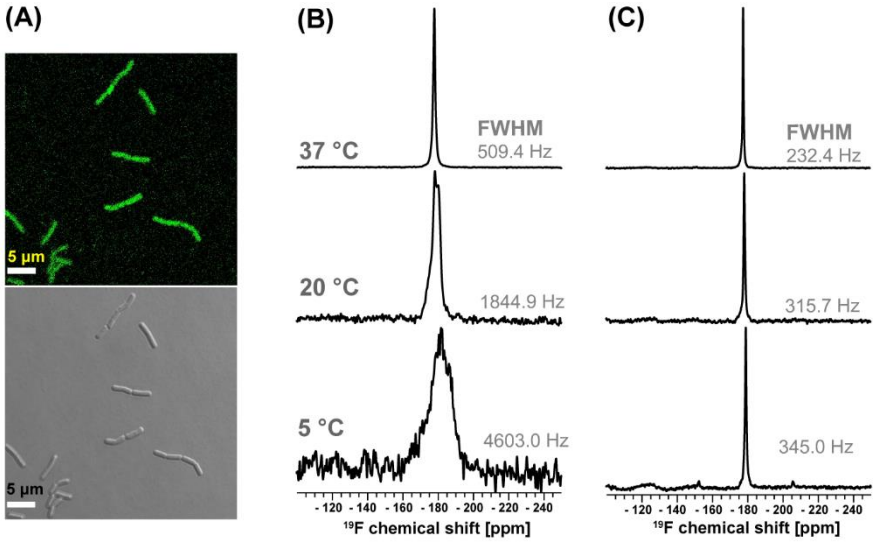

Figure 6.1 : (A) Confocal fluorescence microscopy images of fluorinated *B. subtilis*, in which PA-F(8) is incorporated with fluorescent NBD-PAs. (B) Static and (C) MAS (at 10 kHz) ^{19}F SS-NMR spectra of bacteria incorporating PA-F(8) recorded at different temperatures. Static spectra were obtained with 12k scans (7h) and MAS spectra were obtained with 6k scans (3h). All experiments were performed with ^{1}H decoupling. The full width at half maximum (FWHM) is presented for comparison.

As seen in Fig. 6.1, PA-F(8) is effectively incorporated into *B. subtilis'* membranes, following the protocol described elsewhere[69]. The membrane morphology of *B. subtilis* is unaltered and an incorporation of PA-F(8) of up to 40-60 % is obtained (data not shown). Static and MAS ^{19}F SS-NMR spectra reveal a noticeable reduction in line width with increasing temperature (Fig. 6.1B), indicating increased dynamics, and more experiments need to be conducted at additional temperatures to identify the gel and fluid phase boundaries. ^{19}F MAS SS-NMR enabled fast acquisition. Although, data shown in Fig. 6.1C are presented with 6k scans to provide a very high S/N ratio, fewer scans would be sufficient for line width analysis. These preliminary results are promising, and different ^{19}F labels can be utilised. One can also monitor the interaction of antimicrobials in whole cell bacteria labeled with ^{19}F – the future step in this project.

The preliminary lipid profile analysis by MALDI mass spectrometry of fluorinated *B. subtilis* indicated that some fluorinated PAs were converted to fluorinated phospholipids (active labeling, data not shown). However, additional PA peaks were identified in labeled *B. subtilis* lipid extracts, showing that some intact fluorinated PAs were inserted in the bacterial membranes (passive labeling). In principle, either though active or passive labeling, the strategy described in this thesis is useful for prokaryotic and eukaryotic cell membrane studies. For passive labeling, one might need to consider relative proportions of lipids *vs.* exogenous FAs, while compromising with NMR signal intensity, as too many FAs could potentially alter the bilayer structure. A detailed study of such specific lipid/FAs phase diagram may be necessary, as it is necessary to conduct molecular interaction studies with membranes in the fluid phase.

One main disadvantage of using FAs in lipid membranes is the risk of phase separation and domain formation. Shimokawa et *al.*[213] studied the phase behavior of lipid membranes containing FAs, and showed the formation of liquid-ordered and solid-ordered phases in PA-containing DPPC/cholesterol membranes. The phase separation in such multicomponent systems is inevitable, and one might have to choose an ideally mixed condition to replicate the conditions found in native membranes. The binary phase diagram of DPPC/PAs is well studied[239], for example, distinct homogeneous fluid or gel phases are seen at a wide range of temperatures and molar ratios. If an appropriate amount of PA is used, membrane phase behavior and dynamics can be studied. PA labels can report on overall membrane fluidity and its variation, either though ^{2}H or ^{19}F SS-NMR.

6.3 Distance measurement in whole cells

In this thesis, distance measurement methods in lipid membranes are discussed, as seen in Chapter 5 with ^{19}F SS-NMR experiments, to provide useful information on the spatial location of drug molecules in a bilayer environment. Also, numerous efforts have been made to conduct specific distance measurement experiments (e.g. REDOR) in whole cells with AMPs, and were faced with two main challenges: (1) low peptide concentration and (2) high membrane dynamics.

First, for a given NMR rotor, the sample volume is limited, which can be compensated by using specific isotopic labeling of AMPs, such as ^{13}C on particular amino acids. ^{19}F labeling of AMPs is a superior alternative if the peptide activity is unaltered. Second, in order to the reduce membrane dynamics, REDOR experiments are usually performed at extremely low temperatures,

which makes the membrane rigid. Unfortunately, as a consequence of this ordering, the peptide may be expelled from the bilayer's hydrophobic core, the distance becomes longer to membrane acyl chains, and the information gathered would not be biologically relevant. All the different depths of ^{19}F labels used this thesis failed to reveal a contact with ^{13}C-labeled Val-l7 on caerin (data not shown). However, more investigation is required on AMPs with more ^{13}C-labeled sites, or fluorinated amino acids. Since the distance between the ^{19}F atom on the FAs and the guest molecule can depend on the experimental temperature, REDOR might not be the ideal experiment, even though it may provide mechanistic insights on peptide/membrane interactions. Alternatively, one might study the peptide in fluid membranes, and than perform fast freezing and lyophilization, to try preserving the interaction. For example, Tang et *al.*[259] showed the use trehalose as lyoprotection to preserve lipid dynamics as well as the possibility of measuring intramolecular distances in lipids using REDOR. Caution is advised to interpret such results in case of membrane-peptide interactions, and conformational changes could occur. Also, low temperature experiments can be facilitated using faster NMR signal acquisition by employing other advance methods such as DNP. Separovic et *al.*[274] discussed the possibility of using REDOR. They showed that DNP enhanced the ^{15}N NMR signals from nucleic acids, proteins, and lipids in *E.coli* cells, and reported the multi-target impact of AMPs but no direct contact between lipids and peptides. Kuzhelev et *al.*[275] also introduced the possibility of fluid-phase DNP experiments with lipids and showed the 32-time signal enhancement in ^{1}H NMR, which reinforces the possibility of DNP applications in whole cells. Any experiments performed in the fluid phase with intact cells will be superior, with specific labels such as ^{19}F, and can be complemented with specific distance measurement experiments in the gel phase. In a fluid membrane phase, measuring NOE contacts provides a greater opportunity as shown in Chapter 6, but ^{1}H-^{1}H NOESY is indeed difficult in case of whole cells due to overlapping of ^{1}H NMR signals from different cell constituents, Here again, the NOE approach will make ^{19}F labels very useful, in fluid membranes and for whole cell interaction studies.

6.4 Future directions

The AMPs aurein 1.2 and caerin 1.1 show an efficient membrane activity and interact with both bacterial and erythrocyte membranes. Perhaps it is too preliminary to decide the therapeutic merits of these AMPs, and further development could increase their selectivity towards bacteria, by peptide engineering, and improve their commercial potential. For example, Lorenzón et *al.*[276] showed that dimerization of aurein results in a less pronounced lytic effect on both bacteria and RBCs, suggesting a different mechanism of action. As discussed by Marta de Zotti in New and notable report[277] on this thesis chapter 3 "*The next step may be the spectroscopic study of peptide-membrane interactions in the presence of both bacteria and RBCs, orthogonally labeled to be studied at the same time*". As labeling methodology described in this thesis, membrane of ghosts and bacteria could be labeled separately using two different types of PA labels - ^{2}H-PAs for ghosts and ^{19}F-PAs for bacteria. After labeling, the ghosts and bacteria could be mixed, and AMPs can be added to observe their interaction with the membrane. This method allows for monitoring of membrane interactions with both ^{2}H and ^{19}F in the same sample, making it an efficient way to study membrane interactions. Likewise, PA-F(4) and PA-F(8) can be used to study membrane interactions by SS-NMR with ghosts and bacteria, respectively. FROCSA experiments could be used to monitor changes in ^{19}F anisotropy (CSA) with AMPs, as CSA changes are expected from membrane perturbations and could be measured accurately with membranes of both cells.

This thesis improved our understanding of AMPs mechanistic behavior, but by providing a new methodological approach based on ^{2}H and ^{19}F labeling, it contributed to advance the study of specific details regarding the localisation of AMPs in plasma membranes. The labeling strategies presented with RBC ghosts are in principle amenable to other cell types, including intact erythrocytes to answer specific questions such as the association of cytoskeleton with bilayer or to study membrane dynamics of erythrocytes. Some cell types could be more challenging, such as algal cells, but FA metabolism in algae may first need to be controlled because PAs are often directed towards lipid droplets. PAs labeling in human neuron and pancreatic cells would open the possibility to address other pathologies, such as amyloid diseases, but it may also require fine tuning since those cells are also more fragile and may not resist centrifugation and MAS. Overall, this thesis contributed to expand our knowledge of membrane biophysics and improved our understanding of the action of AMPs on biological membranes.

Appendix A

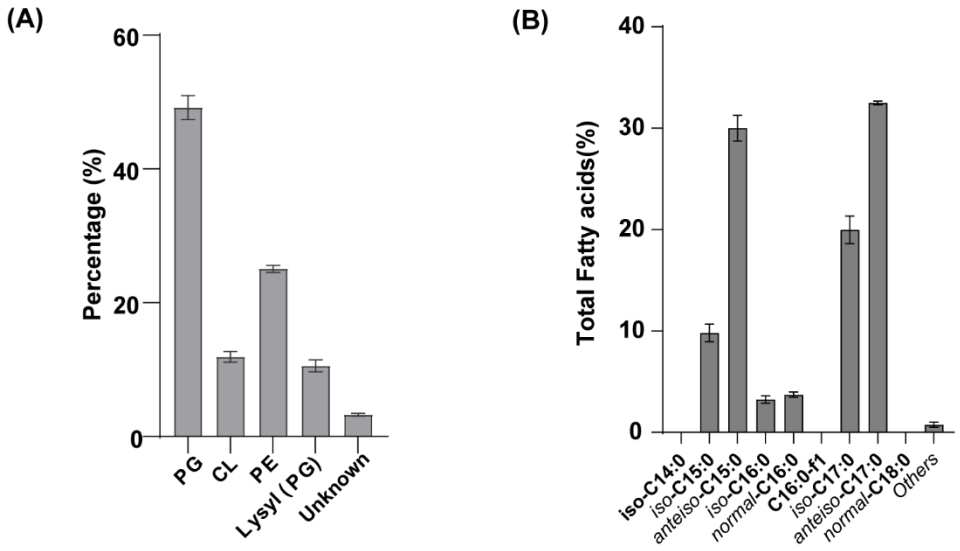

Additional figure : (A) Lipids, (B) FAs profile of *B. subtilis*, extracted at stationary phases.

Appendix B

General information

The following includes general experimental procedures, specific details for representative reactions, isolation and spectroscopic information for the new compounds prepared. All commercial compounds were used as received. Solvents were used as purchased unless stated as dry. THF, CH_2Cl_2 and Et_2O were purified using a Vacuum Atmospheres Inc. Solvent Purification System. All air and water sensitive reactions were carried out under argon atmosphere. Reactions were monitored by TLC on pre-coated plates (Silicycle silica gel 60 Å F254 230-240 mesh) and products were visualized under 254 nm UV light followed by staining with $KMnO_4$ or PMA. Purification by flash column chromatography was carried out on silica gel (Silicycle silica gel 60 Å, 230-400 mesh) or on Biotage® Isolera One Flash Chromatography System using the same silica gel in SNAP cartridges. All reported yields are based on weighted mass of desired product, except if stated otherwise. NMR spectra were recorded on an Agilent DD2 500 spectrometer or on a Varian Inova 400 spectrometer in the indicated solvent at 298 K. Chemical shifts for ^{1}H and ^{13}C spectra are reported on the delta scale in ppm and were referenced to TMS reference. For ^{19}F, $CFCl_3$ is used as external standard. Resonances are reported as follows: chemical shift (δ ppm), multiplicity (s = singlet, d = doublet, t = triplet, q = quartet, m = multiplet, br. s = broad signal), coupling constant (Hz), integration. High-resolution mass spectra (HRMS) were obtained on a LC/MS-TOF Agilent 6210 using electrospray ionization (ESI). Infrared spectra were recorded on an ABB MB3000 FT-IR spectrometer. Melting points were measured on a Stanford Research System OptiMelt MPA100 automated melting point apparatus and are uncorrected.

1. General procedure for the synthesis of fluorinated palmitic acids

Following synthetic pathway was inspired by our previously reported method.[1]

[1] Guimond-Tremblay, J.; Gagnon, M.-C.; Pineault-Maltais, J.-A.; Turcotte, V.; Auger, M.; Paquin, J.-F. *Org. Biomol. Chem.* **2012**, *10*, 1145-1148.

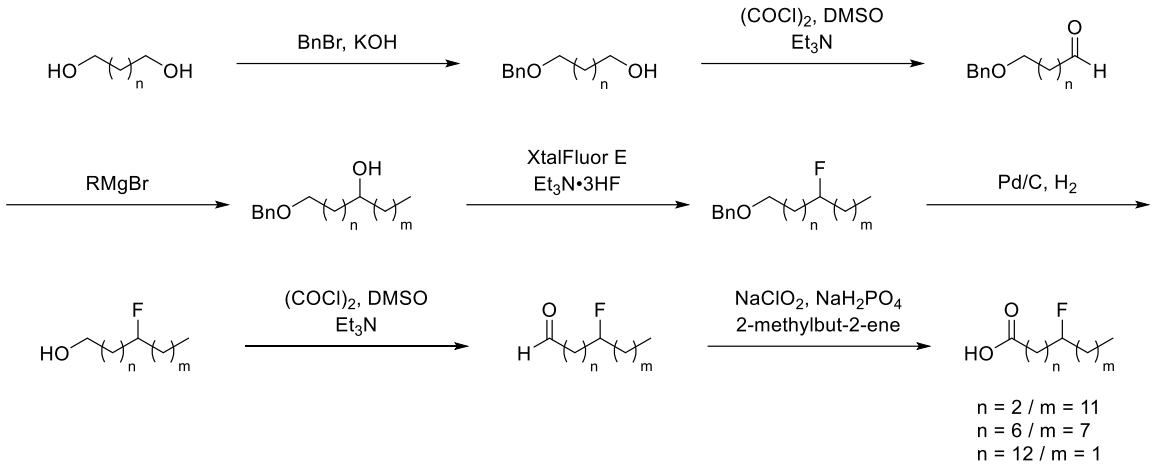

General procedure A: monobenzylation of diol

KOH (4.1 equiv) and BnBr (1 equiv) were added in 4 portions on heated diol (4.4 equiv) over 1 h. The reaction was stirred over the melting point of the diol for 3 hours. Water and EtOAc were added and the aqueous layer was extracted with EtOAC (3x). The organic layer was dried over Na_2SO_4, filtered and evaporated *in vacuo*. The crude material was purified by flash silica gel chromatography.

General procedure B: Swern oxidation to aldehyde

Anhydrous DMSO (2.4 equiv) was added dropwise to a solution of $(COCl)_2$ (1.2 equiv) in dry CH_2Cl_2 (0.2 M) cooled to -78 °C. After 20 minutes, a solution of alcohol (1 equiv) in dry CH_2Cl_2 (0.2 M) was added slowly. After 20 minutes, Et_3N (6 equiv) was added slowly. After 20 minutes, the cold bath was removed and the reaction was allowed to heat to room temperature for 1 hour. 1 M HCl was added and the mixture was stirred vigorously for 30 minutes. The aqueous layer was then extracted with CH_2Cl_2 (3x). The organic layer was washed with brine (1x), dried over Na_2SO_4, filtered and evaporated *in vacuo*. The crude material was purified by flash silica gel chromatography.

General procedure C: Grignard reaction

Grignard reagent solution (2 equiv) was added dropwise to a solution of aldehyde (1 equiv) in dry THF (0.2 M) cooled to 0 °C. After 15 minutes, the cool bath was removed and the reaction was allowed to heat to room temperature for 3 hours. 1 M HCl and EtOAc were added and the aqueous layer was then extracted with EtOAc (3x). The organic layer was washed with brine (1x),

dried over Na_2SO_4, filtered and evaporated *in vacuo*. The crude material was purified by flash silica gel chromatography.

General procedure D: deoxofluorination and deprotection

$Et_3N{\cdot}3HF$ (2 equiv) was added dropwise to a solution of alcohol (1 equiv) and XtalFluor E (1.5 equiv) in dry CH_2Cl_2 (0.4 M) cooled to 0 °C. After 15 minutes, the cool bath was removed and the reaction was allowed to heat to room temperature for 18 hours. Saturated aqueous $NaHCO_3$ was added dropwise and the aqueous layer was extracted with CH_2Cl_2 (3x). The organic layer was washed with brine (1x), dried over Na_2SO_4, filtered and evaporated *in vacuo*. The crude material was purified by flash silica gel chromatography. The mixture of fluorination and elimination compounds was used directly for the deprotection reaction.

The mixture was dissolved in EtOAc (0.2 M) and added with Pd/C (10% wt.) in a glass reactor which was purged three times with H_2 (Parr Shaker Hydrogenation Apparatus). The pressure was then set to 50 psi of H_2 for 18 hours. The reaction mixture was filtered through a Celite pad and evaporated *in vacuo*. The crude material was purified by flash silica gel chromatography.

General procedure E: oxidation to carboxylic acid in two steps

Swern oxidation was carried out following the general procedure B, without the silica gel purification. It was followed directly by Pinnick oxidation on the crude mixture.

Sodium chlorite (2.5 equiv) was added to a solution of aldehyde (1 equiv), sodium dihydrogen phosphate dihydrate (2 equiv) and 2-methylbut-2-ene (3 equiv) in *t*-BuOH and water (3:1, 0.1 M) at room temperature. The reaction was stirred at room temperature for 90 minutes. EtOAc was added, and the aqueous layer was extracted with EtOAc (3x). The organic layer was washed with brine (1x), dried over Na_2SO_4, filtered and evaporated *in vacuo*. The crude material was purified by flash silica gel chromatography.

4-(Benzyloxy)butan-1-ol (SI-1)

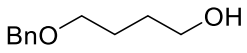

Prepared according to the general procedure A on 15.1 mmol of BnBr, using 2.2 equiv of 1,4-butanediol and 2.2 equiv of KOH. The reaction was carried out at 50 °C. The desired product (2.47 g, 13.7 mmol, 90%) was isolated as a colorless oil after purification by automated flash chromatography (15-50% EtOAc/hexanes). ^{1}H NMR (400 MHz, $CDCl_3$) δ (ppm) = 7.38–7.32 (m, 4H), 7.31–7.25 (m, 1H), 4.52 (s, 2H), 3.64 (t, *J* = 5.7 Hz, 2H), 3.52 (t, *J* = 5.9 Hz, 2H), 2.29 (br s, 1H), 1.78–1.61 (m, 2H). Data are in accordance with the one described in the literature.[2]

4-(Benzyloxy)butanal (SI-2)

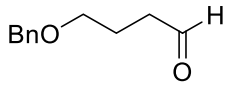

Prepared according to the general procedure B on 13.5 mmol of **SI-1**. The crude mixture was used for next step without further purification as it quickly reacts with water to generate the hydrate.

1-(Benzyloxy)hexadecan-4-ol (SI-3)

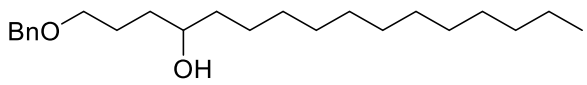

Prepared according to the general procedure C on crude mixture of **SI-2** with dodecylmagnesium bromide (1 M in Et_2O). The reaction is carried out in dry Et_2O instead of THF. The desired product (1.96 g, 5.62 mmol, 42% on 2 steps) was isolated as a white solid after purification by automated flash chromatography (10-20% EtOAc/hexanes). ^{1}H NMR (400 MHz, $CDCl_3$) δ (ppm) = 7.37–7.31 (m, 4H), 7.30–7.26 (m, 1H), 4.52 (s, 2H), 3.64–3.55 (m, 1H), 3.51 (t, *J* = 6.0 Hz, 2H), 2.22 (br s, 1H), 1.78–1.40 (m, 6H), 1.33–1.23 (m, 20H), 3.51 (t, *J* = 6.9 Hz, 3H). Data are in accordance with the one described in the literature.[3]

[2] Crimmins, M. T.; DeBaillie, A. C. *J. Am. Chem. Soc.* **2006**, *128*, 4936-4937.
[3] Liu, R.-C.; Wei, J.-H.; Wei, B.-G.; Lin, G.-Q. *Tetrahedron Asymmetry* **2008**, *19*, 2731-2734.

4-Fluorohexadecan-1-ol (SI-4)

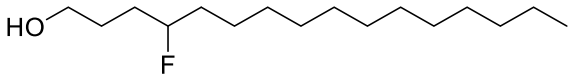

Prepared according to the general procedure D on 5.61 mmol of **SI-3**. The first purification was done by automated flash chromatography (0-5% EtOAc/hexanes). The desired product (180 mg, 0.691 mmol, 18% on 2 steps) was isolated as a white solid after purification by automated flash chromatography (5-15% EtOAc/hexanes). Mp: 57.2–58.9 °C; FT-IR ν (cm^{-1}) = 3273, 2916, 2847, 1063; ^{1}H NMR (500 MHz, $CDCl_3$) δ (ppm) = 4.60–4.42 (m, 1H), 3.69 (br. s, 3H), 1.79–1.58 (m, 5H), 1.58–1.40 (m, 2H), 1.39–1.22 (m, 20H), 0.88 (t, J = 6.9 Hz, 3H); ^{13}C NMR (126 MHz, $CDCl_3$) δ (ppm) = 94.5 (d, J_{C-F} = 166.9 Hz), 62.7, 35.2 (d, J_{C-F} = 20.9 Hz), 31.9, 31.5 (d, J_{C-F} = 21.3 Hz), 29.68, 29.65, 29.57, 29.54, 29.49, 29.36, 28.5 (d, J_{C-F} = 3.7 Hz), 25.1 (d, J_{C-F} = 4.7 Hz), 22.7, 14.1; ^{19}F NMR (470 MHz, $CDCl_3$) δ (ppm) = -179.9 – -180.3 (m, 1F); HRMS (ESI-TOF) m/z calcd for $C_{16}H_{37}FNO$ $[M+NH_4]^+$ 278.2854; found 278.2858.

4-Fluorohexadecanoic acid / PA-4(F)

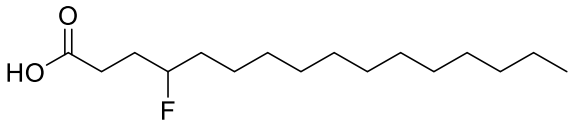

Prepared according to the general procedure E on 0.680 mmol of **SI-4** with. The desired product (77 mg, 0.281 mmol, 41% on 2 steps) was isolated as a white solid after purification by automated flash chromatography (15-50% EtOAc/hexanes). Mp: 69.5–71.4 °C; FT-IR ν (cm^{-1}) = 2916, 2849, 2737, 1699, 1296, 943; ^{1}H NMR (500 MHz, $CDCl_3$) δ (ppm) = 10.98 (br. s, 1H), 4.51 (dtt, J = 49.4, 8.0, 4.1 Hz, 1H), 2.61–2.45 (m, 2H), 2.01–1.85 (m, 2H), 1.71–1.34 (m, 4H), 1.33–1.23 (m, 18H), 0.88 (t, J = 7.0 Hz, 3H); ^{13}C NMR (126 MHz, $CDCl_3$) δ (ppm) = 178.0, 93.3 (d, J_{C-F} = 168.3 Hz), 35.1 (d, J_{C-F} = 20.5 Hz), 31.9, 30.0 (d, J_{C-F} = 21.4 Hz), 29.67, 29.64, 29.55, 29.50, 29.42, 29.36, 25.0 (d, J_{C-F} = 4.7 Hz), 22.7, 14.1; ^{19}F NMR (470 MHz, $CDCl_3$) δ (ppm) = -182.8 – -183.1 (m, 1F); HRMS (ESI-TOF) m/z calcd for $C_{16}H_{30}FO_2$ $[M-H]^-$ 273.2235; found 273.2237.

8-(Benzyloxy)octan-1-ol (SI-5)

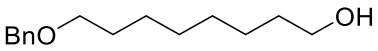

Prepared according to the general procedure A on 12.1 mmol of BnBr, using 1,8-octanediol. The reaction was carried out at 80 °C. The desired product (2.16 g, 9.14 mmol, 75%) was isolated as a colorless oil after purification by automated flash chromatography (20-50% EtOAc/hexanes). ^{1}H NMR (500 MHz, $CDCl_3$) δ (ppm) = 7.38–7.32 (m, 4H), 7.30–7.26 (m, 1H), 4.50 (s, 2H), 3.63 (t, *J* = 6.7 Hz, 2H), 3.46 (t, *J* = 6.6 Hz, 2H), 1.65–1.52 (m, 4H), 1.40–1.28 (m, 8H). Data are in accordance with the one described in the literature.[4]

8-(Benzyloxy)octanal (SI-6)

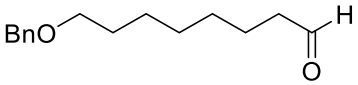

Prepared according to the general procedure B on 9.14 mmol of **SI-5**. The desired product (1.77 g, 7.55 mmol, 83%) was isolated as a colorless oil after purification by automated flash chromatography (0-10% EtOAc/hexanes). ^{1}H NMR (400 MHz, $CDCl_3$) δ (ppm) = 9.76 (t, *J* = 1.8 Hz, 1H), 7.39–7.30 (m, 4H), 7.31–7.26 (m, 1H), 4.50 (s, 2H), 3.46 (t, *J* = 6.6 Hz, 2H), 2.41 (td, *J* = 7.4, 1.9 Hz, 2H), 1.67–1.57 (m, 4H), 1.43–1.28 (m, 6H). Data are in accordance with the one described in the literature.[5]

1-(Benzyloxy)hexadecan-8-ol (SI-7)

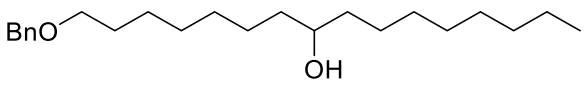

Prepared according to the general procedure C on 7.55 mmol of **SI-6** with octylmagnesium bromide (2 M in THF). The desired product (2.07 g, 5.94 mmol, 79%) was isolated as a white solid after purification by automated flash chromatography (0-10% EtOAc/hexanes). Mp: 39.8–41.8 °C; FT-IR ν (cm^{-1}) = 3266, 2970, 1695, 1300, 1215, 949, 698; ^{1}H NMR (400 MHz, $CDCl_3$) δ (ppm) =

[4] Gao, X.; Hall, D. G. *J. Am. Chem. Soc.* **2005**, *127*, 1628-1629
[5] Madda, J.; Khandregula, S.; Bandari, S. K.; Kommu, N.; Yadav, J. S. *Tetrahedron Asymmetry* **2014**, *25*, 1494 1500.

7.37–7.32 (m, 4H), 7.31–7.25 (m, 1H), 4.50 (s, 2H), 3.58 (br. s, 1H), 3.46 (t, J = 6.6 Hz, 2H), 1.66–1.54 (m, 2H), 1.47–1.23 (m, 25H), 0.88 (t, J = 6.8 Hz, 3H); ^{13}C NMR (126 MHz, $CDCl_3$) δ (ppm) = 138.7, 128.4, 127.6, 127.5, 72.9, 72.0, 70.5, 37.53, 37.48, 31.9, 29.8, 29.74, 29.66, 29.6, 29.5, 29.3, 26.2, 25.7, 25.6, 22.7, 14.1; HRMS (ESI-TOF) m/z calcd for $C_{23}H_{41}O_2$ $[M+H]^+$ 349.3101; found 349.3112.

8-Fluorohexadecan-1-ol (SI-8)

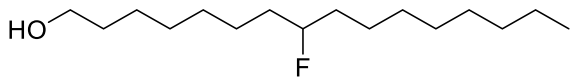

Prepared according to the general procedure D on 5.94 mmol of **SI-7**. The first purification was done by automated flash chromatography (0-5% EtOAc/hexanes). The desired product (329 mg, 1.26 mmol, 21% on 2 steps) was isolated as a white solid after purification by automated flash chromatography (5-15% EtOAc/hexanes). Mp: 54.0–54.9 °C; FT-IR ν (cm^{-1}) = 3265, 2918, 2849, 1472, 1128, 1063; ^{1}H NMR (500 MHz, $CDCl_3$) δ (ppm) = 4.45 (dtt, J = 49.1, 7.9, 3.9 Hz, 1H), 3.64 (t, J = 6.7 Hz, 2H), 1.67–1.42 (m, 8H), 1.40–1.22 (m, 19H), 0.88 (t, J = 6.8 Hz, 3H); ^{13}C NMR (126 MHz, $CDCl_3$) δ (ppm) = 94.6 (d, J_{C-F} = 166.4 Hz), 63.1, 35.2 (d, J_{C-F} = 20.9 Hz), 35.1 (d, J_{C-F} = 20.9 Hz), 32.8, 31.9, 29.53, 29.51, 29.46, 29.32, 29.25, 25.7, 25.14 (d, J_{C-F} = 4.4 Hz), 25.07 (d, J_{C-F} = 4.6 Hz), 22.7, 14.1; ^{19}F NMR (470 MHz, $CDCl_3$) δ (ppm) = -179.8 – -180.2 (m, 1F); HRMS (ESI-TOF) m/z calcd for $C_{16}H_{37}FNO$ $[M+NH_4]^+$ 278.2854; found 278.2861

8-Fluorohexadecanoic acid /PA-F(8)

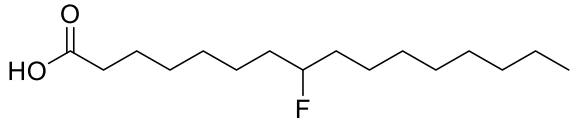

Prepared according to the general procedure E on 1.20 mmol of **SI-8** with. The desired product (211 mg, 0.769 mmol, 64% on 2 steps) was isolated as a white solid after purification by automated flash chromatography (20-40% EtOAc/hexanes). Mp: 65.4–68.2 °C; FT-IR ν (cm^{-1}) = 2916, 2849, 2728, 1701, 1472, 1296, 943; ^{1}H NMR (500 MHz, $CDCl_3$) δ (ppm) = 11.11 (br. s, 1H), 4.45 (dtt, J = 48.9, 7.8, 3.8 Hz, 1H), 2.36 (t, J = 7.5 Hz, 2H), 1.69–1.41 (m, 8H), 1.40–1.22 (m, 16H), 0.88 (t, J = 6.9 Hz, 3H); ^{13}C NMR (101 MHz, $CDCl_3$) δ (ppm) = 179.5, 94.5 (d, J_{C-F} = 166.5 Hz), 35.2 (d, J_{C-F} = 20.9 Hz), 35.1 (d, J_{C-F} = 21.0 Hz), 33.9, 31.9, 29.52, 29.51, 29.3, 29.1, 28.9, 25.1 (d, J_{C-}

$_F$ = 4.6 Hz), 25.0 (d, J_{C-F} = 4.5 Hz), 24.6, 22.7, 14.1; ^{19}F NMR (470 MHz, $CDCl_3$) δ (ppm) = -179.9 – -180.5 (m, 1F); HRMS (ESI-TOF) m/z calcd for $C_{16}H_{30}FO_2$ $[M-H]^-$ 273.2235; found 273.2237.

14-(Benzyloxy)tetradecan-1-ol (SI-9)

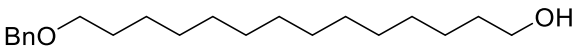

Prepared according to the general procedure A on 3.03 mmol of BnBr, using 1,14-tetradecanediol. The reaction was carried out at 110 °C. The desired product (515 mg, 1.61 mmol, 53%) was isolated as a white solid after purification by column flash chromatography (20% EtOAc/hexanes). ^{1}H NMR (500 MHz, $CDCl_3$) δ (ppm) = 7.36–7.33 (m, 4H), 7.30–7.25 (m, 1H), 4.50 (s, 2H), 3.63 (t, J = 6.7 Hz, 2H), 3.46 (t, J = 6.7 Hz, 2H), 1.66–1.51 (m, 4H), 1.39–1.23 (m, 20H). Data are in accordance with the one described in the literature.[6]

14-(Benzyloxy)tetradecanal (SI-10)

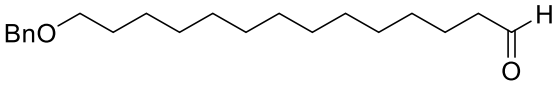

Prepared according to the general procedure B on 3.56 mmol of **SI-9**. The desired product (940 mg, 2.95 mmol, 83%) was isolated as an oily solid after purification by automated flash chromatography (0-5% EtOAc/hexanes). FT-IR ν (cm^{-1}) = 2920, 2851, 1701, 1653, 1200, 667; ^{1}H NMR (500 MHz, $CDCl_3$) δ (ppm) = 9.76 (t, J = 1.9 Hz, 1H), 7.36–7.32 (m, 4H), 7.30–7.25 (m, 1H), 4.50 (s, 2H), 3.46 (t, J = 6.7 Hz, 2H), 2.42 (td, J = 7.4, 1.9 Hz, 2H), 1.66–1.58 (m, 4H), 1.39–1.23 (m, 18H); ^{13}C NMR (126 MHz, $CDCl_3$) δ (ppm) = 203.0, 138.7, 128.3, 127.6, 127.6, 72.9, 70.5, 43.9, 29.8, 29.60, 29.58 29.56, 29.5, 29.42, 29.36, 29.2, 26.2, 22.1; HRMS (ESI-TOF) m/z calcd for $C_{21}H_{35}O_2$ $[M+H]^+$ 319.2632; found 319.2647.

16-(Benzyloxy)hexadecan-3-ol (SI-11)

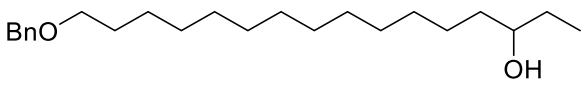

[6] Muller, T.; Coowar, D.; Hanbali, M.; Heuschling, P.; Luu, B. *Tetrahedron* **2006**, *62*, 12025-12040.

Prepared according to the general procedure C on 2.95 mmol of **SI-10** with ethylmagnesium chloride (2 M in THF). The desired product (841 mg, 2.41 mmol, 82%) was isolated as a white solid after purification by automated flash chromatography (0-10% EtOAc/hexanes). Mp: 40.5–42.5 °C; FT-IR ν (cm^{-1}) = 2918, 2851, 1456, 1103, 696; ^{1}H NMR (500 MHz, $CDCl_3$) δ (ppm) = 7.38–7.30 (m, 4H), 7.31–7.24 (m, 1H), 4.50 (s, 2H), 3.51 (br. s, 1H), 3.46 (t, *J* = 6.7 Hz, 2H), 1.65–1.58 (m, 2H), 1.57–1.22 (m, 25H), 0.94 (t, *J* = 7.5 Hz, 3H); ^{13}C NMR (126 MHz, $CDCl_3$) δ (ppm) = 138.7, 128.3, 127.6, 127.5, 73.3, 72.9, 70.5, 37.0, 30.1, 29.8, 29.7, 29.64, 29.61, 29.60, 29.5, 26.2, 25.7, 9.9; HRMS (ESI-TOF) m/z calcd for $C_{23}H_{41}O_2$ $[M+H]^+$ 349.3101; found 349.3113.

14-Fluorohexadecan-1-ol (SI-12)

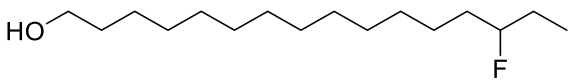

In a glass round-bottom flask, Deoxo-Fluor® (2,7 M in toluene, 1.3 mL, 3.51 mmol, 1.3 equiv) was added dropwise to a solution of **SI-11** (961 mg, 2.76 mmol, 1 equiv) in dry CH_2Cl_2 (14 mL, 0.2 M) cooled to 0 °C. After 10 minutes, the cool bath was removed and the reaction was allowed to heat to room temperature for 3 hours. Saturated aqueous $NaHCO_3$ was added dropwise and the aqueous layer was extracted with CH_2Cl_2 (3x). The organic layer was washed with brine (1x), dried over Na_2SO_4, filtered and evaporated *in vacuo*. The crude material was purified by flash silica gel chromatography (0-5% EtOAc/hexanes). The mixture of fluorination and elimination compounds was used directly for the deprotection reaction.

The mixture was dissolved in EtOAc (5 mL, 0.55 M) and added with Pd/C (97 mg, 10% wt.) in a glass reactor which was purged three times with H_2 (Parr Shaker Hydrogenation Apparatus). The pressure was then set to 50 psi of H_2 for 19 hours. The reaction mixture was filtered through a Celite pad and evaporated *in vacuo*. The desired product (193 mg, 0.741 mmol, 27% on 2 steps) was isolated as a white solid after purification by automated flash chromatography (0-15% EtOAc/hexanes). Mp: 51.0–52.7 °C; FT-IR ν (cm^{-1}) = 3313, 3232, 2916, 2849, 1464, 1063, 926, 719; ^{1}H NMR (500 MHz, $CDCl_3$) δ (ppm) = 4.49–4.31 (m, 1H), 3.64 (td, *J* = 6.2, 5.8 Hz, 2H), 1.68–1.53 (m, 6H), 1.52–1.41 (m, 2H), 1.38–1.24 (m, 18H), 1.23–1.20 (m, 1H), 0.96 (t, *J* = 7.4 Hz, 3H); ^{13}C NMR (126 MHz, $CDCl_3$) δ (ppm) = 95.9 (d, J_{C-F} = 166.6 Hz), 63.3, 34.8 (d, J_{C-F} = 20.9 Hz), 33.0, 29.77, 29.75, 29.73, 29.71, 29.69, 29.67, 29.6, 28.2 (d, J_{C-F} = 21.5 Hz), 25.9, 25.3 (d, J_{C-F} = 4.7 Hz), 9.6 (d, J_{C-F} = 5.8 Hz); ^{19}F NMR (470 MHz, $CDCl_3$) δ (ppm) = -181.2 (dtt, *J* = 48.0,

29.0, 18.3 Hz, 1F); HRMS (ESI-TOF) m/z calcd for $C_{16}H_{37}FNO$ $[M+NH_4]^+$ 278.2854; found 278.2854.

14-Fluorohexadecanoic acid /PA-F(14)

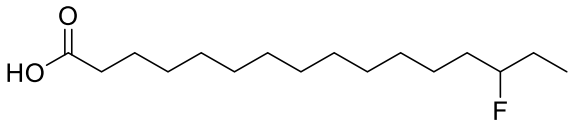

Prepared according to the general procedure E on 0.726 mmol of **SI-12** with. The desired product (98 mg, 0.357 mmol, 49% on 2 steps) was isolated as a white solid after purification by automated flash chromatography (15-40% EtOAc/hexanes). Mp: 72.9–74.5 °C; FT-IR ν (cm^{-1}) = 2912, 2849, 2635, 1697, 1472, 1439, 1211, 939; ^1H NMR (500 MHz, $CDCl_3$) δ (ppm) = 10.98 (br. s, 1H), 4.50–4.30 (m, 1H), 2.35 (t, J = 7.5 Hz, 2H), 1.67–1.41 (m, 7H), 1.37–1.24 (m, 18H), 0.96 (t, J = 7.4 Hz, 3H); ^{13}C NMR (101 MHz, $CDCl_3$) δ (ppm) = 179.5, 95.9 (d, J_{C-F} = 166.8 Hz), 34.8 (d, J_{C-F} = 20.9 Hz), 34.1, 29.74, 29.71, 29.70, 29.68, 29.67, 29.4, 29.2, 28.2 (d, J_{C-F} = 21.5 Hz), 25.3 (d, J_{C-F} = 4.5 Hz), 24.8, 9.6 (d, J_{C-F} = 5.8 Hz); ^{19}F NMR (470 MHz, $CDCl_3$) δ (ppm) = -181.2 (dtt, J = 47.7, 28.8, 18.3 Hz, 1F); HRMS (ESI-TOF) m/z calcd for $C_{16}H_{30}FO_2$ $[M-H]^-$ 273.2235; found 273.2239.

RFFRENCES

(1) Hutchings, M. I., Truman, A. W. et Wilkinson, B. (2019). Antibiotics: past, present and future. *Current opinion in microbiology*, *51*, 72-80.

(2) Ligon, B. L. (2004). Penicillin: its discovery and early development. (p. 52-57). Seminars in pediatric infectious diseases, Elsevier.

(3) van Driel, M. L., Merlo, G., Baillie, E., Dartnell, J., Hall, L. et Heal, C. (2022). Preserving antibiotics for the future. *Australian Journal of General Practice*, *51*(1/2), 10-13.

(4) Barber, M. et Rozwadowska-Dowzenko, M. (1948). Infection by Penicillin-Resistant Staphyloeoeci. *Lancet*, 641-644.

(5) Finland, M. (1955). Emergence of antibiotic-resistant bacteria. *New England Journal of Medicine*, *253*(23), 1019-1028.

(6) Horcajada, J. P., Montero, M., Oliver, A., Sorlí, L., Luque, S., Gómez-Zorrilla, S., Benito, N. et Grau, S. (2019). Epidemiology and treatment of multidrug-resistant and extensively drug-resistant Pseudomonas aeruginosa infections. *Clinical microbiology reviews*, *32*(4).

(7) Alekshun, M. N. et Levy, S. B. (2007). Molecular mechanisms of antibacterial multidrug resistance. *Cell*, *128*(6), 1037-1050.

(8) Vestergaard, M., Frees, D. et Ingmer, H. (2019). Antibiotic resistance and the MRSA problem. *Microbiology spectrum*, *7*(2).

(9) Peng, J.-J., Balasubramanian, B., Ming, Y.-Y., Niu, J.-L., Yi, C.-M., Ma, Y. et Liu, W.-C. (2021). Identification of antimicrobial resistance genes and drug resistance analysis of Escherichia coli in the animal farm environment. *Journal of Infection and Public Health*, *14*(12), 1788-1795.

(10) Levy, S. B. (1998). The challenge of antibiotic resistance. *Scientific American*, *278*(3), 46-53.

(11) Brown, K., Uwiera, R. R., Kalmokoff, M. L., Brooks, S. P. et Inglis, G. D. (2017). Antimicrobial growth promoter use in livestock: a requirement to understand their modes of action to develop effective alternatives. *International journal of antimicrobial agents*, *49*(1), 12-24.

(12) Barbosa, T. M. et Levy, S. B. (2000). The impact of antibiotic use on resistance development and persistence. *Drug resistance updates*, *3*(5), 303-311.

(13) WHO. (2001). *WHO global strategy for containment of antimicrobial resistance*.

(14) Murray, C. J., Ikuta, K. S., Sharara, F., Swetschinski, L., Aguilar, G. R., Gray, A., Han, C., Bisignano, C., Rao, P. et Wool, E. (2022). Global burden of bacterial antimicrobial resistance in 2019: a systematic analysis. *The Lancet*, *399*(10325), 629-655.

(15) Rosini, R., Nicchi, S., Pizza, M. et Rappuoli, R. (2020). Vaccines against antimicrobial resistance. *Frontiers in immunology*, *11*, 1048.

(16) Laxminarayan, R. (2014). Antibiotic effectiveness: balancing conservation against innovation. *science*, *345*(6202), 1299-1301.

(17) Butler, M. S., Henderson, I. R., Capon, R. J. et Blaskovich, M. A. (2023). Antibiotics in the clinical pipeline as of December 2022. *The Journal of Antibiotics*, 1-43.

(18) Levy, S. B. (1992). Future Prospects: New Advances against Potential Disaster. Dans *The Antibiotic Paradox: How Miracle Drugs Are Destroying the Miracle* (p. 183-204). Springer.

(19) Lei, J., Sun, L., Huang, S., Zhu, C., Li, P., He, J., Mackey, V., Coy, D. H. et He, Q. (2019). The antimicrobial peptides and their potential clinical applications. *American journal of translational research*, *11*(7), 3919.

(20) Nguyen, L. T., Haney, E. F. et Vogel, H. J. (2011). The expanding scope of antimicrobial peptide structures and their modes of action. *Trends in biotechnology*, *29*(9), 464-472.

(21) Le, C.-F., Fang, C.-M. et Sekaran, S. D. (2017). Intracellular targeting mechanisms by antimicrobial peptides. *Antimicrobial agents and chemotherapy*, *61*(4), 10.1128/aac. 02340-02316.

(22) Magana, M., Pushpanathan, M., Santos, A. L., Leanse, L., Fernandez, M., Ioannidis, A., Giulianotti, M. A., Apidianakis, Y., Bradfute, S. et Ferguson, A. L. (2020). The value of antimicrobial peptides in the age of resistance. *The lancet infectious diseases*, *20*(9), e216-e230.

(23) Brown, K. L. et Hancock, R. E. (2006). Cationic host defense (antimicrobial) peptides. *Current opinion in immunology*, *18*(1), 24-30.

(24) Ganz, T. (2003). Defensins: antimicrobial peptides of innate immunity. *Nature reviews immunology*, *3*(9), 710-720.

(25) Gawde, U., Chakraborty, S., Waghu, F. H., Barai, R. S., Khanderkar, A., Indraguru, R., Shirsat, T. et Idicula-Thomas, S. (2023). CAMPR4: a database of natural and synthetic antimicrobial peptides. *Nucleic Acids Research*, *51*(D1), D377-D383.

(26) Munk, J. K., Ritz, C., Fliedner, F. P., Frimodt-Møller, N. et Hansen, P. R. (2014). Novel method to identify the optimal antimicrobial peptide in a combination matrix, using anoplin as an example. *Antimicrobial agents and chemotherapy*, *58*(2), 1063-1070.

(27) Vizioli, J. et Salzet, M. (2002). Antimicrobial peptides from animals: focus on invertebrates. *Trends in pharmacological sciences*, *23*(11), 494-496.

(28) Powers, J.-P. S. et Hancock, R. E. (2003). The relationship between peptide structure and antibacterial activity. *Peptides*, *24*(11), 1681-1691.

(29) White, S. H. et Wimley, W. C. (1998). Hydrophobic interactions of peptides with membrane interfaces. *Biochimica et Biophysica Acta (BBA)-Reviews on Biomembranes*, *1376*(3), 339-352.

(30) Malanovic, N., Marx, L., Blondelle, S. E., Pabst, G. et Semeraro, E. F. (2020). Experimental concepts for linking the biological activities of antimicrobial peptides to their molecular modes of action. *Biochimica et Biophysica Acta (BBA)-Biomembranes*, *1862*(8), 183275.

(31) Koehbach, J. et Craik, D. J. (2019). The vast structural diversity of antimicrobial peptides. *Trends in pharmacological sciences*, *40*(7), 517-528.

(32) Booth, V., Warschawski, D. E., Santisteban, N. P., Laadhari, M. et Marcotte, I. (2017). Recent progress on the application of ^{2}H solid-state NMR to probe the interaction of antimicrobial peptides with intact bacteria. *Biochimica et Biophysica Acta (BBA)-Proteins and Proteomics*, *1865*(11), 1500-1511.

(33) Alkatheri, A. H., Yap, P. S.-X., Abushelaibi, A., Lai, K.-S., Cheng, W.-H. et Lim, S.-H. E. (2022). Host‑Bacterial Interactions: Outcomes of Antimicrobial Peptide Applications. *Membranes*, *12*(7), 715.

(34) Malanovic, N. et Lohner, K. (2016). Gram-positive bacterial cell envelopes: The impact on the activity of antimicrobial peptides. *Biochimica et Biophysica Acta (BBA)-Biomembranes*, *1858*(5), 936-946.

(35) Carey, A. B., Ashenden, A. et Köper, I. (2022). Model architectures for bacterial membranes. *Biophysical Reviews*, *14*(1), 111-143.

(36) Sewell, E. W. et Brown, E. D. (2014). Taking aim at wall teichoic acid synthesis: new biology and new leads for antibiotics. *The Journal of Antibiotics*, *67*(1), 43-51.

(37) Vollmer, W. et Holtje, J.-V. (2004). The architecture of the murein (peptidoglycan) in gram-negative bacteria: vertical scaffold or horizontal layer (s)? *Journal of bacteriology*, *186*(18), 5978-5987.

(38) Matsuzaki, K. (2009). Control of cell selectivity of antimicrobial peptides. *Biochimica et Biophysica Acta (BBA)-Biomembranes*, *1788*(8), 1687-1692.

(39) Nandi, S., Nair, K. S. et Bajaj, H. (2023). Bacterial outer-membrane-mimicking giant unilamellar vesicle model for detecting antimicrobial permeability. *Langmuir*, *39*(16), 5891-5900.

(40) Kumar, K., Sebastiao, M., Arnold, A. A., Bourgault, S., Warschawski, D. E. et Marcotte, I. (2022). In situ solid-state NMR study of antimicrobial peptide interactions with erythrocyte membranes. *Biophysical journal*, *121*(8), 1512-1524.

(41) Brender, J. R., McHenry, A. J. et Ramamoorthy, A. (2012). Does cholesterol play a role in the bacterial selectivity of antimicrobial peptides? *Frontiers in immunology*, *3*, 195.

(42) Bagheri, A., Taheri-Araghi, S. et Ha, B.-Y. (2015). How cell concentrations are implicated in cell selectivity of antimicrobial peptides. *Langmuir*, *31*(29), 8052-8062.

(43) Melo, M. N., Ferre, R. et Castanho, M. A. (2009). Antimicrobial peptides: linking partition, activity and high membrane-bound concentrations. *Nature Reviews Microbiology*, *7*(3), 245-250.

(44) Bacalum, M. et Radu, M. (2015). Cationic antimicrobial peptides cytotoxicity on mammalian cells: an analysis using therapeutic index integrative concept. *International Journal of Peptide Research and Therapeutics*, *21*, 47-55.

(45) Melo, M. N. et Castanho, M. A. (2012). The mechanism of action of antimicrobial peptides: lipid vesicles vs. bacteria. *Frontiers in immunology*, *3*, 236.

(46) Jepson, A. K., Schwarz-Linek, J., Ryan, L., Ryadnov, M. G. et Poon, W. C. (2016). What is the ‘Minimum Inhibitory Concentration’ (MIC) of pexiganan acting on Escherichia coli?−A cautionary case study. *Biophysics of infection*, 33-48.

(47) Imura, Y., Choda, N. et Matsuzaki, K. (2008). Magainin 2 in action: distinct modes of membrane permeabilization in living bacterial and mammalian cells. *Biophysical journal*, *95*(12), 5757-5765.

(48) Shin, A., Lee, E., Jeon, D., Park, Y.-G., Bang, J. K., Park, Y.-S., Shin, S. Y. et Kim, Y. (2015). Peptoid-substituted hybrid antimicrobial peptide derived from papiliocin and

magainin 2 with enhanced bacterial selectivity and anti-inflammatory activity. *Biochemistry*, *54*(25), 3921-3931.

(49) Neshani, A., Zare, H., Eidgahi, M. R. A., Kakhki, R. K., Safdari, H., Khaledi, A. et Ghazvini, K. (2019). LL-37: Review of antimicrobial profile against sensitive and antibiotic-resistant human bacterial pathogens. *Gene Reports*, *17*, 100519.

(50) Memariani, H., Memariani, M., Shahidi-Dadras, M., Nasiri, S., Akhavan, M. M. et Moravvej, H. (2019). Melittin: from honeybees to superbugs. *Applied microbiology and biotechnology*, *103*, 3265-3276.

(51) Ko, S. J., Park, E., Asandei, A., Choi, J.-Y., Lee, S.-C., Seo, C. H., Luchian, T. et Park, Y. (2020). Bee venom-derived antimicrobial peptide melectin has broad-spectrum potency, cell selectivity, and salt-resistant properties. *Scientific reports*, *10*(1), 10145.

(52) Dijksteel, G. S., Ulrich, M. M., Middelkoop, E. et Boekema, B. K. (2021). Lessons learned from clinical trials using antimicrobial peptides (AMPs). *Frontiers in microbiology*, *12*, 616979.

(53) Starr, C. G. et Wimley, W. C. (2017). Antimicrobial peptides are degraded by the cytosolic proteases of human erythrocytes. *Biochimica et Biophysica Acta (BBA)-Biomembranes*, *1859*(12), 2319-2326.

(54) Pandi, A., Adam, D., Zare, A., Trinh, V. T., Schaefer, S. L., Wiegand, M., Klabunde, B., Bobkova, E., Kushwaha, M. et Foroughijabbari, Y. (2022). Cell-free biosynthesis combined with deep learning accelerates de novo-development of antimicrobial peptides. *bioRxiv*, 2022.2011. 2019.517184.

(55) Browne, K., Chakraborty, S., Chen, R., Willcox, M. D., Black, D. S., Walsh, W. R. et Kumar, N. (2020). A new era of antibiotics: the clinical potential of antimicrobial peptides. *International journal of molecular sciences*, *21*(19), 7047.

(56) Apponyi, M. A., Pukala, T. L., Brinkworth, C. S., Maselli, V. M., Bowie, J. H., Tyler, M. J., Booker, G. W., Wallace, J. C., Carver, J. A. et Separovic, F. (2004). Host-defence peptides of Australian anurans: structure, mechanism of action and evolutionary significance. *Peptides*, *25*(6), 1035-1054.

(57) Laadhari, M., Arnold, A. A., Gravel, A. E., Separovic, F. et Marcotte, I. (2016). Interaction of the antimicrobial peptides caerin 1.1 and aurein 1.2 with intact bacteria by ^{2}H solid-state NMR. *Biochimica et Biophysica Acta (BBA)-Biomembranes*, *1858*(12), 2959-2964.

(58) Fernandez, D. I., Sani, M.-A., Miles, A. J., Wallace, B. A. et Separovic, F. (2013). Membrane defects enhance the interaction of antimicrobial peptides, aurein 1.2 versus caerin 1.1. *Biochimica et Biophysica Acta (BBA)-Biomembranes*, *1828*(8), 1863-1872.

(59) Mechler, A., Praporski, S., Atmuri, K., Boland, M., Separovic, F. et Martin, L. L. (2007). Specific and selective peptide-membrane interactions revealed using quartz crystal microbalance. *Biophysical journal*, *93*(11), 3907-3916.

(60) Wegener, K. L., Carver, J. A. et Bowie, J. H. (2003). The solution structures and activity of caerin 1.1 and caerin 1.4 in aqueous trifluoroethanol and dodecylphosphocholine micelles. *Biopolymers: Original Research on Biomolecules*, *69*(1), 42-59.

(61) Fernandez, D. I., Le Brun, A. P., Whitwell, T. C., Sani, M.-A., James, M. et Separovic, F. (2012). The antimicrobial peptide aurein 1.2 disrupts model membranes via the carpet mechanism. *Physical Chemistry Chemical Physics*, *14*(45), 15739-15751.

(62) Bretscher, M. S. (1985). The molecules of the cell membrane. *Scientific American*, *253*(4), 100-109.

(63) Janmey, P. et Kinnunen, P. K. (2006). Biophysical properties of lipids and dynamic membranes. *Trends in cell biology*, *16*(10), 538-546.

(64) Harayama, T. et Riezman, H. (2018). Understanding the diversity of membrane lipid composition. *Nature reviews Molecular cell biology*, *19*(5), 281-296.

(65) Shohet, S. B. (1977). Red blood cells. Dans *Lipid metabolism in mammals* (p. 191-208). Springer.

(66) Doole, F. T., Kumarage, T., Ashkar, R. et Brown, M. F. (2022). Cholesterol stiffening of lipid membranes. *The Journal of Membrane Biology*, *255*(4-5), 385-405.

(67) Kögl, F., De Gier, J., Mulder, I. et Van Deenen, L. (1960). Metabolism and functions of phosphatides specific fatty acid composition of the red blood cell membranes. *Biochimica et Biophysica Acta*, *43*, 95-103.

(68) Rehal, R. P., Marbach, H., Hubbard, A. T., Sacranie, A. A., Sebastiani, F., Fragneto, G. et Harvey, R. D. (2017). The influence of mild acidity on lysyl-phosphatidylglycerol biosynthesis and lipid membrane physico-chemical properties in methicillin-resistant Staphylococcus aureus. *Chemistry and physics of lipids*, *206*, 60-70.

(69) Laydevant, F., Mahabadi, M., Llido, P., Bourgouin, J.-P., Caron, L., Arnold, A. A., Marcotte, I. et Warschawski, D. E. (2022). Growth-phase dependence of bacterial membrane lipid

profile and labeling for in-cell solid-state NMR applications. *Biochimica et Biophysica Acta (BBA)-Biomembranes*, *1864*(2), 183819.

(70) Hart, M. E. et Champlin, F. R. (1988). Susceptibility to hydrophobic molecules and phospholipid composition in Pasteurella multocida and Actinobacillus lignieresii. *Antimicrobial agents and chemotherapy*, *32*(9), 1354-1359.

(71) Fuller, C. A., Brignac, P. J. et Champlin, F. R. (1993). Phospholipid fatty acid ester composition of Pasteurella multocida and Actinobacillus lignieresii. *Current Microbiology*, *27*, 237-240.

(72) Exterkate, F., Otten, B., Wassenberg, H. et Veerkamp, J. (1971). Comparison of the phospholipid composition of Bifidobacterium and Lactobacillus strains. *Journal of bacteriology*, *106*(3), 824-829.

(73) Veerkamp, J. (1971). Fatty acid composition of Bifidobacterium and Lactobacillus strains. *Journal of bacteriology*, *108*(2), 861-867.

(74) Durham, D. R. et Kloos, W. E. (1978). Comparative study of the total cellular fatty acids of Staphylococcus species of human origin. *International Journal of Systematic and Evolutionary Microbiology*, *28*(2), 223-228.

(75) Nagle, J. F. et Tristram-Nagle, S. (2000). Structure of lipid bilayers. *Biochimica et Biophysica Acta (BBA)-Reviews on Biomembranes*, *1469*(3), 159-195.

(76) Baumgart, T., Hunt, G., Farkas, E. R., Webb, W. W. et Feigenson, G. W. (2007). Fluorescence probe partitioning between Lo/Ld phases in lipid membranes. *Biochimica et Biophysica Acta (BBA)-Biomembranes*, *1768*(9), 2182-2194.

(77) Frolov, V. A., Shnyrova, A. V. et Zimmerberg, J. (2011). Lipid polymorphisms and membrane shape. *Cold Spring Harbor perspectives in biology*, *3*(11), a004747.

(78) Bagatolli, L. A. et Mouritsen, O. G. (2013). Is the fluid mosaic (and the accompanying raft hypothesis) a suitable model to describe fundamental features of biological membranes? What may be missing? *Frontiers in plant science*, *4*, 457.

(79) Brown, M. F. (2012). Curvature forces in membrane lipid‐protein interactions. *Biochemistry*, *51*(49), 9782-9795.

(80) Ollila, O. S., Louhivuori, M., Marrink, S. J. et Vattulainen, I. (2011). Protein shape change has a major effect on the gating energy of a mechanosensitive channel. *Biophysical journal*, *100*(7), 1651-1659.

(81) Shahane, G., Ding, W., Palaiokostas, M. et Orsi, M. (2019). Physical properties of model biological lipid bilayers: insights from all-atom molecular dynamics simulations. *Journal of molecular modeling*, *25*, 1-13.

(82) Israelachvili, J. N., Mitchell, D. J. et Ninham, B. W. (1976). Theory of self-assembly of hydrocarbon amphiphiles into micelles and bilayers. *Journal of the Chemical Society, Faraday Transactions 2: Molecular and Chemical Physics*, *72*, 1525-1568.

(83) Warschawski, D. E., Arnold, A. A. et Marcotte, I. (2018). A new method of assessing lipid mixtures by ^{31}P magic-angle spinning NMR. *Biophysical journal*, *114*(6), 1368-1376.

(84) Epand, R. M. (1998). Lipid polymorphism and protein‐lipid interactions. *Biochimica et Biophysica Acta (BBA)-Reviews on Biomembranes*, *1376*(3), 353-368.

(85) Haney, E. F., Nathoo, S., Vogel, H. J. et Prenner, E. J. (2010). Induction of non-lamellar lipid phases by antimicrobial peptides: a potential link to mode of action. *Chemistry and physics of lipids*, *163*(1), 82-93.

(86) Lee, A. (1977). Lipid phase transitions and phase diagrams I. Lipid phase transitions. *Biochimica et Biophysica Acta (BBA)-Reviews on Biomembranes*, *472*(2), 237-281.

(87) Armstrong, C. L., Marquardt, D., Dies, H., Kučerka, N., Yamani, Z., Harroun, T. A., Katsaras, J., Shi, A.-C. et Rheinstädter, M. C. (2013). The observation of highly ordered domains in membranes with cholesterol. *PLoS One*, *8*(6), e66162.

(88) Hallock, K. J., Lee, D.-K. et Ramamoorthy, A. (2003). MSI-78, an analogue of the magainin antimicrobial peptides, disrupts lipid bilayer structure via positive curvature strain. *Biophysical journal*, *84*(5), 3052-3060.

(89) Seelig, J. et Seelig, A. (1980). Lipid conformation in model membranes and biological membranes. *Quarterly reviews of biophysics*, *13*(1), 19-61.

(90) Marsh, D. (2009). Cholesterol-induced fluid membrane domains: a compendium of lipid-raft ternary phase diagrams. *Biochimica et Biophysica Acta (BBA)-Biomembranes*, *1788*(10), 2114-2123.

(91) Almeida, P. F., Pokorny, A. et Hinderliter, A. (2005). Thermodynamics of membrane domains. *Biochimica et Biophysica Acta (BBA)-Biomembranes*, *1720*(1-2), 1-13.

(92) Sklar, L. A. (1984). Fluorescence polarization studies of membrane fluidity: Where do we go from here? *Membrane fluidity*, 99-131.

(93) Keough, K. et Davis, P. (1984). Thermal analysis of membranes. *Membrane fluidity*, 55-97.

(94) Matsumoto, K., Kusaka, J., Nishibori, A. et Hara, H. (2006). Lipid domains in bacterial membranes. *Molecular microbiology*, *61*(5), 1110-1117.

(95) Nicolson, G. L. (2014). The Fluid−Mosaic Model of Membrane Structure: Still relevant to understanding the structure, function and dynamics of biological membranes after more than 40 years. *Biochimica et Biophysica Acta (BBA)-Biomembranes*, *1838*(6), 1451-1466.

(96) Bramkamp, M. (2022). Fluidity is the way to life: lipid phase separation in bacterial membranes. *The EMBO Journal*, *41*(5), e110737.

(97) Margineanu, D. (1987). Equilibrium and non-equilibrium approaches in biomembrane thermodynamics. *Archives internationales de physiologie et de biochimie*, *95*(4), 381-422.

(98) Schneider, E. D. et Kay, J. J. (1995). Order from disorder: the thermodynamics of complexity in biology. *What is life? The next fifty years: Speculations on the future of biology*, 161-172.

(99) Gómez, J., Sagués, F. et Reigada, R. (2009). Nonequilibrium patterns in phase-separating ternary membranes. *Physical Review E*, *80*(1), 011920.

(100) de Almeida, R. F., Loura, L. M., Fedorov, A. et Prieto, M. (2002). Nonequilibrium phenomena in the phase separation of a two-component lipid bilayer. *Biophysical journal*, *82*(2), 823-834.

(101) Pinigin, K., Volovik, M., Batishchev, O. et Akimov, S. (2020). Interaction of ordered lipid domain boundaries and amphipathic peptides regulates probability of pore formation in membranes. *Biochemistry (Moscow), Supplement Series A: Membrane and Cell Biology*, *14*, 319-330.

(102) Jain, M. K. et Wagner, R. C. (1988). Introduction to biological membranes.

(103) Molugu, T. R., Lee, S. et Brown, M. F. (2017). Concepts and methods of solid-state NMR spectroscopy applied to biomembranes. *Chemical Reviews*, *117*(19), 12087-12132.

(104) Luckey, M. (2016). Introduction to the structural biology of membrane proteins. *Computational Biophysics of Membrane Proteins*, 1-18.

(105) Warschawski, D. E., Arnold, A. A., Beaugrand, M., Gravel, A., Chartrand, É. et Marcotte, I. (2011). Choosing membrane mimetics for NMR structural studies of transmembrane proteins. *Biochimica et Biophysica Acta (BBA)-Biomembranes*, *1808*(8), 1957-1974.

(106) Brown, M. F. et Williams, G. D. (1985). Membrane NMR: a dyanmic research area. *Journal of biochemical and biophysical methods*, *11*(2-3), 71-81.

(107) Giuliano, C. B., Cvjetan, N., Ayache, J. et Walde, P. (2021). Multivesicular vesicles: preparation and applications. *ChemSystemsChem*, *3*(2), e2000049.

(108) Kim, C., Spano, J., Park, E.-K. et Wi, S. (2009). Evidence of pores and thinned lipid bilayers induced in oriented lipid membranes interacting with the antimicrobial peptides, magainin-2 and aurein-3.3. *Biochimica et Biophysica Acta (BBA)-Biomembranes*, *1788*(7), 1482-1496.

(109) Mani, R., Buffy, J. J., Waring, A. J., Lehrer, R. I. et Hong, M. (2004). Solid-state NMR investigation of the selective disruption of lipid membranes by protegrin-1. *Biochemistry*, *43*(43), 13839-13848.

(110) Fernandez, D. I., Gehman, J. D. et Separovic, F. (2009). Membrane interactions of antimicrobial peptides from Australian frogs. *Biochimica et Biophysica Acta (BBA)-Biomembranes*, *1788*(8), 1630-1638.

(111) Sutherland, M., Kwon, B. et Hong, M. (2021). Interactions of HIV gp41's membrane-proximal external region and transmembrane domain with phospholipid membranes from ^{31}P NMR. *Biochimica et Biophysica Acta (BBA)-Biomembranes*, *1863*(11), 183723.

(112) Sani, M.-A., Carne, S., Overall, S. A., Poulhazan, A. et Separovic, F. (2017). One pathogen two stones: are Australian tree frog antimicrobial peptides synergistic against human pathogens? *European Biophysics Journal*, *46*, 639-646.

(113) Strandberg, E. et Ulrich, A. S. (2004). NMR methods for studying membrane-active antimicrobial peptides. *Concepts in Magnetic Resonance Part A: An Educational Journal*, *23*(2), 89-120.

(114) Dufourc, E. J., Parish, E. J., Chitrakorn, S. et Smith, I. C. (1984). Structural and dynamical details of cholesterol-lipid interaction as revealed by deuterium NMR. *Biochemistry*, *23*(25), 6062-6071.

(115) Warschawski, D. E. et Devaux, P. F. (2005). Order parameters of unsaturated phospholipids in membranes and the effect of cholesterol: a ^{1}H-^{13}C solid-state NMR study at natural abundance. *European Biophysics Journal*, *34*, 987-996.

(116) Clarke, J. A., Seddon, J. M. et Law, R. V. (2009). Cholesterol containing model membranes studied by multinuclear solid state NMR spectroscopy. *Soft Matter*, *5*(2), 369-378.

(117) Scott, H. et Cheng, W. H. (1979). A theoretical model for lipid mixtures, phase transitions, and phase diagrams. *Biophysical journal*, *28*(1), 117-132.

(118) Nickels, J. D., Smith, M. D., Alsop, R. J., Himbert, S., Yahya, A., Cordner, D., Zolnierczuk, P., Stanley, C. B., Katsaras, J. et Cheng, X. (2019). Lipid rafts: buffers of cell membrane physical properties. *The Journal of Physical Chemistry B*, *123*(9), 2050-2056.

(119) Semrau, S. et Schmidt, T. (2009). Membrane heterogeneity‐from lipid domains to curvature effects. *Soft Matter*, *5*(17), 3174-3186.

(120) De Almeida, R. F., Fedorov, A. et Prieto, M. (2003). Sphingomyelin/phosphatidylcholine/cholesterol phase diagram: boundaries and composition of lipid rafts. *Biophysical journal*, *85*(4), 2406-2416.

(121) Halling, K. K., Ramstedt, B., Nyström, J. H., Slotte, J. P. et Nyholm, T. K. (2008). Cholesterol interactions with fluid-phase phospholipids: effect on the lateral organization of the bilayer. *Biophysical journal*, *95*(8), 3861-3871.

(122) Engberg, O., Hautala, V., Yasuda, T., Dehio, H., Murata, M., Slotte, J. P. et Nyholm, T. K. (2016). The affinity of cholesterol for different phospholipids affects lateral segregation in bilayers. *Biophysical journal*, *111*(3), 546-556.

(123) Pinigin, K. V. et Akimov, S. A. (2023). The Membrane-Mediated Interaction of Liquid-Ordered Lipid Domains in the Presence of Amphipathic Peptides. *Membranes*, *13*(10), 816.

(124) Pinigin, K. V., Galimzyanov, T. R. et Akimov, S. A. (2021). Amphipathic peptides impede lipid domain fusion in phase-separated membranes. *Membranes*, *11*(11), 797.

(125) Klinken, S. P. (2002). Red blood cells. *The international journal of biochemistry & cell biology*, *34*(12), 1513-1518.

(126) Hamidi, M. et Tajerzadeh, H. (2003). Carrier erythrocytes: an overview. *Drug delivery*, *10*(1), 9-20.

(127) Dodge, J. T., Mitchell, C. et Hanahan, D. J. (1963). The preparation and chemical characteristics of hemoglobin-free ghosts of human erythrocytes. *Archives of biochemistry and biophysics*, *100*(1), 119-130.

(128) Hoffman, J. F. (1958). Physiological characteristics of human red blood cell ghosts. *The Journal of general physiology*, *42*(1), 9-28.

(129) Steck, T. L. (1974). Preparation of impermeable inside-out and right-side-out vesicles from erythrocyte membranes. Dans *Methods in Membrane Biology: Volume 2* (p. 245-281). Springer.

(130) Schwoch, G. et Passow, H. (1973). Preparation and properties of human erythrocyte ghosts. *Molecular and cellular biochemistry*, *2*(2), 197-218.

(131) Veatch, S. L., Leung, S. S., Hancock, R. E. et Thewalt, J. L. (2007). Fluorescent probes alter miscibility phase boundaries in ternary vesicles. *The Journal of Physical Chemistry B*, *111*(3), 502-504.

(132) Gruebele, M. et Pielak, G. J. (2021). Dynamical spectroscopy and microscopy of proteins in cells. *Current Opinion in Structural Biology*, *70*, 1-7.

(133) Warnet, X. L., Arnold, A. A., Marcotte, I. et Warschawski, D. E. (2015). In-cell solid-state NMR: an emerging technique for the study of biological membranes. *Biophysical journal*, *109*(12), 2461-2466.

(134) Ghassemi, N., Poulhazan, A., Deligey, F., Mentink-Vigier, F., Marcotte, I. et Wang, T. (2021). Solid-state NMR investigations of extracellular matrixes and cell walls of algae, bacteria, fungi, and plants. *Chemical Reviews*, *122*(10), 10036-10086.

(135) Sani, M.-A. et Separovic, F. (2015). Progression of NMR studies of membrane-active peptides from lipid bilayers to live cells. *Journal of Magnetic Resonance*, *253*, 138-142.

(136) Sebastiao, M., Babych, M., Quittot, N., Kumar, K., Arnold, A. A., Marcotte, I. et Bourgault, S. (2023). Development of a novel fluorescence assay for studying lipid bilayer perturbation induced by amyloidogenic peptides using cell plasma membrane vesicles. *Biochimica et Biophysica Acta (BBA)-Biomembranes*, *1865*(3), 184118.

(137) Yan, X., Kumar, K., Miclette Lamarche, R., Youssef, H., Shaw, G. S., Marcotte, I., DeWolf, C. E., Warschawski, D. E. et Boisselier, E. (2021). Interactions between the cell membrane repair protein S100A10 and phospholipid monolayers and bilayers. *Langmuir*, *37*(32), 9652-9663.

(138) Poulhazan, A., Dickwella Widanage, M. C., Muszyński, A., Arnold, A. A., Warschawski, D. E., Azadi, P., Marcotte, I. et Wang, T. (2021). Identification and quantification of glycans in whole cells: architecture of microalgal polysaccharides described by solid-state nuclear magnetic resonance. *Journal of the American Chemical Society*, *143*(46), 19374-19388.

(139) Tardy-Laporte, C., Arnold, A. A., Genard, B., Gastineau, R., Morançais, M., Mouget, J.-L., Tremblay, R. et Marcotte, I. (2013). A ^{2}H solid-state NMR study of the effect of antimicrobial agents on intact Escherichia coli without mutating. *Biochimica et Biophysica Acta (BBA)-Biomembranes*, *1828*(2), 614-622.

(140) Kumari, S. et Booth, V. (2022). Antimicrobial Peptide Mechanisms Studied by Whole-Cell Deuterium NMR. *International journal of molecular sciences*, *23*(5), 2740.

(141) Cullis, P. et Grathwohl, C. (1977). Hydrocarbon phase transitions and lipid-protein interactions in the erythrocyte membrane. A ^{31}P NMR and fluorescence study. *Biochimica et Biophysica Acta (BBA)-Biomembranes*, *471*(2), 213-226.

(142) McLaughlin, A., Cullis, P., Hemminga, M., Hoult, D., Radda, G., Ritchie, G., Seeley, P. et Richards, R. (1975). Application of ^{31}P NMR to model and biological membrane systems. *FEBS letters*, *57*(2), 213-218.

(143) Davis, J., Maraviglia, B., Weeks, G. et Godin, D. (1979). Bilayer rigidity of the erythrocyte membrane ^{2}H-NMR of a perdeuterated palmitic acid probe. *Biochimica et Biophysica Acta (BBA)-Biomembranes*, *550*(2), 362-366.

(144) Maraviglia, B., Davis, J. H., Bloom, M., Westerman, J. et Wirtz, K. W. (1982). Human erythrocyte membranes are fluid down to− 5° C. *Biochimica et Biophysica Acta (BBA)-Biomembranes*, *686*(1), 137-140.

(145) Hore, P. J. (2015). *Nuclear magnetic resonance*. Oxford University Press, USA.

(146) Duer, M. J. (2008). *Solid state NMR spectroscopy: principles and applications*. John Wiley & Sons.

(147) McDermott, A. E. et Polenova, T. (2012). *Solid state NMR studies of biopolymers*. John Wiley & Sons.

(148) Davis, J. H. (1983). The description of membrane lipid conformation, order and dynamics by ^{2}H-NMR. *Biochimica et Biophysica Acta (BBA)-Reviews on Biomembranes*, *737*(1), 117-171.

(149) Kumar, A., Grace, R. C. R. et Madhu, P. (2000). Cross-correlations in NMR. *Progress in Nuclear Magnetic Resonance Spectroscopy*, *37*(3), 191-319.

(150) Juhl, D. W., Tošner, Z. et Vosegaard, T. (2020). Versatile NMR simulations using SIMPSON. Dans *Annual Reports on NMR Spectroscopy* (vol. 100, p. 1-59). Elsevier.

(151) Klauda, J. B., Roberts, M. F., Redfield, A. G., Brooks, B. R. et Pastor, R. W. (2008). Rotation of lipids in membranes: molecular dynamics simulation, ^{31}P spin-lattice relaxation, and rigid-body dynamics. *Biophysical journal*, *94*(8), 3074-3083.

(152) Gagnon, M.-C., Strandberg, E., Ulrich, A. S., Paquin, J.-F. et Auger, M. (2018). New insights into the influence of monofluorination on dimyristoylphosphatidylcholine

membrane properties: A solid-state NMR study. *Biochimica et Biophysica Acta (BBA)-Biomembranes*, *1860*(3), 654-663.

(153) Drouin, M., Wadhwani, P., Grage, S. L., Bürck, J., Reichert, J., Tremblay, S., Mayer, M. S., Diel, C., Staub, A. et Paquin, J. F. (2020). Monofluoroalkene-Isostere as a ^{19}F NMR Label for the Peptide Backbone: Synthesis and Evaluation in Membrane-Bound PGLa and (KIGAKI) 3. *Chemistry–A European Journal*, *26*(7), 1511-1517.

(154) Lesage, A. (2009). Indirect Coupling & Connectivity. *NMR Crystallography*, *4*, 209.

(155) Golota, N. C., Fredin, Z. P., Banks, D. P., Preiss, D., Bahri, S., Patil, P., Langford, W. K., Blackburn, C. L., Strand, E. et Michael, B. (2023). Diamond rotors. *Journal of Magnetic Resonance*, *352*, 107475.

(156) Warnet, X. L., Laadhari, M., Arnold, A. A., Marcotte, I. et Warschawski, D. E. (2016). A ^{2}H magic-angle spinning solid-state NMR characterisation of lipid membranes in intact bacteria. *Biochimica et Biophysica Acta (BBA)-Biomembranes*, *1858*(1), 146-152.

(157) Shcherbakov, A. A., Medeiros-Silva, J., Tran, N., Gelenter, M. D. et Hong, M. (2021). From angstroms to nanometers: measuring interatomic distances by solid-state NMR. *Chemical Reviews*, *122*(10), 9848-9879.

(158) Auger, M. (2010). Structural and dynamics studies of lipids by solid-state NMR. *Encycl. Mag. Reson. Chichester, UK: John Wiley & Sons Ltd*, 463-472.

(159) Engberg, O. et Huster, D. (2022). The Lipid Phase of the Stratum Corneum Studied by Solid-state NMR: A Not So Rigid Barrier. Dans *NMR Spectroscopy for Probing Functional Dynamics at Biological Interfaces* (p. 656-680).

(160) Holte, L. L., Peter, S. A., Sinnwell, T. M. et Gawrisch, K. (1995). ^{2}H nuclear magnetic resonance order parameter profiles suggest a change of molecular shape for phosphatidylcholines containing a polyunsaturated acyl chain. *Biophysical journal*, *68*(6), 2396-2403.

(161) Hwang, T. L., Kadkhodaei, M., Mohebbi, A. et Shaka, A. (1992). Coherent and incoherent magnetization transfer in the rotating frame. *Magnetic resonance in chemistry*, *30*(13), S24-S34.

(162) Huster, D., Arnold, K. et Gawrisch, K. (1998). Influence of docosahexaenoic acid and cholesterol on lateral lipid organization in phospholipid mixtures. *Biochemistry*, *37*(49), 17299-17308.

(163) Huster, D. et Gawrisch, K. (1999). NOESY NMR crosspeaks between lipid headgroups and hydrocarbon chains: spin diffusion or molecular disorder? *Journal of the American Chemical Society*, *121*(9), 1992-1993.

(164) Chen, Z.-J. et Stark, R. E. (1996). Evaluating spin diffusion in MAS-NOESY spectra of phospholipid multibilayers. *Solid State Nuclear Magnetic Resonance*, *7*(3), 239-246.

(165) Huster, D., Yao, X. et Hong, M. (2002). Membrane protein topology probed by 1H spin diffusion from lipids using solid-state NMR spectroscopy. *Journal of the American Chemical Society*, *124*(5), 874-883.

(166) Arnold, A. A., Bourgouin, J.-P., Genard, B., Warschawski, D. E., Tremblay, R. et Marcotte, I. (2018). Whole cell solid-state NMR study of Chlamydomonas reinhardtii microalgae. *Journal of biomolecular NMR*, *70*, 123-131.

(167) Guo, C., Fritz, M. P., Struppe, J., Wegner, S., Stringer, J., Sergeyev, I. V., Quinn, C. M., Gronenborn, A. M. et Polenova, T. (2021). Fast ^{19}F magic angle spinning NMR crystallography for structural characterization of fluorine-containing pharmaceutical compounds. *Analytical chemistry*, *93*(23), 8210-8218.

(168) Toke, O., O'Connor, R., Weldeghiorghis, T. K., Maloy, W. L., Glaser, R. W., Ulrich, A. S. et Schaefer, J. (2004). Structure of $(KIAGKIA)_3$ aggregates in phospholipid bilayers by solid-state NMR. *Biophysical journal*, *87*(1), 675-687.

(169) *World Health Organization (WHO), Global priority list of antibiotic-resistant bacteria to guide research, discovery and development of new antibiotics. Geneva, Switzerland.* (2021).

(170) *World Health Organization (WHO), Antimicrobial resistance global report on surveillance: 2014 summary.*

(171) Yeaman, M. R. et Yount, N. Y. (2003). Mechanisms of antimicrobial peptide action and resistance. *Pharmacological reviews*, *55*(1), 27-55.

(172) Hancock, R. E. et Scott, M. G. (2000). The role of antimicrobial peptides in animal defenses. *Proceedings of the National Academy of Sciences*, *97*(16), 8856-8861.

(173) Mookherjee, N., Anderson, M. A., Haagsman, H. P. et Davidson, D. J. (2020). Antimicrobial host defence peptides: functions and clinical potential. *Nature Reviews Drug Discovery*, 1-22.

(174) Mor, A. (2009). Multifunctional host defense peptides: antiparasitic activities. *The FEBS journal*, *276*(22), 6474-6482.

(175) Hoskin, D. W. et Ramamoorthy, A. (2008). Studies on anticancer activities of antimicrobial peptides. *Biochimica et Biophysica Acta (BBA)-Biomembranes*, *1778*(2), 357-375.

(176) Umnyakova, E. S., Zharkova, M. S., Berlov, M. N., Shamova, O. V. et Kokryakov, V. N. (2020, May). Human antimicrobial peptides in autoimmunity. *Autoimmunity*, *53*(3), 137-147.

(177) Lambert, P. (2002). Cellular impermeability and uptake of biocides and antibiotics in Gram-positive bacteria and mycobacteria. *Journal of applied microbiology*, *92*, 46S-54S.

(178) Costerton, J., Irvin, R., Cheng, K.-J. et Sutherland, I. (1981). The role of bacterial surface structures in pathogenesis. *CRC critical Reviews in Microbiology*, *8*(4), 303-338.

(179) Zhao, W., Róg, T., Gurtovenko, A. A., Vattulainen, I. et Karttunen, M. (2007). Atomic-scale structure and electrostatics of anionic palmitoyloleoylphosphatidylglycerol lipid bilayers with Na^+ counterions. *Biophysical journal*, *92*(4), 1114-1124.

(180) Guilhelmelli, F., Vilela, N., Albuquerque, P., Derengowski, L., Silva-Pereira, I. et Kyaw, C. (2013). Antibiotic development challenges: the various mechanisms of action of antimicrobial peptides and of bacterial resistance. *Frontiers in microbiology*, *4*, 353.

(181) Schmidtchen, A., Pasupuleti, M. et Malmsten, M. (2014). Effect of hydrophobic modifications in antimicrobial peptides. *Advances in colloid and interface science*, *205*, 265-274.

(182) Wessels, J. et Veerkamp, J. (1973). Some aspects of the osmotic lysis of erythrocytes III. Comparison of glycerol permeability and lipid composition of red blood cell membranes from eight mammalian species. *Biochimica et Biophysica Acta (BBA)-Biomembranes*, *291*(1), 190-196.

(183) Bechinger, B. (2015). The SMART model: Soft Membranes Adapt and Respond, also Transiently, in the presence of antimicrobial peptides. *Journal of Peptide Science*, *21*(5), 346-355.

(184) Aisenbrey, C., Marquette, A. et Bechinger, B. (2019). The mechanisms of action of cationic antimicrobial peptides refined by novel concepts from biophysical investigations. *Antimicrobial Peptides*, 33-64.

(185) Greco, I., Molchanova, N., Holmedal, E., Jenssen, H., Hummel, B. D., Watts, J. L., Håkansson, J., Hansen, P. R. et Svenson, J. (2020). Correlation between hemolytic activity, cytotoxicity and systemic in vivo toxicity of synthetic antimicrobial peptides. *Scientific reports*, *10*(1), 1-13.

(186) Balla, M., Bowie, J. et Separovic, F. (2004). Solid-state NMR study of antimicrobial peptides from Australian frogs in phospholipid membranes. *European Biophysics Journal*, *33*(2), 109-116.

(187) Marcotte, I., Wegener, K. L., Lam, Y.-H., Chia, B. C., de Planque, M. R., Bowie, J. H., Auger, M. et Separovic, F. (2003). Interaction of antimicrobial peptides from Australian amphibians with lipid membranes. *Chemistry and physics of lipids*, *122*(1-2), 107-120.

(188) Bechinger, B. (1999). The structure, dynamics and orientation of antimicrobial peptides in membranes by multidimensional solid-state NMR spectroscopy. *Biochimica et Biophysica Acta (BBA)-Biomembranes*, *1462*(1-2), 157-183.

(189) Poulhazan, A., Arnold, A. A., Warschawski, D. E. et Marcotte, I. (2018). Unambiguous ex situ and in cell 2D ^{13}C solid-state NMR characterization of starch and its constituents. *International journal of molecular sciences*, *19*(12), 3817.

(190) Rozek, T., Wegener, K. L., Bowie, J. H., Olver, I. N., Carver, J. A., Wallace, J. C. et Tyler, M. J. (2000). The antibiotic and anticancer active aurein peptides from the Australian bell frogs Litoria aurea and Litoria raniformis: the solution structure of aurein 1.2. *European Journal of Biochemistry*, *267*(17), 5330-5341.

(191) Wong, H., Bowie, J. H. et Carver, J. A. (1997). The solution structure and activity of caerin 1.1, an antimicrobial peptide from the Australian green tree frog, Litoria splendida. *European Journal of Biochemistry*, *247*(2), 545-557.

(192) Wegener, K. L., Brinkworth, C. S., Bowie, J. H., Wallace, J. C. et Tyler, M. J. (2001). Bioactive dahlein peptides from the skin secretions of the Australian aquatic frog Litoria dahlii: sequence determination by electrospray mass spectrometry. *Rapid Communications in Mass Spectrometry*, *15*(18), 1726-1734.

(193) Preté, P. S., Domingues, C. C., Meirelles, N. C., Malheiros, S. V., Goñi, F. M., de Paula, E. et Schreier, S. (2011). Multiple stages of detergent-erythrocyte membrane interaction− a spin label study. *Biochimica et Biophysica Acta (BBA)-Biomembranes*, *1808*(1), 164-170.

(194) Laydevant, F., Mahabadi, M., Llido, P., Bourgouin, J.-P., Caron, L., Arnold, A. A., Marcotte, I. et Warschawski, D. E. (2021). Growth-phase dependence of bacterial membrane lipid profile and labeling for in-cell solid-state NMR applications. *Biochimica et Biophysica Acta (BBA)-Biomembranes*, 183819.

(195) Pernet, F. et Tremblay, R. (2003). Effect of ultrasonication and grinding on the determination of lipid class content of microalgae harvested on filters. *Lipids*, *38*(11), 1191-1195.

(196) Balsgart, N. M., Mulbjerg, M., Guo, Z., Bertelsen, K. et Vosegaard, T. (2016). High throughput identification and quantification of phospholipids in complex mixtures. *Analytical chemistry*, *88*(4), 2170-2176.

(197) Rance, M. et Byrd, R. A. (1983). Obtaining high-fidelity spin-12 powder spectra in anisotropic media: Phase-cycled Hahn echo spectroscopy. *Journal of Magnetic Resonance (1969)*, *52*(2), 221-240.

(198) Moroi, Y. (1992). *Micelles: theoretical and applied aspects* (N. y. a. L. Plenum press, dir.). Springer Science & Business Media, Plenum Press, New York and London.

(199) Patist, A., Kanicky, J. R., Shukla, P. K. et Shah, D. O. (2002). Importance of micellar kinetics in relation to technological processes. *Journal of colloid and interface science*, *245*(1), 1-15.

(200) Ollivon, M., Lesieur, S., Grabielle-Madelmont, C. et Paternostre, M. t. (2000). Vesicle reconstitution from lipid‑detergent mixed micelles. *Biochimica et Biophysica Acta (BBA)-Biomembranes*, *1508*(1-2), 34-50.

(201) Høyrup, P., Davidsen, J. et Jørgensen, K. (2001). Lipid membrane partitioning of lysolipids and fatty acids: effects of membrane phase structure and detergent chain length. *The Journal of Physical Chemistry B*, *105*(13), 2649-2657.

(202) Heerklotz, H. et Seelig, J. (2000). Correlation of membrane/water partition coefficients of detergents with the critical micelle concentration. *Biophysical journal*, *78*(5), 2435-2440.

(203) Koley, D. et Bard, A. J. (2010). Triton X-100 concentration effects on membrane permeability of a single HeLa cell by scanning electrochemical microscopy (SECM). *Proceedings of the National Academy of Sciences*, *107*(39), 16783-16787.

(204) Ijare, O. B., Baskin, D. S. et Pichumani, K. (2019). Ex Vivo 1H NMR study of pituitary adenomas to differentiate various immunohistochemical subtypes. *Scientific reports*, *9*(1), 1-8.

(205) MacKenzie, A., Vyssotski, M. et Nekrasov, E. (2009). Quantitative analysis of dairy phospholipids by ^{31}P NMR. *Journal of the American Oil Chemists' Society*, *86*(8), 757-763.

(206) Nouri-Sorkhabi, M. H., Agar, N. S., Sullivan, D. R., Gallagher, C. et Kuchel, P. W. (1996). Phospholipid composition of erythrocyte membranes and plasma of mammalian blood including Australian marsupials; quantitative ^{31}P NMR analysis using detergent. *Comparative Biochemistry and Physiology Part B: Biochemistry and Molecular Biology*, *113*(2), 221-227.

(207) Bouhlel, Z., Arnold, A. A., Warschawski, D. E., Lemarchand, K., Tremblay, R. et Marcotte, I. (2019). Labeling strategy and membrane characterization of marine bacteria Vibrio splendidus by in vivo ^{2}H NMR. *Biochimica et Biophysica Acta (BBA)-Biomembranes*, *1861*(4), 871-878.

(208) Brian Chia, C., Gong, Y., Bowie, J. H., Zuegg, J. et Cooper, M. A. (2011). Membrane binding and perturbation studies of the antimicrobial peptides caerin, citropin, and maculatin. *Peptide Science*, *96*(2), 147-157.

(209) Lorenzon, E., Sanches, P., Nogueira, L., Bauab, T. et Cilli, E. M. (2013). Dimerization of aurein 1.2: effects in structure, antimicrobial activity and aggregation of Candida albicans cells. *Amino Acids*, *44*(6), 1521-1528.

(210) Ramezanzadeh, M., Saeedi, N., Mesbahfar, E., Farrokh, P., Salimi, F. et Rezaei, A. (2021). Design and characterization of new antimicrobial peptides derived from aurein 1.2 with enhanced antibacterial activity. *Biochimie*, *181*, 42-51.

(211) Yang, Y., Yao, H. et Hong, M. (2015). Distinguishing bicontinuous lipid cubic phases from isotropic membrane morphologies using ^{31}P solid-state NMR spectroscopy. *The Journal of Physical Chemistry B*, *119*(15), 4993-5001.

(212) Li, J., Koh, J.-J., Liu, S., Lakshminarayanan, R., Verma, C. S. et Beuerman, R. W. (2017). Membrane active antimicrobial peptides: translating mechanistic insights to design. *Frontiers in neuroscience*, *11*, 73.

(213) Shimokawa, N., Mukai, R., Nagata, M. et Takagi, M. (2017). Formation of modulated phases and domain rigidification in fatty acid-containing lipid membranes. *Physical Chemistry Chemical Physics*, *19*(20), 13252-13263.

(214) Lee, T.-H., Hofferek, V., Sani, M.-A., Separovic, F., Reid, G. E. et Aguilar, M.-I. (2021). The impact of antibacterial peptides on bacterial lipid membranes depends on stage of growth. *Faraday Discussions*.

(215) Gautier, R., Douguet, D., Antonny, B. et Drin, G. (2008). HELIQUEST: a web server to screen sequences with specific α-helical properties. *Bioinformatics*, *24*(18), 2101-2102.

(216) Harmouche, N. et Bechinger, B. (2018). Lipid-mediated interactions between the antimicrobial peptides magainin 2 and PGLa in bilayers. *Biophysical journal*, *115*(6), 1033-1044.

(217) Naito, A., Matsumori, N. et Ramamoorthy, A. (2018). Dynamic membrane interactions of antibacterial and antifungal biomolecules, and amyloid peptides, revealed by solid-state

NMR spectroscopy. *Biochimica et Biophysica Acta (BBA)-General Subjects*, *1862*(2), 307-323.

(218) Meier, M. et Seelig, J. (2010). Lipid and peptide dynamics in membranes upon insertion of n-alkyl- β -D-glucopyranosides. *Biophysical journal*, *98*(8), 1529-1538.

(219) Marcotte, I. et Auger, M. (2005). Bicelles as model membranes for solid-and solution-state NMR studies of membrane peptides and proteins. *Concepts in Magnetic Resonance Part A: An Educational Journal*, *24*(1), 17-37.

(220) Pius, J., Morrow, M. R. et Booth, V. (2012, Jan 10). ^{2}H solid-state nuclear magnetic resonance investigation of whole Escherichia coli interacting with antimicrobial peptide MSI-78. *Biochemistry*, *51*(1), 118-125.

(221) Macdonald, P. M., Sykes, B. D. et McElhaney, R. N. (1985). Fluorine-19 nuclear magnetic resonance studies of lipid fatty acyl chain order and dynamics in Acholeplasma laidlawii B membranes. A direct comparison of the effects of cis-and trans-cyclopropane ring and double-bond substituents on orientational order. *Biochemistry*, *24*(17), 4651-4659.

(222) McDonough, B., Macdonald, P. M., Sykes, B. D. et McElhaney, R. N. (1983). Fluorine-19 nuclear magnetic resonance studies of lipid fatty acyl chain order and dynamics in Acholeplasma laidlawii B membranes. A physical, biochemical, and biological evaluation of monofluoropalmitic acids as membrane probes. *Biochemistry*, *22*(22), 5097-5103.

(223) Gent, M., Cottam, P. F. et Ho, C. (1978). Fluorine-19 nuclear magnetic resonance studies of Escherichia coli membranes. *Proceedings of the National Academy of Sciences*, *75*(2), 630-634.

(224) Gent, M., Cottam, P. et Ho, C. (1981). A biophysical study of protein-lipid interactions in membranes of Escherichia coli. Fluoromyristic acid as a probe. *Biophysical journal*, *33*(2), 211-223.

(225) Potvin-Fournier, K., Valois-Paillard, G., Gagnon, M.-C., Lefèvre, T., Audet, P., Cantin, L., Paquin, J.-F., Salesse, C. et Auger, M. (2018). Novel approaches to probe the binding of recoverin to membranes. *European Biophysics Journal*, *47*, 679-691.

(226) Koch, K., Afonin, S., Ieronimo, M., Berditsch, M. et Ulrich, A. S. (2012). Solid-state ^{19}F-NMR of peptides in native membranes. *Solid state NMR*, 89-118.

(227) Strandberg, E., Wadhwani, P., Tremouilhac, P., Dürr, U. H. et Ulrich, A. S. (2006). Solid-state NMR analysis of the PGLa peptide orientation in DMPC bilayers: structural fidelity of ^{2}H-labels versus high sensitivity of ^{19}F-NMR. *Biophysical journal*, *90*(5), 1676-1686.

(228) Michurin, O. M., Afonin, S., Berditsch, M., Daniliuc, C. G., Ulrich, A. S., Komarov, I. V. et Radchenko, D. S. (2016). Delivering Structural Information on the Polar Face of Membrane-Active Peptides: ^{19}F-NMR Labels with a Cationic Side Chain. *Angewandte Chemie*, *128*(47), 14815-14819.

(229) Macdonald, P. M., Sykes, B. D. et McElhaney, R. N. (1984). Fluorine-19 nmr studies of lipid fatty acyl chain order and dynamics in Acholeplasma laidlawii B membranes. fluorine-19 nmr line shape and orientational order in the gel state. *Biochemistry*, *23*(19), 4496-4502.

(230) Gagnon, M.-C., Turgeon, B., Savoie, J.-D., Parent, J.-F., Auger, M. et Paquin, J.-F. (2014). Evaluation of the effect of fluorination on the property of monofluorinated dimyristoylphosphatidylcholines. *Organic & Biomolecular Chemistry*, *12*(28), 5126-5135.

(231) Gagnon, M.-C., Auger, M. et Paquin, J.-F. (2018). Progress in the synthesis of fluorinated phosphatidylcholines for biological applications. *Organic & Biomolecular Chemistry*, *16*(27), 4925-4941.

(232) Gagnon, M.-C., Ouellet, P., Auger, M. et Paquin, J.-F. (2018). Towards the use of monofluorinated dimyristoylphosphatidylcholines as ^{19}F NMR reporters in bacterial model membranes. *Journal of Fluorine Chemistry*, *206*, 43-47.

(233) Guimond-Tremblay, J., Gagnon, M.-C., Pineault-Maltais, J.-A., Turcotte, V., Auger, M. et Paquin, J.-F. (2012). Synthesis and properties of monofluorinated dimyristoylphosphatidylcholine derivatives: Potential fluorinated probes for the study of membrane topology. *Organic & Biomolecular Chemistry*, *10*(6), 1145-1148.

(234) Fulco, A. J. (1983). Fatty acid metabolism in bacteria. *Progress in Lipid Research*, *22*(2), 133-160.

(235) Ibarguren, M., López, D. J. et Escribá, P. V. (2014). The effect of natural and synthetic fatty acids on membrane structure, microdomain organization, cellular functions and human health. *Biochimica et Biophysica Acta (BBA)-Biomembranes*, *1838*(6), 1518-1528.

(236) Koynova, R., Tenchovl, B., Quinn, P. et Laggner, P. (1988). Structure and phase behavior of hydrated mixtures of L-dipalmitoylphosphatidylcholine and palmitic acid. Correlations between structural rearrangements, specific volume changes and endothermic events. *Chemistry and physics of lipids*, *48*(3-4), 205-214.

(237) Allen, M. E., Elani, Y., Brooks, N. J. et Seddon, J. M. (2021). The effect of headgroup methylation on polymorphic phase behaviour in hydrated N-methylated phosphoethanolamine: palmitic acid membranes. *Soft Matter*, *17*(23), 5763-5771.

(238) Pauls, K. P., MacKay, A. L. et Bloom, M. (1983). Deuterium nuclear magnetic resonance study of the effects of palmitic acid on dipalmitoylphosphatidylcholine bilayers. *Biochemistry*, *22*(26), 6101-6109.

(239) Inoue, T., Yanagihara, S.-i., Misono, Y. et Suzuki, M. (2001). Effect of fatty acids on phase behavior of hydrated dipalmitoylphosphatidylcholine bilayer: saturated versus unsaturated fatty acids. *Chemistry and physics of lipids*, *109*(2), 117-133.

(240) Marquardt, D., Heberle, F. A., Miti, T., Eicher, B., London, E., Katsaras, J. et Pabst, G. (2017). ^{1}H NMR shows slow phospholipid flip-flop in gel and fluid bilayers. *Langmuir*, *33*(15), 3731-3741.

(241) Bera, I. et Klauda, J. B. (2017). Molecular simulations of mixed lipid bilayers with sphingomyelin, glycerophospholipids, and cholesterol. *The Journal of Physical Chemistry B*, *121*(20), 5197-5208.

(242) Wang, T., Cady, S. D. et Hong, M. (2012). NMR determination of protein partitioning into membrane domains with different curvatures and application to the influenza M2 peptide. *Biophysical journal*, *102*(4), 787-794.

(243) Smart, B. E. (2001). Fluorine substituent effects (on bioactivity). *Journal of Fluorine Chemistry*, *109*(1), 3-11.

(244) Biffinger, J. C., Kim, H. W. et DiMagno, S. G. (2004). The polar hydrophobicity of fluorinated compounds. *ChemBioChem*, *5*(5), 622-627.

(245) Porcelli, F., Verardi, R., Shi, L., Henzler-Wildman, K. A., Ramamoorthy, A. et Veglia, G. (2008). NMR structure of the cathelicidin-derived human antimicrobial peptide LL-37 in dodecylphosphocholine micelles. *Biochemistry*, *47*(20), 5565-5572.

(246) Nielsen, N. C., Malmendal, A. et Vosegaard, T. (2004). Techniques and applications of NMR to membrane proteins. *Molecular membrane biology*, *21*(3), 129-141.

(247) Aucoin, D., Camenares, D., Zhao, X., Jung, J., Sato, T. et Smith, S. O. (2009). High-resolution ^{1}H MAS RFDR NMR of biological membranes. *Journal of Magnetic Resonance*, *197*(1), 77-86.

(248) Mandala, V. S., Williams, J. K. et Hong, M. (2018). Structure and dynamics of membrane proteins from solid-state NMR. *Annual review of biophysics*, *47*, 201-222.

(249) Marassi, F. M. et Opella, S. J. (1998). NMR structural studies of membrane proteins. *Current Opinion in Structural Biology*, *8*(5), 640-648.

(250) Macdonald, P., Sykes, B., McElhaney, R. et Gunstone, F. (1985). ^{19}F NMR studies of lipid fatty acyl chain order and dynamics in Acholeplasma laidlawii B membranes. Orientational order in the presence of a series of positional isomers of cis-octadecenoic acid. *Biochemistry*, *24*, 177-184.

(251) Kumar, K., Arnold, A. A., Gauthier, R., Mamone, M., Paquin, J.-F., Warschawski, D. E. et Marcotte, I. (2024). ^{19}F solid-state NMR approaches to probe antimicrobial peptide interactions with membranes in whole cells. *Biochimica et Biophysica Acta (BBA)-Biomembranes*, 184269.

(252) Penkauskas, T., Zentelyte, A., Ganpule, S., Valincius, G. et Preta, G. (2020). Pleiotropic effects of statins via interaction with the lipid bilayer: A combined approach. *Biochimica et Biophysica Acta (BBA)-Biomembranes*, *1862*(9), 183306.

(253) Galiullina, L. F., Scheidt, H. A., Huster, D., Aganov, A. et Klochkov, V. (2019). Interaction of statins with phospholipid bilayers studied by solid-state NMR spectroscopy. *Biochimica et Biophysica Acta (BBA)-Biomembranes*, *1861*(3), 584-593.

(254) Kuba, J. O., Yu, Y. et Klauda, J. B. (2021). Estimating localization of various statins within a POPC bilayer. *Chemistry and physics of lipids*, *236*, 105074.

(255) Chan, J. C. et Tycko, R. (2003). Recoupling of chemical shift anisotropies in solid-state NMR under high-speed magic-angle spinning and in uniformly ^{13}C-labeled systems. *The Journal of Chemical Physics*, *118*(18), 8378-8389.

(256) Lau, S., Stanhope, N., Griffin, J., Hughes, E. et Middleton, D. A. (2019). Drug orientations within statin-loaded lipoprotein nanoparticles by 19 F solid-state NMR. *Chemical Communications*, *55*(88), 13287-13290.

(257) Mapley, B., Townsend, D., Griffin, J., Ashton, L. et Middleton, D. A. (2021). ^{19}F Solid-State NMR and Vibrational Raman Characterization of Corticosteroid Drug-Lipid Membrane Interactions. *ChemPlusChem*, *86*(11), 1517-1523.

(258) Smith, S. O., Hamilton, J., Salmon, A. et Bormann, B. J. (1994). Rotational resonance NMR determination of intra-and intermolecular distance constraints in dipalmitoylphosphatidylcholine bilayers. *Biochemistry*, *33*(20), 6327-6333.

(259) Tang, M., Waring, A. J. et Hong, M. (2007). Trehalose-protected lipid membranes for determining membrane protein structure and insertion. *Journal of Magnetic Resonance*, *184*(2), 222-227.

(260) Lin, P., Chen, X., Moktan, H., Arrese, E. L., Duan, L., Wang, L., Soulages, J. L. et Zhou, D. H. (2014). Membrane attachment and structure models of lipid storage droplet protein 1. *Biochimica et Biophysica Acta (BBA)-Biomembranes*, *1838*(3), 874-881.

(261) Hirsh, D. J., Hammer, J., Maloy, W. L., Blazyk, J. et Schaefer, J. (1996). Secondary structure and location of a magainin analogue in synthetic phospholipid bilayers. *Biochemistry*, *35*(39), 12733-12741.

(262) Smith, S. O., Kawakami, T., Liu, W., Ziliox, M. et Aimoto, S. (2001). Helical structure of phospholamban in membrane bilayers. *Journal of molecular biology*, *313*(5), 1139-1148.

(263) Toke, O., Maloy, W. L., Kim, S. J., Blazyk, J. et Schaefer, J. (2004). Secondary structure and lipid contact of a peptide antibiotic in phospholipid bilayers by REDOR. *Biophysical journal*, *87*(1), 662-674.

(264) Toraya, S., Nishimura, K. et Naito, A. (2004). Dynamic structure of vesicle-bound melittin in a variety of lipid chain lengths by solid-state NMR. *Biophysical journal*, *87*(5), 3323-3335.

(265) Shu, N. S., Chung, M. S., Yao, L., An, M. et Qiang, W. (2015). Residue-specific structures and membrane locations of pH-low insertion peptide by solid-state nuclear magnetic resonance. *Nature Communications*, *6*(1), 7787.

(266) Griffiths, J., Bennett, A., Engelhard, M., Siebert, F., Raap, J., Lugtenburg, J., Herzfeld, J. et Griffin, R. (2000). Structural investigation of the active site in bacteriorhodopsin: geometric constraints on the roles of Asp-85 and Asp-212 in the proton-pumping mechanism from solid state NMR. *Biochemistry*, *39*(2), 362-371.

(267) Crocker, E., Patel, A. B., Eilers, M., Jayaraman, S., Getmanova, E., Reeves, P. J., Ziliox, M., Khorana, H. G., Sheves, M. et Smith, S. O. (2004). Dipolar assisted rotational resonance NMR of tryptophan and tyrosine in rhodopsin. *Journal of biomolecular NMR*, *29*, 11-20.

(268) Hiller, M., Krabben, L., Vinothkumar, K. R., Castellani, F., van Rossum, B. J., Kühlbrandt, W. et Oschkinat, H. (2005). Solid-state magic-angle spinning NMR of outer-membrane protein G from Escherichia coli. *ChemBioChem*, *6*(9), 1679-1684.

(269) Volke, F. et Pampel, A. (1995). Membrane hydration and structure on a subnanometer scale as seen by high resolution solid state nuclear magnetic resonance: POPC and POPC/$C_{12}EO_4$ model membranes. *Biophysical journal*, *68*(5), 1960-1965.

(270) Ramamoorthy, A. et Xu, J. (2013). 2D $^{1}H/^{1}H$ RFDR and NOESY NMR experiments on a membrane-bound antimicrobial peptide under magic angle spinning. *The Journal of Physical Chemistry B*, *117*(22), 6693-6700.

(271) Cramariuc, O., Rog, T., Javanainen, M., Monticelli, L., Polishchuk, A. V. et Vattulainen, I. (2012). Mechanism for translocation of fluoroquinolones across lipid membranes. *Biochimica et Biophysica Acta (BBA)-Biomembranes*, *1818*(11), 2563-2571.

(272) Roos, M., Wang, T., Shcherbakov, A. A. et Hong, M. (2018). Fast magic-angle-spinning ^{19}F spin exchange NMR for determining nanometer ^{19}F-^{19}F distances in proteins and pharmaceutical compounds. *The Journal of Physical Chemistry B*, *122*(11), 2900-2911.

(273) Edidin, M. (2003). Lipids on the frontier: a century of cell-membrane bilayers. *Nature reviews Molecular cell biology*, *4*(5), 414-418.

(274) Separovic, F., Hofferek, V., Duff, A. P., McConville, M. J. et Sani, M.-A. (2022). In-cell DNP NMR reveals multiple targeting effect of antimicrobial peptide. *Journal of Structural Biology: X*, *6*, 100074.

(275) Kuzhelev, A. A., Dai, D., Denysenkov, V. et Prisner, T. F. (2022). Solid-like dynamic nuclear polarization observed in the fluid phase of lipid bilayers at 9.4 T. *Journal of the American Chemical Society*, *144*(3), 1164-1168.

(276) Lorenzón, E., Sanches, P., Nogueira, L., Bauab, T. et Cilli, E. M. (2013). Dimerization of aurein 1.2: effects in structure, antimicrobial activity and aggregation of Candida albicans cells. *Amino Acids*, *44*, 1521-1528.

(277) De Zotti, M. (2022). Bloody spin: I caught you at last. *Biophysical journal*, *121*(8), 1352-1353.